

Syracuse University

SURFACE

Physics - Dissertations

College of Arts and Sciences

12-2011

The Design and Construction of a Green Laser and Fabry-Perot Cavity System for Jefferson Lab's Hall A Compton Polarimeter

Abdurahim Rakhman
Syracuse University

Follow this and additional works at: https://surface.syr.edu/phy_etd



Part of the [Physics Commons](#)

Recommended Citation

Rakhman, Abdurahim, "The Design and Construction of a Green Laser and Fabry-Perot Cavity System for Jefferson Lab's Hall A Compton Polarimeter" (2011). *Physics - Dissertations*. 117.

https://surface.syr.edu/phy_etd/117

This Dissertation is brought to you for free and open access by the College of Arts and Sciences at SURFACE. It has been accepted for inclusion in Physics - Dissertations by an authorized administrator of SURFACE. For more information, please contact surface@syr.edu.

Abstract

A high finesse Fabry-Perot cavity with a frequency doubled green laser (CW, 532 nm) have been built and installed in Hall A of Jefferson Lab for high precision Compton polarimetry project in spring of 2010. It provides a high intensity circularly polarized photon target for measuring the polarization of electron beam with energies from 1.0 GeV to 11.0 GeV in a nondestructive manner. The IR beam (CW, 1064 nm) from a Ytterbium doped fiber laser amplifier seeded by a Nd:YAG narrow linewidth NPRO laser is frequency doubled in by a single-pass Periodically Poled Lithium Niobate (PPMgLN) crystal. The maximum achieved green power at 5 W IR pump power was 1.74 W with a total conversion efficiency of 34.8%. The frequency locking of this green light to the cavity resonance frequency is achieved by giving a feedback to Nd:YAG crystal via laser piezoelectric (PZT) actuator by Pound-Drever-Hall (PDH) technique. The data shows the maximum amplification gain of our cavity is about 4,000 with a corresponding maximum intra-cavity power of 3.7 kW. The polarization transfer function has been measured in order to determine the intra-cavity laser polarization within the measurement uncertainty of 0.7%. The PREx experiment at JLab, used this system for the first time and achieved 1.0% precision in electron beam polarization measurement at 1.0 GeV.

**THE DESIGN AND CONSTRUCTION OF A GREEN LASER
AND FABRY-PEROT CAVITY SYSTEM FOR
JEFFERSON LAB'S HALL A COMPTON POLARIMETER**

by
Abdurahim Rakhman

B.S./M.S., Xinjiang University, China 2000
Diploma, The Abdus Salam ICTP, Italy 2003
M.S., Syracuse University 2005

Dissertation
Submitted in Partial Fulfillment of the Requirements for the Degree of
Doctor of Philosophy in Physics

Syracuse University
December, 2011

Copyright © 2011 Abdurahim Rakhman

All Rights Reserved

*To my lovely wife Fazilat
To my family*

“You can’t connect the dots looking forward; you can only connect them looking backwards. So you have to trust that the dots will somehow connect in your future. You have to trust in something – your gut, destiny, life, karma, whatever. This approach has never let me down, and it has made all the difference in my life.”

Steve Jobs (Stanford commencement speech, June 2005)

Acknowledgements

Throughout the long journey of my graduate career, I received endless support and help from countless people both in research and in life. This thesis would not have been possible without the great help from them.

I feel extremely fortunate to have been able to participate in the Compton laser project at JLab where I've had the opportunity to grow academically and professionally and also had an opportunity to work and make friends with many people.

Taking this opportunity, I want to express my deepest gratitude to my academic and research advisor Prof. Paul Souder. It is Paul who gave me constant support, encouragement, guidance and freedom over the last six years. Paul has been extremely supportively identifying critical steps to achieving success in my graduate life. Without him, I wouldn't have been able to reach this level.

I would like to thank my JLab on-site supervisor Dr. Sirish Nanda who brought me involved in the Jefferson Lab collaboration and gave me the opportunity to work and learn many things in Compton lab where I got lot of passion and knowledge on lasers and optics. I am very grateful to his guidance and help during my stay at JLab over the last four years.

I'm very grateful to Prof. Gordon Cates at UVA for all the inspiration, enthusiasm and confidence he gave me through many valuable conversations. The Compton laser project would not have been successful without his constant help and precious advice.

I'm very lucky to have met with Prof. Kent Paschke from UVA. Kent was an energetic physicist with invaluable resource of knowledge. I learned not only an immense amount of physics from working with him but also learned how to be a successful person in anything I'm doing in my life.

I'm very proud of having such good friends like Al Tobias and Vladimir Nelyubin in my life. Because of their immeasurable help and effort, Compton installation became 10 times more successful than what we originally have thought. I was very impressed by their experiences and wonderful personality throughout my life even after the Compton project. I can't forget those nights we spent in the tunnel during the installation of cavity and always miss those meals we had together. Al and Vladimir gave me all the joy I have in my life during my stay in Virginia.

I also would like to thank all the physics professors at SU who taught my graduate courses there. Special thanks to Diane Sanderson, Linda Pesce, Linda Terramiggi, Penny Davis and Patti Ford for their administrative support and help during my graduate life in physics department at SU.

Many thanks to Robert Michaels, Kirishna Kumar, Gregg Franklin, Brian Quinn, Rich Holmes, Alexandre Camsonne, Eugene Chudakov, Seamus Riordan, Juliette Mammei, Dustin McNulty and all the other scientists, professors, postdocs and grad students in the collaboration who made the parity collaboration successful and prosperous.

I thank JLab designers Joyce Miller and Alan Gavalya for their great help and suggestion with mechanical design of the cavity and other parts. Many thanks to Casy Apeldoorn in JLab machine shop for finishing the parts in time regardless of many short notices. Thanks to Greg Marble and Elliott Smythe in JLab vacuum group for all the support and help. Many thanks to Dan Sexton in JLab FEL group for helping with the cavity locking electronics development. Special thanks to Matt Poelker and John Hansknecht for all the help with laser and optics related issues. Thanks to Christ Curtis in JLab test lab for helping with setting up a cleanroom in Compton lab. Thanks to all the other accelerator division and Hall A staffs for being so supportive.

I have to thank all my friends at JLab who shared many experience with me and made life a bit more exciting. Many thanks to Ramesh Subedi for all his help and tips about living and working in the Newport News. Thanks to Amrendra Narayan,

Ali Akguner, Nebi Demez, Ibrahim Albayrak, Ozgur Ates, Mustafa Canan, Serkan Golge, Mohamed Hafez, Kalyan Allada, Eric Fuchey, Rupesh Silval, Luis Mercado Mark Dalton, Megan Friend, Diana Parno, Tharanga Jinasundera, Chunhua Song, Russell Kincaid, Sadia Khalil and Lawrence Lee for their friendship and all the good time.

I would like to thank my mother and late father for all their love, their persistent support and everything they have done for me in their life. I'd like to thank my brother and two sisters who gave me the desire to learn and always encouraged me to do what was interesting to me. Their support and love has always been the constant in my life, and encourage me to overcome difficulties in my life.

Lastly, I would like to thank my lovely wife, Fazilat, for all her love and support to me through both easy and difficult times during all these years together. I'm indebted for her sacrifice, patience and understanding, and without her, I don't think I could have achieved anything. I would like to thank my two young sons, Arslan (4) and Arman (2), for making home less noisy while I'm writing this dissertation. They give me more passion and energy in my life when I'm looking at them.

Abdurahim Rakhman
Newport News, VA
November, 2011

Contents

Abstract	i
Acknowledgements	v
Table of Contents	viii
List of Figures	x
List of Tables	xv
1 Introduction	1
2 Experimental Apparatus	5
2.1 Overview	5
2.2 TJNAF	6
2.3 Hall A	7
2.3.1 Beam Monitors	7
2.3.2 Target and Raster	9
2.3.3 High Resolution Spectrometers (HRS)	10
2.4 Electron Beam	11
2.4.1 Polarized Electron Source	11
2.4.2 Polarized Electron Beam	15
2.5 Electron Beam Polarimetry	22
2.5.1 Mott Polarimetry	23
2.5.2 Møller Polarimetry	26
3 Compton Polarimetry	30
3.1 Measurement Principle	30
3.1.1 The Physics of Compton Scattering	31
3.1.2 Compton Cross Section and Asymmetry	35
3.1.3 Interaction Luminosity	39
3.1.4 Methods of Electron Beam Polarization Measurement	41
3.2 Compton Polarimetry	47
3.2.1 Overview	47

3.2.2	Compton Upgrade Project in Hall A at JLab	51
3.3	Elements of Compton Polarimeter	53
3.3.1	Magnetic Chicane	57
3.3.2	Optical Setup	60
3.3.3	Photon Detector	63
3.3.4	Electron Detector	64
3.3.5	Data Acquisition	66
4	Building Green Laser Source via Second Harmonic Generation	70
4.1	Motivation	70
4.2	Nonlinear Optics	71
4.2.1	Nonlinear Optical Interactions	71
4.2.2	Second Harmonic Generation	73
4.2.3	Phase-matching	77
4.2.4	Nonlinear Interactions with Focused Gaussian Beam	81
4.2.5	Periodically Poled Materials	82
4.3	Tuning and Tolerances in Quasi-phase Matching	83
4.3.1	Domain Period	84
4.3.2	Spectral Bandwidth	85
4.3.3	Temperature Bandwidth	85
4.3.4	Angle Tuning and Angular Acceptance	86
4.4	Limitations on Nonlinear Devices	87
4.4.1	Photo-refraction	87
4.4.2	Thermo-optic Effect	88
4.5	Frequency Doubling with PPLN Crystal	89
4.5.1	Periodically Poled Lithium Niobate Crystals	89
4.5.2	Experimental Setup	91
4.5.3	Properties of the Second Harmonic Beam	95
5	Fabry-Perot Cavity	102
5.1	Cavity in an Electro Magnetic Field	102
5.1.1	Gaussian Beams	103
5.1.2	High Reflectance Mirrors	109
5.1.3	Optical Response of Fabry-Perot Cavity	113
5.2	Laser Frequency Control	120
5.2.1	Variations in Laser and Cavity Resonance Frequencies	120
5.2.2	Feedback Control of Laser Frequency	122
5.2.3	Pound-Drever-Hall Technique	125
5.3	Description of the Cavity System	131
5.3.1	Mechanical Design of the Cavity	131
5.3.2	The Control System	138
5.4	Experimental Procedures	144
5.4.1	Cavity Mode Matching	145

5.4.2	Cavity and Beam Alignment	154
5.4.3	Determination of Cavity Parameters	158
6	Beam Polarization	166
6.1	Polarization of Light	167
6.1.1	Introduction	167
6.1.2	Jones Representation	169
6.1.3	Stokes Parameters	170
6.1.4	Creating Circularly Polarized Light	172
6.2	Intra-Cavity Polarization	176
6.2.1	Laser Polarization Measurement	177
6.2.2	Polarization Transfer Function	184
6.2.3	Determination of the DOCP at the CIP	189
6.2.4	The Birefringence of the Cavity System	193
6.3	Electron Beam Polarization	194
6.3.1	Compton Spectrum	194
6.3.2	Experimental Asymmetry	196
6.3.3	Electron Beam Polarization	197
7	Conclusions	200
	Appendices	203
A	Technical Drawings of Cavity System	203
	Bibliography	208
	Biographical Data	219

List of Figures

2.1	TJNAF Accelerator Layout	7
2.2	General Hall A configuration.	8
2.3	Two High Resolution Spectrometers (HRS).	10
2.4	A diagram of the bandgap and energy levels for strained GaAs. The arrows indicate the allowed transitions for right and left helicity photons.	13
2.5	One of the electron beam helicity patterns (octet) for PREx.	14
2.6	Spin orientation of electrons in the electron beam reference.	19
2.7	Schematic of the 5 MeV Mott scattering chamber with detectors.	24
2.8	Layout of Hall A Møller polarimeter.	27
3.1	Feynman Diagrams for Compton Scattering.	30
3.2	A diagram of Compton scattering.	31
3.3	Maximum energy of the scattered photon as a function of the crossing angle.	32
3.4	Scattered photon energy k' as a function of scattering angle θ_γ	34
3.5	Scattered electron energy E' as a function of scattering angle θ_e	35
3.6	Compton cross section and asymmetry plot.	37
3.7	Longitudinal differential asymmetry at 1.0 GeV and 6.0 GeV electron beam energies for two different photon energies.	38
3.8	Electron and Photon Beam Crossing.	39
3.9	Luminosity as function of crossing angle and photon beam size.	41
3.10	The luminosity as a function of the distance between the centroids of the electron and photon beams.	42
3.11	A summary plot of Compton polarimetry projects in terms of beam energy and current it operates.	50
3.12	A schematic of a simplified view of Compton polarimeter in Hall A at JLab.	54
3.13	A in-scale 3D view of Compton polarimeter in Hall A accelerator tunnel.	55
3.14	A schematic of Hall A Compton polarimeter with the location of the various elements that make up the polarimeter.	56
3.15	Vertical deviation of electron beam trajectory in magnetic chicane.	59
3.16	A 3D view of the Fabry-Perot cavity and optical elements on optics table in Hall A Compton polarimeter at JLab.	61

3.17	The GSO photon detector	63
3.18	Electron detector assembly and Si micro strips.	64
3.19	Schematic of electron and photon detector layout in polarimeter.	65
3.20	Simplified schematic of the upgraded integrating Compton DAQ.	67
3.21	Typical small (normal) and big (background) signals with the thresholds for the Integrating FADC DAQ.	68
4.1	Geometry of Second Harmonic Generation.	73
4.2	SHG conversion efficiency as a function of phase mismatch.	77
4.3	SHG output power as a function of crystal length (L) normalized to the coherence length (L_c) for various phase matching conditions: perfectly phasematched, first-order quasi-phasematched, not phasematched.	78
4.4	Schematic representation of second harmonic generation in a periodically poled nonlinear crystal with a uniform grating period.	83
4.5	Crystal structure of LiNbO_3	89
4.6	A schematic of experimental setup used for frequency doubling in PPLN.	92
4.7	The geometry of PPLN Crystal.	92
4.8	The schematic of temperature stabilizing oven for PPLN crystal to achieve quasi-phase matching.	94
4.9	The PPLN crystal is mounted inside an oven on a stage. The green beam is generated after the incoming IR beam is passing through the crystal that effectively doubles its frequency.	94
4.10	Measured temperature tuning curve for PPLN. The solid line is the theoretical values and the dotted points are the experimental results.	97
4.11	532 nm average power (solid circles) in PPLN and corresponding phase matching temperature (open squares) versus 1064 nm pump power of the Yb doped fiber amplifier. The continuous line is the theoretical fit to extract the normalized SHG conversion efficiency.	98
4.12	IR and Green beam profiles in 2D and 3D measured by Spiricon CCD camera.	99
4.13	Divergence profile of green beam. Closed and Open circles are the beam waist sizes in x (horizontal) and y (vertical) directions, respectively and continuous line shows the theoretical fit to extract the M^2 factor.	99
4.14	The stability of SHG output power was monitored at 1.74 W for 12 hours.	100
5.1	A longitudinal profile of a Gaussian beam.	105
5.2	Hermite-Gaussian Modes.	108
5.3	Laguerre-Gaussian Modes.	109
5.4	Reflection and transmission of optical fields from a dielectric layer on a mirror substrate.	110
5.5	Fabry-Perot cavity in optical field.	114

5.6	Circulating and reflected power in a cavity plotted versus the resonance frequency ν is normalized to the cavity free spectral range (FSR). . .	117
5.7	Cavity gain $G(\Delta\nu)$ and phase $\Phi_r(\Delta\nu)$ of a 85 cm symmetric cavity, with two different sets of identical mirror with bandwidth of 3kHz and 10 kHz, respectively.	119
5.8	A block diagram shows a laser frequency stabilization feedback loop. .	123
5.9	A PZT transducer bonded to the top non-optical face of the Nd:YAG crystal of a non-planar ring oscillator (NPRO) laser for fast frequency actuation while the Nd:YAG crystal is placed on a Peltier module (TEC) for slow frequency variation.	124
5.10	Principles of Pound-Drever-Hall method. The beam reflected by the cavity is extracted from the incident beam and detected by a fast photodiode. The signal obtained is then multiplied by a demodulation signal in mixer. The electronic circuit allows to build an error signal which is summed with the modulation signal before being sent to an actuator to control the laser frequency.	126
5.11	The Pound-Drever-Hall error signal along (red curve) with the corresponding reflected signal (blue curve) versus the frequency deviation between the laser frequency (ν) and cavity resonance frequency (ν_c). The modulation frequency $\Omega = 928$ kHz, cavity finesse (\mathcal{F}) is around 10,000, the phase modulation index $\beta = 0.4$ and cavity length is 85 cm.	127
5.12	The Pound-Drever-Hall error signal ϵ (red curve) versus the frequency deviation between the laser frequency ν and cavity resonance frequency ν_c . The slope (blue curve) shows the proportionality constant D . The modulation frequency $\Omega = 928$ kHz, cavity finesse (\mathcal{F}) is around 10,000 and the phase modulation index $\beta = 0.4$	130
5.13	Schematic of crossing angle between the laser beam and electron beam.	132
5.14	Schematic of cavity mirror geometry.	133
5.15	A front view of the cavity sitting on an optics table with pneumatic isolators.	134
5.16	The structure of gimbal mounts used for cavity mirror alignment.	134
5.17	Two picomotors are mounted to a pair of gimbal mounts that are used to align a cavity mirror on one side of the cavity.	135
5.18	(a) Technical drawing of the stainless steel flange with the vacuum window is welded to it. (b) Technical drawing of the aluminum mount that holds a 0.5 inch turning mirror oriented at 45° with respect to the incident laser beam.	136
5.19	A slot with an opening of 1cm in the aluminum mount allows the electron beam passes through and crosses with the laser beam at the center of the cavity.	136
5.20	Technical drawing of the cavity with two ion pumps attached to it.	137

5.21	A picture shows the cavity installed in Hall A accelerator tunnel at JLab. The electron beam pipe above the cavity is used for a straight beam when the Compton chicane is not used.	138
5.22	Functional view of the feedback electronics built by Saclay.	140
5.23	A printed circuit board (PCB) layout of the feedback electronics built by Saclay used for cavity locking.	141
5.24	A schematic illustration of automatic locking procedure of cavity. . .	142
5.25	A functional view of the cavity system.	143
5.26	A Gaussian beam in a cavity.	145
5.27	A schematic illustration of axial and angular mismatch of the laser to the cavity.	147
5.28	A schematic illustration of waist size and location mismatch.	147
5.29	A counter plot shows the coupling coefficient of fundamental mode (TEM_{00}) to the cavity versus mismatch in waist sizes and waist locations of the laser and cavity.	148
5.30	A schematic of optics and electronic feedback system.	150
5.31	Schematic view of the optical scheme with the locations of optical elements (units are in mm).	151
5.32	A to-scale schematic drawing of laser and optical components by OptoCad.	152
5.33	The calculated beam size versus the distance along the beam path from the face of PPLN doubler.	153
5.34	A picture shows the steering mirror M_1 mounted on a motorized mirror frame with two servo actuators and the lens L_3 is placed on a motorized linear stage equipped with another servo actuator.	155
5.35	A schematic shows a periscope system composed of two motorized mirrors achieve displacement and tilt of laser spot on cavity mirror. . . .	155
5.36	A schematic of a pinhole used for aligning the laser beam to cavity optical axis.	156
5.37	The fundamental mode and higher order modes observed by a CCD camera at the end of the cavity.	158
5.38	Decay time of the cavity. The theoretical curve (red line) is fitted to the experimental data (black dots) to extract the cavity decay time. The finesse is corrected for the laser decay time of $6\mu s$	160
5.39	A snapshot of a digital oscilloscope shows cavity locking signals correspond to locked and unlocked state of the cavity.	162
5.40	A theoretical fit to the reflection and transmission signals used to extract the cavity bandwidth when the cavity is in “open loop” mode. .	163
5.41	The intra-cavity power stability is monitored for 7 hours.	164
6.1	The rotated polarization ellipse.	168
6.2	A schematic illustration of extracting the cavity-reflected beam from the incident beam.	176

6.3	A schematic illustration of a polarization measurement station with linear polarizer and a detector.	177
6.4	A plot of linear polarizer scan angle versus the transmitted power that was used for measuring the polarization. The dots are the data and the blue and red curves are the theoretical fit to extract the polarization.	180
6.5	A schematic of polarization measurement station at the cavity exit line.	181
6.6	Extraction of Stokes parameters from a quarter-wave plate scan at the cavity exit. The plot shows a total power measured by two photodiodes S_1 and S_2 versus the scan angle.	183
6.7	A propagation of polarization ellipse from the CIP to the entrance of cavity exit line. The schematic illustrates a case when the cavity between the two stands is removed.	185
6.8	A schematic illustration of an eigenstate generator at the CIP.	187
6.9	A counter view of the transfer function for the left and right circularly polarized states of the CIP with respect to the exit DOCP and ellipse angle.	189
6.10	The evolution of polarization at the cavity exit versus time with electron beam in Compton chicane.	191
6.11	Scattered Compton photon rates (red) along with the background rates (black) during a run.	195
6.12	A measured Compton photon energy spectrum.	195
6.13	Histograms of the Compton asymmetry for an entire run.	197
6.14	Histogram of a background subtracted Compton asymmetry taken for every pair in a single one hour run.	198
6.15	Asymmetry versus left and right circularly polarized laser cycles for an entire run. An average asymmetry is used for calculating the electron beam polarization for a typical run.	198
A.1	Cavity essembly.	204
A.2	Gimbal Mounts.	205
A.3	Cavity Mirorr Holder Mount.	206
A.4	Cavity Mirorr Holder.	207

List of Tables

3.1	A summary table of Compton polarimetry projects.	49
3.2	Comparison of relevant quantities of the Compton kinematics for the infrared ($\lambda_\gamma = 1064$ nm), green ($\lambda_\gamma = 532$ nm) and ultraviolet ($\lambda_\gamma = 248$ nm) lasers with different cavity gain G for achieving a statistical precision of $\frac{\delta\mathcal{P}_e}{\mathcal{P}_e} = 1.0\%$. The following parameters are used: $E_e = 1.0$ GeV, $I_e = 50$ μ A, $\mathcal{P}_e = 90\%$, $\mathcal{P}_\gamma = 100\%$, $\sigma_e = 100$ μ m, $\sigma_\gamma = 100$ μ m, $\alpha_c = 23.5$ mrad. $\langle\mathcal{A}_E^L\rangle$ is the longitudinal mean analyzing power for the energy weighted method with a detection threshold set to 0. Y_{Det} is the maximum vertical gap between the primary and scattered electron beams after the 3rd dipole. The detection efficiency of photon detector assumed as 100%.	52
4.1	Nonlinear coefficients of some popular nonlinear materials (The comparisons are for the wavelength of 1064 nm). [57–59]	90
4.2	Sellmeier coefficients for PPLN crystal.	96
5.1	Characterization of the cavity parameters during PREx.	162
6.1	Measurement of the degree of linear polarization (DOLP) after various optical elements.	173
6.2	Measurement of the degree of circular polarization (DOCP) after quarter-wave plate and at the CIP without cavity mirrors.	175
6.3	A DOCP and ellipse orientation measurement at the cavity exit line with respect to a series of left circular polarization states of 92.0% set at the CIP.	187
6.4	The measured and calculated values of DOCP and ellipse angle at the CIP.	188
6.5	Calculation of the DOCP at the CIP from the DOCP and θ measured at the cavity exit line using the transfer function.	190
6.6	The average DOCP and ellipse angle calculated at the CIP and measured at the cavity exit line during PREx.	191
6.7	Summary of errors on the measurement of the polarization in the center of the cavity.	192

Chapter 1

Introduction

Before the discovery of parity violation (parity non-conservation), it was widely accepted that the laws of physics describing a process were the same under spatial inversion. At that time, the parity conservation in the electromagnetic and strong interactions was confirmed by experimental data, but the parity conservation in the weak interaction was not yet verified. In 1956, C. S. Wu [1] and collaborators reported the parity violating weak interaction in their polarized ^{60}Co beta-decay experiment. The electroweak theory developed by Weinberg, Salam and Glashow unified the electromagnetic and weak interactions and predicted the existence of the charged bosons (W^\pm) and a neutral boson (Z^0) in addition to the known neutral massless boson (γ). The discovery of a parity violating asymmetry in inelastic electron scattering of longitudinally polarized electrons off unpolarized deuterium was pivotal to confirm Weinberg-Salam-Glashow's electroweak model [2]. Since then, weak neutral current interactions have become a useful tool for testing the structure of the Standard Model and for probing the structure of the nucleon.

The physics program at JLab includes many experiments using a polarized electron beam in the $1 \sim 6.0$ GeV energy range for currents up to $\sim 200 \mu\text{A}$. A polarized source produces a beam polarized up to 90%. Some experiments and in particular the high precision parity violation experiments will need a fast and an accurate beam polarization measurement and monitoring. These experiments will seek to extract

the contribution of strange quarks to the charge density and magnetization of the nucleon by measuring the parity violating asymmetry in elastic scattering:

$$A_{PV} = \frac{(\sigma_R - \sigma_L)}{(\sigma_R + \sigma_L)}, \quad (1.1)$$

where $\sigma_R(\sigma_L)$ is the cross section for incident electrons of right(left) helicity. When the electron spin is parallel(antiparallel) to the beam direction, it is defined as the right(left) helicity state. A_{PV} arises from the interference of the weak and electromagnetic amplitudes. The physics asymmetry A_{phy} is formed from A_{raw} by correcting for beam polarization, backgrounds, and finite acceptance:

$$A_{phy} = \frac{K}{\mathcal{P}_b} \frac{A_{raw} - \mathcal{P}_b \sum_i A_i f_i}{1 - \sum_i f_i}, \quad (1.2)$$

where \mathcal{P}_b is the beam polarization, f_i are background fractions and A_i the associated background asymmetries, and K accounts for the range of kinematic acceptance. Since this asymmetry is scaled by the beam polarization, therefore the beam polarization must be carefully measured and monitored throughout the experiment. The systematic error in the physics asymmetry due to the beam polarization is just the fractional error in the beam polarization because the polarization contributes as a scale factor to the asymmetry. For this reason, the systematic error due to polarization is one of the dominant errors in the asymmetry.

At JLab energies, the simplest way to measure the polarization is through Mott and Møller Polarimeters. Unfortunately, both techniques are destructive, so that measuring the polarization prevents running an experiment downstream of the beam line. Furthermore, they can only be used at low current, and experiments requiring high intensity have to assume that beam polarization is intensity independent. Compton polarimetry offers an alternative to the above two techniques by providing the opportunity to follow the variations of polarization of the electron beam during the experiment. It is based on Compton scattering of circularly polarized photons off electrons. Compton polarimetry, although it is more complicated, is a very attractive technique, since it is minimally destructive to the electron beam so that the beam

polarization can be measured simultaneously with the data acquisition and that can be used at high current.

The Saclay and Clermont-Ferrand LPC was the first to design and construction of Compton polarimeter in Hall A at JLab in the late 90s. Due to a special energy ($1 \sim 6$ GeV) and current range (100 nA ~ 100 μ A) of JLab electron beam, unlike those storage rings and high energy accelerators such as SLAC [3], NIKHEF [4], HERA [5], MIT Bates [6] and MAMI [7], it requires the use of high power density as well as high energy photons which cannot be achieved by commercially available lasers. The polarimeter Saclay and LPC built uses a high-finesse monolithic Fabry-Perot optical cavity which amplifies a 300mW laser beam about 7,000 times of its power coupled to the cavity [8]. The power density available at the center of the cavity for interaction with the electron beam was then of the order of 800 kW/cm². The Compton chicane consists of 4 dipole magnets that bend the electron beam pass through to the interaction region. The back scattered photons and electrons are collected by a photon calorimeter [9] which composed of 5×5 array of PbWO₅ crystals and a silicon micro-strip electron detector respectively.

However, this Polarimeter uses an infra-red (1064 nm, 1.16 eV) laser as its photon source, which is not capable of giving a good signal to noise ratio at beam energies below 2 GeV. To reach an accuracy of 1% in the polarization measurement, as required by high-precision parity violation experiments like PREx [10] and Qweak [11], a green laser (532 nm, 2.33 eV) with a Fabry-Perot cavity was proposed.

This thesis describes all the experimental techniques we used and developed to meet the required specifications for building a green laser source and Fabry-Perot cavity for an upgraded Compton polarimeter for Jefferson Lab's experimental Hall A.

Chapter 2 gives a general overview of the Lead Radius Experiment (PREx), which tested the green Compton polarimeter for the first time, and polarized electron source and its basic principle at TJNAF. It also describes general Hall A equipment, especially the beam position and current monitors, target, raster, High Resolution

Spectrometer(HRS)s and polarimetry techniques used for measuring electron beam polarization etc.

Chapter 3 presents the mechanism of Compton polarimeter, its components, the data acquisition system and the working principle of them. The motivation for choosing the photon source is discussed.

Chapter 4 explains the optical principle of building a green laser source via second harmonic generation. A brief description of nonlinear optics, the frequency doubling setup and results are presented in here.

Chapter 5 is dedicated to Fabry-Perot cavity. It includes the mechanical design characteristics of the adjustable cavity. The principle of cavity response to an electromagnetic wave, cavity feedback control, the performance of cavity during PREx experiment that includes the cavity parameters and the optical coupling of laser light to the cavity is discussed.

Chapter 6 studies the polarization of the laser light. It describes the modeling of an optical cavity in Jones representations and determines the transfer function between Compton Interaction Point(CIP) and the cavity exit. It summarizes the sources of errors in the determination of the degree of circular polarization of light inside the cavity and gives an estimate of birefringence in cavity mirrors. The Compton spectrum, asymmetry and polarization measurements during PREx experiment will be presented.

Chapter 7 summarizes our work and discusses the limitations of this system and points to future direction for building a new laser system for a Compton polarimeter.

Chapter 2

Experimental Apparatus

2.1 Overview

The Lead Radius Experiment (PREx) [10] ran from March to June, 2010 in Hall A of the Thomas Jefferson National Accelerator Facility (TJNAF) in Newport News, VA. The goal of this experiment was to measure the RMS charge radius of the neutron in 1% precision in a model independent way as compared to the classic measurements [12]. The experiment measures the parity violating asymmetry in elastic scattering in equation(1.1). This asymmetry arises due to the interference of the Z^0 boson amplitude of the weak neutral interaction with the photon amplitude. The asymmetry is sensitive mainly to the neutron radius R_n because the weak charge of the neutron is much larger than that of the proton. In Plane Wave Impulse Approximation (PWIA), the relationship between the asymmetry and the neutron form factor is:

$$A_{LR} = \frac{G_F Q^2}{4\pi\alpha\sqrt{2}} \left[1 - 4 \sin^2 \theta_W - \frac{F_n(Q^2)}{F_p(Q^2)} \right], \quad (2.1)$$

where G_F is the Fermi constant, $\alpha = \frac{1}{137}$ is the fine structure constant, θ_W is the Weinberg angle, $F_n(Q^2)$ and $F_p(Q^2)$ are the neutron and proton form factors of the nucleus. The proton form factor is well known, so one can extract the neutron density distribution from the neutron form factor from the measured asymmetry. Therefore, the physics results of the experiment are the weak charge density, the point neutron

density and R_n .

PREx ran at 1.063 GeV energy and a 5° scattering angle in Hall A using the two high resolution spectrometer (HRS) system with a new warm-temperature septum magnet which focus elastically scattered electrons onto quartz detectors in their focal planes. A $50 \mu\text{A}$, 85% polarized beam at 120 Hz helicity reversal rate scatters from a foil of lead (^{208}Pb). The PREx detectors measure the detector flux normalized to beam current integrated in the helicity period and the parity violating asymmetry is calculated by dividing the helicity-correlated difference over the sum as shown in equation(1.1). Separate studies at lower current measure backgrounds, acceptance, and Q^2 . Polarization measurements are done by Møller and Compton polarimeters.

2.2 TJNAF

The Thomas Jefferson National Accelerator Facility (TJNAF) is a medium energy electron scattering laboratory designed to conduct research for understanding subatomic particles such as quarks and gluons. The accelerator consists of an injector, two linear accelerators ('linacs'), and two recirculation (ARC) magnets (Figure 2.1). In the injector, the electrons are polarized up to 90% with current up to $200 \mu\text{A}$ by shining circularly polarized laser light on a strained superlattice GaAs photo-cathode. An RF chopping system operating at 499 MHz is used to create a 3-beam 1497 MHz bunch train at 100 keV. The beam is then longitudinally compressed in the bunching section to provide 2 ps bunches, which are then accelerated up to 67 MeV and injected into north linac. Each linacs are composed of 20 RF cryomodules composed of 8 superconducting 5-cell Nb cavities that further accelerate the electron up to 570 MeV with acceleration gradient of 15MV/m. More than 2000 quadrupole and dipole magnets in two arcs provide the field which focuses and steers the beam as it passes through each arc and keeps the beam on a precise orbit. The linacs have identical gain which can be set from 400 to 600 MeV. Once the RF cavities tuned correctly, after maximum 5 passes, the linacs can provide an energy from 0.8 GeV to maximum

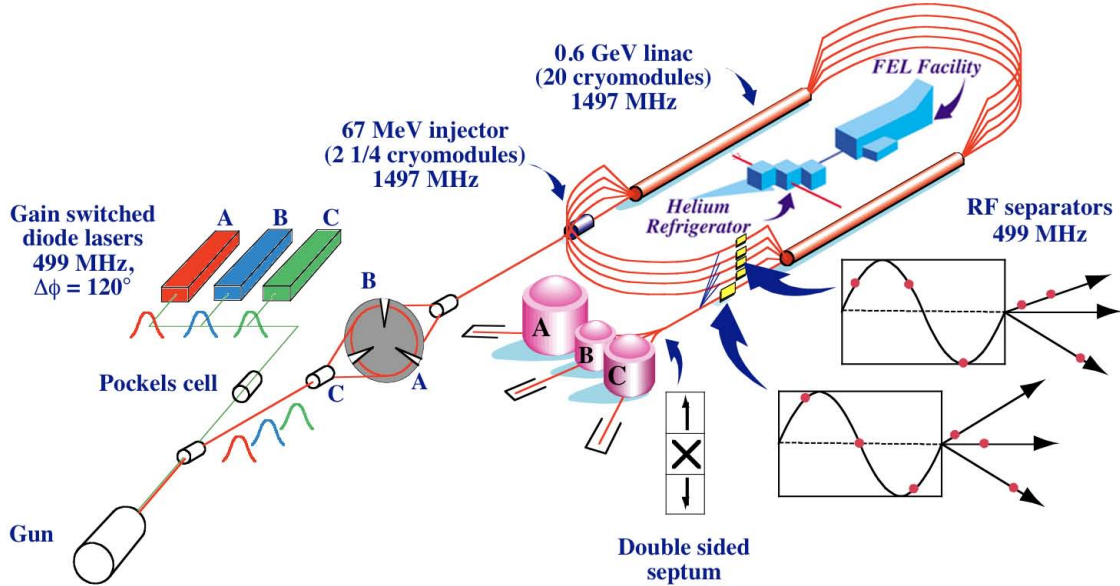


Figure 2.1 (color) TJNAF Accelerator Layout and Experimental Halls.

6.07 GeV. After passing through the south linac, the RF separator that operates at 499 MHz can be activated to extract every third beam bunch, sending one pulse to one of the Halls (Hall A, B, C) so that each hall can run simultaneously at three different currents and energies.

2.3 Hall A

At TJNAF, all three experimental halls located underground and shielded with thick layers of concrete walls. Hall A is the largest in volume with a diameter of 174 ft and height of 55 ft. Figure 2.2 shows a general Hall A configuration. The central elements include the beamline, target in the scattering chamber and two High Resolution Spectrometers (HRS).

2.3.1 Beam Monitors

Beam current monitors (BCMs) and beam position monitors (BPMs) are located throughout the accelerator and the experimental halls. Selected monitors from the

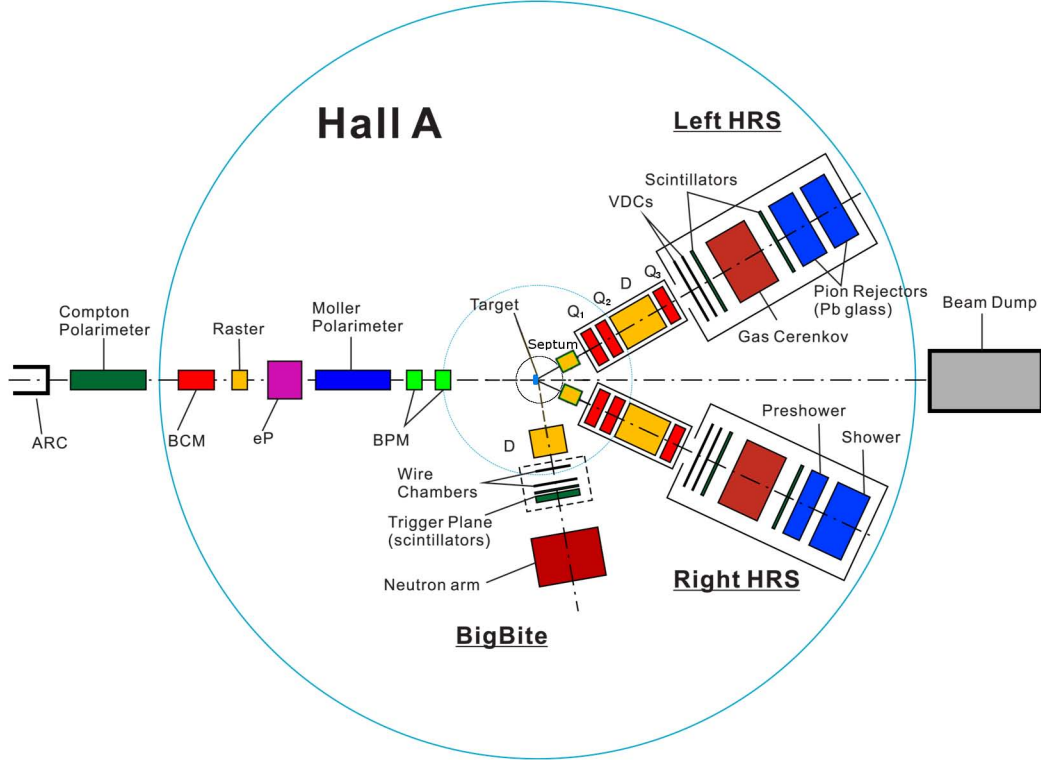


Figure 2.2 (color) General Hall A configuration.

injector region and the Hall A beamline are read out in the data stream. For parity violation experiments, the beam monitors should be quiet and sensitive in order to precisely measure the helicity-correlated beam differences which affect the raw asymmetry measurement.

The BCMs of Hall A is designed for a stable, low-noise, non-interfering beam current measurement [13]. They located ~ 25 m upstream of the target. They consist of an Unser monitor, two RF resonant cavities called “BCM1” and “BCM2”, associated electronics and a data-acquisition system. The RF cavities are used to measure the beam current during production running. The cavities are tuned to the frequency of the accelerator such that they output a voltage signal proportional to the beam current.

There are two BPMs, BPM4A and BPM4B, both of them are located ~ 6 m and ~ 1 m upstream of the target respectively, determine the helicity-correlated position

and angle differences of the beam. Another BPM, called BPM12, located in the highly dispersive region of Hall A bend used to measuring energy differences. For PREx, the required beam position differences is $\leq 1 \pm 0.1 \text{ nm}$.

Beam modulation, also referred to as “dithering”, is a technique used by the experiment to measure the change in the detector flux for a known change in position and energy on the target.

2.3.2 Target and Raster

The cryogenic target system is mounted inside the scattering chamber along with sub-systems for cooling, gas handling, temperature and pressure monitoring, target control and motion, and an attached calibration and solid target ladder. PREx used ^{208}Pb as its main target. Improving the thermal properties of the target is necessary since lead has a low melting temperature. A 0.5 mm foil of lead is sandwiched between two 0.15 mm sheets of diamond, which is pure ^{12}C [10]. This sandwich is clamped in a spring loaded copper block assembly which is cooled by liquid helium. The copper block has a hole to allow the beam to pass through; the beam only sees ^{208}Pb and ^{12}C . The extremely high thermal conductivity of diamond keeps the lead thermally stable at high current.

Because of its small size, the beam spot can cause local damage to the target at high beam currents. To minimize this, two simultaneous methods are used to control beam heating of the target. Heat is quickly dissipated by using a flow of helium transverse to the beam direction, and the heat is distributed by rastering the electron beam to a diameter of a few mm. The raster consists of two pairs of horizontal and vertical air-core dipoles located 23 m upstream of the target. The raster is driven by certain waveforms, sinusoidal or triangular, such that the beam is uniformly distributed over a rectangular area on the target. With rastered beam, usually the density fluctuations from beam heating can be controlled at the ppm level.

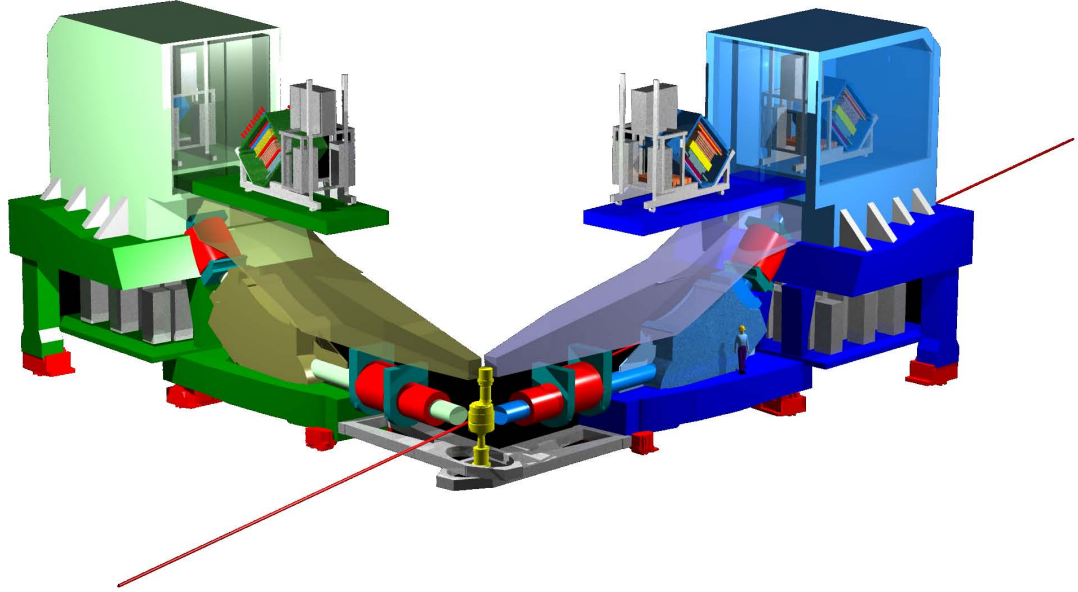


Figure 2.3 (color) Two High Resolution Spectrometers (HRS).

2.3.3 High Resolution Spectrometers (HRS)

The core of the Hall A equipment is a pair of identical spectrometers, each weighing about 1000 tons. Their basic layout is shown in Figure 2.3. The vertically bending design includes a pair of superconducting quadrupoles followed by a 6.6 m long dipole magnet with focussing entrance and exit polefaces and including additional focussing from a field gradient in the dipole. Following the dipole is a third superconducting quadrupole. The second and third quadrupoles of each spectrometer are identical in design and construction because they have similar field and size requirements. As the electron beam is incident on the target, the right HRS serves as a electron arm and the left HRS detects recoiled hadrons. The combination of quadrupoles and dipole provides a momentum resolution of better than 2×10^{-4} and a horizontal angular resolution of better than 2 mrad at a designed maximum central momentum of $4\text{GeV}/c$ [13]. For PREx, the required spectrometer angular resolution is $\pm 0.02^\circ$.

Due to large volume of HRSs, they can only be positioned at an angle larger than 12.5 degrees. To achieve the requested 5 degrees in PREx, two warm-temperature septum magnets were installed to bend the scattered charged particles by additional 7.5 degrees.

There are other important Hall A components such as detectors, trigger electronics and Data Acquisition System (DAQ) for successful running of an experiment, which will not be discussed here.

Specific to PREx, its DAQ system is unique from the standard Hall A DAQ because it integrates and digitizes the signals from the detectors and beam monitors. To obtain the necessary statistical precision and achieve the necessary electronic noise requirement, the DAQ uses high resolution 18-bit ADCs (analog-to-digital converters). It is triggered at 120 Hz synchronized to the helicity signal. To achieve a narrow pulse-pair width from the integrating detector for 1 GeV, new quartz detectors are developed.

2.4 Electron Beam

Polarized electron sources have been developed since the early 70's and the first beam of high energy polarized electrons was delivered at SLAC in 1974 [14]. In this paragraph, we describe the physical principle that allows the production of polarized electron beam at the electron source of TJNAF.

2.4.1 Polarized Electron Source

The polarized electrons are generated by photoemission from a GaAs photocathode while shined by circularly polarized laser light onto it. Photons incident on the photocathode are absorbed in the crystal exciting electrons from the valence band to the conduction band. Inverting the high voltage on the Pockels cell changes the helicity of the circular polarization and thus the helicity of the electrons. The crystal

is held at a bias voltage of -100 kV in order to pull the electrons from the conduction band into the accelerator.

The wavelength of the circularly polarized laser light is tuned such that it matches the energy gap between the energy levels. As long as the wavelength tuning is precise enough such that it falls between E_g and $E_g + \Delta$, angular momentum selection rules will only allow the transitions shown in Figure 2.4. The electrons are released from the cathode in a polarized state because of the properties of the crystal and laser light incident on the cathode. The crystal structure of the cathode consists of a $P_{\frac{3}{2}}$ valence band and an $S_{\frac{1}{2}}$ conduction band. There are two types of cathodes have been used in TJNAF injector which are described as the “strained-layer” cathode and the “superlattice” cathode [15]. The strained-layer cathode has a 100 nm thick layer of GaAs grown on a 250 μm thick layer of GaAsP. The superlattice cathode is made up of alternating layers of GaAs and GaAsP only a few nanometers thick grown on a 2.5 μm thick layer of GaAsP. One can get higher polarized ($\sim 90\%$) electrons with a higher quantum efficiency ($\sim 1.0\%$) from a superlattice cathode while the strained-layer cathode gives somewhat lower polarization ($\sim 75\%$) and has lower quantum efficiency ($\sim 0.2\%$). Quantum efficiency is defined as the number of electrons emitted from the cathode relative to the intensity of light incident on the cathode. For PREx, a high-power Ti-Sapphire laser with wavelength of 781 nm was used with a superlattice cathode. The intensity of the electron beam emitted by the photocathode can be written as the function of quantum efficiency as [16],

$$I_e[mA] = P[W] \cdot \lambda(nm) \cdot QE(\%) \cdot 8.065 \times 10^{-3}, \quad (2.2)$$

where P is the laser power and λ is its wavelength. For example, with a laser of $\lambda = 781 \text{ nm}$, $P = 25 \text{ mW}$ and a quantum efficiency of 1.0%, we obtain a beam intensity of 150 μA .

In strained-layer cathode, the lattice mismatch causes the strain which breaks the four-fold degeneracy of the valence band found in “bulk” GaAs. Because of the degeneracy breaking, it is theoretically possible for the cathode to produce a

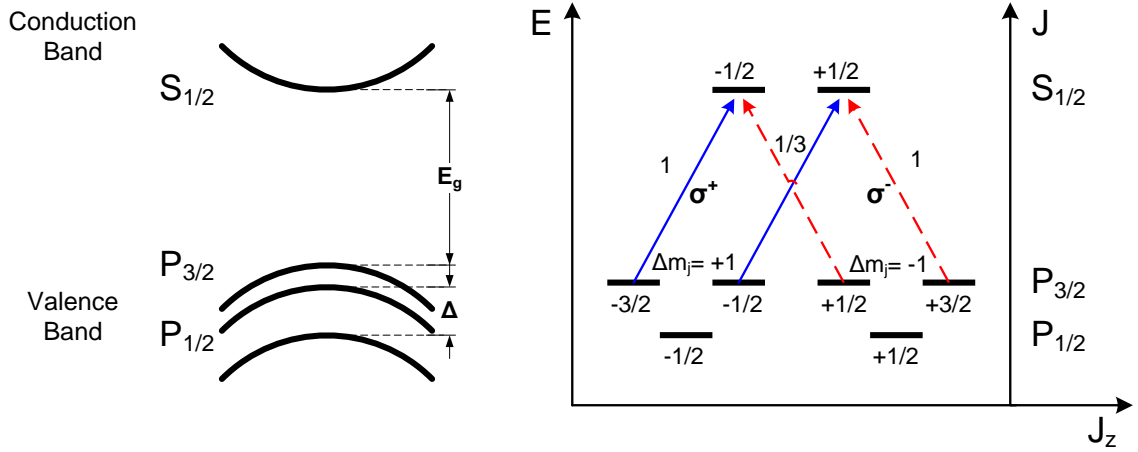


Figure 2.4 (color) A diagram of the bandgap and energy levels for strained GaAs. The arrows indicate the allowed transitions for right and left helicity photons.

100% polarized beam of electrons when illuminated with laser light of the proper wavelength. Left-circularly polarized light excites electrons into the $m_j = -\frac{1}{2}$ state in the conduction band while right-circularly polarized light excites electrons into the $m_j = +\frac{1}{2}$ state in the conduction band [22].

In order to have three experimental halls to operate simultaneously and independently, the light from the three lasers needs to be combined into a single beam that will then pass through the same location of the subsequent optical elements [16]. The pulses of the three lasers are out of phase with each other and synchronized with the frequency of accelerating cavities (1497 MHz). Using three independent pulsed lasers each producing short light pulses with 499 MHz repetition frequency (1/3 of the accelerating frequency) creates three bunch trains; the bunch trains are offset in phase (by one 1497 MHz RF period or 120°) to form a single 1497 MHz bunch train. The charge of every third bunch is the same; it can be varied by varying the intensity of the corresponding laser.

The photo-cathode is kept in a vacuum chamber ($< 10^{-11}$ Torr) and held at a negative voltage so as to generate an initial acceleration of the ejected electron. It is then injected into the north linac. The nature of this process means that the electron

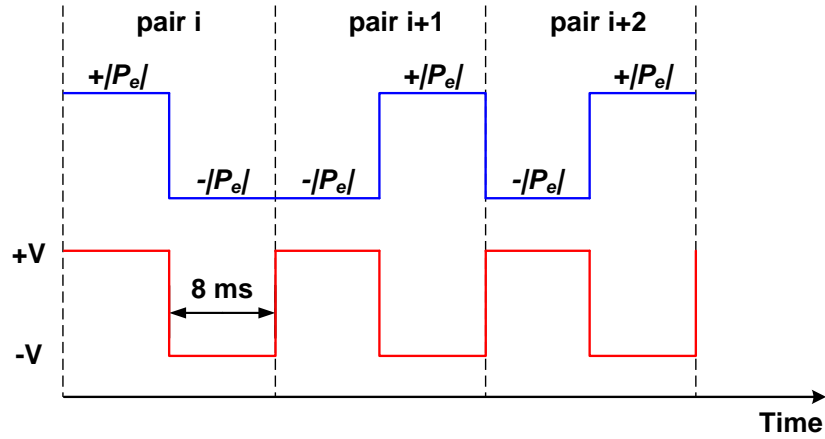


Figure 2.5 (color) One of the electron beam helicity patterns (octet) used for PREx. There are three pairs of electron beam polarization in each cycle. Each pair is composed of a polarization state $+|P_e|$ and $-|P_e|$ which corresponds to a voltage $+V$ and $-V$ applied to the Pockels cell respectively.

beam will be polarized when leaving the injector site. The electron gun is situated at an angle of 15° with respect to the accelerator beamline. A solenoid is used to bend the electrons into the accelerator. Since the electron beam is “steered” along its way to the Halls by magnetic fields, the spins of the electrons precess according to the beam’s energy, E_b , and bend angle θ_{bend} [22]:

$$S_e = \frac{(g - 2)}{2m_e} \cdot E_b \cdot \theta_{bend}, \quad (2.3)$$

where g and m_e are the g - factor and mass of the electron, respectively. A Wien filter is used to compensate the beam’s precession by setting the polarization angle of the electrons as they enter the accelerator. The angle is set such that the electron is longitudinally polarized in the experimental hall. A Wien filter is a static electromagnetic device. It consists of crossed electric and magnetic fields transverse to the particle motion. The usefulness of a Wien filter is that the polarization of a beam passing through the device can be rotated without deflecting the outgoing central orbit. The beam polarization measured in the Hall is a function of the Wien angle and for PREx a double Wien filter was used.

The electron beam at JLab has about 90% polarization, and it can also be flipped

to reduce systematic effects. For PREx, the polarity of the HV on Pockels cell is switched at a rate of 120 Hz to reverse the helicity of the outgoing laser light. The corresponding helicity schematic is shown in Figure 2.5. There is also an insertable half-wave plate (IHWP) just upstream of the Pockels cell which provides a slow reversal of the laser beam helicity; and therefore, a reversal of the electron beam helicity. If a half-wave plate is inserted into the system before the light reaches the cathode, the laser will be left-circularly polarized. The exiting electrons would then have the opposite polarization.

2.4.2 Polarized Electron Beam

The polarization of a beam of particles is an important concept to understand as we talk about the polarimeter.

Spin of a Particle

In classical mechanics, a rigid object has two kinds of angular momentum: orbital ($\vec{L} = \vec{r} \times \vec{P}$), associated with the motion of the center of mass, and spin ($\vec{S} = I\vec{\omega}$), associated with motion about the center of mass [17]. In quantum mechanics, the electron carries another form of angular momentum, which has nothing to do with motion in space, but which is somewhat analogous to classical spin. Like the other elementary particles, it carries an “intrinsic” angular momentum, which is called spin (\vec{S}), in addition to its “extrinsic” angular momentum (\vec{L}) [18].

The concept of spin was first introduced by W. Pauli in 1927. When P. Dirac proposed his relativistic quantum mechanics in 1928, electron spin was an essential part of it. In quantum mechanics, it is represented by an operator \hat{s} . In Cartesian coordinate frame, we can decompose this operator into three components \hat{s}_x , \hat{s}_y and \hat{s}_z which describe the spin value measured respectively in the \hat{x} , \hat{y} and \hat{z} . These components are such that:

$$\hat{s}^2 = \hat{s}_x^2 + \hat{s}_y^2 + \hat{s}_z^2, \quad (2.4)$$

which satisfies the following commutation rule,

$$[\hat{s}_x, \hat{s}_y] = i\hat{s}_z, \quad [\hat{s}_y, \hat{s}_z] = i\hat{s}_x, \quad [\hat{s}_z, \hat{s}_x] = i\hat{s}_y, \quad (2.5)$$

These non-commuting relationships tell us that two components of intrinsic angular momentum can be measured simultaneously. The operator \hat{s}^2 commutes with each of the components \hat{s}_x , \hat{s}_y and \hat{s}_z . It means that we can simultaneously determine its own value and another component of it.

The number s , the eigenvalue of the operator \hat{s} can take either integer or half-integer numbers. For a given s , the component s_z takes values between $s, s-1, \dots, -s$. Every elementary particles has a specific and immutable values of its spin: π mesons have spin 0; photons have spin 1; deltas have spin $\frac{3}{2}$; gravitons have spin 2; and so on. Electrons, positrons, protons, neutrons, muons, hyperons have spin $\frac{1}{2}$, therefore they are called Fermions. In case of spin $\frac{1}{2}$ ($s = \frac{1}{2}, s_z = \pm\frac{1}{2}$), which is the spin of the particles that make up ordinary matter (protons, neutrons, and electrons), as well as all quarks and all leptons, the components \hat{s}_x , \hat{s}_y and \hat{s}_z can be expressed by a 2×2 matrices in the following way,

$$\hat{s} = \frac{1}{2}\hat{\sigma}, \quad (2.6)$$

$$\hat{\sigma}_x \equiv \begin{pmatrix} 0 & 1 \\ 1 & 0 \end{pmatrix}; \quad \hat{\sigma}_y \equiv \begin{pmatrix} 0 & -i \\ i & 0 \end{pmatrix}; \quad \hat{\sigma}_z \equiv \begin{pmatrix} 1 & 0 \\ 0 & -1 \end{pmatrix}, \quad (2.7)$$

which are the famous Pauli spin matrices.

For a particle which carries a spin, the wave-function must not only depend on the three continuous variables that are the coordinates of the particle, but also a discrete variable indicating the value of the projection of spin in a given direction in space according to the chosen quantization axis. i.e. $\Phi(x, y, z, \sigma)$. The position variables are independent of the spin variable, therefore it can be separated into two functions $\Phi(x, y, z, \sigma) = \Psi(x, y, z)\chi(\sigma)$, where $\chi(\sigma)$ is called a spin wave-function. For a spin $\frac{1}{2}$ case, there are just two eigenstates: $|\frac{1}{2}, \frac{1}{2}\rangle$, which we call spin up, and $|\frac{1}{2}, -\frac{1}{2}\rangle$, which

we call spin down. Using these vectors, the $\chi(\sigma)$ can be expressed as a two-element column matrix (or spinor):

$$\chi = \begin{pmatrix} a_1 \\ a_2 \end{pmatrix} = a_1 \begin{pmatrix} 1 \\ 0 \end{pmatrix} + a_2 \begin{pmatrix} 0 \\ 1 \end{pmatrix}, \quad (2.8)$$

where $\frac{|a_1|^2}{|a_1|^2 + |a_2|^2}$ is the probability of finding the state $|\frac{1}{2}, \frac{1}{2}\rangle$, and $\frac{|a_2|^2}{|a_1|^2 + |a_2|^2}$ is the probability of finding the state $|\frac{1}{2}, -\frac{1}{2}\rangle$.

Polarization of Electron Beam

An ensemble of electrons is said to be polarized if the electron spins have a preferential orientation so that there exists a direction for which the two possible spin states are not equally populated.

(1) Pure Spin State:

We assume that all the electrons have the same spin direction with respect to their quantization axis \hat{z} and can be described by the spin wave-function χ . The polarization of a set of electrons with spin $\frac{1}{2}$ can be defined as the average over all electrons of the Pauli spin operator,

$$\mathcal{P} = \langle \sigma \rangle = \langle \chi | \sigma | \chi \rangle = (a_1^*, a_2^*) \sigma \begin{pmatrix} a_1 \\ a_2 \end{pmatrix}, \quad (2.9)$$

after applying the operators of a spin wave-function, we obtain:

$$\sigma_x \begin{pmatrix} a_1 \\ a_2 \end{pmatrix} = \begin{pmatrix} a_2 \\ a_1 \end{pmatrix}, \quad \sigma_y \begin{pmatrix} a_1 \\ a_2 \end{pmatrix} = \begin{pmatrix} -ia_2 \\ ia_1 \end{pmatrix}, \quad \sigma_z \begin{pmatrix} a_1 \\ a_2 \end{pmatrix} = \begin{pmatrix} a_1 \\ -a_2 \end{pmatrix}, \quad (2.10)$$

and the three components of the polarization vector \mathcal{P} can be written in the following way:

$$\mathcal{P} = \begin{pmatrix} \mathcal{P}_x \\ \mathcal{P}_y \\ \mathcal{P}_z \end{pmatrix} = \begin{pmatrix} a_1^* a_2 + a_2^* a_1 \\ i(a_2^* a_1 - a_1^* a_2) \\ |a_1|^2 - |a_2|^2 \end{pmatrix}, \quad (2.11)$$

or the norm of \mathcal{P} is:

$$|\mathcal{P}| = \sqrt{\mathcal{P}_x^2 + \mathcal{P}_y^2 + \mathcal{P}_z^2}, \quad (2.12)$$

after we normalized the wave-function, the polarization can be written as:

$$\mathcal{P} = \frac{\langle \chi | \sigma | \chi \rangle}{\langle \chi | \chi \rangle}, \quad (2.13)$$

We define the propagation direction of electron beam in the coordinate frame $Oxyz$ as in Figure 2.6. Let \vec{u} be the unit vector, characterized by the angles θ and ϕ , which denotes the spin orientation of electrons in this frame [19]. In general, we write its components:

$$u_x = \sin \theta \cos \phi, \quad (2.14)$$

$$u_y = \sin \theta \sin \phi, \quad (2.15)$$

$$u_z = \cos \theta, \quad (2.16)$$

where $\vec{\sigma} \cdot \vec{u}$ represents the projection of the spin operator on the direction defined by the vector \vec{u} . If we want to determine the components of the spin wave function, we must solve the eigenvalue equation:

$$(\vec{\sigma} \cdot \vec{u})\chi = \lambda\chi, \quad (2.17)$$

Now we can write the three components of equation(2.17) in the following way: S

$$(\sigma_x u_x)\chi = \begin{pmatrix} a_2 \sin \theta \cos \phi \\ a_1 \sin \theta \cos \phi \end{pmatrix}, \quad (2.18)$$

$$(\sigma_y u_y)\chi = \begin{pmatrix} -ia_2 \sin \theta \sin \phi \\ ia_1 \sin \theta \sin \phi \end{pmatrix}, \quad (2.19)$$

$$(\sigma_z u_z)\chi = \begin{pmatrix} a_1 \cos \theta \\ -a_2 \cos \theta \end{pmatrix}, \quad (2.20)$$

and the eigenvalue of equation(2.17) is:

$$(\vec{\sigma} \cdot \vec{u})\chi = \begin{pmatrix} a_2 \sin \theta e^{-i\phi} + a_1 \cos \theta \\ a_1 \sin \theta e^{i\phi} - a_2 \cos \theta \end{pmatrix} = \lambda \begin{pmatrix} a_1 \\ a_2 \end{pmatrix}, \quad (2.21)$$

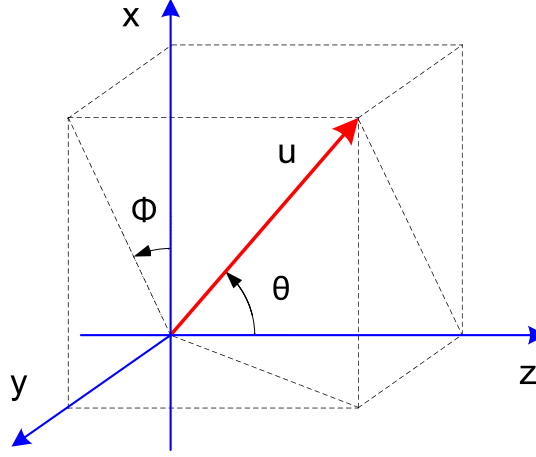


Figure 2.6 (color) Spin orientation of electrons in the electron beam reference.(redrawn from [19])

after solving it for $\lambda = \pm 1$ cases, we can determine the values of a_1 and a_2 :

$$\lambda = +1, \quad a_1 = \cos\left(\frac{\theta}{2}\right), \quad a_2 = \sin\left(\frac{\theta}{2}\right)e^{i\phi}, \quad (2.22)$$

$$\lambda = -1, \quad a_1 = \sin\left(\frac{\theta}{2}\right), \quad a_2 = -\cos\left(\frac{\theta}{2}\right)e^{i\phi}, \quad (2.23)$$

The spin wave-functions which we have to determine the components are the eigenfunctions of the spin operator with respect to the direction \vec{u} and it has eigenvalues ± 1 . One can notice that in equation(2.23), if we replace θ with $\pi - \theta$ and ϕ with $\phi + \pi$, we will get the same a_1 and a_2 as in equation(2.22). Both wave-functions are respectively associated to the case where one considers the direction $+\vec{u}$ and $-\vec{u}$. It is enough from now to consider the wave-function associated with the spin direction $+\vec{u}$. It represents the states where the spin in the direction \vec{u} possesses value $\pm \frac{1}{2}$.

With these notations and using the equation(2.11), we can determine the components of the polarization vector when the spin of the electron beam is oriented along the direction defined by the vector \vec{u} :

$$\mathcal{P} = \begin{pmatrix} \mathcal{P}_x \\ \mathcal{P}_y \\ \mathcal{P}_z \end{pmatrix} = \begin{pmatrix} \sin \theta \cos \phi \\ \sin \theta \sin \phi \\ \cos \theta \end{pmatrix}, \quad (2.24)$$

The longitudinal polarization is the component of polarization vector which is parallel to the direction of propagation:

$$\mathcal{P}_L = \mathcal{P}_z = \cos \theta, \quad (2.25)$$

and transverse component (component in plane Oxy and perpendicular to \hat{z} axes) is defined by:

$$\mathcal{P}_\perp = \sqrt{\mathcal{P}_x^2 + \mathcal{P}_y^2} = \sin \theta, \quad (2.26)$$

The case study of a pure spin state (for a spin $\frac{1}{2}$) can bring out the general properties of the polarization vector. In this case, all the spins are aligned to one direction and the polarization is one. The projection of the polarization vector, or $\mathcal{P} \cdot \vec{u}$, on any axis, gives the degree of polarization along that axis.

(2) Statistical Mixture of Polarized States:

Now consider a partially polarized beam. It is a mixture of different pure spin states. In this case, the total polarization of the system is the average of polarization vector $\mathcal{P}^{(n)}$ over non-normalized individual systems $\chi^{(n)}$ in pure spin states [19].

$$\mathcal{P} = \frac{\sum_n \langle \chi^{(n)} | \sigma | \chi^{(n)} \rangle}{\sum_n \langle \chi^{(n)} | \chi^{(n)} \rangle} = \sum_n \left(\frac{\langle \chi^{(n)} | \chi^{(n)} \rangle}{\sum_n \langle \chi^{(n)} | \chi^{(n)} \rangle} \right) \mathcal{P}^{(n)}, \quad (2.27)$$

If we introduce the concept of density matrix operator, the polarization vector can be written as following:

$$\rho = \sum_n w^{(n)} \begin{pmatrix} |a_1^{(n)}|^2 & a_1^{(n)} a_2^{(n)*} \\ a_1^{(n)*} a_2^{(n)} & |a_2^{(n)}|^2 \end{pmatrix} = \sum_n w^{(n)} |\chi^{(n)}\rangle \langle \chi^{(n)}|, \quad (2.28)$$

where the weighting factors $w^{(n)}$ take into account the relative proportion of the states $\chi^{(n)}$ by $w^{(n)} = \frac{N^{(n)}}{\sum_n N^{(n)}}$, and $N^{(n)}$ is the number of electrons in the state $\chi^{(n)}$. The individual matrices of this sum are the density matrices of pure states. Using the definition of the Pauli matrices, we can show that the density matrix of the global

system and its polarization are linked by the relationship:

$$\mathcal{P} = \frac{\text{tr}(\rho\sigma)}{\text{tr}(\rho)}, \quad (2.29)$$

We can then express the elements of the density matrix by the components of polarization and we get:

$$\frac{\rho}{\text{tr}(\rho)} = \frac{1}{2} \begin{pmatrix} 1 + \mathcal{P}_z & \mathcal{P}_x - i\mathcal{P}_y \\ \mathcal{P}_x + i\mathcal{P}_y & 1 - \mathcal{P}_z \end{pmatrix} = \frac{1}{2}[\mathbb{I} + \mathcal{P}\sigma], \quad (2.30)$$

where \mathbb{I} is the identity matrix.

The density matrix will have its simplest form if one takes the direction of the resultant polarization as the \hat{z} axis of the coordinate system shown in Figure 2.6, i.e. chooses $\mathcal{P}_x = \mathcal{P}_y = 0$, $\mathcal{P} = \mathcal{P}_z$. Then one has:

$$\rho = \frac{1}{2} \begin{pmatrix} 1 + \mathcal{P} & 0 \\ 0 & 1 - \mathcal{P} \end{pmatrix}, \quad (2.31)$$

This form of the density matrix illustrates the meaning of \mathcal{P} : since $|a_1^{(n)}|^2$ is the probability that the eigenvalue $+\frac{1}{2}$ will be obtained from a spin measurement in the \hat{z} direction on the n th subsystem, the probability is $\sum_n w^{(n)}|a_1^{(n)}|^2$ that this measurement on the total beam will give the value $+\frac{1}{2}$. This probability can also be expressed as $N_+/(N_+ + N_-)$, where N_+ is the of measurements that yield the value $+\frac{1}{2}$ and $(N_+ + N_-)$ is the total number of measurements. (Correspondingly, $\sum_n w^{(n)}|a_2^{(n)}|^2 = N_-/(N_+ + N_-)$ is the probability that the value $-\frac{1}{2}$ will be obtained.) Now if we compare equation (2.28) and equation (2.31), we will obtain the polarization:

$$\mathcal{P} = \frac{N_+ - N_-}{N_+ + N_-}, \quad (2.32)$$

In general, the polarization is also described as the sum of the polarization vector \mathcal{P} of pure spin states. In the pure case, the \mathcal{P} is 1 and we call the beam is completely polarized. In mixed case, the \mathcal{P} is between 0 and 1 and we call the beam is partially polarized. A system with $\mathcal{P} = 0$ called non-polarized.

(3) Average Value of the Helicity:

In many experiments, the term helicity (h) of an individual electron is defined as the value of the projection of spin on its axis of propagation. Strictly speaking, the quantization axis varies from one particle to another when one considers a beam. At TJNAF, a very good and parallel beam with the emittance of $\sim 10^{-9}$ *mrad* [20] is routinely achievable (a non-invasive method called Tiefenbach method is being used to measure the beam energy), this means the value of helicity is very close to that of the polarization along the beam axis. For a system of N electrons with spin σ_i and individual and mean momentum of k_i and k , one can define the helicity as following [19]:

$$\langle h \rangle = \left\langle \frac{\sigma_i \cdot k_i}{|k_i|} \right\rangle = \frac{1}{N} \sum_{i=1}^N \frac{\sigma_i \cdot k_i}{|k_i|} \quad (2.33)$$

By introducing the polarization vector: $\mathcal{P} = \frac{1}{N} \sum_{i=1}^N \sigma_i$, we finally obtain:

$$\langle h \rangle = \mathcal{P} \cdot \frac{k}{|k|} - \langle \sigma_i \cdot \Delta d_i \rangle \quad (2.34)$$

where $\Delta d_i = \frac{k}{|k|} - \frac{k_i}{|k_i|}$ called energy dispersion. Given the characteristics of electron beam (energy spread better than 10^{-5}), after Schwartz inequality, we have:

$$\langle \sigma_i \cdot \Delta d_i \rangle \leq \frac{1}{2} |\Delta d_i| \leq 10^{-5} \quad (2.35)$$

Therefore the difference between $\langle h \rangle$ and $\mathcal{P} \cdot \frac{k}{|k|}$ is negligible in the experimental precision point of view. For PREx, the required precision of polarization measurement is about 1%.

2.5 Electron Beam Polarimetry

It is important to measure the electron beam polarization and orientation during the experiment. Electron beam polarimetry is the technique of separating scattered particles for detection using a spin dependent interaction between the polarized electrons

(\mathcal{P}_e) and the known total analyzing power (\mathcal{A}_{tot}) of the polarimeter's target. The target is itself polarized in many polarimeters and \mathcal{A}_{tot} is then proportional to the product of the target polarization and the analyzing power of the interaction. Electron beam polarization (\mathcal{P}_e) is deduced from the measured experimental asymmetry (\mathcal{A}_{exp}) and total analyzing power of the polarimeter's target (\mathcal{A}_{tot}):

$$\mathcal{A}_{exp} = \mathcal{A}_{tot} \cdot \mathcal{P}_e \quad (2.36)$$

The kinematics and design of each polarimeter determine which components of the total beam polarization can be measured. At TJNAF, the polarization of the beam electrons is measured in a number of different ways, the spin-dependent Mott polarimetry at the injector, and the Compton and Møller polarimetry. In this paragraph we will describe the Mott and Møller polarimetries. The Compton polarimetry will be discussed in detail in the following chapter.

2.5.1 Mott Polarimetry

In order to measure the spin polarization near the injector at TJNAF, a 5 MeV Mott scattering polarimeter has been developed [21] (see Figure 2.7). The polarimeter uses the counting rate asymmetry in the single elastic Mott scattering process which exists if the polarization vector is not parallel to the scattering plane. The Sherman function determines the relation between measured asymmetry and the degree of polarization of the electron beam. Accurate polarimetry is ensured by addressing three concerns:

- The determination of the theoretical Sherman function for the single elastic scattering process.
- The correct measurement of the asymmetry for every target by the achievement of pure energy spectra.
- The understanding of the foil - thickness extrapolation to target thickness zero.

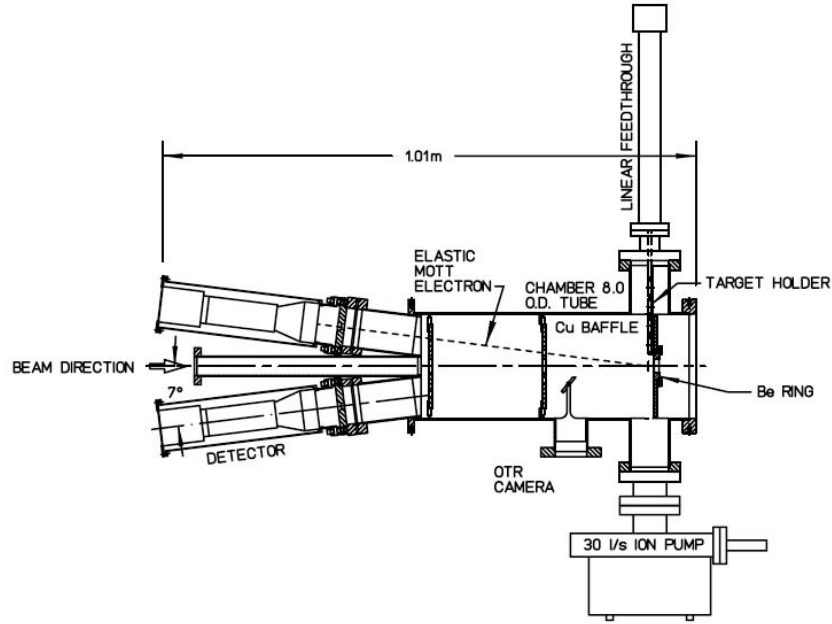


Figure 2.7 Schematic of the 5 MeV Mott scattering chamber with detectors. [21]

The Mott scattering asymmetry results from the spin-orbit coupling between the incident polarized beam electrons and the potential of the target nucleus of atoms with a large nuclear charge (gold, silver, copper) [22]. The scattered electron experiences a magnetic field in its rest frame resulting from the motion of the electric field of the nucleus. The interaction of the orbital angular momentum (magnetic field) with the magnetic moment of the scattered electron (spin) leads to a spin-orbit coupling term in the scattering potential. The results in a term in the Mott cross-section which depends on the incident electron spin orientation. The cross-section for the scattering angle θ is written as:

$$\sigma(\theta) = \sigma_0(\theta)[1 + S(\theta)\vec{\mathcal{P}} \cdot \hat{n}], \quad (2.37)$$

where $\sigma_0(\theta)$ is the unpolarized cross-section.

$$\sigma_0(\theta) = \left(\frac{Ze^2}{2mc^2} \right)^2 \frac{(1 - \beta^2)(1 - \beta^2 \sin^2(\frac{\theta}{2}))}{\beta^4 \sin^4(\frac{\theta}{2})}, \quad (2.38)$$

where $S(\theta)$ is known as the Sherman function and $\vec{\mathcal{P}}$ is the incident electron polarization. \hat{n} is the unit vector normal to the scattering plane.

The importance of the value of the Sherman function is that it determines the size of the scattering asymmetry, or how well the interaction distinguishes between the two spin states. The unpolarized part of the cross-section effectively averages over the initial spin state, whereas, the Sherman function contains the angular scattering amplitude which includes the initial spin state. This formalism describes the scattering from a single atom where the Sherman function is calculated from the basic electron nucleus cross-section. In reality, a target foil contains so many atoms that multiple and plural scattering also occurs. Therefore, the effective Sherman function $S_{eff}(\theta)$ should be measured.

Consider an electron beam with polarization \mathcal{P} transverse to the scattering plane of a target, i.e., parallel or antiparallel to \hat{n} . The number of electrons scattered through an angle θ to the right and detected, N_+ , is proportional to $1 + \mathcal{P}S_{eff}(\theta)$ and the number scattered to left and detected, N_- , is proportional to $1 - \mathcal{P}S_{eff}(\theta)$. The scattering asymmetry is defined as,

$$\mathcal{A} = \frac{N_+ - N_-}{N_+ + N_-} = \mathcal{P}S_{eff}(\theta), \quad (2.39)$$

The effective Sherman function depends upon the foil material (Z) and target thickness (density). Measurement is done by measuring the experimental asymmetries for a fixed polarization (known or unknown) for a variety of target thicknesses. The measured asymmetries are plotted versus target thickness and extrapolated to the zero target thickness to give \mathcal{A}_0 , the asymmetry expected for scattering from a single atom. The functional form of the fit is made assuming that the scattering rate depends to first and second order on the target thickness. The linear dependence carries the single elastic scattering dependence. The quadratic term carries no analyzing strength and corresponds to multiple scattering in the target.

$$N_{\pm} = (1 \pm \mathcal{P}\mathcal{A}_0) \cdot t + \alpha \cdot t^2, \quad (2.40)$$

By applying equation(2.39) the resulting scattering asymmetry is determined.

$$\mathcal{A} \sim \frac{\mathcal{P}\mathcal{A}_0}{1 + \alpha t}, \quad (2.41)$$

In this way \mathcal{A}_0 and α are determined. Using the single atom Sherman function $S(\theta)_{thy}$ the polarization of the beam is finally calculated

$$\mathcal{P} = \frac{\mathcal{A}_0}{S(\theta)_{thy}}, \quad (2.42)$$

The polarimeter measures only the transverse components of the beam polarization over a range of energies (2 - 5 MeV). It is an invasive measurement and accuracy is limited by determination of Sherman function.

2.5.2 Møller Polarimetry

The Møller polarimeter along the Hall A beamline measures the polarization of the electron beam delivered to the Hall [23]. The system (see Figure 2.8) consists of,

- A magnetized iron foil placed in the beam path. The foil acts as a polarized electron target and it can be selected from a set of four different foils. A pair of superconducting Helmholtz coils (~ 4 T peak field) magnetizes the in-beam foil. The foils are located 17.5 m upstream of the nominal pivot of the Hall A High Resolution Spectrometers.
- A magnetic spectrometer system consisting of three quadrupole magnets and a dipole magnet. The spectrometer focuses electrons scattered in a certain kinematic range onto the Møller detector package.
- The detector package and its associated shielding house.
- An stand-alone data acquisition system.
- An off-line analysis software package to extract the beam polarization. Roughly, the beam polarization is calculated by taking the difference in the counting rates of two different beam helicity samples.

A Møller polarimeter exploits the process of Møller scattering of polarized electrons off polarized atomic electrons in a magnetized foil $e^+ + e^- \rightarrow e^- + e^-$. The

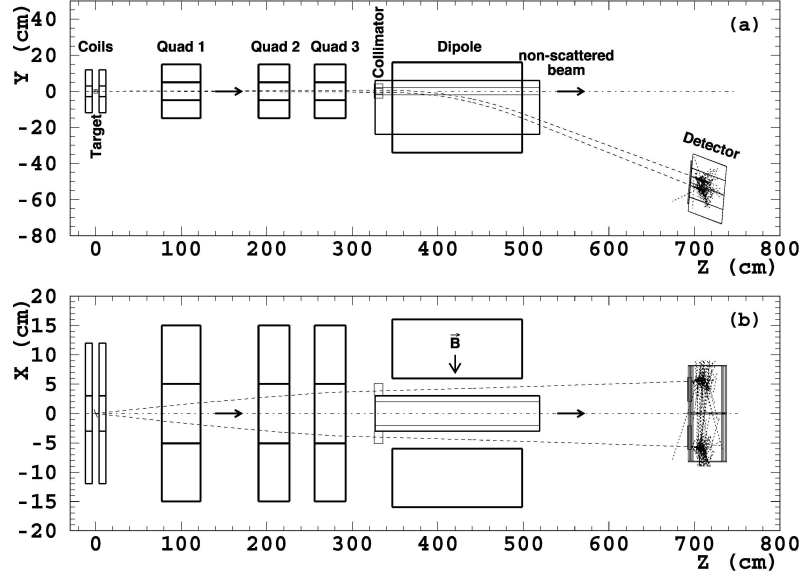


Figure 2.8 Layout of Hall A Møller polarimeter. (a) presents a side view while, (b) represents a top view. [23]

reaction cross section depends on the beam and target polarizations \mathcal{P}^{beam} and \mathcal{P}^{target} as:

$$\sigma \propto \left[1 + \sum_{i=X,Y,Z} (\mathcal{A}_{ii} \cdot \mathcal{P}_i^{target} \cdot \mathcal{P}_i^{beam}) \right], \quad (2.43)$$

where $i = X, Y, Z$ defines the projections of the polarizations. The analyzing power \mathcal{A} depends on the scattering angle in the center of mass (CM) frame, θ_{CM} . Assuming that the beam direction is along the Z -axis and that the scattering happens in ZX plane:

$$\mathcal{A}_{ZZ} = -\frac{\sin^2 \theta_{CM}(7 + \cos^2 \theta_{CM})}{(3 + \cos^2 \theta_{CM})^2}, \quad \mathcal{A}_{XX} = -\frac{\sin^4 \theta_{CM}}{(3 + \cos^2 \theta_{CM})^2}, \quad \mathcal{A}_{YY} = -\mathcal{A}_{XX}, \quad (2.44)$$

The analyzing power does not depend on the beam energy. At $\theta_{CM} = 90^\circ$ the analyzing power has its maximum $\mathcal{A}_{ZZ}^{max} = 7/9$. A transverse polarization also leads to an asymmetry, though the analyzing power is lower: $\mathcal{A}_{XX}^{max} = \mathcal{A}_{ZZ}^{max}/7$. The main purpose of the polarimeter is to measure the longitudinal component of the beam polarization. The Møller polarimeter in Hall A detects pairs of scattered electrons in a range of $75^\circ < \theta_{CM} < 105^\circ$. The average analyzing power is about $\langle \mathcal{A}_{ZZ} \rangle = 0.76$.

The target consists of a thin magnetically saturated ferromagnetic foil. In such a material about 2 electrons per atom can be polarized. The maximal electron polarization for fully saturated pure iron is 8.52%. In Hall A Møller polarimeter, the foil is magnetized by a 3 T field parallel to the beam axis and perpendicular to the foil plane. Proper levels of liquid nitrogen and helium are required for the magnet to become superconducting and remain so while performing a polarimetry measurement. The target foil can be tilted at various angles to the beam in the horizontal plane, providing a target polarization that has both longitudinal and transverse components. The spin of the incoming electron beam may have a transverse component due to precession in the accelerator and in the extraction arc. The asymmetry is measured at two target angles of about $\pm 20^\circ$ and the average is taken. Because the transverse contributions have opposite signs for these target angles, the transverse contributions cancel in the average. Additionally, this method reduces the impact of uncertainties in the target angle measurements. At a given target angle two sets of measurements with opposite directions of the target polarization are taken. Averaging the results helps to cancel some of the false asymmetries, such as that coming from the residual helicity-driven asymmetry of the beam flux.

The secondary electron pairs pass through a magnetic spectrometer (Figure 2.8) consisting of a sequence of three quadrupole magnets and a dipole magnet which selects particles in a certain kinematic region. Two electrons are detected with a two-arm detector which consists of lead-glass calorimeter modules and the coincidence counting rate of the two arms is measured. The non-scattered electron beam passes through a 4 cm diameter hole in a vertical steel plate 6 cm thick, positioned at the dipole midplane, which serves as a collimator for the scattered electrons and as a magnetic shield for the beam. The helicity driven asymmetry of the coincidence counting rate is used to derive the beam polarization.

The beam longitudinal polarization is measured as:

$$\mathcal{P}_Z^{beam} = \frac{N_+ - N_-}{N_+ + N_-} \cdot \frac{1}{\mathcal{P}^{foil} \cdot \langle \mathcal{A}_{ZZ} \rangle}, \quad (2.45)$$

where N_+ and N_- are the measured counting rates with two opposite mutual orientation of the beam and target polarizations, while $\langle \mathcal{A}_{ZZ} \rangle$ is obtained using Monte-Carlo calculation of the Møller spectrometer acceptance, \mathcal{P}^{foil} is derived from special magnetization measurements in bulk material.

The polarization measurements with the Møller polarimeter are invasive and the asymmetry is independent of electron beam energy. Target heating limits maximum beam current to $\sim 5\mu A$. Accuracy limited by target polarization uncertainties. Usually one measurement takes few hours, providing a statistical accuracy of about 0.2%.

Chapter 3

Compton Polarimetry

3.1 Measurement Principle

The principle of Compton polarimetry is based on the elastic scattering of two polarized particles: the electron and photon. The Compton effect was observed by A. H. Compton in 1923 [24], and earned the 1927 Nobel Prize in Physics for the discovery. The reaction cross section depends on the orientation of the spin of the electron relative to that of the *spin* of photon (Figure 3.1). The reversing of electron and photon beam polarizations allows measurement of an experimental asymmetry proportional to them and the known theoretical Compton asymmetry.

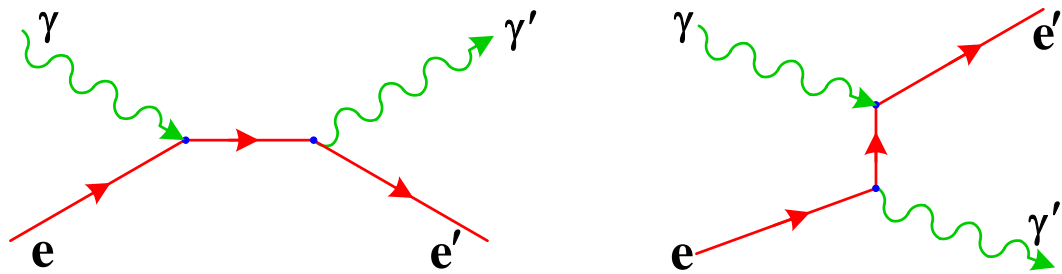


Figure 3.1 (color) Feynman Diagrams for Compton Scattering.

3.1.1 The Physics of Compton Scattering

Compton scattering is the elastic scattering of a photon on an electron. Let us consider the laboratory frame with the conventions used in Figure 3.2. The Z -axis is defined as the direction of incoming electrons and the incoming photons lie on the $X - Z$ plane and cross the electron beam with an angle α_c . The polar angles noted as θ_γ and θ_e are the scattering angles of a photon and an electron respectively, and the azimuth angle ϕ defines the scattering plane.

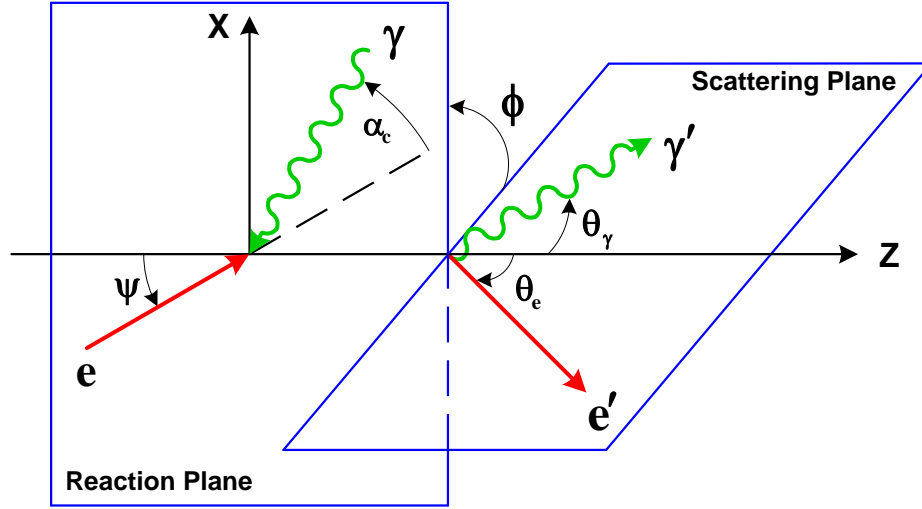


Figure 3.2 (color) A diagram of Compton scattering.

The four-vector energy-momentum $p^\mu = (E, \vec{p})$ of an incident electron e with energy E and $k^\mu = (k, \vec{k})$ of an incident photon γ with energy k can be written as:

$$p^\mu = (E, p \sin \psi, 0, p \cos \psi), \quad (3.1)$$

$$k^\mu = (k, -k \sin(\psi + \alpha_c), 0, -k \cos(\psi + \alpha_c)), \quad (3.2)$$

Similarly, for the scattered electron e' with energy E' and photon γ' with energy k' , we have,

$$p'^\mu = (E', p' \sin \theta_e \cos \phi, p' \sin \theta_e \sin \phi, p' \cos \theta_e), \quad (3.3)$$

$$k'^\mu = (k', k' \sin \theta_\gamma \cos \phi, k' \sin \theta_\gamma \sin \phi, k' \cos \theta_\gamma), \quad (3.4)$$

Since the momentum and energy is conserved, the angle ψ can be expressed as,

$$\tan \psi = \frac{k \sin \alpha_c}{p - k \cos \alpha_c}, \quad (3.5)$$

In this 2-body kinematic, we only need to know the ϕ to determine the whole process. The relationship between the initial and final photon energy with the relevant scattering angle can be expressed as following,

$$k' = \frac{k(E + p \cos \alpha_c)}{E - p \cos \theta_\gamma + k[1 + \cos(\alpha_c - \theta_\gamma)]}, \quad (3.6)$$

From this equation, it is easy to determine the crossing angle α_c dependence of the maximum scattered photon energy k'_{max} with the following condition on the scattering angle,

$$\left. \frac{dk'}{d\theta_\gamma} \right|_{\theta_\gamma^{max}} = 0 \quad \Longleftrightarrow \quad \theta_\gamma^{max} = \arctan \left(\frac{k \sin \alpha_c}{k \cos \alpha_c - p} \right), \quad (3.7)$$

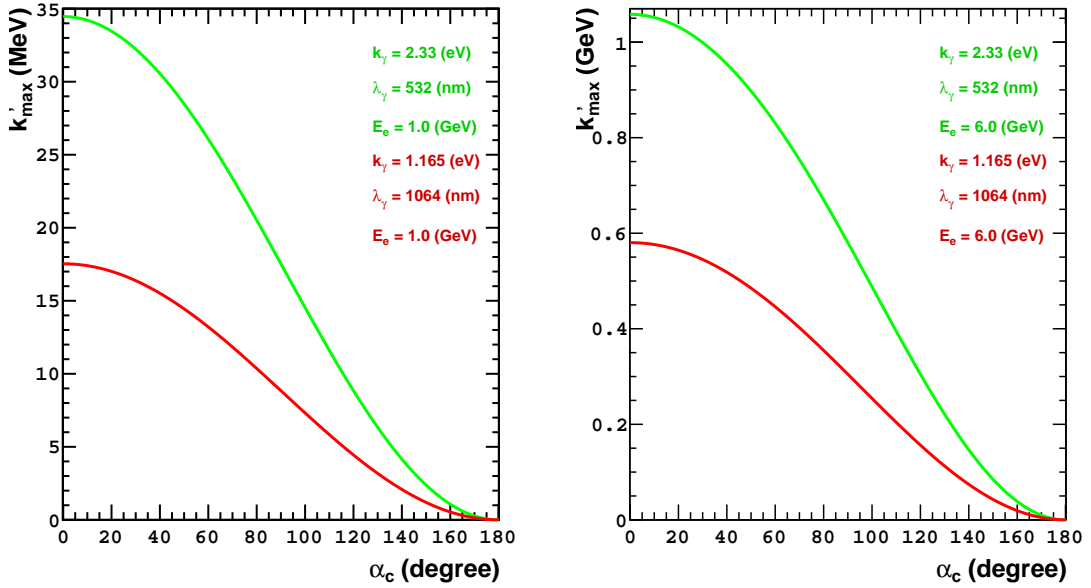


Figure 3.3 (color) Maximum energy of the scattered photon as a function of the crossing angle with two different lasers ($\lambda_\gamma = 532$ nm, 1064 nm) and electron beam energies ($E_e = 1.0$ GeV, 6.0 GeV).

We can see from the curve in Figure 3.3 that the crossing angle α_c reduces the energy range of the scattered photon, but it is pretty flat for small angles ($< 10^\circ$)

and then falls down to 0 for $\alpha_c = 180^\circ$. In the real Compton polarimeter, we can only detect the those photons which interact in the opposite direction to the electron beam. The other photons, almost collinear to the electron beam also interact but their scattered energy is very low (~ 0) and always below the threshold of detection. For a green photon ($\lambda_\gamma = 532$ nm, $k_\gamma = 2.33$ eV) scattered from a 1.0 GeV electron, the maximum energy of scattering, which often called a Compton edge, lies at 34.5 MeV. While this energy is at about 1.05 GeV for the same photon scattered from a 6.0 GeV electron.

For a small crossing angle (usually few degrees) between electron and photon beams, the α_c has a negligible effect on the scattered photon beam energy. For a case of $\alpha_c = 0$ and $\theta_\gamma \ll 1$, the equation(3.6) has a simplified form,

$$k' = \frac{E(1-a)}{1+a\left(\frac{\theta_\gamma E}{m}\right)^2}, \quad (3.8)$$

where $a = \frac{m^2}{m^2 + 4kE}$ and m is the rest mass of an electron. Here we used an ultra-relativistic approximation of $\beta = \frac{p}{E} = 1$ and the limit of $|\vec{k}| \ll |\vec{p}|$.

From Figure 3.4, one can see that for an incident electron beam of $E_e = 1.0$ GeV, and a given laser beam of $\lambda_\gamma = 532$ nm ($k_\gamma = 2.33$ eV), used in our Compton polarimeter, most of the scattered photons are emitted in a cone of 4.0 mrad. However, for the same photons scattered from higher energy electrons, this cone angle is much smaller.

The maximum scattered photon energy k'_{max} , correspond to the minimum scattered electron energy E'_{min} , is reached for $\theta_\gamma = 0$.

$$k'_{max} = E(1-a), \quad (3.9)$$

$$E'_{min} = E - k'_{max} + k \simeq Ea, \quad (3.10)$$

while the minimum scattered photon energy k'_{min} , correspond to the maximum scat-

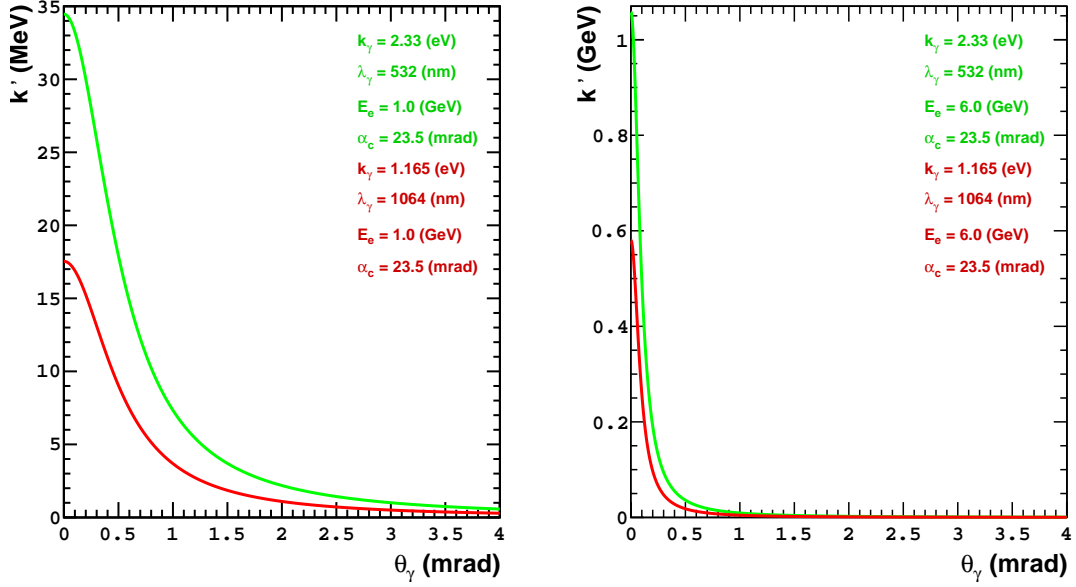


Figure 3.4 (color) Scattered photon energy k' as a function of scattering angle θ_γ with two different lasers ($\lambda_\gamma = 532$ nm, 1064 nm) and electron beam energies ($E_e = 1.0$ GeV, 6.0 GeV).

tered electron energy E'_{max} , is for $\theta_\gamma = \pi$,

$$k'_{min} = k, \quad (3.11)$$

$$E'_{max} = E - k'_{min} + k = E, \quad (3.12)$$

The scattered electron energy E' is related to the scattered electron angle θ_e through its momentum p' by a second-order equation,

$$\begin{aligned} p'^2(C^2 - B^2) - 2ABp' + m^2C^2 - A^2 &= 0, \\ p' &= \frac{AB \pm C\sqrt{(A^2 - m^2(C^2 - B^2))}}{C^2 - B^2}, \end{aligned} \quad (3.13)$$

where

$$\begin{aligned} A &= m^2 + Ek + kp \cos \alpha_c, \\ B &= p \cos \theta_e - k \cos(\theta_e - \alpha_c), \\ C &= E + k, \end{aligned}$$

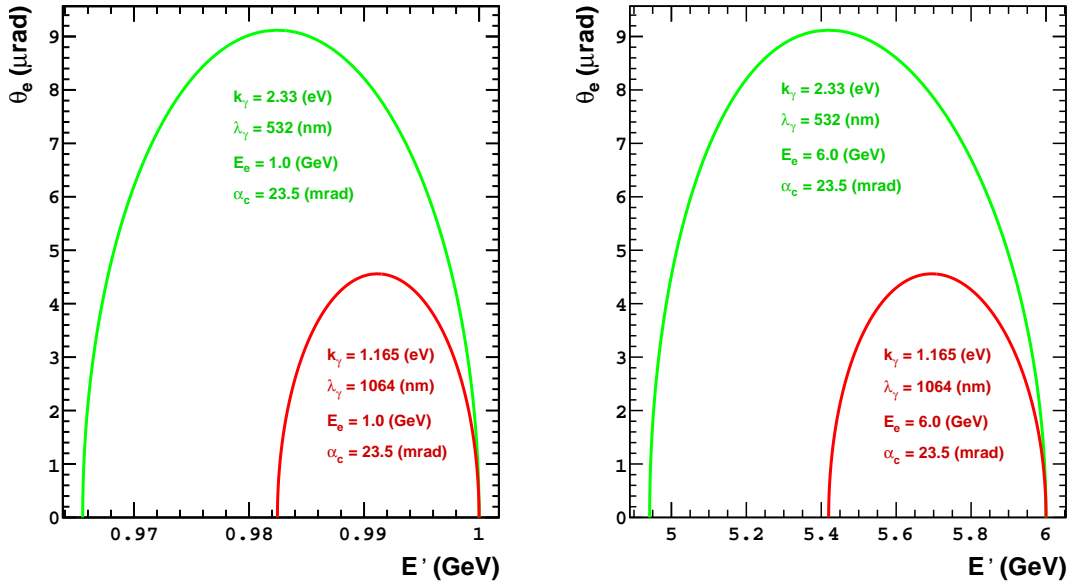


Figure 3.5 (color) Scattered electron energy E' as a function of scattering angle θ_e with two different laser ($\lambda_\gamma = 532$ nm, 1064 nm) and electron beam energies ($E_e = 1.0$ GeV, 6.0 GeV).

Figure 3.5 shows the scattered electron energy E' as a function of scattered electron angle θ_e at different electron and photon beam energies. We can see both from Figure 3.4 and Figure 3.5 that scattered electrons and photons have a very small cone angle. If we want to separate those particles from incident electrons and photons and be able to detect them, we need a magnetic field. This is done by using a magnetic chicane which deflects and separates the scattered and incident electrons and makes the scattered photon and electron detection possible in photon and electron detectors respectively. We will discuss the Compton chicane later in this chapter.

3.1.2 Compton Cross Section and Asymmetry

A cross section is a prediction of a probability of a particle being scattered by another particle. It is always measured by the effective surface area seen by the incident particles. In polarized Compton scattering, a circularly polarized photon beam interacts with a polarized electron beam. In Figure 3.2, let's consider the electron polarization

vector $\vec{\mathcal{P}}_e$ which has an angle ψ with respect to the Z -axis in $X-Z$ plane. We can decompose it along the longitudinal and transverse directions, such that $\mathcal{P}_e^L = \mathcal{P}_e \cos \psi$ and $\mathcal{P}_e^T = \mathcal{P}_e \sin \psi$. The photon beam has a circular polarization of \mathcal{P}_γ with a crossing angle α_c relative to the propagation direction of the electron beam. Given the fact that the newly installed Compton polarimeter has a crossing angle of 24.0 mrad (1.4 degree) and the effect of a small α_c (order of 10^{-2} rad) to the polarized cross section is very small (order of α_c^2) [25], we can neglect the influence of α_c for this case.

In the laboratory frame, in the case of zero crossing angle with circularly polarized photons, the second order differential cross section can be expressed in terms of a dimensionless parameter ρ [26],

$$\frac{d^2\sigma^\mp}{d\rho d\phi} = \frac{d^2\sigma_0}{d\rho d\phi} \mp \mathcal{P}_e \mathcal{P}_\gamma \left[\cos \psi \frac{d^2\sigma_L}{d\rho d\phi} + \sin \psi \cos \phi \frac{d^2\sigma_T}{d\rho d\phi} \right], \quad (3.14)$$

where

$$\rho = \frac{k'}{k'_{max}} = \frac{1}{1 + a \left(\frac{\theta_\gamma E}{m} \right)^2},$$

and the unpolarized differential cross section is defined as,

$$\frac{d^2\sigma_0}{d\rho d\phi} = r_0^2 a \left[1 + \frac{\rho^2(1-a)^2}{1-\rho(1-a)} + \left(\frac{1-\rho(1+a)}{1-\rho(1-a)} \right)^2 \right], \quad (3.15)$$

and the longitudinal and transverse differential cross sections are defined as,

$$\frac{d^2\sigma_L}{d\rho d\phi} = r_0^2 a \left[(1-\rho(1+a)) \left(1 - \frac{1}{(1-\rho(1-a))^2} \right) \right], \quad (3.16)$$

$$\frac{d^2\sigma_T}{d\rho d\phi} = r_0^2 a \left[\rho(1-a) \frac{\sqrt{4a\rho(1-\rho)}}{1-\rho(1-a)} \right], \quad (3.17)$$

where r_0 is the classical electron radius. The “+” and “-” signs are defined by the helicity states of electrons and photons. The last term represents an azimuthal dependence in the cross section. It appears because of transverse component of electron spin. It is the same if the incident photon contains a linear polarization component

mixed with a circular polarization. This dependence will vanish if our detector is symmetric in azimuth angle ϕ . After integration over ϕ , the equation (3.14) becomes,

$$\frac{d\sigma^\mp}{d\rho} = \frac{d\sigma_0}{d\rho} \mp \mathcal{P}_e \mathcal{P}_\gamma \cos \psi \frac{d\sigma_L}{d\rho}, \quad (3.18)$$

the term $\frac{d\sigma_L}{d\rho}$ is the origin of the cross section asymmetry when the helicity of the electron and photon beam is reversed. The above equation now can be rewritten as,

$$\frac{d\sigma^\mp}{d\rho} = \frac{d\sigma_0}{d\rho} \left(1 \mp \mathcal{P}_e^L \mathcal{P}_\gamma \mathcal{A}_L \right), \quad (3.19)$$

where \mathcal{A}_L is called the longitudinal differential asymmetry and it is defined as,

$$\mathcal{A}_L = \frac{\left(d\sigma_L/d\rho \right)}{\left(d\sigma_0/d\rho \right)}, \quad (3.20)$$

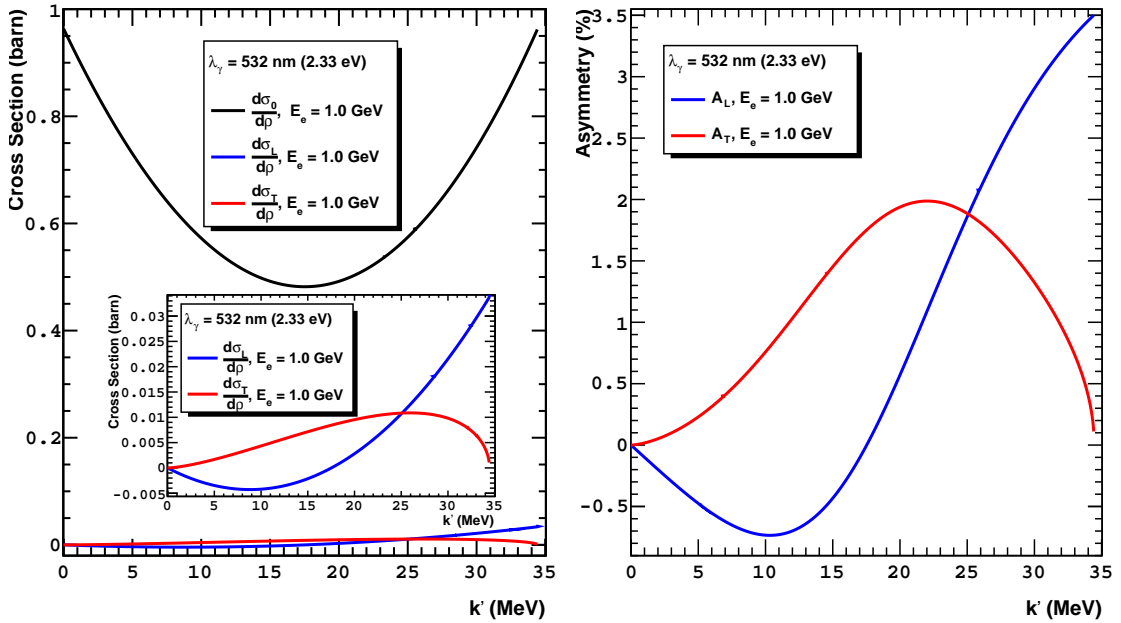


Figure 3.6 (color) The left plot shows the unpolarized (black line), transverse (blue line) and longitudinal (red line) differential cross section as a function of scattered photon energy k' . The right plot shows the longitudinal (blue line) and transverse (red line) Compton asymmetry as a function of scattered photon energy k' .

Similarly the transverse differential asymmetry \mathcal{A}_T also can be defined as,

$$\mathcal{A}_T = \frac{\left(\frac{d\sigma_L}{d\rho}\right)}{\left(\frac{d\sigma_0}{d\rho}\right)}, \quad (3.21)$$

Figure 3.6 plots the differential cross sections (unpolarized, longitudinal and transverse) and asymmetries (longitudinal and transverse) for an electron beam of 1.0 GeV and a photon beam of $k_\gamma = 2.33$ eV ($\lambda_\gamma = 532$ nm) as a function of scattered photon energy k' .

Figure 3.7 shows the longitudinal asymmetry values as a function of scattered photon energy for 1.0 and 6.0 GeV electrons with green ($\lambda_\gamma = 532$ nm) and infrared ($\lambda_\gamma = 1064$ nm) photons. From the plot one can see that for green photons scattered from an electron beam of 1.0 GeV, the maximum longitudinal differential asymmetry is at about 3.5 %, but for infrared photons, it is at about 1.8 %. For an electron beam of 6.0 GeV, these values are at about 18.0 % and 10.0 % respectively.

The longitudinal differential asymmetry is in its maximum when the scattered

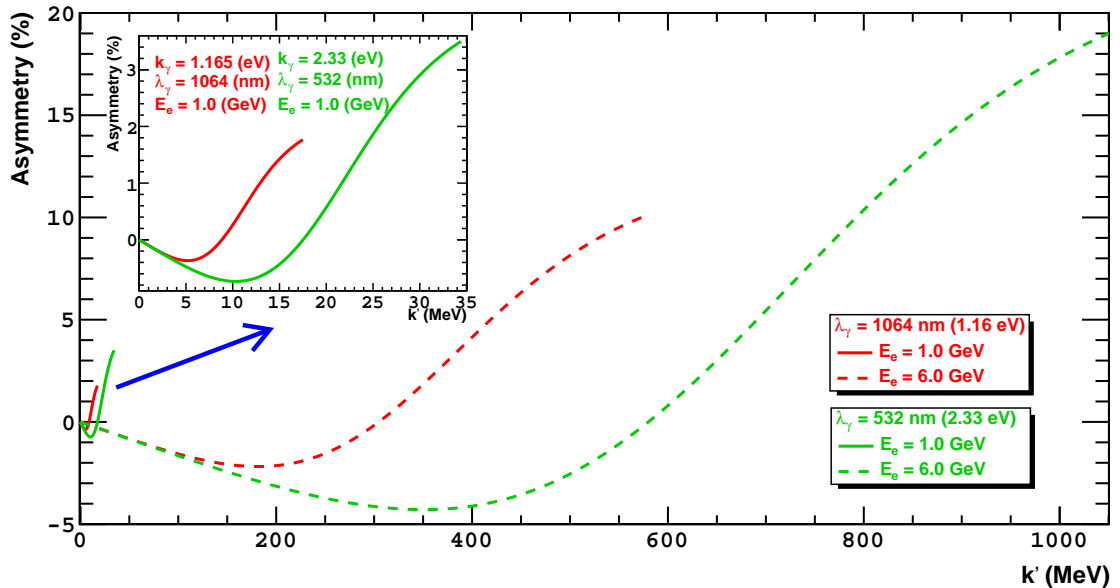


Figure 3.7 (color) Longitudinal differential asymmetry at 1.0 GeV (solid line) and 6.0 GeV (dashed line) electron beam energies for photon energies of 1.165 eV (red line) and 2.33 eV (green line).

photon energy $k' = k'_{max}$ and becomes negative, zero and positive when k' is less than, equal and greater than k'_0 , where k'_0 is defined as,

$$k'_0 = \frac{E(1-a)}{(1+a)}, \quad (3.22)$$

We use the characteristics of differential asymmetry as a function of scattered photon energy to determine the electron beam polarization which will be described later in this chapter.

3.1.3 Interaction Luminosity

The luminosity is an important value to characterize the total number of events in Compton scattering. Let's assume that the electron and photon beam intersects at an angle α_c in $X-Z$ plane with a relative velocity $c(1 + \alpha_c)$ in laboratory frame, as shown in Figure 3.8. The luminosity of interaction between two beams with densities $\rho_e(x, y, z)$ and $\rho_\gamma(x, y, z)$ has the general expression [20],

$$\mathcal{L} = \int \int \int c(1 + \cos \alpha_c) \rho_e(x, y, z) \rho_\gamma(x, y, z) dx dy dz, \quad (3.23)$$

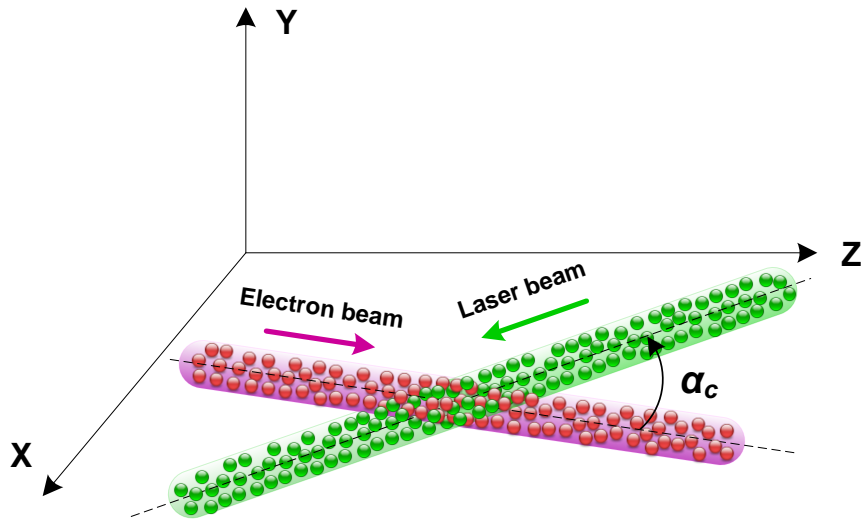


Figure 3.8 (color) Electron and Photon Beam Crossing.

The beam density is the product of two normalized Gaussians in X and Y directions with a normalization factor N_0 ,

$$\rho(x, y, z) = N_0 \left(\frac{1}{\sqrt{2\pi}\sigma_x(z)} e^{-\frac{x^2}{2\sigma_x^2(z)}} \right) \left(\frac{1}{\sqrt{2\pi}\sigma_y(z)} e^{-\frac{y^2}{2\sigma_y^2(z)}} \right), \quad (3.24)$$

where $\sigma_x(z)$ and $\sigma_y(z)$ are the beam sizes in X and Y direction at z . The normalization factor N_0 for electron beam with current I_e and photon beam with laser power P_L and wavelength λ is defined as,

$$N_{0e} = \frac{I_e}{ec} \quad \text{and} \quad N_{0\gamma} = \frac{P_L \lambda}{hc^2}, \quad (3.25)$$

With the assumption of the angular divergence of two beams is small as compared to the crossing angle α_c so that the beam sizes $\sigma_{x,y}$ are constant, the total luminosity can be written as,

$$\mathcal{L}_0 \simeq \frac{1}{\sqrt{2\pi}} \frac{I_e}{ec} \frac{P_L \lambda}{hc} \frac{(1 + \cos \alpha_c)}{\sin \alpha_c} \frac{1}{\sqrt{\sigma_{ey}^2 + \sigma_{\gamma y}^2}}, \quad (3.26)$$

Note that in equation (3.26), only the transverse component of beam sizes σ_{ey} and $\sigma_{\gamma y}$ are involved in the luminosity after the integration, which means in current coordinate frame, only the transverse size of the two beams is playing a role in luminosity.

In Figure 3.9, the left plot shows the total luminosity \mathcal{L}_0 as a function α_c for green ($\lambda_\gamma = 532$ nm) and infrared ($\lambda_\gamma = 1064$ nm) photons with 3.5 kW laser power at 100 μA electron beam current with a size of $\sigma_e = 100$ μm . On the right plot the photon beam size σ_γ dependence of luminosity is shown. From the figure, one can see that, the \mathcal{L}_0 is very sensitive to α_c while it is relatively less sensitive to σ_γ . For the same photon beam power and electron beam current, \mathcal{L}_0 is inversely proportional to photon beam energy. That is the reason of green photons generally give smaller luminosity than the infrared photons. In general, we prefer to have smaller beam sizes and a smaller crossing angle in order to maximize the interaction.

In reality, for a good sampling of electrons beam polarization, we would like a good overlap between two beams which requires $\sigma_e \sim \sigma_\gamma$. From Figure 3.8, one can see

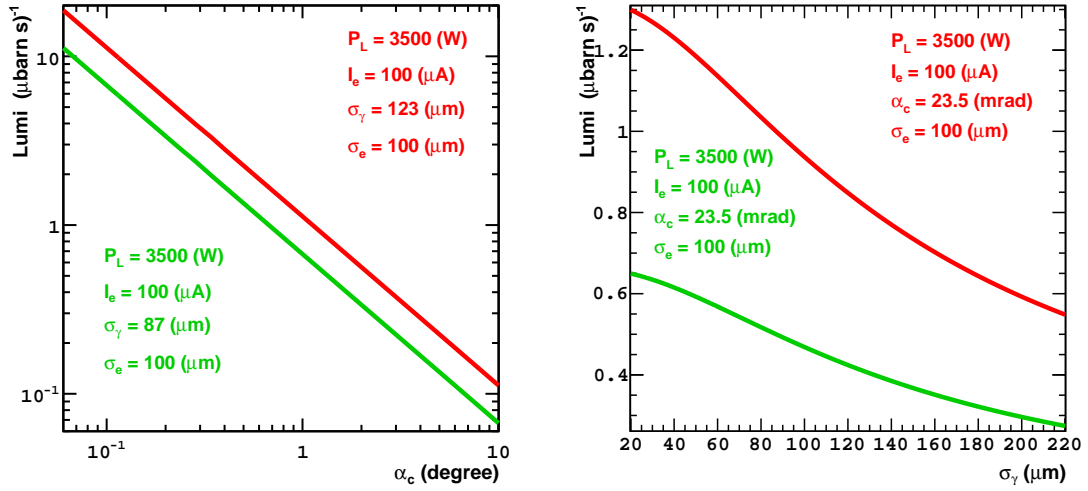


Figure 3.9 (color) On the left, the luminosity as function of crossing angle for the green ($\lambda_\gamma = 532$ nm) (green line) and infrared ($\lambda_\gamma = 1064$ nm) (red line) photons. On the right, luminosity as a function of photon beam size for green (green line) and infrared (red line) photons.

that, If the crossing takes place with a vertical gap $\Delta y = y_e - y_\gamma$ between the centroids of two beams, then the luminosity becomes less. We can calculate it by integrating the differential luminosity $d\mathcal{L}/dy$ over Δy and then the luminosity becomes [20],

$$\mathcal{L} = \mathcal{L}_0 e^{-\frac{(\Delta y)^2}{2(\sigma_{ey}^2 + \sigma_{\gamma y}^2)}}, \quad (3.27)$$

As plotted in Figure 3.10, the luminosity \mathcal{L} decreases exponentially as a function of the distance separating the two beams. In order to get the maximum luminosity so that the scattering rate which contributes to measure the the Compton asymmetry is maximum, we always hope to make Δy equals to 0. This is done by steering the electron beam vertically by a pair of dipoles in Compton chicane and this procedure is often called “vertical scan”.

3.1.4 Methods of Electron Beam Polarization Measurement

We defined the polarization of an electron beam in equation 2.32, where $N_{+(-)}$ is the number of electrons with spin parallel (anti parallel) to the beam direction. In Comp-

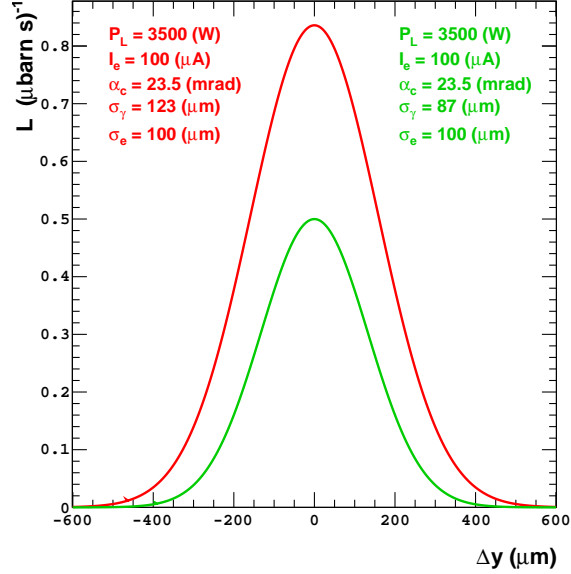


Figure 3.10 (color) The luminosity as a function of the vertical distance between the centroids of the electron and photon beams plotted for the green ($\lambda_\gamma = 532$ nm) (green line) and infrared ($\lambda_\gamma = 1064$ nm) photons with different beam sizes cross with the electron beam of 1.0 GeV and beam size of $100 \mu\text{m}$.

ton polarimetry, the longitudinal polarization \mathcal{P}_e^L of the electron beam is extracted from the experimental asymmetry \mathcal{A}_{exp} between two measurements of Compton scattering with electron polarization is parallel (+) and anti parallel (−) to the laser polarization states. This asymmetry may be defined as,

$$\mathcal{A}_{exp} = \frac{n^+ - n^-}{n^+ + n^-} = \mathcal{P}_e^L \mathcal{P}_\gamma \mathcal{A}_L, \quad (3.28)$$

where n^\pm is the scattering rate for events before and after the laser polarization reversal ($\mathcal{P}_\gamma \rightarrow -\mathcal{P}_\gamma$). In each measurement, n^\pm will be measured with a luminosity \mathcal{L}^\pm during a time T^\pm and will be normalized to the same integrated luminosity. In equation 3.28, the \mathcal{A}_{exp} and \mathcal{P}_γ are the measured quantities and \mathcal{A}_L is calculated in the framework of the standard model, so that the only unknown quantity is the longitudinal electron beam polarization \mathcal{P}_e^L . From now on, we call the longitudinal polarization \mathcal{P}_e^L electron beam polarization and label it as \mathcal{P}_e for simplicity. In reality,

we calculate the average value of \mathcal{A}_L in finite interval by taking into account the detector resolution and $\langle \mathcal{A}_L \rangle$ is often called an analyzing power. There are three methods of extracting electron beam polarization measurement.

Differential Polarization Measurement

The numbers of Compton scattering events n_{\pm}^i are measured as a function of the scattered photon or electron energy in energy bin N_b by a following integral,

$$n_{\pm}^i = \mathcal{L}_{\pm} T_{\pm} \int_{\rho_i}^{\rho_{i+1}} \epsilon_{\pm}(\rho) \frac{d\sigma_0(\rho)}{d\rho} (1 \pm \mathcal{P}_e \mathcal{P}_{\gamma} \mathcal{A}_L(\rho)) d\rho, \quad (3.29)$$

where $\frac{d\sigma_0(\rho)}{d\rho}$ is the unpolarized differential cross section (Eq. 3.15), $\mathcal{A}_L(\rho)$ is the differential longitudinal asymmetry (Eq. 3.20), $\epsilon_{\pm}(\rho)$ is the detection efficiency, $[\rho_i, \rho_{i+1}]$ is the width of each energy bin and ρ is the scattered photon energy normalized to its maximum.

Now, the experimental asymmetry for each energy bin is defined as,

$$\mathcal{A}_{exp}^i = \frac{n_+^i - n_-^i}{n_+^i + n_-^i} = \mathcal{P}_e^i \mathcal{P}_{\gamma} \frac{\int_{\rho_i}^{\rho_{i+1}} \epsilon(\rho) \frac{d\sigma_0(\rho)}{d\rho} \mathcal{A}_L(\rho) d\rho}{\int_{\rho_i}^{\rho_{i+1}} \epsilon(\rho) \frac{d\sigma_0(\rho)}{d\rho} d\rho} = \mathcal{P}_e^i \mathcal{P}_{\gamma} \langle \mathcal{A}_L \rangle_i \simeq \mathcal{P}_e^i \mathcal{P}_{\gamma} \mathcal{A}_L^i, \quad (3.30)$$

where \mathcal{A}_L^i is the longitudinal asymmetry at the center of the bin. The electron polarization \mathcal{P}_e^i measured for each energy bin i is given by,

$$\mathcal{P}_e^i = \frac{\mathcal{A}_{exp}^i}{\mathcal{P}_{\gamma} \langle \mathcal{A}_L \rangle_i} \simeq \frac{\mathcal{A}_{exp}^i}{\mathcal{P}_{\gamma} \mathcal{A}_L^i}, \quad (3.31)$$

which is independent of detection efficiency. The relative statistical error in this measurement is,

$$\frac{\Delta \mathcal{P}_e^i}{\mathcal{P}_e^i} = \frac{\Delta \mathcal{A}_{exp}^i}{\mathcal{A}_{exp}^i} = \left[\frac{4n_+^i n_-^i}{(n_+^i + n_-^i)^3} \right]^{\frac{1}{2}} \times \frac{1}{\mathcal{A}_{exp}^i}, \quad (3.32)$$

After defining the total number of events n_t^i for the bin i as,

$$n_t^i = n_+^i + n_-^i = \mathcal{L} T \int_{\rho_i}^{\rho_{i+1}} \epsilon(\rho) \frac{d\sigma_0(\rho)}{d\rho} d\rho = \mathcal{L} T \sigma_0^i, \quad (3.33)$$

The statistical error has the following form,

$$\frac{\Delta \mathcal{P}_e^i}{\mathcal{P}_e^i} = \left[\frac{1 - (\mathcal{P}_e^i \mathcal{P}_\gamma \mathcal{A}_L^i)^2}{\mathcal{L} T \sigma_0^i} \right]^{\frac{1}{2}} \frac{1}{\mathcal{P}_e^i \mathcal{P}_\gamma \mathcal{A}_L^i}, \quad (3.34)$$

The final electron polarization is the weighted mean of these polarization measurements,

$$\mathcal{P}_e = \frac{\sum_{i=1}^{N_b} \frac{\mathcal{P}_e^i}{\Delta \mathcal{P}_e^{i2}}}{\sum_{i=1}^{N_b} \frac{1}{\Delta \mathcal{P}_e^{i2}}}, \quad (3.35)$$

$$\Delta \mathcal{P}_e = \sum_{i=1}^{N_b} \Delta \mathcal{P}_e^i = \frac{1}{\sqrt{\mathcal{L} T \mathcal{P}_\gamma}} \sum_{i=1}^{N_b} \left[\frac{1 - (\mathcal{P}_e^i \mathcal{P}_\gamma \mathcal{A}_L^i)^2}{\sigma_0^i \mathcal{A}_L^{i2}} \right]^{\frac{1}{2}}, \quad (3.36)$$

with the assumption that \mathcal{A}_L^i is very small (few %) and $\mathcal{P}_e^i \mathcal{P}_\gamma < 1$, we can neglect $(\mathcal{P}_e^i \mathcal{P}_\gamma \mathcal{A}_L^i)^2$ and the above equation becomes,

$$\Delta \mathcal{P}_e = \frac{1}{\sqrt{\mathcal{L} T \mathcal{P}_\gamma}} \sum_{i=1}^{N_b} \left(\frac{1}{\sigma_0^i \mathcal{A}_L^{i2}} \right)^{\frac{1}{2}}, \quad (3.37)$$

for a limit of $\Delta \rho = \rho_{i+1} - \rho_i \rightarrow 0$ and a threshold energy ρ_{min} below which no Compton event is detected, we will have the following relation,

$$\left(\frac{\Delta \mathcal{P}_e}{\mathcal{P}_e} \right)^2 = \frac{1}{\mathcal{L} T \mathcal{P}_e^2 \mathcal{P}_\gamma^2 \sigma_0^t \langle \mathcal{A}_L^2 \rangle}, \quad (3.38)$$

where

$$\langle \mathcal{A}_L^2 \rangle = \frac{\int_{\rho_{min}}^1 \epsilon(\rho) \frac{d\sigma_0(\rho)}{d\rho} \mathcal{A}_L^2(\rho) d\rho}{\int_{\rho_{min}}^1 \epsilon(\rho) \frac{d\sigma_0(\rho)}{d\rho} d\rho}, \quad \sigma_0^t = \int_{\rho_{min}}^1 \epsilon(\rho) \frac{d\sigma_0(\rho)}{d\rho} d\rho, \quad (3.39)$$

The time t_D to get a statistical precision $\frac{\Delta \mathcal{P}_e}{\mathcal{P}_e}$ is,

$$t_D = \frac{1}{\mathcal{L} \left(\frac{\Delta \mathcal{P}_e}{\mathcal{P}_e} \right)^2 \mathcal{P}_e^2 \mathcal{P}_\gamma^2 \sigma_0^t \langle \mathcal{A}_L^2 \rangle}, \quad (3.40)$$

Note that the needed time t_D and the square of the error are inversely proportional to the value of $\langle \mathcal{A}_L^2 \rangle$ through ρ_{min} .

Integrated Polarization Measurement

Without energy measurement for the scattered particles, only the numbers of Compton scattering events integrated over the energy range n_+ and n_- can be measured and they are,

$$n_{\pm} = \mathcal{L}_{\pm} T_{\pm} \int_{\rho_{min}}^1 \epsilon_{\pm}(\rho) \frac{d\sigma_0(\rho)}{d\rho} (1 \pm \mathcal{P}_e \mathcal{P}_{\gamma} \mathcal{A}_L(\rho)) d\rho, \quad (3.41)$$

The experimental integrated asymmetry is defined as,

$$\mathcal{A}_{exp} = \frac{n_+ - n_-}{n_+ + n_-} = \mathcal{P}_e \mathcal{P}_{\gamma} \frac{\int_{\rho_{min}}^1 \epsilon(\rho) \frac{d\sigma_0(\rho)}{d\rho} \mathcal{A}_L(\rho) d\rho}{\int_{\rho_{min}}^1 \epsilon(\rho) \frac{d\sigma_0(\rho)}{d\rho} d\rho} = \mathcal{P}_e \mathcal{P}_{\gamma} \langle \mathcal{A}_L \rangle, \quad (3.42)$$

The measured electron polarization,

$$\mathcal{P}_e = \frac{\mathcal{A}_{exp}}{\mathcal{P}_{\gamma} \langle \mathcal{A}_L \rangle}, \quad (3.43)$$

is proportional to the inverse of the mean longitudinal asymmetry which is depend on the detection efficiency and on the energy threshold ρ_{min} . The relative statistical error in measurement of electron polarization is equal to the error in integrated experimental asymmetry,

$$\left(\frac{\Delta \mathcal{P}_e}{\mathcal{P}_e} \right)^2 = \left(\frac{\Delta \mathcal{A}_{exp}}{\mathcal{A}_{exp}} \right)^2 = \frac{1 - \mathcal{P}_e^2 \mathcal{P}_{\gamma}^2 \langle \mathcal{A}_L \rangle^2}{\mathcal{L} T \mathcal{P}_e^2 \mathcal{P}_{\gamma}^2 \sigma_0^t \langle \mathcal{A}_L \rangle^2} \simeq \frac{1}{\mathcal{L} T \mathcal{P}_e^2 \mathcal{P}_{\gamma}^2 \sigma_0^t \langle \mathcal{A}_L \rangle^2}, \quad (3.44)$$

where the σ_0^t is given by equation 3.39. The needed time t_I to achieve an accuracy $\frac{\Delta \mathcal{P}_e}{\mathcal{P}_e}$ is,

$$t_I = \frac{1}{\mathcal{L} \left(\frac{\Delta \mathcal{P}_e}{\mathcal{P}_e} \right)^2 \mathcal{P}_e^2 \mathcal{P}_{\gamma}^2 \sigma_0^t \langle \mathcal{A}_L \rangle^2}, \quad (3.45)$$

here the needed time t_I and the square of the error are inversely proportional to the value of $\langle \mathcal{A}_L \rangle^2$ through ρ_{min} and detection efficiency $\epsilon(\rho)$.

Energy Weighted Polarization Measurement

We only measure the energies E_+ and E_- over the energy range and over the time t and they are given by,

$$E_{\pm} = \mathcal{L}_{\pm} T_{\pm} \int_0^1 E \epsilon_{\pm}(\rho) \frac{d\sigma_0(\rho)}{d\rho} (1 \pm \mathcal{P}_e \mathcal{P}_{\gamma} \mathcal{A}_L(\rho)) d\rho, \quad (3.46)$$

with a statistical error dE_{\pm} due to the fluctuation of the unmeasured number of events $\frac{dN_{\pm}}{d\rho}$,

$$\begin{aligned} \frac{dN_{\pm}}{d\rho} &= \mathcal{L}_{\pm} T_{\pm} \epsilon_{\pm}(\rho) \frac{d\sigma_0(\rho)}{d\rho} (1 \pm \mathcal{P}_e \mathcal{P}_{\gamma} \mathcal{A}_L), \\ dE_{\pm}^2 &= \mathcal{L} \frac{T}{2} \int_0^1 E^2 \epsilon_{\pm}(\rho) \frac{d\sigma_0(\rho)}{d\rho} (1 \pm \mathcal{P}_e \mathcal{P}_{\gamma} \mathcal{A}_L(\rho)) d\rho, \end{aligned} \quad (3.47)$$

The experimental integrated energy asymmetry is related to the electron polarization by,

$$\mathcal{A}_{exp} = \frac{E_+ - E_-}{E_+ + E_-} = \mathcal{P}_e \mathcal{P}_{\gamma} \frac{\int_0^1 \epsilon(\rho) \frac{d\sigma_0(\rho)}{d\rho} E \mathcal{A}_L(\rho) d\rho}{\int_0^1 \epsilon(\rho) \frac{d\sigma_0(\rho)}{d\rho} E d\rho} = \mathcal{P}_e \mathcal{P}_{\gamma} \frac{\langle E \mathcal{A}_L \rangle}{\langle E \rangle}, \quad (3.48)$$

and the measured electron polarization,

$$\mathcal{P}_e = \frac{\mathcal{A}_{exp}}{\mathcal{P}_{\gamma} \frac{\langle E \mathcal{A}_L \rangle}{\langle E \rangle}}, \quad (3.49)$$

The time needed to achieve an accuracy $\frac{\Delta \mathcal{P}_e}{\mathcal{P}_e}$ is,

$$t_E = \frac{1 + \mathcal{P}_e^2 \mathcal{P}_{\gamma}^2 \left(\frac{\langle E \mathcal{A}_L \rangle^2}{\langle E \rangle^2} - 2 \frac{\langle E \mathcal{A}_L \rangle \langle E^2 \mathcal{A}_L \rangle}{\langle E \rangle \langle E^2 \rangle} \right)}{\mathcal{L} \left(\frac{\Delta \mathcal{P}_e}{\mathcal{P}_e} \right)^2 \mathcal{P}_e^2 \mathcal{P}_{\gamma}^2 \sigma_0^t \frac{\langle E \mathcal{A}_L \rangle^2}{\langle E^2 \rangle}} \simeq \frac{1}{\mathcal{L} \left(\frac{\Delta \mathcal{P}_e}{\mathcal{P}_e} \right)^2 \mathcal{P}_e^2 \mathcal{P}_{\gamma}^2 \sigma_0^t \frac{\langle E \mathcal{A}_L \rangle^2}{\langle E^2 \rangle}}, \quad (3.50)$$

In Hall A Compton polarimeter at JLab, a new technique based on energy weighted method has been developed. It computes the longitudinal asymmetry \mathcal{A}_L in the

energy-weighted integral of the photon signal and it is less sensitive to low-energy uncertainties in the detector response function as compared to the differential method. In this method the actual asymmetry is weighted by detector signal S_{\pm} ,

$$S_{\pm} = \mathcal{L}T \int_0^1 S(\rho) \frac{d\sigma_0(\rho)}{d\rho} (1 \pm \mathcal{P}_e \mathcal{P}_\gamma \mathcal{A}_L(\rho)) d\rho, \quad (3.51)$$

where $S(\rho)$ is the average detector signal for normalized photon energy ρ . The experimental energy weighted asymmetry \mathcal{A}_{exp} is,

$$\mathcal{A}_{exp} = \frac{S_+ - S_-}{S_+ + S_-} = \mathcal{P}_e \mathcal{P}_\gamma \frac{\int_0^1 S(\rho) \frac{d\sigma_0(\rho)}{d\rho} \mathcal{A}_L(\rho) d\rho}{\int_0^1 S(\rho) \frac{d\sigma_0(\rho)}{d\rho} d\rho} = \mathcal{P}_e \mathcal{P}_\gamma \langle \mathcal{A}_L \rangle_S, \quad (3.52)$$

where $\langle \mathcal{A}_L \rangle_S$ is the signal asymmetry which is called the analyzing power. The measured electron polarization is then,

$$\mathcal{P}_e = \frac{\mathcal{A}_{exp}}{\mathcal{P}_\gamma \langle \mathcal{A}_L \rangle_S} \quad (3.53)$$

The energy weighted method is mainly driven by the need of PREx experiment which runs at an electron beam of ~ 1.0 GeV and results a very small Compton asymmetry (few %). It removes two of the main systematic errors, those due to the detector response function and the deadtime.

We just explained the principle of Compton polarimetry. We will now describe the Compton polarimetry projects around the world and then discuss how we chose a photon source to build a new Compton polarimeter at JLab.

3.2 Compton Polarimetry

3.2.1 Overview

Originally suggested by Baier and Khoze [27], the Compton polarimeter with a laser beam has become a part of the standard equipment in many accelerators. The first Compton polarimeter ever built was at SLAC in the late 70s [32], which monitors the

transverse polarization of beams circulating in the SLAC e^+e^- storage ring SPEAR. In this setup, a circularly polarized photon beam from an Ar-Ion laser was focused on an electron or positron beam at an angle of 8 *mrad* and the backscattered photons were collected by a NaI crystal combined with a set of scintillators and a drift chamber. The polarization measurement was achieved by a measurement of up-down asymmetry in the backscattered gamma rates. A statistical precision of $\pm 5.0\%$ was achieved by peak laser power of 80 W and at a beam energy of 3.7 GeV in 2 minutes. Since then many high-energy storage rings [3, 28–31, 33] have adopted the Compton polarimeter as a powerful diagnostics tool to measure beam polarization. In these storage rings, the Compton analyzing powers are large, and the measurement is non-destructive. Therefore no reduction of beam lifetime is expected. The common feature of these polarimeters is that they all use a single shot pulsed or continuous wave (CW) laser with a wavelength of 514.5 nm or 532 nm, and the required average laser power was only from few Watts to tens of Watts in order to achieve a reasonable statistical precision in beam polarization in a relatively short time. Furthermore they all use the scattered photon detection as their main tool to extract the e^+ or e^- beam polarization.

For JLab experimental conditions, getting a fast and precise beam polarization with a Compton polarimeter is challenging. Mainly due to the relatively low beam current combined with an insufficient laser power from commonly available commercial lasers results very low electron-photon collision luminosity, and it makes the polarization measurements rather difficult to achieve a good precision in a reasonable amount of time. In 1996, JLab proposed to build a Compton polarimeter in its experimental Hall A [20]. It involves to build an optical cavity, a scattered photon and an electron detector and a Compton chicane which consists of four magnetic dipoles. The heart of this polarimeter is a high-finesse monolithic Fabry-Perot cavity, pumped by a narrow linewidth CW laser. It amplifies a primary 300 mW infrared laser ($\lambda_\gamma = 1064$ nm) beam by about a gain factor of 7000. The electron beam crosses a highly circularly polarized laser beam at an angle of 23.5 *mrad* in the middle of the cavity [8], and the scattered photons and electrons are detected by an array of PbWO_4 crystals [34] and

a Si micro-strip detector respectively in downstream [9]. This large enhancement in laser power by optical cavity resulted in a system capable of making polarization measurements with 1% statistical precision in about an hour at beam currents of 10 μ A and at beam energy of 3 GeV [38]. More recently, Compton polarimetry has been applied with good success to lower energy accelerators in the few GeV regime [4, 6, 7, 36].

Project Name	Electron Energy (GeV)	Electron Current (mA)	Photon Source	Average Photon Power	Date
SPEAR [32]	3.7	20	Ar-Ion pulsed Laser, $\lambda_\gamma = 514.5$ nm	1.0 W	1979
LEP [33]	46.0	0.8	Nd:YAG pulsed laser with 30 Hz repetition rate, $\lambda_\gamma = 532$ nm	5.7 W	1989
SLD [3]	45.6	0.001	Nd:YAG pulsed Laser with 17 Hz repetition rate, $\lambda_\gamma = 532$ nm	100 mJ	1992
AmPS [4]	0.75	200	Ar-Ion CW Laser, $\lambda_\gamma = 514.5$ nm	10 W	1998
CEBAF [8]	3.0	0.1	Nd:YAG CW Laser amplified by an external FP cavity, $\lambda_\gamma = 1064$ nm	1.5 kW	2001
TESLA [35]	250	0.045	Nd:YAG pulsed laser, $\lambda_\gamma = 524$ nm	0.5 W	2001
ELSA [36]	3.5	100	Ar-Ion CW Laser, $\lambda_\gamma = 514.5$ nm	10 W	2002
Bates [6]	1.0	200	Nd:YAG CW Laser, $\lambda_\gamma = 532$ nm	5 W	2003
MAMI [7]	1.5	0.11	Ar-Ion CW Laser amplified by an internal FP cavity, $\lambda_\gamma = 514.5$ nm	90 W	2003
HERA [37]	27.5	80	Nd:YAG CW Laser amplified by an external FP cavity, $\lambda_\gamma = 1064$ nm	3.0 kW	2003
This Project	1.0	0.05	Nd:YAG CW Laser amplified by an external FP cavity, $\lambda_\gamma = 532$ nm	3.5 kW	2010

Table 3.1 A summary table of Compton polarimetry projects.

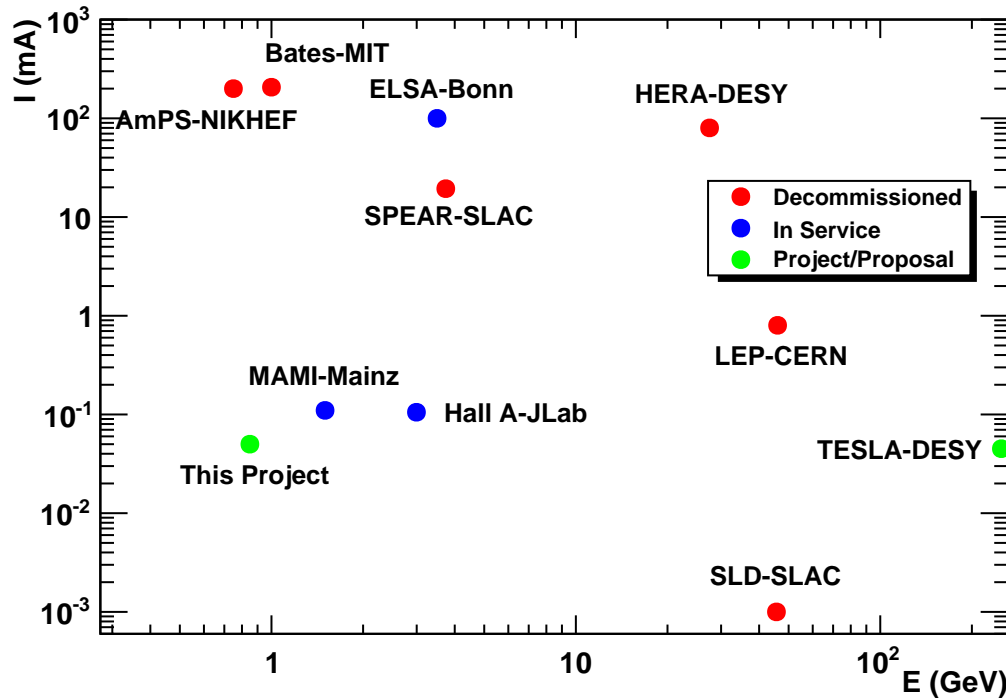


Figure 3.11 (color) A summary plot of Compton polarimetry projects in terms of beam energy and current it operates.

The existing and past Compton polarimetry projects have been summarized in Table 3.1. Since the first implementation of Fabry-Perot enhancement technique in JLab Hall A, similar cavities have been built at other labs [7, 37] for Compton polarimetry purpose.

However, the small asymmetry of the Compton scattering process at low energies makes it difficult to control systematic errors. This was addressed using simultaneous measurement of the backscattered photon and scattered electron, combined with novel analysis techniques to minimize sensitivity to the detector response function, resulting in systematic errors approaching 1% at 3 GeV [38].

3.2.2 Compton Upgrade Project in Hall A at JLab

Through the evolution of JLab physics program, the idea of using parity violating electron scattering to do precision measurements of Standard Model parameters is becoming increasingly popular. These type measurements have stringent requirements on the measurement of the beam polarisation, with this often being the leading systematic uncertainty. Some experiments like PREx [10] also uses parity violating electron scattering to precisely measure the neutron skin thickness at 1.0% level, which requires to get 1.0% relative polarization accuracy at 1 GeV¹ which cannot be achieved by the old infrared ($\lambda_\gamma = 1064$ nm) laser based Compton polarimeter. Therefore an upgrade of existing Compton polarimeter was proposed [39].

At 1.0 GeV and with the infrared laser ($\lambda_\gamma = 1064$ nm), the scattered Compton electrons remain too close to the primary beam (< 3 mm) (see Table 3.2) to be detected. With no response function of the photon detector, the only way to keep the systematics below the 2% level is to perform an energy weighted polarization measurement where the beam polarization is deduced from asymmetry of counting rates integrated over the whole Compton energy range. If the detection threshold is negligible compared with the Compton edge the uncertainties from the resolution and the calibration don't contribute, only the detection efficiency has to be known. This method is well-suited to stand-alone photon detector running: accurate asymmetries may be measured even without calibration against the scattered-electron detector. However the drawback is that the mean Compton asymmetry is very small (0.88%) (see Table 3.2) and leads to long running time to reach the $\frac{\delta\mathcal{P}_e}{\mathcal{P}_e} = 1\%$ statistical accuracy.

Requirements for the photon detector are a good detection efficiency in the range of few 100 keV to 35 MeV, a large light yield to reach low detection thresholds and high counting rate. Using a photon detector with a high light yield can bring the detection threshold small enough with respect to the Compton edge so that it can be

¹PREx initially proposed to run at 0.85 GeV, later changed to run at 1.063 GeV

	$k_\gamma = 1.165$ eV $P_L = 0.25$ W G = 6000	$k_\gamma = 2.33$ eV $P_L = 1.0$ W G = 3000	$k_\gamma = 5.00$ eV $P_L = 0.5$ W G = 3000
k'_{max} (MeV)	17.5	34.5	71.1
$\theta_\gamma(E_\gamma > 10$ MeV) (μ rad)	447	813	1311
E'_{emin} (GeV)	0.982	0.965	0.929
θ_{emax} (μ rad)	4.56	9.12	19.57
Y_{Det} (mm)	4.1	8.3	17.8
σ_{total} (barn)	0.653	0.642	0.618
\mathcal{A}_{max}^L (%)	1.77	3.51	7.37
$\langle \mathcal{A}_E^L \rangle$ (%)	0.88	1.72	3.53
Rate (kHz)	118	116	26
\mathcal{L} (μ barn $^{-1}$ s $^{-1}$)	0.1807	0.1807	0.0421
t_E (s)	1351	360	381

Table 3.2 Comparison of relevant quantities of the Compton kinematics for the infrared ($\lambda_\gamma = 1064$ nm), green ($\lambda_\gamma = 532$ nm) and ultraviolet ($\lambda_\gamma = 248$ nm) lasers with different cavity gain G for achieving a statistical precision of $\frac{\delta \mathcal{P}_e}{\mathcal{P}_e} = 1.0\%$. The following parameters are used: $E_e = 1.0$ GeV, $I_e = 50$ μ A, $\mathcal{P}_e = 90\%$, $\mathcal{P}_\gamma = 100\%$, $\sigma_e = 100$ μ m, $\sigma_\gamma = 100$ μ m, $\alpha_c = 23.5$ mrad. $\langle \mathcal{A}_E^L \rangle$ is the longitudinal mean analyzing power for the energy weighted method with a detection threshold set to 0. Y_{Det} is the maximum vertical gap between the primary and scattered electron beams after the 3rd dipole. The detection efficiency of photon detector assumed as 100%.

assumed to be negligible. Then the sensitivity to the detector response, main source of systematic errors, is highly reduced.

The beam polarization obtained from the electron detector is also a way to cross check the systematic errors in polarization measured by photon detector as well. The energy of the scattered Compton electron is directly related to its measured position in the detector. A detector made of micro strip Si has been used to detect the

scattered Compton electrons in the past. Usually a high segmentation in the strips gives better energy resolution of the scattered electron energy. To first order, reducing the micro-strip size can reduce the systematic error.

The most efficient way to improve the Compton figure of merit is to shorten the laser wavelength. Going to a green laser ($\lambda_\gamma = 532$ nm) brings the mean asymmetry to 1.72% (see Table 3.2) at 1.0 GeV. At the Compton edge the photon energy is 34.5 MeV and the associated scattered electron is 8.3 mm (see Table 3.2) above the primary beam at the location of the electron detector. Assuming that laser power is 3.0 kW at the Compton interaction point and the detection efficiency of photon detector is 100%, a 1% statistical accuracy is achieved within 6 minutes.

The upgrade project includes building a green laser, a Fabry-Perot cavity, a single crystal Gd_2SiO_5 (GSO) photon detector with an integrating data acquisition system based on 12-bit FADC (Flash Analog-to-Digital Converter) and a high resolution Si micro-strip electron detector. In the following section, we describe these elements.

3.3 Elements of Compton Polarimeter

Installed in the accelerator tunnel of Hall A, the Compton polarimeter consists of a magnetic chicane, a photon source (a laser system, optical elements and an optical cavity), a photon detector, and an electron detector as shown in Figure 3.13. The electron beam enters from the left and deflects vertically by four identical dipoles of the chicane referred to as D_1 , D_2 , D_3 and D_4 , and crosses the photon beam at the center of the chicane which we call it Compton Interaction Point (CIP). The crossing angle between the two beams is 24.0 mrad. The electrons undergo Compton scattering with circularly polarized photons in resonance in a Fabry-Perot cavity fed by a frequency doubled CW green laser ($\lambda_\gamma = 532$ nm). The photon polarization is periodically flipped between right- and left-circular in order to control for systematic effects. The backscattered photons are detected in the single crystal GSO photon detector. The scattered electrons can be detected in the Si micro strip detector located

a few mm above the primary beam in front of D_4 . Approximately one electron in every 10^9 undergoes Compton scattering. Unscattered electrons, separated from the Compton-scattered particles by D_3 in the chicane, continue on into the hall for the primary experiment. A fast front-end electronics and data acquisition system collects the data at rates of up to 250 MHz.

The optical cavity is located between the dipoles D_2 and D_3 (Figure 3.13). It is inclosed in a vacuum chamber connected to the beam pipe upstream and downstream and sits on an optics table where the laser and optical elements are located. The CIP is in the center of the cross section between the dipoles D_2 and D_3 . There are two beam position monitors (BPM) located on both sides of the cavity. They are used to monitor changes in beam position of the electron beam during measurements. Elements called “beam diagnostics” (BD) can detect the beam halo at four positions of the chicane (Figure 3.14). Each element is composed of 4 scintillator bars fixed to photomultiplier tubes. The beam pipes are surrounded by those scintillator bars attached to them at those positions. Pneumatic gate valves are used to control the chicane vacuum so that it can isolate the chicane beam pipe from the rest of the beam pipe when it is necessary. Two ion pumps in section $D_2 - D_3$ can provide a vacuum of 10^{-9} Torr inside the cavity.

The photon detector is located under the dipole D_4 after the dipole D_3 . It is

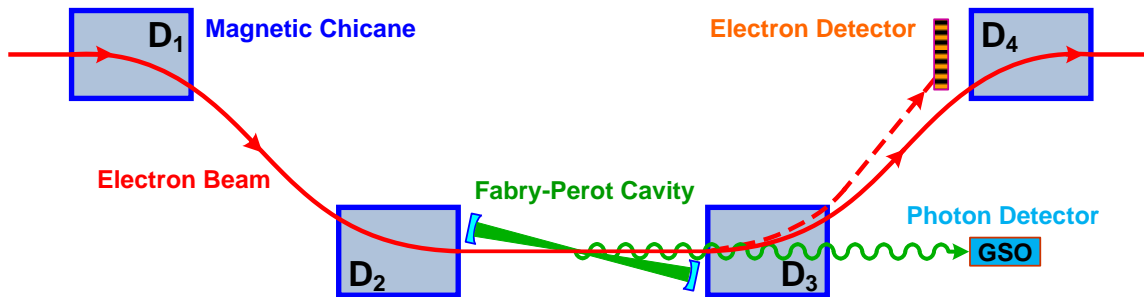


Figure 3.12 (color) A schematic of a simplified view of Compton polarimeter in Hall A at JLab.

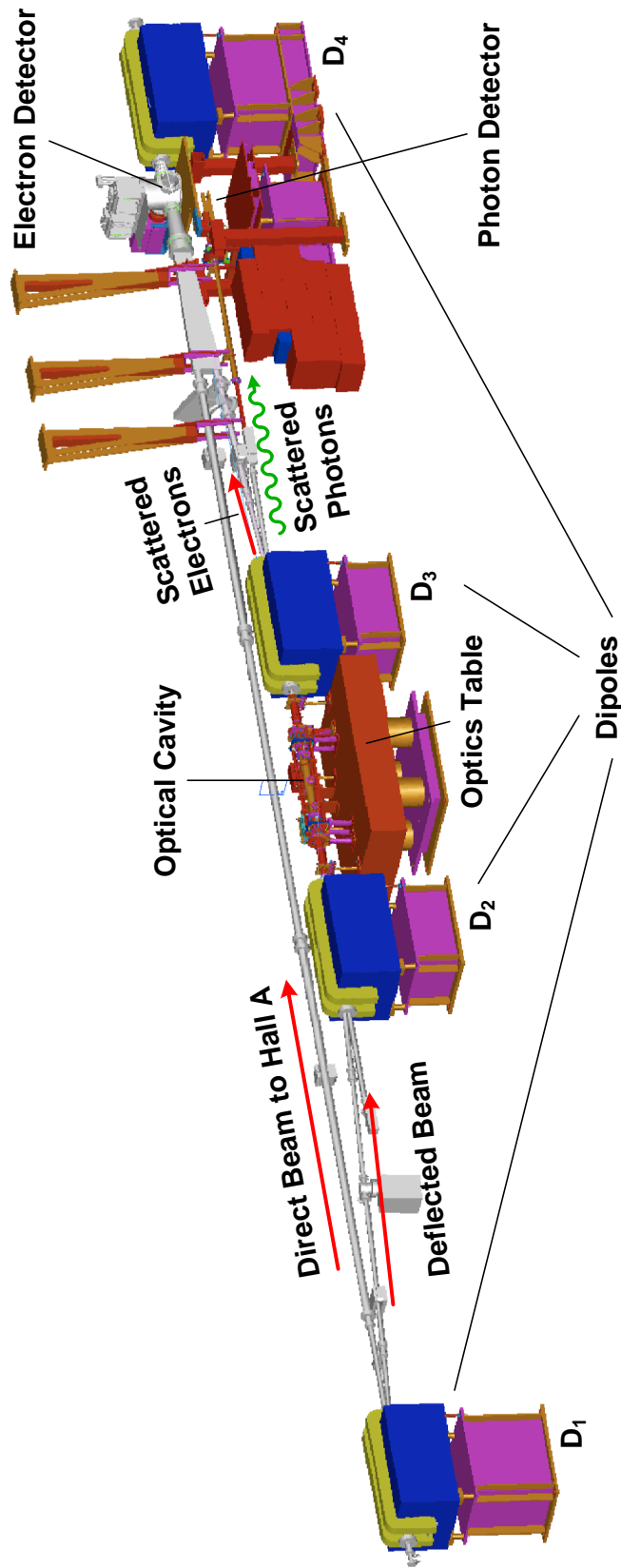


Figure 3.13 (color) A in-scale 3D view of Compton polarimeter in Hall A accelerator tunnel.

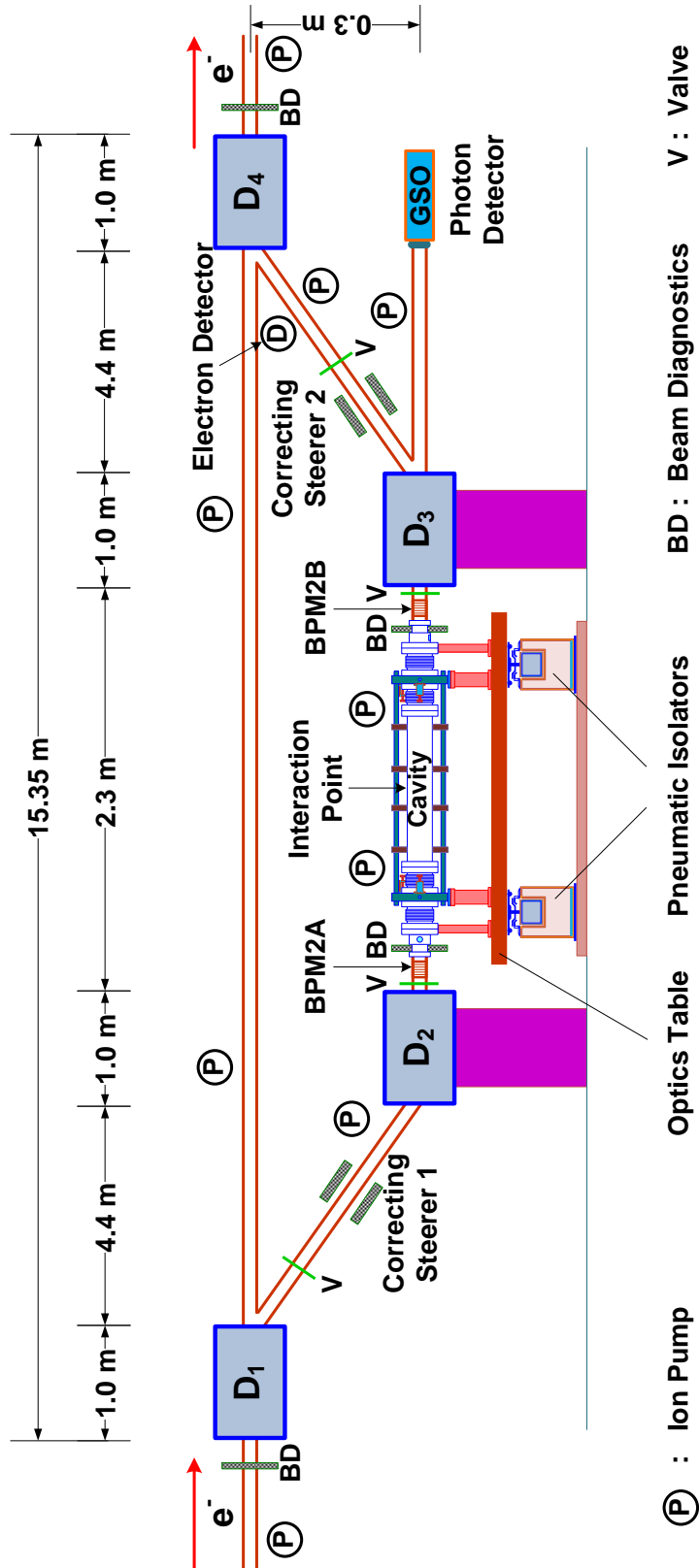


Figure 3.14 (color) A schematic of Hall A Compton polarimeter with the location of the various elements that make up the polarimeter (adapted from [8]).

mounted on a motorized table with remote-controllable motion along both axes (horizontal and vertical) transverse to the beam direction. The scattered photons from the CIP go through a vacuum tube before they hit the detector window. A 5 cm thick lead collimator with a diameter of opening of 2 cm combined with a 1 mm thick lead filter was used to block the unwanted backgrounds and synchrotron radiation.

The electron detector is mounted in between dipole D_3 and dipole D_4 . It consists of four Si micro strip planes mounted on a motorized vertical stage which is also remote controlled during measurements.

We will now describe more in detail the magnetic chicane and then the optical part of the polarimeter. Finally, we will describe the photon detector and electron detector and their data acquisition systems.

3.3.1 Magnetic Chicane

When the polarimeter is in operation, the dipoles are powered and the beam is deflected by the magnetic field they produced and travels through the optical cavity. A vacuum pipe between D_1 and D_4 allows the electron beam moving in a straight line to the Hall A target located downstream of the polarimeter when it is not in use. The chicane has a total length of 15.35 m. The length of each dipole is 1m. The distances between the dipoles are shown in Figure 3.14. The dipoles are powered in series and each can provide a magnetic field up to 1.5 Tesla. This allows the transport of electron beams of energy up to 8 GeV (the applied field varies linearly with the energy of the electron beam).

For a constant \vec{B} field along the magnetic length (L_d) of a dipole (Figure 3.15), the bending radius (R_d) of the trajectory of the incident electrons is given by [20],

$$R_d[m] = \frac{p[GeV]}{0.3B[T]}, \quad (3.54)$$

where p is the momentum of incident electrons. The bending angle θ_e has the following relation,

$$\sin \theta_e = \frac{L_d}{R_d}, \quad (3.55)$$

If we call H_{12} is the vertical deflection of the beam over a horizontal distance D_{12} between the exit of dipole D_1 and the entrance of dipole D_2 ,

$$\tan \theta_e = \frac{H_{12}}{D_{12}}, \quad (3.56)$$

Now, the total vertical deflection (d) of the beam between the entrance of the dipole D_1 and the exit of the dipole D_2 is,

$$d = 2h + H_{12} = 2R_d(1 - \cos \theta_e) + D_{12} \tan \theta_e, \quad (3.57)$$

The deflection of the electron beam by a dipole is also given by the following equation:

$$\tan \theta_e = 0.3 \frac{\int \vec{B} d\vec{l}}{p[\text{GeV}]}, \quad (3.58)$$

where $\int \vec{B} d\vec{l}$ is the line integral of the magnetic field. For JLab energy range of 1.0 - 6.0 GeV, and given the fact that the maximum magnetic field each dipole can provide is 1.5 Tesla, calculations have shown that this angle is very small [20]. For example, a PREx beam energy of 1.061 GeV, the bending radius and angle obtained for the corresponding magnetic field $B = 0.204$ T is $R_d = 17.36$ m, $\theta_e = 57.62$ mrad. Therefore under the assumption of θ_e is being very small, and using the results of equations (3.54) and (3.55), we obtain,

$$d \simeq R_d \theta_e^2 + D_{12} \theta_e = 0.3 \frac{B}{p} L_d (L_d + D_{12}), \quad (3.59)$$

From the equation (3.59), one can see that, for a fixed energy E (momentum p) of the electron beam, the angular deviation of the beam depends on the integral field along its trajectory. Therefore, when the field is changed simultaneously in the four dipoles, we do vary the vertical position of the electron beam in the section between D_2 and D_3 . If we call the change in magnetic field $\Delta B = B' - B$, then the vertical displacement Δd is,

$$\Delta d = 0.3 \frac{\Delta B}{p} L_d (L_d + D_{12}), \quad (3.60)$$

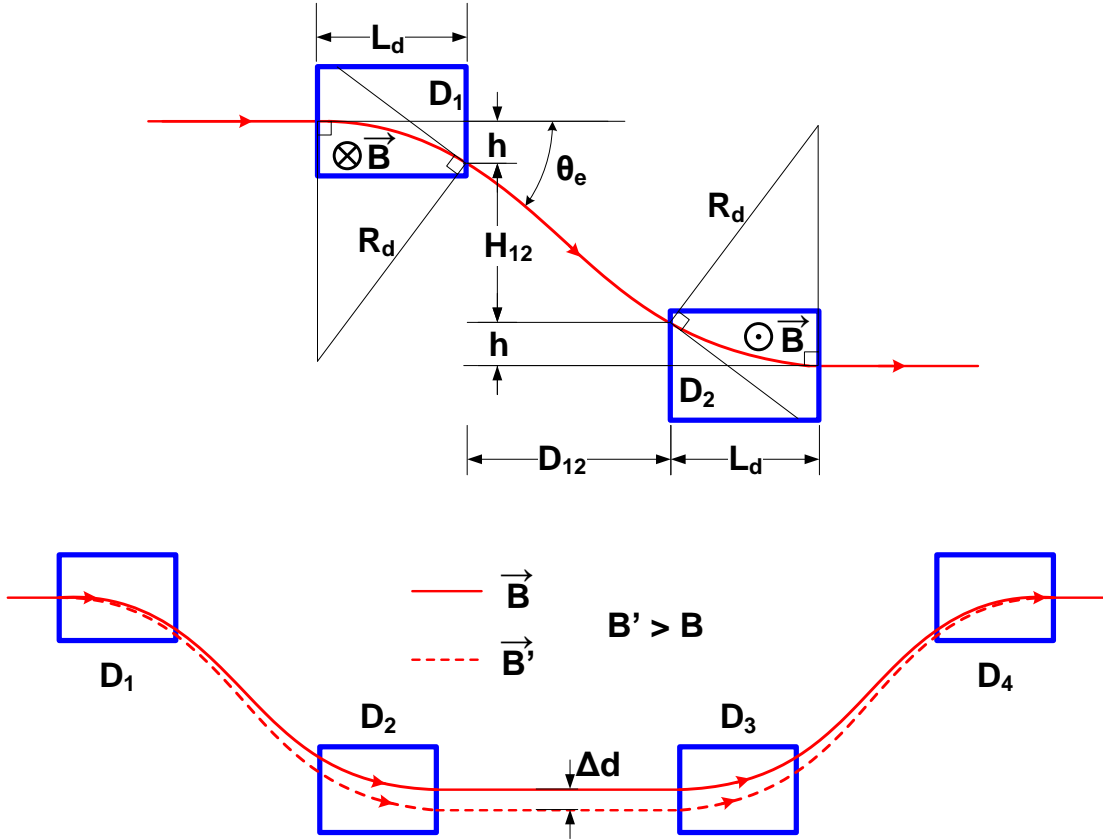


Figure 3.15 (color) Vertical deviation of electron beam trajectory in magnetic chicane (redrawn from [43]).

This procedure allows to maximize the luminosity of electron photon crossing at the CIP by steering the electron beam in the vertical direction. For example, for a beam energy of 1.0 GeV, a change in the dipole field of 1.0 mT can move the beam vertically by ~ 1 mm.

One of the beauties of Compton polarimeter is that it is non-destructive. This means that we must design a system that allows both to detect scattered photons and scattered electrons and return the primary beam to the downstream elements of polarimeter without changing the direction of polarization, the orientation and position of it. Because all the physics is happening at the target which is located at the downstream of the polarimeter. We mentioned in equation 2.3 that a magnetic

field can introduce a precession of the electron spin. These constraints require the selection of a magnetic chicane dipoles such that they must have the same magnetic length and same magnetic fields with opposite signs resulting the four dipoles have a total $\int \vec{B}d\vec{l} = 0$. In other words, each dipole must deflect the electrons the same angle and the next dipole should cancel this angle given by the previous dipole by an exactly opposite field.

3.3.2 Optical Setup

The optical elements of polarimeter are mounted on an optics table placed in a little room located between the dipoles D_3 and D_4 . The room equipped with a laminar flow fan filter system at the top in order to keep the optics clean from the dust and contaminations in the environment.

The optical system of polarimeter has the following considerations:

- Transport, align and focus the laser beam required by the cavity so that there is a resonance on the cavity with a fundamental mode (TEM_{00}). This will be discussed in detail in Chapter 5.
- Ensure that the polarization of the photon beam is circular at the interaction point. This is crucial not only to get high experimental asymmetry but also to achieve a good precision in electron polarization measurement. This will be discussed in detail in Chapter 6.
- Maintaining the gain in the optical cavity requires a feedback control of the laser frequency. This technique uses the reflected light from the cavity which can be extracted from the incident light by an optical element. We will study this in Chapter 5.
- The crossing angle between the electron and photon beams must be as small as possible to maximize the luminosity of Compton scattering.

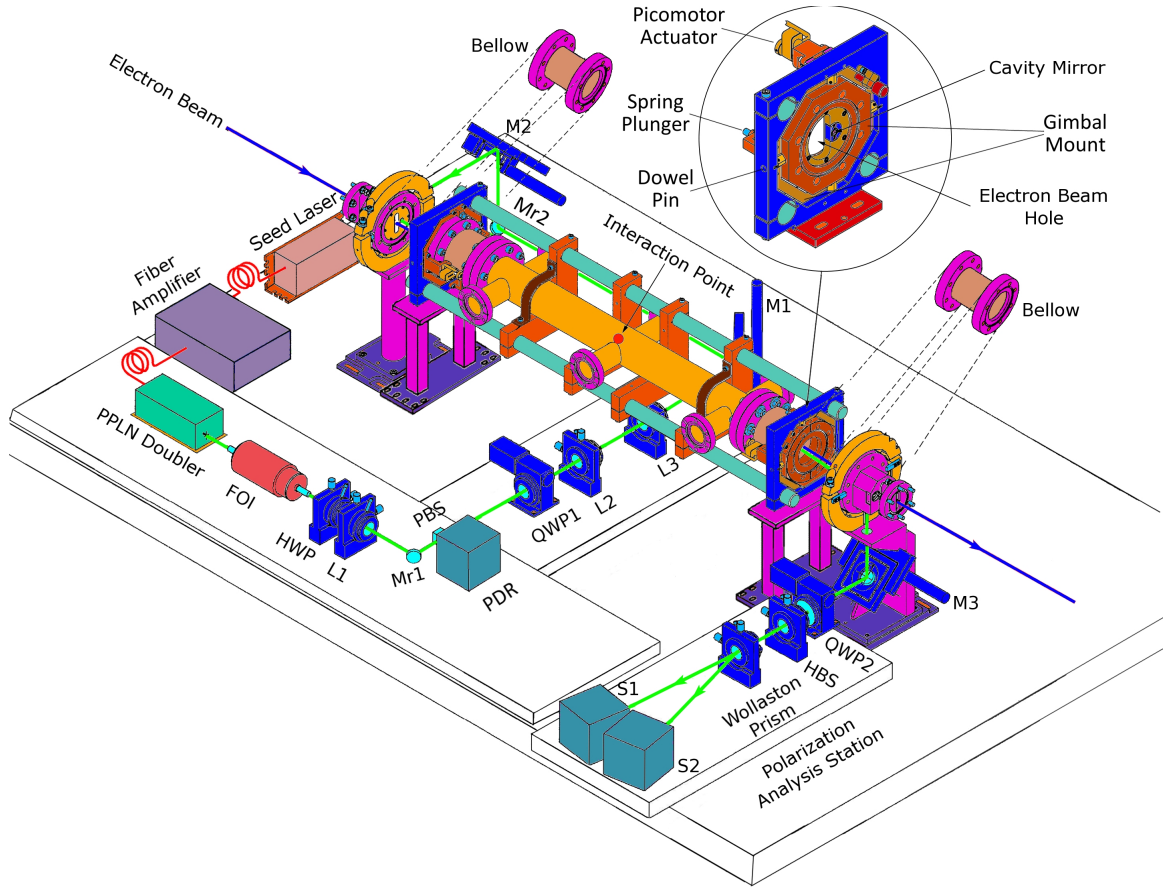


Figure 3.16 (color) A 3D view of the Fabry-Perot cavity and optical elements on optics table in Hall A Compton polarimeter at JLab (adapted from [8]).

A schematic of optical and electronic system of the polarimeter is illustrated in Figure 3.16 and Figure 5.30. Based on their main functionality, we can categorize them into four groups necessary for achieving the required power and circular polarization in the cavity.

The first group is the laser source which provides a green beam at the wavelength of $\lambda = 532$ nm. It is based on three combinations. The seed laser is a diode pumped neodymium-doped yttrium aluminum garnet ($\text{Nd:Y}_3\text{Al}_5\text{O}_{12}$; Nd:YAG) Light-wave laser delivers a continuous wave (CW) IR ($\lambda = 1064$ nm) beam up to 250 mW. It is fiber coupled to a single mode ytterbium doped fiber laser amplifier capable of generating a CW IR ($\lambda = 1064$ nm) beam up to 10 W. A frequency doubling unit

consists of a MgO doped periodically poled lithium niobate (PPLN) crystal and temperature controller necessary for achieving quasi phase matching which doubles the frequency of the IR light. Two dichroic mirrors separate the green beam from the residual IR beam. We will discuss this part more in detail in Chapter 4.

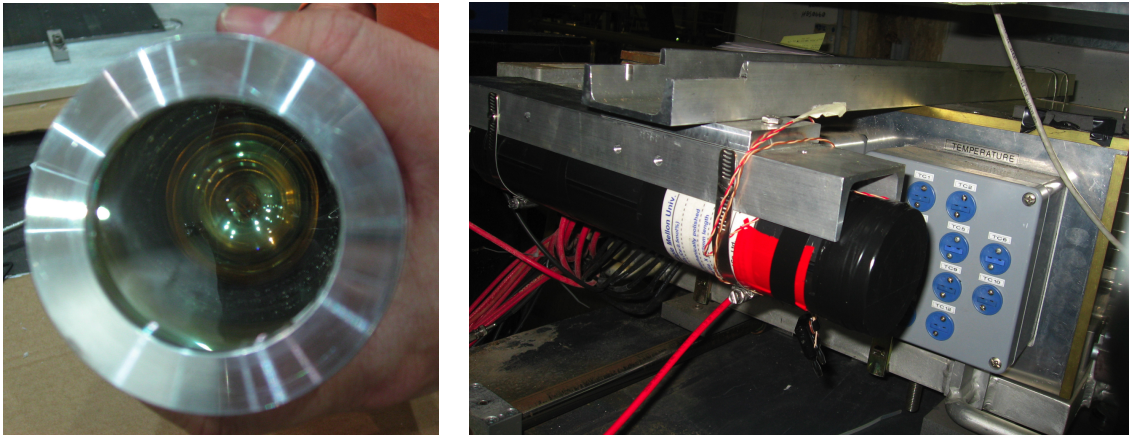
The second group consists of the elements related to transport, align and focus the incident beam to the optical cavity which will be discussed in Chapter 5. The focusing of the incident beam at the CIP is accomplished by three lenses noted as L_1 , L_2 and L_3 respectively. Two motorized mirrors noted as M_1 and M_2 allow four degrees of freedom of motion for the laser beam (2 translations, 2 rotations) with respect to the optical axis of the cavity formed by two cavity mirrors. The mirror M_{r1} , M_{r2} , M_e and M_s are fixed at 45 degrees with respect to the incident beam. A CCD camera facing the mirror M_{r2} monitors the position of incident and reflected beam from the cavity. Another CCD camera at the cavity exit monitors the profile of the transmitted beam.

The third group includes elements for controlling and measuring the polarization that we will discuss in Chapter 6. The polarization of the frequency doubled laser beam is linear before it is being converted to circular by a quarter-wave plate mounted on a stepper motor. At the exit of the cavity, the polarization is measured by a system consists of a quarter-wave plate, a Wollaston prism and two detectors each is mounted on an integrating sphere.

The last group consists of elements which allows the use of the reflected beam in the electronic feedback (servo) system to achieve the frequency locking of the laser to the cavity. This will be discussed more in detail in Chapter 5. A polarized beam splitter combined with a quarter-wave plate used to extract the reflected beam from the incident beam. A fast Si photodiode mounted on an integrating sphere detects the reflected signal and sends it to the servo system.

3.3.3 Photon Detector

The photon detector is a calorimeter with a single crystal Gd_2SiO_5 (GSO) (Figure 3.17(a)) doped with cerium for improved radiation hardness. The crystal has a cylindrical shape with a diameter of 6 cm and a length of 15 cm, it is large enough to capture most of the shower from an incident photon, without the extended cross-calibration and gain matching required for a crystal array. Signal readout is performed with a 12-stage PMT [46]. The calorimeter is located approximately 6 m downstream of the Compton interaction point, and is mounted on a motorized table with remote-controllable motion along both axes (horizontal and vertical) transverse to the beam direction (Figure 3.17(b)). Two narrow converter-scintillator pairs allow precise centering on the beam of Compton-scattered photons, which forms a cone with higher-energy photons at the center.



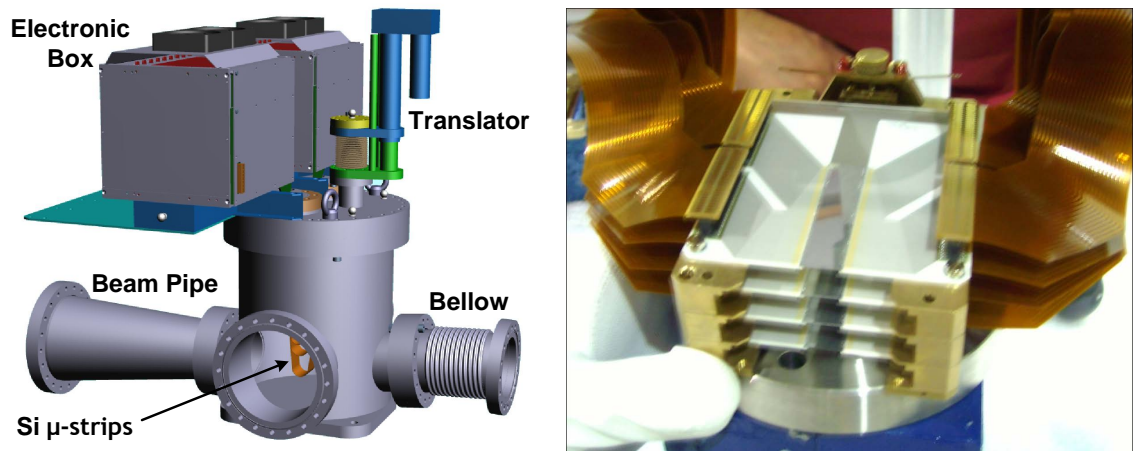
(a) GSO crystal mounted to a PMT (b) inside a steeltube housing mounted in the scattered-photon beamline

Figure 3.17 (color) The GSO photon detector.

The GSO crystal has the following feature: A good detection efficiency in the range of 100 keV - 50 MeV. A high light output with a light yield of $\sim 20\%$ gives a high energy resolution and a fast decay time of < 500 ns is good for high event rate.

3.3.4 Electron Detector

In principle, a Compton asymmetry may also be measured using scattered electrons, or detections of both the scattered photons and electrons in coincidence mode. After the interaction with laser beam, the scattered electrons lose some of their energy and bent a larger angle than the unscattered ones by the dipole D_3 , and can be separated from the primary beam between the dipole D_3 and dipole D_4 in the chicane.



(a) A vacuum chamber houses the electron detector

(b) Micro strip planes in electron detector

Figure 3.18 (color) Electron detector assembly and Si micro strips.

The electron detector is located between the dipoles D_3 and D_4 at a distance of 4.102 m from the center of the dipole D_3 . It consists of four parallel planes spaced horizontally 1 cm from each other and there is a 200 micron vertical upward offset between planes. Each plane consists of 192 strips of silicon with the width of 240 microns. The planes are inclined at an angle of 58 mrad from the vertical position. Figure 3.18(a) shows the vacuum chamber houses the detector and Figure 3.18(b) shows the micro strip planes. The detector is mounted on a translator with remote-controllable stepper motor and can travel vertically up to 120 mm from the main beam.

If we denote p and θ_e as the momentum and bending angle of the primary beam,

and denote p' and θ'_e as the momentum and bending angle of the the scattered beam (Figure 3.19), using equation (3.58), we have the following,

$$\Delta\theta'_e = \theta'_e - \theta_e \simeq 0.3 \int \vec{B} d\vec{l} \left(\frac{1}{p'} - \frac{1}{p} \right), \quad (3.61)$$

where $\int \vec{B} d\vec{l}$ is the line integral of the magnetic field given by the dipole D_3 . Usually, the detector is kept few mm out of the primary beam so that it can detect the scattered electron tracks. By knowing its secure location Y_{Det} from the primary beam, we can reconstruct the trajectory of the scattered electron and deduce its momentum (energy).

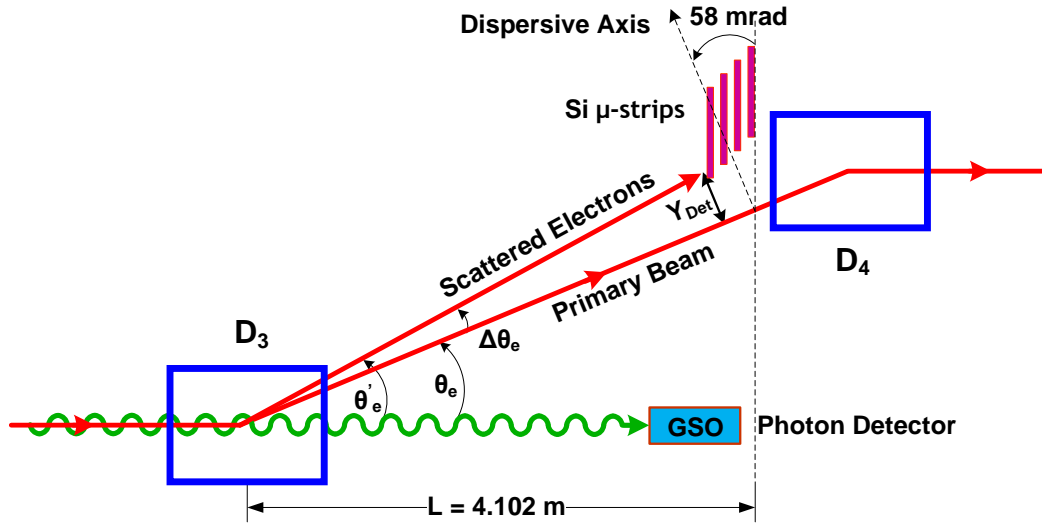


Figure 3.19 (color) Schematic of electron and photon detector layout in polarimeter.

There are two methods used to determine the Y_{Det} . One is using two tungsten wires of 20 microns in diameter placed on a mount in the bottom of the first plane. When a wire moves vertically and crosses the beam, the particles emitted are detected by a scintillation crystal coupled to a photomultiplier tube and the position is recorded. This procedure is performed for beam currents of about $2 \mu\text{A}$ in order not to break the wires. The precision of this method depends on the precision of the vertical motion of the wire controlled by the stepper motor. Another one is measuring the

experimental asymmetry of Compton events as a function of the momentum (energy) of the scattered electrons for each strip, and Y_{Det} is determined from this asymmetry by fitting the asymmetry spectrum to strip locations. Once Y_{Det} is determined, the analyzing power corresponds to strip i is given by [44],

$$\langle \mathcal{A}_L \rangle^i = \frac{\int_{E_{min}^i}^{E_{max}^i} \frac{d\sigma_0(E_i)}{dE_i} \mathcal{A}_L(E_i) dE_i}{\int_{E_{min}^i}^{E_{max}^i} \frac{d\sigma_0(E_i)}{dE_i} dE_i}, \quad (3.62)$$

and the polarization from each strip is determined by,

$$\mathcal{P}_e^i = \frac{\mathcal{A}_{exp}^i}{\mathcal{P}_\gamma \langle \mathcal{A}_L \rangle^i}, \quad (3.63)$$

by fitting the same asymmetry spectrum again to strip numbers in each detector plane. Here \mathcal{A}_{exp}^i is the experimental asymmetry obtained from each individual strips, \mathcal{P}_γ is the laser polarization.

3.3.5 Data Acquisition

The data acquisition system of polarimeter has three modes: photon only mode, electron only mode and electron-photon coincidence mode. Depending on the need and the beam condition, we can run one of the modes independent of another.

Data Acquisition of Photon Detector

The original Compton polarimeter used a counting data acquisition system based on differential polarization measurement method of Compton polarimetry, as described in Section 3.1.4. A small, prescaled percentage of raw waveforms were retained from each helicity window. The remainder of the data were analyzed online by one of two CPU cards in the data acquisition VME (Versa Module Europa) crate; only this analyzed summary was written to disk. This strategy to reduce the amount of disk space required to store the Compton data was made possible by equipping the VME crate with a dual CPU: as one CPU handled the acquisition of data from a helicity

window, the other worked on the online analysis of data from the previous helicity window. Each CPU card handed off control of the crate at the end of its helicity window [44].

The new integrating data acquisition system (DAQ) performs the energy-weighted integration method of Compton polarimetry as described in Section 3.1.4. This integral is performed automatically by the FADC (Flash Analog-to-Digital Converter), so that a minimal amount of information must be written to disk. It is based on a modified 12-bit FADC from Struck [40], running with a sampling rate of 200 MHz. The timing of the write commands is based on helicity timing board that controls the helicity flip rates (usually from 30 Hz to 1 kHz) and provides start-acquisition, stop-acquisition, and write commands based on the master pulse signal (MPS), which marks a brief period of indeterminate beam helicity between helicity windows. Figure 3.20 shows the simplified schematic of the integrating Compton DAQ.

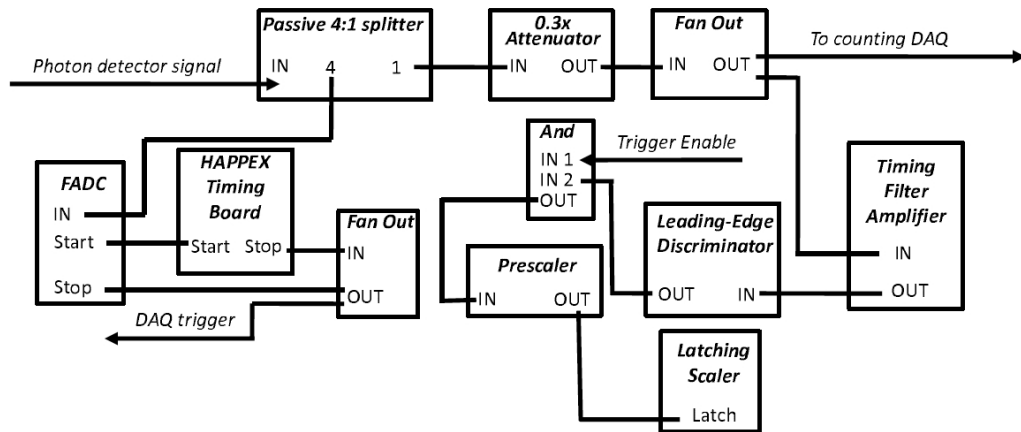


Figure 3.20 Simplified schematic of the upgraded integrating Compton DAQ [45].

A photon detected in the GSO crystal produces a negative pulse via the photomultiplier tube (PMT) attached to it; the area between the waveform of this pulse and the FADCs baseline level (pedestal), is proportional to the energy the photon has deposited in the crystal. Figure 3.21 shows the shape of typical signals from the GSO's PMT. If we know the pedestal value of our data, we can compute our energy-

weighted integral simply by summing the sampled signal in a hardware accumulator. There are six different accumulators, each perform a slightly different integral with several programmable parameters. We introduce two programmable thresholds, one near the pedestal (T_1) and one far from the pedestal (T_2), shown with a plot of two sample photon pulses in Figure 3.21. The first threshold allows us to integrate over a region including only pedestal noise or to exclude that region from an integral. The second threshold allows the exclusion of large background pulses from the integral. When the signal crosses a threshold to enter the range of an accumulator, the N^{before} preceding samples can also be added into the accumulator; the same can be done with the N^{after} samples following a threshold crossing out of the accumulators range.

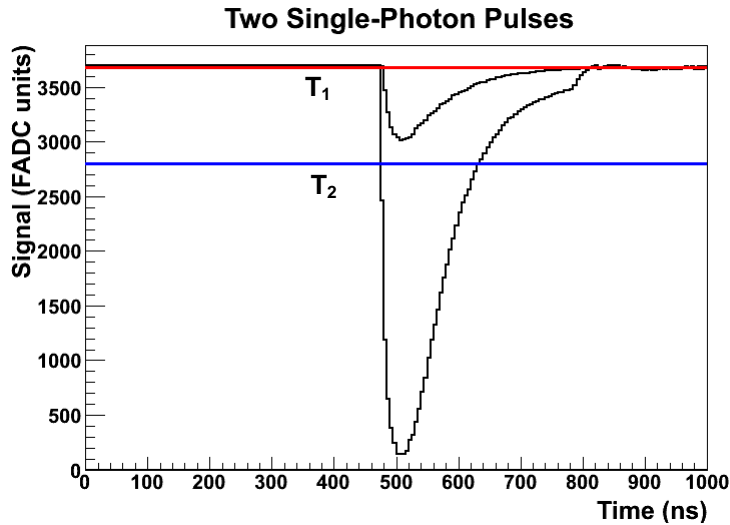


Figure 3.21 (color) Typical small (normal) and big (background) signals with the thresholds for the Integrating FADC DAQ.

Six accumulators with their programmable parameters defined as following [46]:

- Accum0 (All): Accumulates all signal over the entire input range of the FADC.
- Accum1 (Near): Accumulates signal between T_1 and the high (pedestal) end of the input range. This is used to examine pedestal noise.
- Accum2 (Window): Accumulates signal between T_1 and T_2 . Ideally, this should

be set to include nearly the entire range of Compton-scattered photons (with the possible exception of photons with very low energies).

- Accum3 (Far): Accumulates signal between T_2 and the low (saturation) end of the input range. This is used to examine high-energy background pulses.
- Accum4 (Stretched Window): Accumulates signal between T_1 and T_2 , plus the N_4^{before} samples before the signal crosses T_1 as it enters the window, plus the N_4^{after} samples after the signal crosses T_1 as it leaves the window. This accumulator excludes any samples that contribute to the Stretched Far accumulator.
- Accum5 (Stretched Far): Accumulates signal between T_2 and the low (saturation) end of the input range, plus the N_5^{before} samples before the signal crosses T_2 as it enters the accumulator range, plus the N_5^{after} samples after the signal crosses T_2 as it leaves the accumulator range.

In typical running, three accumulators Accum0, Accum2, and Accum4 access the energy range of Compton-scattered photons and can be used to extract a Compton asymmetry.

Data Acquisition of Electron Detector

The electron detector contains four planes of Si detectors, each is $500 \mu\text{m}$ thick with 192 strips at a $250 \mu\text{m}$ pitch. The strips are connected to a kapton flex cable connected to a vacuum feed-thru circuit board bus. The analog signals are then fed to a charge sensitive preamplifier. On the standard Front End cards, the output of pre-amp is sent to a Constant Fraction Discriminator.

The threshold condition can be set by either triggering the photon detector or triggering a specific strip in the electron detector plane. The signals that pass the threshold are directed to a logic module based a field-programmable gate array (FPGA). According to the logical “hit-condition” in the strips of specific planes, the acquisition records the voltages of each strip.

Chapter 4

Building Green Laser Source via Second Harmonic Generation

4.1 Motivation

As we discussed in previous chapter, photons with higher energy (shorter wavelength) give us higher asymmetry and therefore a smaller systematic error in Compton polarimetry. The Hall A Compton Polarimeter Upgrade [39] requires a 532 nm green laser with a narrow line-width and PZT-based tuneability. Amid concerns about the difficulty of locking the very high finesse ($\sim 50,000$) cavity with the commercially available low power narrow line-width green laser (100 mW Prometheus laser [41]), we pursued an approach in which a tunable, narrow line-width 1064 nm laser (Light-wave) used as a pumping source for the ytterbium (Yb) doped fiber amplifier and the frequency of the amplified light is doubled by using a single-pass second harmonic generation in a nonlinear optical crystal called PPLN (Periodically Poled Lithium Niobate).

In this chapter we briefly introduce the basic principles of nonlinear optics, in particular the second harmonic generation and quasi phase matching. The limitations of nonlinear devices will be described. The experimental setup and properties of the frequency doubled green beam will also be discussed.

4.2 Nonlinear Optics

4.2.1 Nonlinear Optical Interactions

Nonlinear optics studies the interaction between a light and a nonlinear media while the light propagates through the medium within its transparency range. The oscillating optical (electromagnetic) field exerts an electrical force on electrons bounded to the medium and as a result it polarizes the medium with an oscillating electric dipoles at the same frequency as that of the driving optical field. With ordinary light sources the field is much smaller than the fields that bind the electrons to the atom and therefore the oscillation is also small. However, if the optical field is sufficiently large so that it is comparable with interatomic fields (10^8 V/cm), then the dielectric polarization responds nonlinearly to the electric field of the light.

In some media, a small portion of the electric dipoles oscillates at a frequency different from the driving optical field and this leads to a generation of new optical field within the medium. During this process, some photons from the driving field are destroyed in order to provide energy for the creation of new photons, and generally it does not involve absorption.

The polarization $\mathbf{P}(\mathbf{t})$ of a medium depends on the strength $\mathbf{E}(\mathbf{t})$ of an applied optical field. In the case of ordinary optics, the induced polarization depends linearly on the electric field strength in a manner that can often be described by the relationship [47]

$$\mathbf{P}(\mathbf{t}) = \epsilon_0 \chi^{(1)} \mathbf{E}(\mathbf{t}), \quad (4.1)$$

where ϵ_0 is the permittivity of free space and $\chi^{(1)}$ is known as the linear susceptibility and is responsible for refraction, dispersion, and diffraction and in this process no new frequencies will be generated. In nonlinear optics, the optical response can often be described by generalizing equation (4.1) by expressing the polarization $\mathbf{P}(\mathbf{t})$ as a

power series in the field strength $\mathbf{E}(\mathbf{t})$ as,

$$\begin{aligned}\mathbf{P}(\mathbf{t}) &= \epsilon_0 \left[\chi^{(1)} \mathbf{E}(\mathbf{t}) + \chi^{(2)} \mathbf{E}^2(\mathbf{t}) + \chi^{(3)} \mathbf{E}^3(\mathbf{t}) + \dots \right] \\ &\equiv \mathbf{P}^{(1)}(\mathbf{t}) + \mathbf{P}^{(2)}(\mathbf{t}) + \mathbf{P}^{(3)}(\mathbf{t}) + \dots\end{aligned}\quad (4.2)$$

The quantity $\chi^{(2)}$ is the second-order nonlinear optical susceptibility which describes the second-order nonlinearities, such as frequency doubling, electro-optic effect, and parametric oscillation, etc. The quantity $\chi^{(3)}$ is called third-order nonlinear optical susceptibility which describes the third-order nonlinearities, such as quadratic Kerr-effect, intensity-dependent refractive index, four-wave mixing, self-focusing, etc. The expression in equation (4.2) often written as the sum of two terms,

$$\mathbf{P}(\mathbf{t}) = \mathbf{P}^{\text{L}}(\mathbf{t}) + \mathbf{P}^{\text{NL}}(\mathbf{t}), \quad (4.3)$$

where the linear polarization is,

$$\mathbf{P}^{\text{L}}(\mathbf{t}) = \epsilon_0 \chi^{(1)} \mathbf{E}(\mathbf{t}), \quad (4.4)$$

The remainder is the nonlinear polarization and is given by,

$$\mathbf{P}^{\text{NL}}(\mathbf{t}) = \epsilon_0 \left[\chi^{(2)} \mathbf{E}^2(\mathbf{t}) + \chi^{(3)} \mathbf{E}^3(\mathbf{t}) + \dots \right], \quad (4.5)$$

The higher order terms of this equation represent terms which can generate new frequencies and these processes are often called as Second Harmonic Generation (SHG), Third Harmonic Generation (THG), High Harmonic Generation (HHG), Sum Frequency Generation (SFG), and Difference Frequency Generation (DFG) etc. In general, the third-order and higher terms in equation (4.5) are very small compared to the second-order term and here we denote the $\mathbf{P}^{\text{NL}}(\mathbf{t}) \simeq \mathbf{P}^{(2)}(\mathbf{t})$ as,

$$\mathbf{P}^{(2)}(\mathbf{t}) = \epsilon_0 \chi^{(2)} \mathbf{E}^2(\mathbf{t}), \quad (4.6)$$

The amount of second harmonic light that is produced depends heavily on the form of the $\chi^{(2)}$ tensor. In order for the $\chi^{(2)}$ not to vanish, the medium (crystal) must not possess inversion symmetry (non-centrosymmetric). Since liquids, gases, amorphous solids (such as glass), and even many crystals display inversion symmetry, and therefore they cannot produce second-order nonlinear optical interaction.

4.2.2 Second Harmonic Generation

Second harmonic generation is also called frequency doubling. It was first demonstrated by P. A. Franken *et al.* at the University of Michigan in 1961 [48]. It is a process whereby an electromagnetic wave oscillating at ω generates a polarization oscillating at 2ω in the nonlinear medium, which in turn the medium radiates an electromagnetic wave oscillating at 2ω - the second harmonic. Another way to interpret this occurrence is as the combination of two pump photons to form a single photon with double the frequency. The efficiency of the process is dictated by the nonlinear coefficients of the crystal, the polarization and intensity of the driving field, and the phase mismatch between the driving and the second harmonic field. Figure 4.1 shows the geometry and energy level diagram of second harmonic generation.

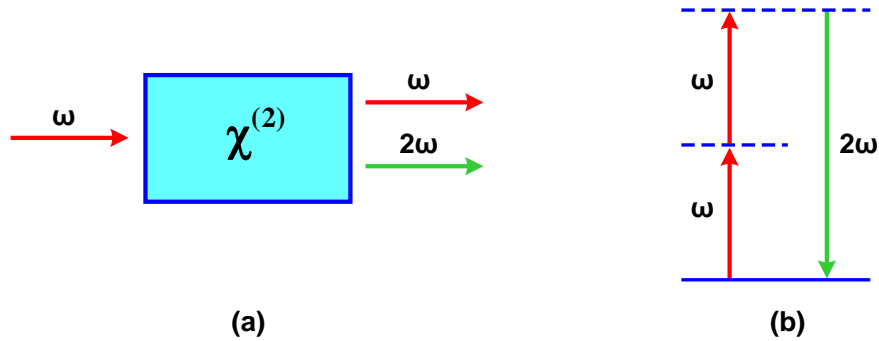


Figure 4.1 (color) (a) Geometry of Second Harmonic Generation. (b) Energy level diagram of Second Harmonic Generation process.

If we assume an optical field of a single frequency ω propagating through a medium that has the necessary type of symmetry to produce the second harmonic 2ω . The field can be noted as $\mathbf{E}(\mathbf{t}) = \mathbf{A}\cos(\omega\mathbf{t})$ and the equation (4.6) becomes,

$$\mathbf{P}^{(2)}(\mathbf{t}) = \epsilon_0\chi^{(2)}\left[\mathbf{A}\cos(\omega\mathbf{t})\right]^2 = d\epsilon_0\mathbf{A}^2\left[1 + \cos(2\omega\mathbf{t})\right], \quad (4.7)$$

where $d = \chi^{(2)}/2$ is the effective nonlinear coefficient, which is obtained from the third-order tensor $\chi^{(2)}$. The susceptibility $\chi^{(2)}$ may be determined by calculating $\mathbf{P}^{(2)}(\mathbf{t})$ quantum mechanically and then determine $\chi^{(2)}$ by comparison with equation

(4.7). We see that the second-order polarization consists of a zero frequency term and a 2ω frequency term. The first term leads to the generation of a static electric field in the nonlinear medium known as optical rectification and the the second term contributes to the generation of second-harmonic frequency.

The propagation of light field in the nonlinear media is always dictated by Maxwell's equations.

$$\nabla \cdot \mathbf{D} = \rho, \quad (4.8)$$

$$\nabla \cdot \mathbf{B} = 0, \quad (4.9)$$

$$\nabla \times \mathbf{E} = -\frac{\partial \mathbf{B}}{\partial t}, \quad (4.10)$$

$$\nabla \times \mathbf{H} = \mathbf{J} - \frac{\partial \mathbf{D}}{\partial t}, \quad (4.11)$$

where \mathbf{E} is the electric field, and \mathbf{D} is the displacement (electric-flux density) vector, \mathbf{J} is the free-current density, and ρ is the free charge density. \mathbf{H} and \mathbf{B} are the magnetic field vector and flux density respectively and have the following relationship,

$$\mathbf{B} = \mu_0 \mathbf{H}, \quad (4.12)$$

Maxwell's equations in a homogenous source-free ($\mathbf{J} = \mathbf{0}$) medium can be written as,

$$\nabla^2 \mathbf{E} = \mu_0 \frac{\partial^2 \mathbf{D}}{\partial t^2}, \quad (4.13)$$

The displacement vector \mathbf{D} and the polarization vector \mathbf{P} has the following relationship in MKS unit,

$$\mathbf{D} = \epsilon_0 \mathbf{E} + \mathbf{P}, \quad (4.14)$$

using the relation in equation (4.13),

$$\nabla^2 \mathbf{E} = \mu_0 \left(\epsilon_0 \frac{\partial^2 \mathbf{E}}{\partial t^2} + \frac{\partial^2 \mathbf{P}^{\text{NL}}}{\partial t^2} \right), \quad (4.15)$$

The nonlinear polarization term \mathbf{P}^{NL} leads to the generation of new field. For interactions where the amplitudes of the fields change slowly on the time scale of the

wavelength in space and the optical period in time, one can invoke the Slowly Varying Envelope Approximation (SVEA) [47],

$$\mathbf{E}_i(\mathbf{x}, \mathbf{y}, \mathbf{z}, \mathbf{t}) = \frac{\mathbf{A}_i(\mathbf{x}, \mathbf{y}, \mathbf{z}, \mathbf{t})}{2} e^{i(\omega_i \mathbf{t} - \mathbf{k}_i \mathbf{z})} + c.c., \quad (4.16)$$

where $k_i = \omega_i n_i / c$ and c is the speed of light and n_i is the refractive index of the medium at ω_i , propagating along the z -axis and substituting into equation (4.15) reduces to,

$$\frac{\partial A_i}{\partial z} e^{i(\omega_i t - k_i z)} + c.c. = i \sqrt{\frac{\mu_0}{\epsilon_0 \epsilon_i}} \frac{1}{\omega_i} \frac{\partial^2 \mathbf{P}^{NL}}{\partial t^2}, \quad (4.17)$$

one can obtain the approximate solution of the above equation,

$$2ik_i \frac{\partial A_i}{\partial z} = \mu_0 \epsilon_0 \omega_i^2 \mathbf{P}^{NL}, \quad (4.18)$$

This is a fundamental equation that collects all the nonlinear polarization source terms into one vector \mathbf{P}^{NL} which describes the generation of a new field $\mathbf{E}_i(\mathbf{x}, \mathbf{y}, \mathbf{z}, \mathbf{t})$.

According to one of the first theoretical treatments of second-harmonic generation by Armstrong et al. [49], if we examine the case where there are two optical fields with frequency ω_1 (driving field) and ω_2 (second-harmonic field) simply co-propagating in the medium,

$$E_1 = \frac{A_1}{2} e^{i(\omega_1 t + k_1 z)} + c.c., \quad (4.19)$$

$$E_2 = \frac{A_2}{2} e^{i(\omega_2 t + k_2 z)} + c.c., \quad (4.20)$$

at the tensor notation for the three-wave mixing process (SHG is a special case of three-wave mixing),

$$P_i^{NL} = \epsilon_0 \chi_{ijk}^{(2)} E_j E_k, \quad (4.21)$$

by examining the special case for SHG where $\omega_2 = 2\omega_1$ and $\chi^{(2)} = d/2 = d_{SHG}/2$, the nonlinear polarization is given by,

$$P^{NL} = \frac{d}{2} \left[A_1^2 e^{i(\omega_2 t - 2k_1 z)} + 2A_1^* A_2 e^{i(\omega_1 t - (k_2 - k_1)z)} + c.c. \right], \quad (4.22)$$

by substituting the above equation into equation (4.18), we can get two differential equations that describe the evolution of the fundamental and second harmonic fields,

$$\frac{\partial A_1}{\partial z} = -i \frac{\omega_1 d}{2cn_1} A_1^* A_2 e^{-i\Delta k z}, \quad (4.23)$$

$$\frac{\partial A_2}{\partial z} = -i \frac{\omega_2 d}{2cn_2} A_1^2 e^{-i\Delta k z}, \quad (4.24)$$

where $\Delta k = k_2 - 2k_1$ which represents the phase mismatch of the material at the two different wavelengths. These two equations are the coupled mode equations for SHG and n_1 and n_2 are the refractive index of the frequencies ω_1 and ω_2 in the medium.

In the limit of low conversion efficiency ($\sim 25\%$) and with the assumption of no absorption and no depletion for the fundamental frequency ($\frac{\partial A_1}{\partial z} = 0$), if we integrate equation (4.24) in z direction from 0 to L (length of nonlinear medium/crystal),

$$A_2(L) - A_2(0) = -i \frac{\omega_2 d}{2cn_2} e^{-i\frac{\Delta k L}{2}} A_1^2 \text{sinc}\left(\frac{\Delta k L}{2}\right), \quad (4.25)$$

We can see that the function is at its maximum when $\Delta k = 0$, and it is called phase-matching. We also can define the conversion efficiency by taking the ratio of the second harmonic intensity $I_2(L) = c\epsilon_0 n_2 |A_2|^2/2$ to the first harmonic intensity $I_1(0) = c\epsilon_0 n_1 |A_1|^2/2$ by [50],

$$\eta_{SHG} = \frac{I_2(L)}{I_1(0)} = \frac{2\omega_1^2 d^2}{n_1^2 n_2 c^3 \epsilon_0} I_1 L^2 \sin^2\left(\frac{\Delta k L}{2}\right), \quad (4.26)$$

It can be seen from the equation that the conversion efficiency is dependent on the intensity of the pump beam (I_1), nonlinear coefficient of the medium (d) and the length of the medium (L). Other than that it is strongly depend on the phase mismatch Δk . Figure 4.2 shows the relationship between η and Δk .

Although equation (4.26) is obtained under the undepleted pump approximation and it is appropriate in many situations, in some cases where the conversion efficiency is moderate to high, it is necessary to include depletion of the fundamental field. Under proper phase matching conditions, the nonlinear oscillations of all dipoles in the medium constructively interfere and the process of SHG can be so efficient that

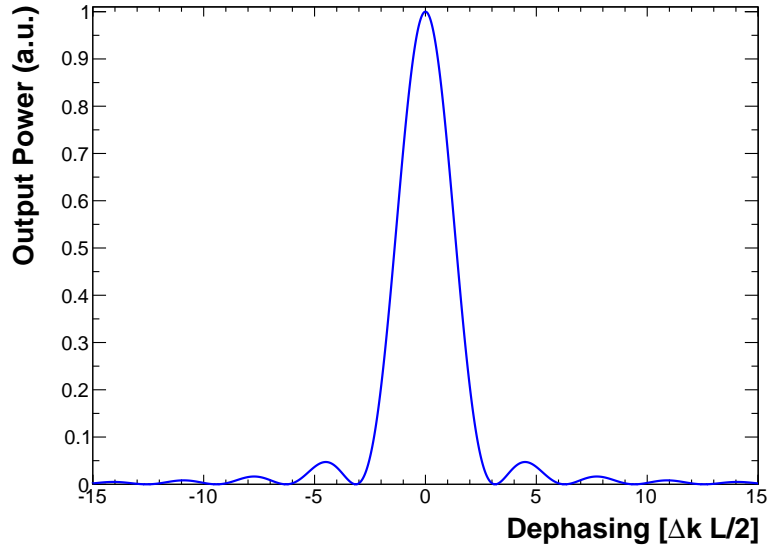


Figure 4.2 (color) SHG conversion efficiency as a function of phase mismatch.

nearly all of the energy in the driving field at frequency ω_1 is transferred to the second-harmonic frequency $2\omega_1$ and it leads to the depletion of ω_1 . This requires a proper phase-matching. A detailed analysis for a depleted plane-wave SHG is described in Ref [49] and for a perfect phase matching condition, the efficiency is reduced to,

$$\eta_{depleted} = \tanh^2 \left(\sqrt{\frac{2\omega_1^2 d^2}{n_1^2 n_2 c^3 \epsilon_0} I_1 L^2} \right), \quad (4.27)$$

In the following section we will describe the interactions involve phase matching.

4.2.3 Phase-matching

Efficient frequency conversion requires phase matching between the fundamental and second harmonic waves. If phase matching is not achieved ($\Delta k \neq 0$), the power will oscillate periodically along the length of the medium due to the oscillation of the relative phase between the driving nonlinear polarization and the generated second harmonic. This oscillation is shown in Figure 4.3. The coherence length $L_c = \frac{\pi}{\Delta k}$, is the length over which the driving nonlinear polarization and the generated second

harmonic stay in a phase relationship where the power flows from the driving nonlinear polarization to the second harmonic. There are two types of techniques to achieve phase matching: birefringent phase matching; quasi-phase matching.

Birefringent Phase Matching

Birefringent phase matching (BPM) was suggested independently by Giordmaine [51] and Maker *et al* [52]. It is a precision technique exploits the birefringence of the nonlinear crystal. The phase matching is achieved by carefully choosing the direction and polarization of the pump beam so that both the fundamental and the second harmonic will experience the same index of refraction: $n_1 = n_2$. In this case, the power of the second harmonic beam will grow the square of the crystal length as shown in Figure 4.3.

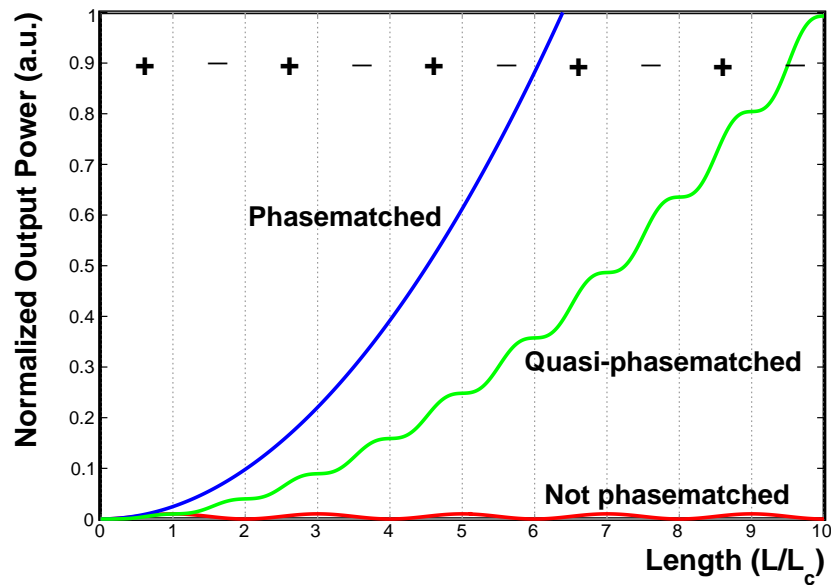


Figure 4.3 (color) SHG output power as a function of crystal length (L) normalized to the coherence length (L_c) for various phase matching conditions: perfectly phasematched, first-order quasi-phasematched, not phasematched.

Birefringent phase matching is not possible in all cases. For a given crystal and a given wavelength combination, there may not be an angle at which the index of

refraction is the same for both wavelengths. Conversely, even if such an angle exists, it may not allow coupling to the highest efficiencies. The effective nonlinear optical coefficient of the crystal depends on the polarization angles of the beams, and it is often not maximized for the birefringent phase matching solution.

Quasi-phase Matching

Quasi-phase matching (QPM) uses a periodic flipping of the sign of the nonlinear susceptibility of the medium to reverse the relative phase between the driving nonlinear polarization and the generated second harmonic at a regular interval. It relies on resetting of the phase mismatch Δk to 0 every coherence length L_c . After one coherence length of propagation, Δk becomes π . If the sign of the nonlinear susceptibility $\chi^{(2)}$ is changed at that location, an additional π phase shift is added to the nonlinear polarization, resetting Δk to 0. If we keep adding this periodic structure correctly, the SHG power grows quasi-quadratically along the entire length of the crystal as shown in Figure 4.3.

In order to better understand the basics of QPM interactions, let us consider a plane-wave SHG with an undepleted continuous-wave pump field. The periodic structure of QPM medium allows for spatially varying nonlinear coefficient $d(z)$ in the form of a square-wave, and equation (4.24) for this case is [53, 54],

$$\frac{\partial A_2}{\partial z} = -i \frac{\omega_2 d(z)}{2cn_2} A_1^2 e^{-i\Delta k z}, \quad (4.28)$$

where $\Delta k = k_2 - 2k_1$. For a crystal of length L , integrating equation (4.28) from $z = 0$ to $z = L$ gives,

$$A_2(L) - A_2(0) = -i \frac{\omega_2}{2cn_2} A_1^2 \int_0^L d(z') e^{-i\Delta k z'} dz', \quad (4.29)$$

In periodically poled QPM medium, only the sign not the amplitude of the nonlinear susceptibility is flipped with a period Λ and a fundamental spatial frequency K_g , where $\Lambda = 2L_c = 2\pi/K_g$. We can write $d(z)$ as a Fourier series,

$$d(z) = \sum_m d_m e^{iK_m z}, \quad (4.30)$$

where the m th spatial harmonic $K_m = mK_g$, and d_m is the corresponding Fourier coefficient. With such a periodic medium, equation (4.29) becomes [54],

$$A_2(L) - A_2(0) = ie^{-\frac{i\Delta k' L}{2}} \frac{\omega_2}{cn_2} A_1^2 L d_m \text{sinc}(\Delta k' L), \quad (4.31)$$

where the effective phase mismatch is $\Delta k' = \Delta k - K_m$. In this case, QPM in periodically poled medium can produce the same result as an SHG process in homogenous medium with an effective nonlinear coefficient d_m and the phase mismatch Δk shifted from 0 to $K_m = 2\pi m/\Lambda$. Since the periodic structure of the medium leads to the modulation of $d(z)$ from $+d_{eff}$ to $-d_{eff}$ with duty cycle D , the Fourier transform of equation (4.30) can be written as,

$$d_m = \left(\frac{2}{m\pi} \right) \sin(\pi D) d_{eff}, \quad (4.32)$$

It can be seen from the above equation that the QPM nonlinear coefficient is reduced by a factor of $2/m\pi$ as compared to the effective nonlinear coefficient d_{eff} in homogenous medium. Interactions involving higher-order QPM further reduces the d_m . Therefore, the strongest nonlinear mixing is obtained in a QPM medium with first-order phase matching and 50% duty cycle. Figure 4.3 shows the first-order QPM plot in green. Following equation (4.26), the conversion efficiency of QPM can also be written as [55],

$$\eta_{QPM} = \frac{I_2(L)}{I_1(0)} = \frac{2\omega_1^2 d_m^2}{n_1^2 n_2 c^3 \epsilon_0} I_1 L^2 \text{sinc}^2 \left(\frac{\Delta k' L}{2} \right), \quad (4.33)$$

The dependencies of QPM efficiency is the same as phase matching in homogenous materials except there is a difference in nonlinear coefficient depend upon the phase matching method we use and there is a factor m which dictates the order of QPM interaction. From Figure 4.3, it seems the first-order QPM is $4/\pi^2$ times less efficient than that the perfect BPM for the same nonlinear coefficient, in reality QPM is often more efficient than the BPM for the following reasons [55]:

- QPM couples the waves of same polarization with the largest nonlinear coefficient and in PBM this coefficient is always very small.

- QPM always allows non-critically phase matched interactions, but BPM cannot be achieved without critical phase matching.
- QPM can provide a level of engineerability through the use of spatially inhomogeneous gratings.

4.2.4 Nonlinear Interactions with Focused Gaussian Beam

So far we have treated all the optical fields involved in nonlinear interactions as plane waves. However, in practical experiments, the incident fundamental beam is focussed into the bulk crystal in order to increase its intensity and hence to increase SHG efficiency. Although tighter focussing allows for higher intensity, but it reduces the interaction length. Loose focusing increases the interaction length, but also reduces the intensity. The most common way to obtain high intensity is to use pulsed lasers. For continuous-wave (CW) lasers, there are two ways to increase the intensity: cavity enhancement and tight focusing. The general theory of focused Gaussian beam is described in Ref [50] and in the low conversion efficiency limit ($\eta \leq 0.2$), the undepleted conversion efficiency is [55],

$$\eta_{focussed} = \frac{16\pi^2 d_m^2}{\lambda^3 n_1 n_2 c \epsilon_0} I_1 L h \left(\alpha, B, \kappa, \xi, \frac{\Delta k L_{conf}}{2} \right), \quad (4.34)$$

where d_m is the nonlinear coefficient of the m th-order QPM, λ is the fundamental wavelength, ϵ_0 is the permittivity of free space, I_1 is the fundamental power, L is the length of the crystal and h is called the Boyd-Kleinman h -factor. The h -factor has the following parameters: the absorptivity (α), the Poynting vector walk-off (B), the focussing parameter ($\xi = \frac{L}{L_{conf}}$, $L_{conf} = \frac{2\pi\omega^2 n_1}{\lambda}$, ω is the $1/e^2$ -intensity radius), the focus position (μ) and the phase-mismatch (Δk). For a QPM interaction, the h -factor is maximized by proper tuning of the phase and usually it is achieved by adjusting the temperature of the crystal. Maximizing h is the collective contribution from other parameters and usually it is depend on the properties of the QPM medium, fundamental beam and the phase matching condition. In general $h = 0.8$ is taken

for confocal focussing and $h = 1.1$ is taken for the optimum, tighter than confocal focus. Confocal focussing is used to reduce the stress on the crystal. Ref [50] gives a detailed information on the relationship between η and h .

For a perfect phase matching with a high-conversion efficiency, we can extend equation (4.34) to the depleted regime. Ref [56] shows a numerical solution which follows the following relation,

$$\eta_{depleted, focussed} = \tanh^2 \left(\sqrt{\frac{16\pi^2 d_m^2}{\lambda^3 n_1 n_2 c \epsilon_0}} I_1 L h \right), \quad (4.35)$$

4.2.5 Periodically Poled Materials

Even though QPM was discovered prior to birefringent phase matching [48, 49], but did not get much attraction due to difficulties in fabricating such a micron-scaled structure. The fabrication of periodically poled QPM materials were possible only after the development in lithographically controlled patterning technology in late 80s.

Periodic poling is a technique which involves an engineering process to periodically reverse the domain orientation of a transparent nonlinear material in order to achieve quasi-phase matching. Periodic poling technology enables the generation and conversion of new laser frequency via periodically poled nonlinear crystals. This type of high-efficiency new frequency generation processes were not possible with traditional laser technology before. When phase matched, periodically poled crystals exhibit up to two-orders of magnitude more efficiency as compared to the same crystal without periodic poling. The materials usually made of wide band gap inorganic crystals such as lithium niobate (LiNbO_3), lithium tantalate (LiTaO_3) and potassium titanyl phosphate (KTiOPO_4) or organic polymers. The periodically poled version of them are often abbreviated as PPLN (periodically poled LN), PPLT (periodically poled LT) and PPKTP (periodically poled KTP).

Quasi-phase matching imposes several constraints on the crystal. Due to difficulties in generating a uniform electric field for the poling process, the crystal thickness (T) is limited to few millimeters or less. Usually, the poling period (Λ) is between a

few microns and some tens of microns which determines the wavelengths for which certain nonlinear processes can be quasi-phase matched. Furthermore, although all types of SHG are temperature dependent (due to thermal variation in refraction indices), the quasi-phase matched process has a stronger temperature dependence due to thermal expansion and contraction of the poling period(Λ). Figure 4.4 shows a typical uniformly structured periodic pattern for periodically poled nonlinear bulk crystal.

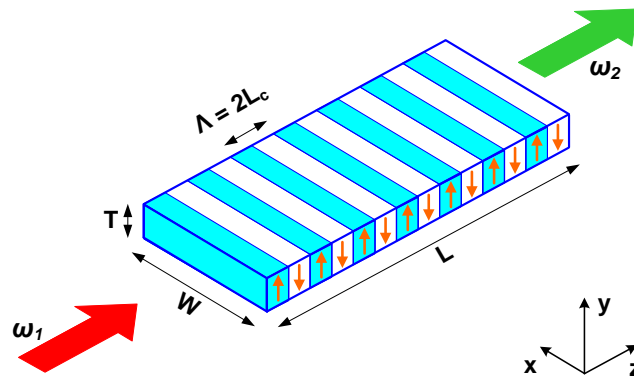


Figure 4.4 (color) Schematic representation of second harmonic generation in a periodically poled nonlinear crystal with a uniform grating period.

Periodic poling can be realized by several techniques such as pulsed electric field [60], thermal pulsing [61], vapor transport equilibration [55, 62] and other methods to relocate the atoms to create reversed domains. This can be achieved either during the growth of the crystal, or subsequently. Domain engineering with pulsed electric field is one of the most common techniques that involves the application of a strong electric field to a ferroelectric crystal via patterned electrodes on the crystal surface.

4.3 Tuning and Tolerances in Quasi-phase Matching

In second harmonic generation the phase matching condition is very sensitive and can be changed by changing one of the following parameters: the domain width of the nonlinear crystal, the wavelength of the laser, the temperature of the nonlinear

crystal and the angle of the nonlinear crystal with respect to the polarization orientation of the laser beam. In designing and tuning the periodically poled devices, one should understand how sensitive the phase matching conditions and therefore the conversion efficiency to these parameters. For example, if the line-width of the laser is larger than the acceptance bandwidth of the crystal, the conversion efficiency will be reduced. If the temperature tuning device has a lower resolution than the temperature tuning bandwidth of the crystal, one may not be able to get maximum conversion efficiency. We will briefly describe these effects for an isotropic medium with plane wave approximation. The more complicated anisotropic medium case is explained in Ref [53] in more detail and it will not be described in here.

4.3.1 Domain Period

For a nonlinear device of length L with a uniform period of Λ , one can define the acceptance bandwidth of QPM interaction by solving the following equation,

$$\frac{\sin^2\left(\frac{\Delta k' L}{2}\right)}{\left(\frac{\Delta k' L}{2}\right)^2} = \frac{1}{2} \quad (4.36)$$

from which we can find the full width at half maximum (FWHM) acceptance bandwidth for several parameters which effect the phase-mismatch $\Delta k'$. Solving the above equation yields $\Delta k' L/2 = 0.4429\pi$. Fejer *et al.* [53] described a theoretical model which estimates the bandwidth of domain error ($\Delta\Lambda$) in periodic poling. For a crystal with domain number of N and a period of Λ ,

$$\Delta\Lambda = \frac{1.77\Lambda}{Nm}, \quad (4.37)$$

where m is the order of QPM. We can see from the above equation that a material with more number of domains and short poling period makes the domain acceptance bandwidth smaller when the conversion efficiency dropped to its half.

4.3.2 Spectral Bandwidth

The second harmonic wavelength acceptance $\Delta\lambda$ is defined by material properties and can be calculated by [53],

$$\Delta\lambda = \frac{0.4429\lambda}{L} \left| \frac{n_2 - n_1}{\lambda} + \frac{\partial n_1}{\partial \lambda} - \frac{1}{2} \frac{\partial n_2}{\partial \lambda} \right|^{-1}, \quad (4.38)$$

where λ is the fundamental wavelength, n_1 and n_2 are the refractive indexes at fundamental and second harmonic wavelengths. The dispersion relations can be obtained numerically from Sellmeier's equation [69] for the material being used. For a BPM case, $n_1 = n_2 = n$ and equation (4.38) become,

$$\Delta\lambda = \frac{0.22145\lambda}{L} \left| \frac{\partial n}{\partial \lambda} \right|^{-1}, \quad (4.39)$$

At longer wavelength the spectral bandwidth increases due to decrease in dispersion. It can also be seen from the equation that longer crystal also makes the wavelength acceptance narrower.

4.3.3 Temperature Bandwidth

The temperature acceptance for a QPM interaction is an important parameter, because it defines the amount of temperature to be stabilized in order to maintain phase matching. Temperature tuning not only changes the phase matching by changing the temperature dependent refractive index of the material, but also induces a thermal expansion which can alter the poling period Λ and the total length L of the device. According to the derivation of Fejer *et al.* [53], the temperature acceptance bandwidth ΔT for a QPM case can be is defined as,

$$\Delta T = \frac{0.4429\lambda}{L} \left| \frac{\partial \Delta n}{\partial T} + \alpha \Delta n \right|^{-1}, \quad (4.40)$$

where $\Delta n = n_2 - n_1$ and the temperature dependence of refractive index is calculated from the Sellmeier's equation [69] and the thermal expansion coefficient α is,

$$\alpha = L_c^{-1} \frac{\partial L_c}{\partial T}, \quad (4.41)$$

where L_c is the coherence length. Like the spectral bandwidth, the thermal bandwidths decreases with longer crystal length and increases with longer wavelength.

4.3.4 Angle Tuning and Angular Acceptance

Even though QPM is called noncritical phase matching, since it is carried out in birefringent crystals, both QPM and BPM can occur simultaneously. Therefore, tuning of it still depends on the angle between domain vector K_m and the fundamental wave vector k_1 . If we assume crystal is perfectly phasematched in all the other direction but not in the direction where the domain vector K_m points to. The phase mismatch is the function of the internal angle (θ) between the beam propagation direction and the vector K_m . Let's assume a case where there is a tilt (ν) between the domain vector K_m and the transverse direction of the crystal. Fejer [53] defined the angular bandwidth $\Delta\theta$ for this critical phasematched case as,

$$\Delta\theta \approx 0.886 \frac{\cos \theta}{\sin(\nu - \theta)} \frac{\Lambda}{L}, \quad (4.42)$$

It explains that for critical phase matching the angular acceptance is inversely proportional to crystal length or inversely proportional to number of domains $N = L/\Lambda$ which indicates that it is harder to achieve angular phase matching in longer devices than shorter devices.

For a noncritically phasematched case, the angular acceptance $\Delta\theta$ can be defined as [53],

$$\Delta\theta = 2\sqrt{1.772 \frac{n_2}{n_1} \frac{L_c}{L} \cos \theta}, \quad (4.43)$$

We can see that $\Delta\theta$ depends inversely on the square root of the crystal length.

It is also possible to calculate the angular acceptances with respect to a rotation about the other crystal axes. The calculation is slightly more complicated in those cases, because we have to take into account the angular dependence of index of refraction. But in these cases, the angular acceptance is slightly smaller than the case we just discussed above. Ref [53] has detailed discussion for these cases as well, therefore we will not describe them in here.

4.4 Limitations on Nonlinear Devices

Nonlinear optical materials have been widely used in photonics technology as a good source for generating new optical frequencies. However, there are many factors which could impose a limitation on the performance of nonlinear devices that made of these materials. Some of these factors are material dependent which is intrinsic to the specific material we use. For example, in the case of lithium niobate, they are lattice-defects and polarons [63] in its structure and they can reduce the second harmonic conversion efficiency and also cause an absorption of both fundamental and second harmonic beams. They can only be reduced by carefully controlling the fabrication process or post-processing of the material such as annealing. Another limitations also come from extrinsic defects such as impurities in the nonlinear material. Sometimes, impurities induced externally can be useful to improve the performance of the device. Intrinsic and extrinsic impurities absorb light, and they both strongly effect the properties of nonlinear crystals.

Due to above factors, nonlinear optical devices are susceptible to “optical-damage” which can be categorized as photo-refraction and thermo-optic effect induced by the laser beam.

4.4.1 Photo-refraction

Optical field induces redistribution of charge which causes a change in refractive index. This redistribution of charge is caused by electronic excitation due to photon absorption. Ref [64] describes a model which explains the photo-refraction in various materials. When a nonlinear optical crystal with defects (impurities and intrinsic defects) pumped by a laser beam, space charges (electrons and holes) will build up and generate a current that induces a change in refractive index through electro-optic effect. It reduces the conversion efficiency by dephasing and distorts the wavefront of the laser beam and causes a scattering of light.

The performance of nonlinear devices can also degrade over time since these

charges can accumulate. Doping with MgO [65] and composition control [66] can greatly reduce the effect of photo-refraction. If photo-refraction effect is excessive, it is also called “photorefractive damage”.

4.4.2 Thermo-optic Effect

Absorbed photons causes heat accumulation due to impurities and intrinsic defects in the crystal. If the absorbed energy is not dissipated instantly it heats the crystal and also changes refractive index due to thermo-optic effect. Absorption of the pump beam or nonlinear output induces dephasing and thermal lensing which ultimately causes either subsequent beam quality degradation or reduction of conversion efficiency or even damage. Laser induced damage can be either on the crystal surface or in the bulk crystal. Laser damage threshold under various conditions is vary depend on the crystal type and its growth conditions. Thermal stresses at cooling interfaces can cause fracture and permanent damage.

Other than extrinsic impurities, color centers can arise from intrinsic defects. The electronic state of intrinsic defects can be altered by the illumination with optical radiation. This change of electronic state can then alter the absorption spectra of the intrinsic defects [55]. For example, green induced infrared absorption (GRIIRA) in lithium niobate (LN) and lithium tantalate (LT) causes the increase of the infrared absorption substantially when illuminated with small intensities of green light. Doping with MgO also can reduce this effect [68]. However, absorption is not always harmful to nonlinear optical interactions. Optical parametric oscillation (OPO) is only possible if the pump power exceeds a certain threshold power. For example, for continuous-wave (CW) singly-resonant OPOs, this threshold power is proportional to the roundtrip losses of the resonant wave [67]. One portion of these losses is attributed to optical absorption in the nonlinear crystals. Therefore, depend on the need, one has to chose what kind doping level to pursue in order to achieve the desired nonlinear optical process.

4.5 Frequency Doubling with PPLN Crystal

4.5.1 Periodically Poled Lithium Niobate Crystals

Lithium niobate (LiNbO_3) is a non-centrosymmetric ferroelectric crystal below the Curie temperature $T_C = 1165^\circ\text{C}$. The crystal structure is shown in Figure 4.5. Due to its unique crystal structure, lithium niobate possess a spontaneous polarization $P_s = 10 \mu\text{C}/\text{cm}^2$ at room temperature [63], and a change in temperature leads to the change in spontaneous polarization P_s of the crystal which we call pyroelectricity. Lithium niobate crystal is not only ferroelectric, but also piezoelectric and birefringent. It is used extensively as optical modulators, acousto-optic devices, optical waveguides, pockels cells, Q-switching devices for lasers and optical switches for gigahertz frequencies.

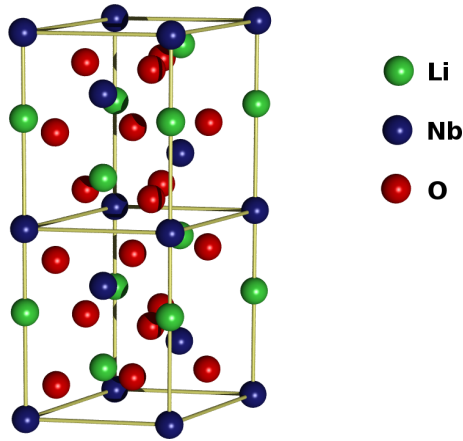


Figure 4.5 (color) Crystal structure of LiNbO_3 [70].

Lithium niobate has been widely used in nonlinear optics due to its high nonlinearity, and the availability of high optical quality substrates. It is transparent from 350 nm to 5000 nm and provides low loss for both the fundamental and second harmonic for visible light generation. When periodically poled, it possesses the highest nonlinear coefficient ($d_{33} = 27 \text{ pm}/\text{V}$) for visible light generation among the all inorganic materials. First-order quasi-phase matching provides $2/\pi$ (63 %) of the full d_{33} , or about 17 pm/V. Table 4.1 summarizes the nonlinear coefficients of some popular

nonlinear materials for a fundamental wavelength of 1064 nm.

Material	Transparency	Nonlinear	Phase Matching	Refractive
	Range (nm)	Coefficient (pm/V)	Schemes	Index (n_e)
LiNbO ₃ , LN	330–5500	$d_{33} = 27$	QPM	2.2
		$d_{31} = 4.3$	BPM	
LiTaO ₃ , LT	280–5500	$d_{33} = 13.8$	QPM	2.2
		$d_{31} = 0.85$	BPM	
KTiOPO ₄ , KTP	350–4500	$d_{33} = 15.3$	QPM	1.86
		$d_{31} = 1.95$	BPM	
KH ₂ PO ₄ , KDP	200–1500	$d_{36} = 0.39$	BPM	1.5
BaB ₂ O ₄ , BBO	185–2600	$d_{31} = 0.08$	BPM	1.6
LiB ₃ O ₅ , LBO	160–2600	$d_{31} = 0.85$	BPM	1.6

Table 4.1 Nonlinear coefficients of some popular nonlinear materials (The comparisons are for the wavelength of 1064 nm). [57–59]

Frequency doubling with periodically poled materials enables the making of visible or ultraviolet light at wavelengths for which lasers are not available traditionally. The advancement in periodic poling technique in nonlinear optical materials made the second harmonic generation (SHG) by quasi-phase matching (QPM) an efficient way to build a compact and low cost lasers. Two most common configurations of frequency doubling have been used so far are single-pass and intra-cavity doubling. The fundamental beam passes through the crystal only once in the single-pass case whereas intra-cavity is makes use of amplified fundamental power inside a resonator. The crystal is placed inside the cavity in the later case and cavity mirrors are designed such that they are highly reflective to the fundamental but transparent to the doubled beam. Generally intra-cavity doubling gives higher efficiency than the single-pass case, but it is difficult to construct.

Potential QPM materials being fabricated with periodic poling technique include KTiOPO_4 , LiTaO_3 , LiB_3O_5 and LiNbO_3 . Among them periodically poled LiNbO_3 (PPLN) has been a very attractive material not only due to its high nonlinear coefficient and therefore high conversion efficiency but also due to its low cost and easiness of fabrication. Quasi-phase matching in PPLN was first demonstrated in 1991 [71]. However, just like other nonlinear materials, it suffers from photo-refractive damage and pointing instability [72] at high powers. To overcome this effect, it is always doped with magnesium oxide (MgO) [73]. Since then few mW levels of frequency doubled light at wavelengths from 437 nm [74] down to 340 nm [75] have been reported. There are more reports on single-pass generation of green light (510 nm \sim 540 nm) with a power level of few Watts [72, 76–79]. According to our knowledge, the highest conversion efficiency reported for 532 nm generation in MgO doped PPLN was 42% [72] in a single-pass and 82% [78] using intra-cavity method.

The Hall A Compton polarimeter requires a Watt level tunable narrow line-width green laser source with good power stability and beam quality in order to establish a frequency locking of it to the Fabry-Perot cavity. In the following section, based on the successes of previous techniques of frequency doubling in PPLN crystal, we will describe our experimental setup and discuss the properties of frequency doubled green beam.

4.5.2 Experimental Setup

Our experimental setup is shown in Figure 4.6. The seed laser (Lightwave series 126 from JDSU) is a diode pumped Nd:YAG narrow line-width ($\Delta\nu = 5.0$ kHz) linearly polarized free space laser that delivers a continuous wave (CW) IR ($\lambda = 1064$ nm) beam up to 250 mW. The output of this laser has been fiber coupled to a single-mode polarization-maintaining fiber through a fiber port collimator at the laser head and is used as the input to an IPG Photonics fiber amplifier (YAR-10K-1064-LP-SF). The amplifier provides a linearly polarized (polarization extinction ratio 20 dB) output

with a maximum power of 10 W at 1064 nm in CW mode.

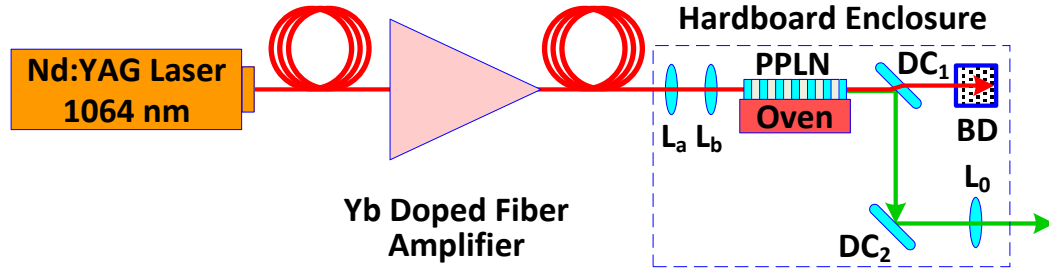


Figure 4.6 (color) A schematic of experimental setup used for frequency doubling in PPLN.

The frequency doubling crystal (from HC Photonics) is PPLN doped with 5% MgO in order to minimize both photo-refractive damage [64] and GRIIRA [68]. The crystal is 0.5 mm thick, 3 mm wide and 50 mm long, and the QPM period is $6.92 \mu\text{m}$ with a 50% duty cycle. The input and output surfaces have been antireflection (AR) coated for 1064 and 532 nm, respectively. Figure 4.7 illustrates the basic geometry of our PPLN crystal.

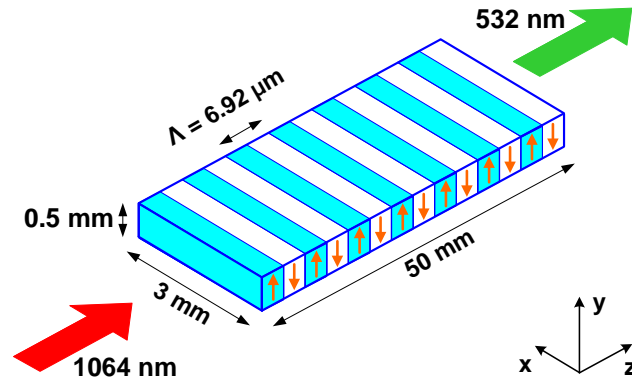


Figure 4.7 (color) The geometry of PPLN Crystal.

The PPLN crystal is placed in an externally controlled, temperature stabilized oven, which was developed in the lab. The oven makes contact with the crystal via a copper holder glued to a 15×60 mm thermoelectric cooler (TEC) Peltier plate (from Custom Thermoelectric). The copper holder has been machined to have a

groove (0.5 mm deep) running across one surface. The bottom of TEC is also glued to a copper heat sink to achieve good thermal stability. The whole temperature stabilizing unit is mounted on a stage composed of four-axis tilt aligner (Model 9071-V from Newport) in order to establish precise alignment for phase matching (Figure 4.9). Due to a small thickness of the crystal, care must be taken to ensure that the beam is not clipped and passing through the center of the crystal. The crystal is held into position by a copper plate with four screws that applies a tiny pressure against its top when they are tightened against the copper holder. A thin layer ($\sim 100 \mu\text{m}$) of indium foil was used between the bottom of the crystal and copper holder in order to establish good heat conductivity. A temperature sensor (from Thermometrics) mounted underneath of the PPLN measures the temperature of the copper holder, which the controller compares to the set point. The copper holder is glued to the hot side of the TEC. The TEC can be turned on to raise the temperature, or turned off to allow the crystal to cool. The temperature controller (from Arroyo Instruments) has a nominal resolution of $0.01 \text{ }^\circ\text{C}$ and during normal operation provides the required phase matching temperature for sustained periods of time. A teflon lid with a small window at the crystal's entry and exit faces provides thermal stability. Figure 4.8 shows the schematics of temperature stabilizing oven for PPLN crystal to achieve quasi phase matching.

A pair of 0.5 inch lenses with a focal lengths of 13.8 and 15 mm are then used to focus the beam waist ($\sim 80 \mu\text{m}$) into the center of the crystal. The generated green light is separated from the IR light after the crystal via a pair of 1.0 inch dichroic mirrors (from Altos Photonics) noted as DC_1 and DC_2 with high reflectivity (99%) in the green and high transmission (95%) in the IR. The residual IR light that transmitted through DC_1 is stopped on a beam dump (BD), while the green light power after DC_2 is monitored by Thorlabs PM140 powermeter.

The lenses, temperature stabilizing unit and dichroic mirrors are all mounted on separate linear translation stage that seats on a rail, and the whole system is contained in a black hardboard enclosure box with a foot print of $355\text{mm} \times 190\text{mm}$ and the

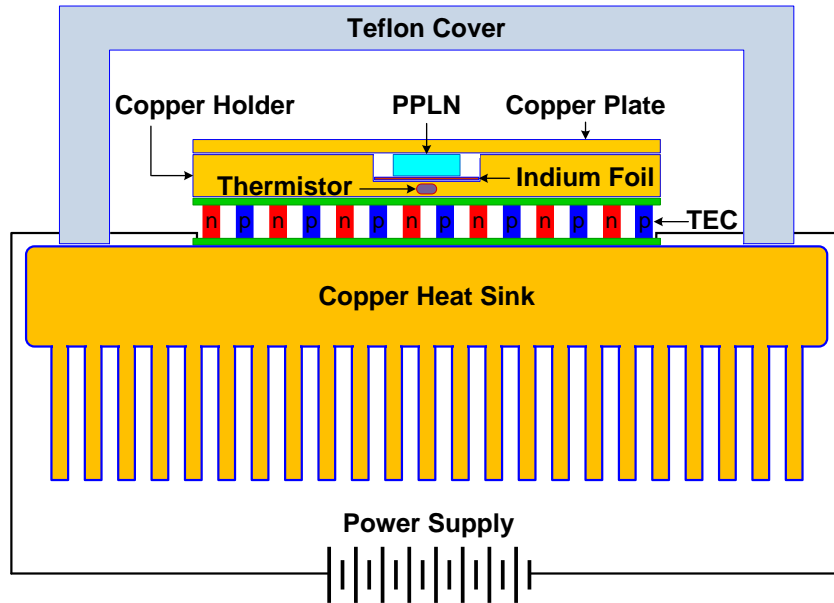


Figure 4.8 (color) The schematic of temperature stabilizing oven for PPLN crystal to achieve quasi-phase matching.

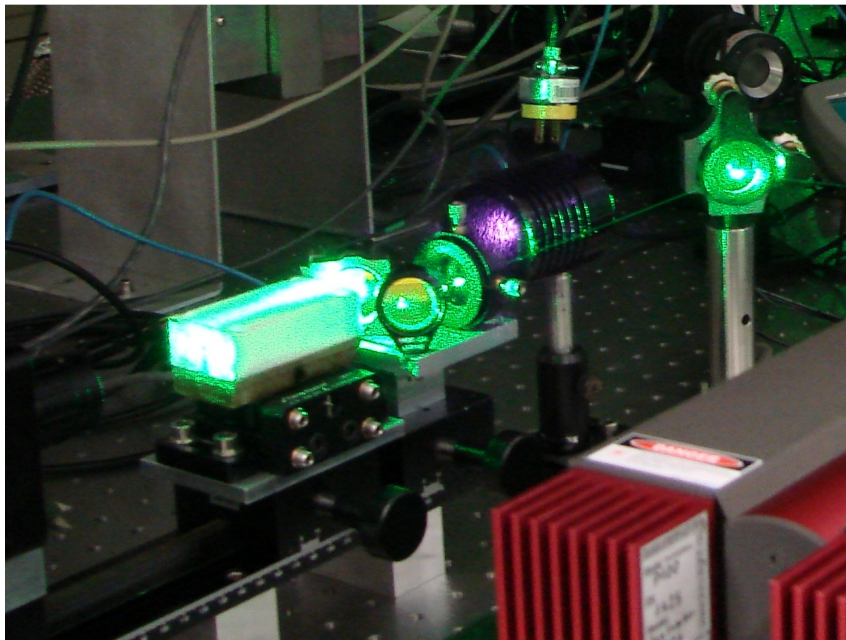


Figure 4.9 (color) The PPLN crystal is mounted inside an oven on a stage. The green beam is generated after the incoming IR beam is passing through the crystal that effectively doubles its frequency.

height of 200mm. There is a small opening on entry side of the box which allows the fiber collimator that coupled to the output fiber of the fiber amplifier to be inserted to the box. Inside the box, the collimator can be mounted and aligned for properly pumping the PPLN. On exit side of the box, a shutter is placed after a transparent AR coated window which is also mounted on the wall of the box so that the beam can be blocked when it is not in use. The whole setup is sealed to protect from any contamination and the box is mounted on a breadboard so that it can be put on the optics table for use.

4.5.3 Properties of the Second Harmonic Beam

With the experimental setup as described above, we measured several properties of the second harmonic beam. The measurements were consistent with our expectations from the theory of second harmonic generation in periodically poled nonlinear crystals.

Generally, after a good alignment of PPLN facet with respect to fundamental 1064 nm beam, we should be able to see some green light after the crystal. We measure the green power as a function of the nominal crystal temperature in order to establish temperature phase matching. We expect a curve that is much look like Figure 4.2. The temperature scan was conducted with an automated procedure run by a Tcl script that controls both the temperature controller and the power meter, and also records the corresponding green power and crystal temperature. The temperature of PPLN can be set remotely via the temperature controller. It takes few seconds to few minutes for the temperature to stabilize depend on the amount of change of set temperature in the controller. The step size of the temperature scan was set to 0.05°C. Figure 4.10 shows the measured temperature bandwidth for 5W IR beam. The red circles show the experimental data while the blue line represents the theoretical fit for first-order QPM interaction predicted by the Sellmeier equations for PPLN crystal [80]. The equation for temperature acceptance bandwidth ΔT can be derived

from equation (4.40),

$$\Delta T = 0.4429 \frac{\lambda}{L \left[\frac{\partial}{\partial T} \left(n\left(\frac{\lambda}{2}\right) - n(\lambda) \right) + \alpha \left(n\left(\frac{\lambda}{2}\right) - n(\lambda) \right) \right]}, \quad (4.44)$$

where λ is the wavelength of fundamental IR beam, L is the crystal length, α is the linear thermal expansion coefficient of PPLN and n is the refractive index which is given by Sellmeier equations,

$$n^2 = a_1 + b_1 f + \frac{a_2 + b_2 f}{\lambda^2 - (a_3 + b_3 f)^2} + \frac{a_4 + b_4 f}{\lambda^2 - a_5^2} - a_6 \lambda^2, \quad (4.45)$$

$$f = (T - 24.5 \text{ } ^\circ\text{C})(T + 570.82), \quad (4.46)$$

where λ is in μm . According to Jundt's [80] calculation, the Sellmeier coefficients $a_{1,2,3,4,5,6}$ and $b_{1,2,3,4}$ for PPLN are summarized as in Table 4.2

Parameter	Value	Parameter	Value
a_1	5.35583	a_2	0.100473
a_3	0.20692	a_4	100
a_5	11.34927	a_6	1.5334×10^{-2}
b_1	4.629×10^{-7}	b_2	3.862×10^{-8}
b_3	-0.89×10^{-8}	b_4	2.657×10^{-5}

Table 4.2 Sellmeier coefficients for PPLN crystal.

Calculation gives the FWHM phase matching temperature bandwidth $\Delta T = 0.72$ $^\circ\text{C}$, whereas the experimental results (open circles) show ΔT of about 0.6 $^\circ\text{C}$ at phase matching temperature 64.0 $^\circ\text{C}$.

It is important to note that the location of the peak changes slightly when the pump power level is changed. The peak, representing the phase matching temperature, lies between 64.0 $^\circ\text{C}$ and 64.3 $^\circ\text{C}$ for a IR pump power level between 200 mW to 5 W. At each point the crystal should be maintained at the peak phase matching temperature. Figure 4.11 shows the average green power (solid circles) in PPLN

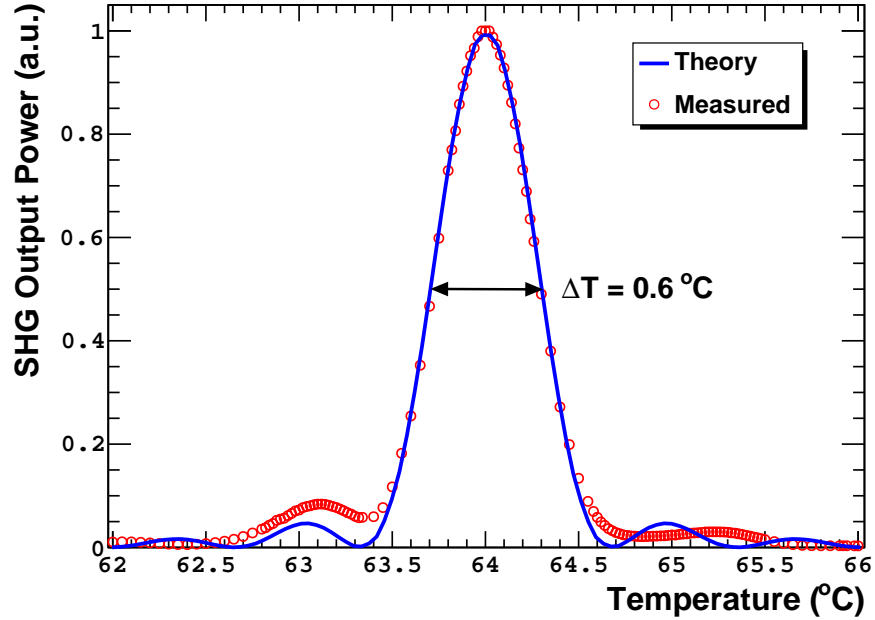


Figure 4.10 (color) Measured temperature tuning curve for PPLN. The solid line is the theoretical values and the dotted points are the experimental results.

and corresponding phase matching temperature (open squares) versus 1064 nm pump power of the Yb doped fiber amplifier. The maximum achieved green power at 5 W pump power was 1.74 W with a conversion efficiency of 34.8%. The continuous line in Figure 4.11 is the theoretical fit to extract the normalized SHG conversion efficiency. According to equation (4.33), for a loosely focussed gaussian beam, the normalized conversion efficiency for first-order QPM is defined as,

$$I_2 = \eta_{mor,QPM} L I_1^2, \quad (4.47)$$

$$\eta_{mor,QPM} = \frac{8\omega_1^2 d^2 L}{n_1^2 n_2 c^3 \epsilon_0 \pi^2}, \quad (4.48)$$

where I_1 and I_2 are the fundamental and SHG powers, L is the length of the crystal, n_1 and n_2 are refractive index at these wavelengths.

In Figure 4.11, as the theoretical fit shows, the green power does indeed vary quadratically with the infrared pump power with normalized conversion efficiency

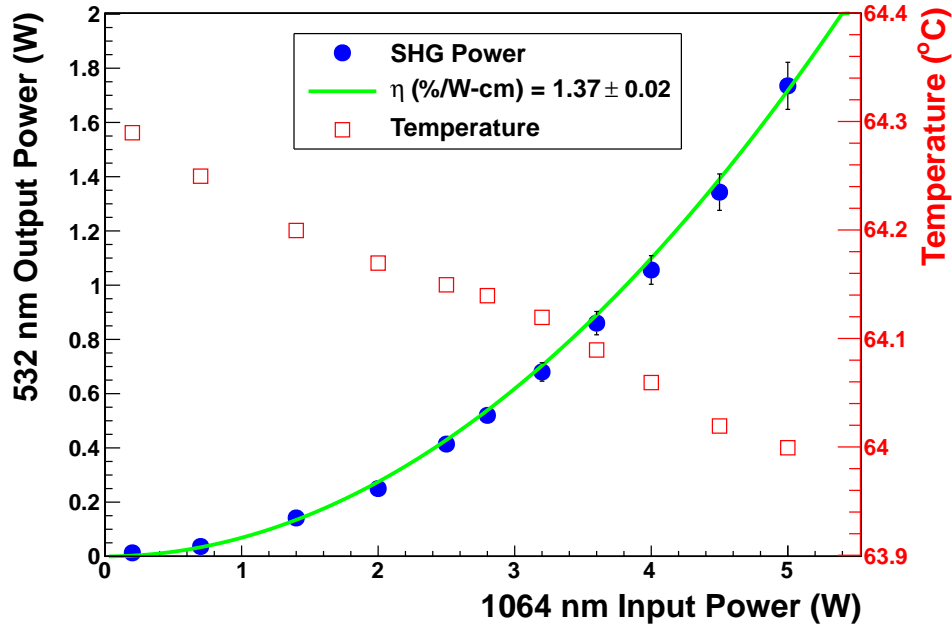


Figure 4.11 (color) 532 nm average power (solid circles) in PPLN and corresponding phase matching temperature (open squares) versus 1064 nm pump power of the Yb doped fiber amplifier. The continuous line is the theoretical fit to extract the normalized SHG conversion efficiency.

η_{mor} of 1.37%/W-cm. It is necessary to point out that all powers are the direct measurements without correction to the residual reflection at the crystal facet and losses in dichroic mirrors. The experimental results also show that there is no sign of saturation in SHG power at 5 W fundamental power. On the other hand, the achieved conversion efficiency is much lower than the ideal conversion efficiency of 2.62%/W-cm which is a case for pump depletion. All of this suggest that thermal lens effects or the optical damages should be negligible. It is worth to note that conversion efficiency of nonlinear crystals grow as a square function of fundamental power. Our data shows that it is possible to get even higher doubling efficiency than the achieved efficiency of 34.8%, and therefore more green power with a higher pump power from the fiber amplifier. One of the goals of Compton green laser project is to develop a frequency doubled, stable and good quality green beam at Watt level, and that is the reason for us not trying to get very high conversion efficiency from PPLN.

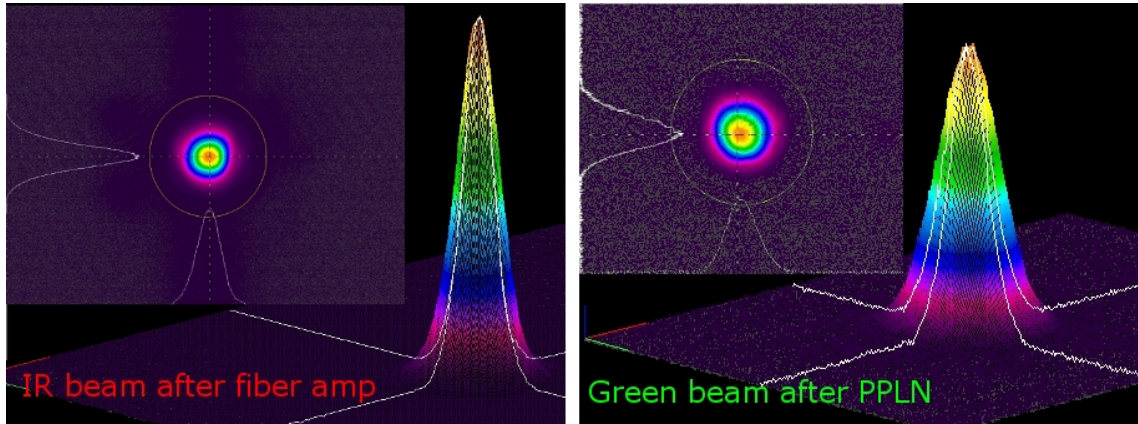


Figure 4.12 (color) IR and Green beam profiles in 2D and 3D measured by Spiricon CCD camera.

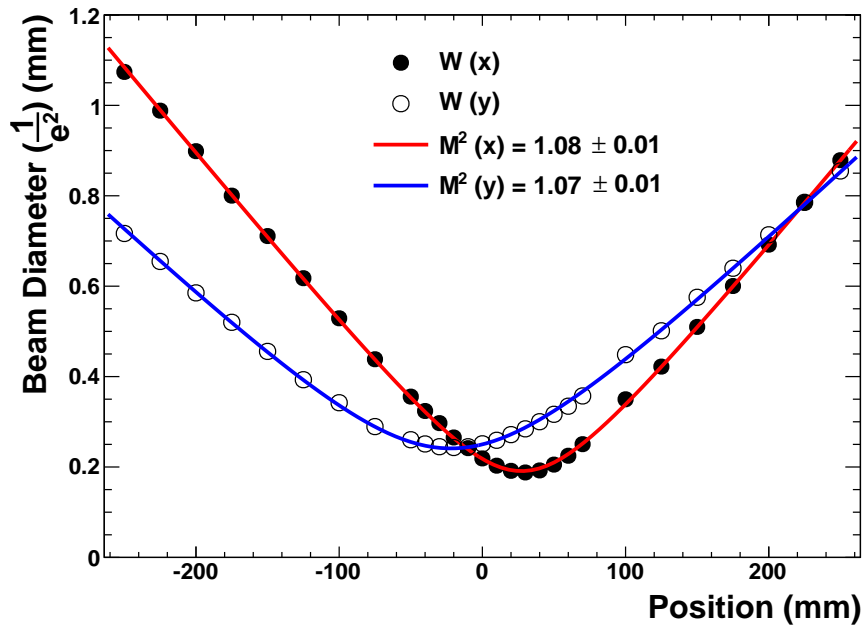


Figure 4.13 (color) Divergence profile of green beam. Closed and Open circles are the beam waist sizes in x (horizontal) and y (vertical) directions, respectively and continuous line shows the theoretical fit to extract the M^2 factor.

We evaluated the quality of frequency doubled green beam at 1.73 W right after PPLN. Figure 4.12 shows the IR and green beam profiles that monitored by Spiricon

CCD camera. In order to get a beam quality factor (M^2), we focused the 532 nm beam after PPLN into 200 μm diameter waist with an additional lens and measured the diameter at different axial position. Figure 4.13 shows the measured beam profile versus theoretical value. Closed and open circles are the measured beam waist sizes in x (horizontal) and y (vertical) directions, respectively. The result of theoretical fit (solid lines) to experimental data indicates that the green beam demonstrates a quality factor M^2 of less than 1.1 in both dimensions. M^2 or beam parameter product (BPP) is a quantity to show the quality of laser beam as a Gaussian beam. It tells how well it can be focused to a small spot or how close the laser to a Gaussian shape. Mostly laser beams have M^2 values greater than 1.0 and only very high quality (Gaussian) beams can have values very close to 1.0. We will describe the definition of M^2 in chapter 5.

The stabilities of green power was evaluated at 1.74 W and are shown in Figure 4.14. The output power stability was about 0.8% for the entire period of 12 hours operation.

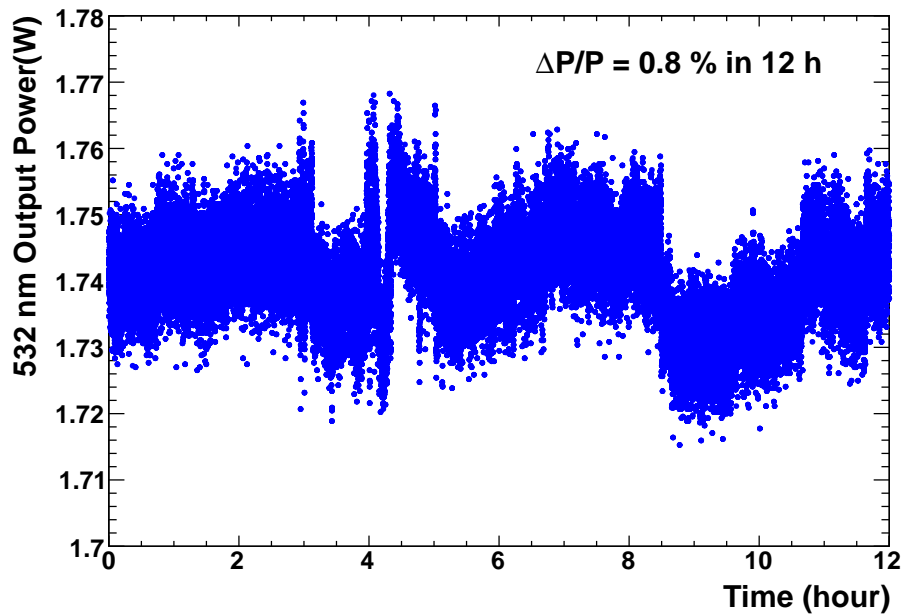


Figure 4.14 (color) The stability of SHG output power was monitored at 1.74 W for 12 hours.

In conclusion, we have demonstrated a high quality, Watt level, stable green laser source based on single-pass SHG of Yb doped fiber laser. It was adequate for achieving several kW intra-cavity power in Fabry-Perot cavity by frequency locking of the IR seed laser to the cavity. The frequency doubled green beam has been used as a laser source for Compton polarimeter during three months of PREx running and shows no sign of degradation. In the following chapter we will describe how we used this frequency doubled green beam to establish Fabry-Perot cavity locking and obtained multi-kW intra-cavity power in Compton polarimeter in Hall A of Jefferson Lab.

Chapter 5

Fabry-Perot Cavity

The heart of the new Compton polarimeter installed in JLab's Hall A is a high-finesse Fabry-Perot cavity which amplifies a primary 1.74 W continuous wave frequency doubled green laser coupled to it. In this chapter, we will start from Gaussian beams and Fabry-Perot cavity basics, and explain the response of Fabry-Perot cavity to the optical field. We will introduce the locking mechanism and feedback technique to achieve power amplification inside the cavity and describe the feedback system used in our setup. The mechanics of the cavity system along with the optical method to increase the laser beam coupling to the cavity will also be presented. At the end, we will discuss the optical parameters that characterize the cavity.

5.1 Cavity in an Electro Magnetic Field

This section is a brief description of the Gaussian laser beam propagation and Fabry-Perot cavities. It gives an overview of the basic introduction to standard spherical mirrors cavities, and their response to optical field generated by Gaussian beams. The reader familiar with these techniques can jump to section [5.2](#).

5.1.1 Gaussian Beams

Paraxial Wave Equation

The electromagnetic radiation from lasers is monochromatic, the electric and magnetic fields have minimal phase and amplitude variations in the first-order approximation. The behavior of these fields in free space (homogeneous and isotropic medium) can be described by the scalar wave equation (Helmholtz equation) [81],

$$\left[\nabla^2 + k^2 \right] E(x, y, z) = 0, \quad (5.1)$$

where $E(x, y, z)$ is the phasor amplitude of a complex electric field, ∇^2 is the Laplacian operator and k is the laser wavenumber. If the field propagates mainly in the z direction, with a slow variation of amplitude and phase along the transverse direction, the field can be written as,

$$E(x, y, z) = u(x, y, z)e^{-ikz}, \quad (5.2)$$

where u is called envelope function which describes the transverse profile of the beam. Substituting this into equation (5.1) gives,

$$\frac{\partial^2 u}{\partial x^2} + \frac{\partial^2 u}{\partial y^2} + \frac{\partial^2 u}{\partial z^2} - 2ik \frac{\partial u}{\partial z} = 0, \quad (5.3)$$

If the z dependence of the envelope function is slow compared to the optical wavelength and to the transverse variations of the field, we can describe their properties using the paraxial wave approximation,

$$\left| \frac{\partial^2 u}{\partial z^2} \right| \ll \left| 2k \frac{\partial u}{\partial z} \right|, \quad (5.4)$$

$$\left| \frac{\partial^2 u}{\partial z^2} \right| \ll \left| \frac{\partial^2 u}{\partial x^2} \right|, \quad (5.5)$$

$$\left| \frac{\partial^2 u}{\partial z^2} \right| \ll \left| \frac{\partial^2 u}{\partial y^2} \right|, \quad (5.6)$$

and the equation (5.3) reduces to the paraxial wave equation [81],

$$\frac{\partial^2 u}{\partial x^2} + \frac{\partial^2 u}{\partial y^2} - 2ik \frac{\partial u}{\partial z} = 0, \quad (5.7)$$

Gaussian Beams

A simplest solution of Helmholtz equation in the paraxial approximation (5.7) can be expressed as,

$$u(r, z) = u_0 \frac{w_0}{w(z)} \exp \left[-\frac{r^2}{w^2(z)} \right] \exp \left[-ik \frac{r^2}{2R(z)} \right] \exp \left[-ikz + i \arctan \left(\frac{z}{z_R} \right) \right], \quad (5.8)$$

where z is the axial distance from the beam's narrowest point (the "waist"); w_0 and $w(z)$ are the beam radius at the waist and at z where the field intensity drops to $1/e^2$ of their axial values, respectively; $r = \sqrt{x^2 + y^2}$ is the radial distance from the center axis of the beam; u_0 is the amplitude of the field at $u(0, 0)$; $R(z)$ is the radius of curvature of the beam's wavefronts at z ; z_R is a constant called the Rayleigh range. All these parameters are defined by following equations,

$$w_0 = \sqrt{\frac{\lambda z_R}{\pi}}, \quad (5.9)$$

$$w(z) = w_0 \sqrt{1 + \left(\frac{z}{z_R} \right)^2}, \quad (5.10)$$

$$R(z) = z \left[1 + \left(\frac{z_R}{z} \right)^2 \right], \quad (5.11)$$

The intensity (or irradiance) distribution is the square modulus of equation (5.8),

$$I(r, z) = |u(r, z)|^2 = |u_0|^2 \left(\frac{w_0}{w(z)} \right)^2 \exp \left[-\frac{2r^2}{w^2(z)} \right], \quad (5.12)$$

which shows it has a Gaussian distribution and therefore it is called Gaussian beam. In general, outputs of spherical mirror cavities (resonators) and lasers are often close to Gaussian beams. Figure 5.1 shows a notation for a Gaussian beam diverging away from its waist.

Note that the beam radius $w(z)$ has a hyperbolic shape along z and has a focus w_0 at $z = 0$. The Rayleigh range z_R defines if the beam radius $w(z)$ is close to its focus or diverging from it. From Figure 5.1 we can see that in far field ($|z| \gg z_R$) the beam radius $w(z)$ approaches straight line and the beam propagates in the form of a cone of an angle θ , called beam divergence, given by

$$\theta \approx \tan \theta = \frac{2\lambda}{\pi w_0}, \quad (5.13)$$

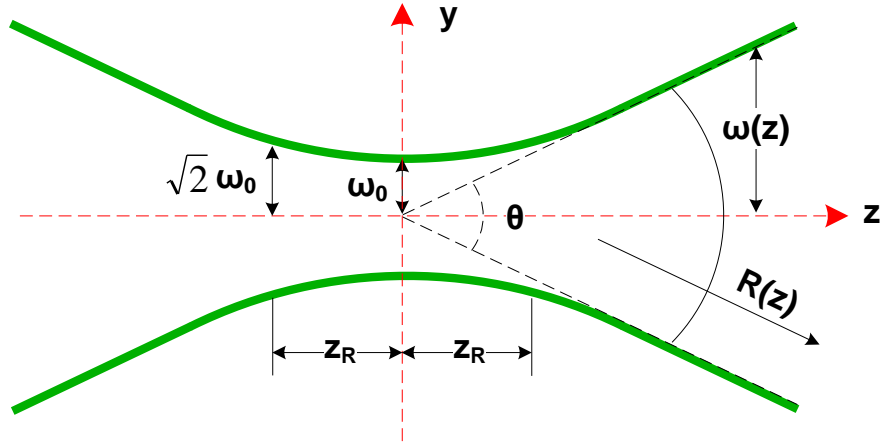


Figure 5.1 (color) A longitudinal profile of a Gaussian beam.

where we used a small angle approximation for the paraxial Gaussian beam. Due to diffraction, a Gaussian laser beam that is focused to a small spot diverges rapidly as it propagates away from that spot. Therefore a well collimated Gaussian laser beam usually has a larger diameter.

When we work with laser beam, depend on the need of our work, we may need the laser beam has specific shapes such as a Gaussian or a top hat (super Gaussian). Usually there is a quantity to show how close the laser beam to the ideal Gaussian beam. The laser beam quality factor (mostly known as M^2 factor) is quantified by the beam parameter product (BPP) which is the product of the beam's divergence and waist radius w_0 . The ratio of the BPP of the real beam to that of an ideal Gaussian beam at the same wavelength is known as M^2 ("M squared"). It is often tricky to accurately measure the beam divergence in the far field that effects the accuracy of BPP. There is another way of measuring M^2 defined as [82],

$$\sigma^2(z) = \sigma_0^2 + \left(\frac{M^2 \lambda}{\pi \sigma_0} \right)^2 (z - z_0)^2, \quad (5.14)$$

where $\sigma^2(z)$ is the second moment of the distribution (4σ beam width) in the x or y direction, λ is the wavelength of the laser beam, and z_0 is the location of the beam waist with second moment width of σ_0 . Fitting the data points (at least 10) yields

M^2 , z_0 , and σ_0 .

The last exponential term in equation (5.8) contains an important phase information about the Gaussian beam. The first term in the exponential is the phase of a plane wave ikz propagating with the same frequency as the Gaussian beam. The second term is called the Gouy phase shift and represents a small deviation from planarity. The Gouy term represents a phase retardation compared to the plane wave. Because of the arctan form, the retardation amounts to a total of π in phase over all z . The Gouy phase is important in computing the resonant frequencies of optical cavities.

By analyzing equation (5.11), we can see that at the waist ($z = 0$), $R(z) \rightarrow \infty$, i.e., the wavefront is flat, and that in far field ($|z| \gg z_R$), $R(z) \sim z$, i.e., the wavefront is a sphere centered at beam waist. In a cavity, the boundary conditions imposed by the cavity mirrors require that the curvature of the spherical mirrors and the curvature of the wave fronts match.

Even though it is complex, the Gaussian beam can be uniquely characterized by a few parameters such as w_0 (or z_R) and λ . The propagation of Gaussian beam in free space can be easily computed by using a complex radius of curvature $q(z)$, or q -parameter, defined by [81],

$$\frac{1}{q(z)} = \frac{1}{R(z)} - i \frac{\lambda}{\pi w^2(z)}, \quad (5.15)$$

and this parameter obeys the propagation law,

$$q(z) = z + iz_R, \quad (5.16)$$

Between two planes along the optical axis z , one can have two parameters $q(z_2)$ and $q(z_1)$ with the following propagation law,

$$q(z_2) = q(z_1) + z_2 - z_1, \quad (5.17)$$

which is the basics of so-called ‘‘ABCD’’ matrix formalism for propagating Gaussian beam through various optical elements.

The Gaussian beam is the fundamental mode solution of Helmholtz equation in the paraxial approximation (5.7). However, Helmholtz equation has other solutions with more complex combination of functions and they are useful when we deal with Gaussian beam coupling to the optical cavity. In contrary to the fundamental mode, those solutions are often called higher order modes.

Higher Order Modes

As we mentioned earlier, Gaussian beams are just one possible (simplest) solution to the paraxial wave equation (5.7). In fact it has other solutions with a combination of a complete and orthogonal set of functions called propagation modes. Any real laser can be described as the superposition of these modes and they are particularly useful when we model the laser beam circulating inside optical cavities.

(1) Hermite-Gaussian Modes

In cartesian coordinates, Hermite-Gaussian modes describe the reflection symmetry in the plane perpendicular to the laser beam's propagation direction. They can be written as,

$$u_{m,n}(x, y, z) = \sqrt{\frac{2}{\pi 2^{m+n} m! n! w^2(z)}} H_m\left(\frac{\sqrt{2}x}{w(z)}\right) H_n\left(\frac{\sqrt{2}y}{w(z)}\right) \exp\left[-\frac{x^2 + y^2}{w^2(z)}\right] \exp\left[-ikz + i(m+n+1) \arctan\left(\frac{z}{z_R}\right)\right] \exp\left[-ik\frac{x^2 + y^2}{2R(z)}\right], \quad (5.18)$$

where the functions $H_m(x)$ are the Hermite polynomials of order m and the parameters $w(z)$, $R(z)$ and z_R are the same as for the fundamental Gaussian mode as given in equation (5.7). The corresponding electromagnetic waves to these laser modes usually can be approximated as transverse electric and magnetic ($\text{TEM}_{m,n}$) waves or called $\text{TEM}_{m,n}$ modes, where m and n are the polynomial indices in the x and y directions. A Gaussian beam is a fundamental mode called $\text{TEM}_{0,0}$ mode. Figure 5.2 shows the intensity pattern of some common Hermite-Gaussian modes with different orders.

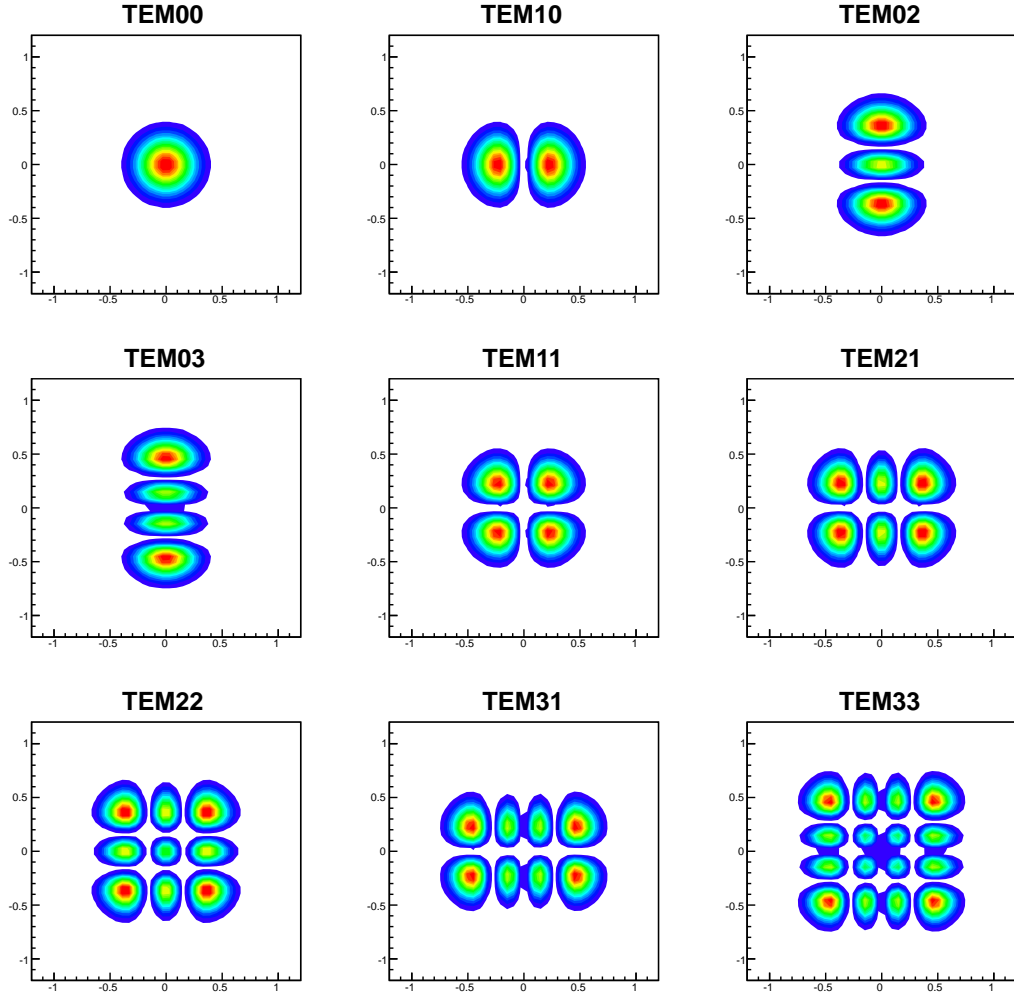


Figure 5.2 (color) Hermite-Gaussian Modes.

(2) Laguerre-Gaussian Modes

In cylindrical coordinates (r, ϕ, z) , we can equally express the Hermite-Gaussian modes in Laguerre-Gaussian polynomials and they are called Laguerre-Gaussian (LG) modes,

$$\begin{aligned}
 u_{pm}(r, \phi, z) = & \sqrt{\frac{4p!}{\pi(1 + \delta_{m0})(m + p)!}} \left(\frac{\sqrt{2}r}{w(z)} \right)^m L_p^m \left(\frac{2r^2}{w^2(z)} \right) \frac{\exp \left[-\frac{r^2}{w^2(z)} \right]}{w(z)} \cos(m\phi) \\
 & \exp \left[-ikz + i(2p + m + 1) \arctan \left(\frac{z}{z_R} \right) \right] \exp \left[-ik \frac{r^2}{2R(z)} \right], \quad (5.19)
 \end{aligned}$$

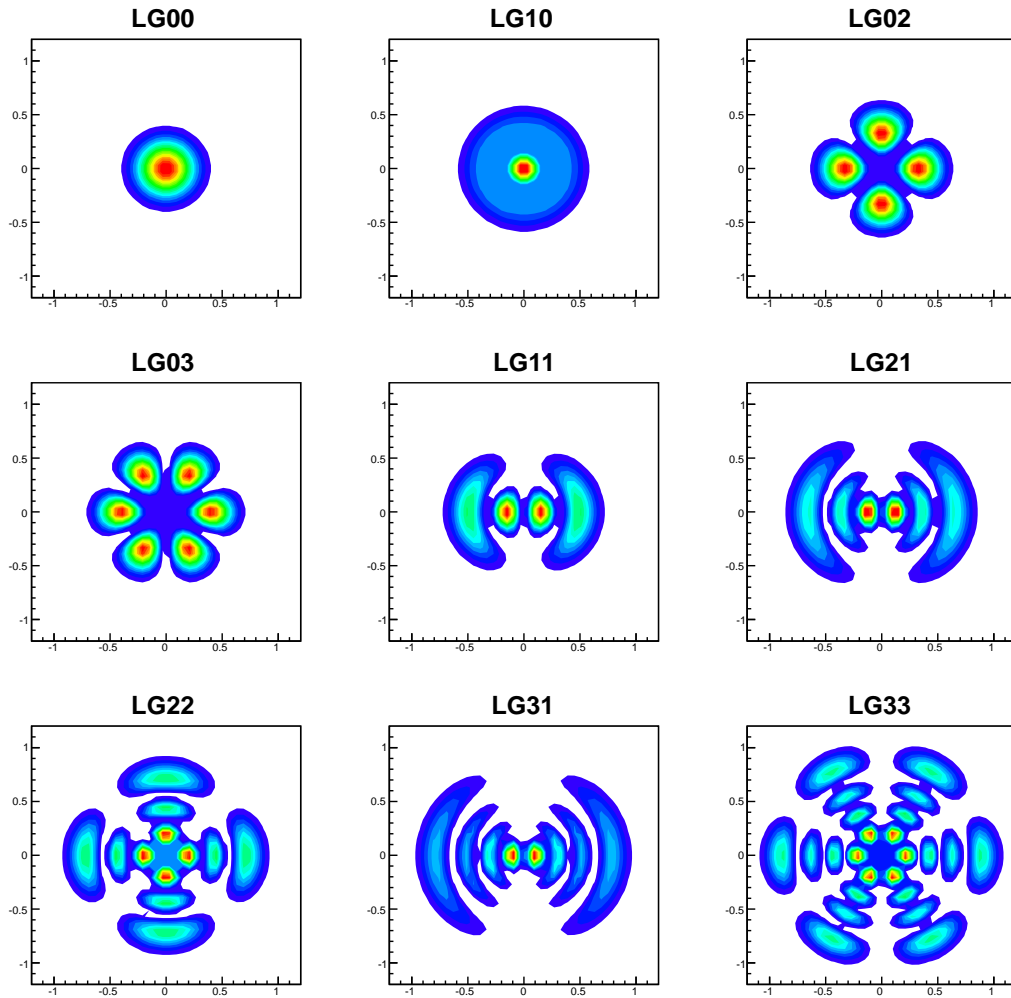


Figure 5.3 (color) Laguerre-Gaussian Modes.

where the integer $p \geq 0$ is the radial index and the integer m is the azimuthal mode index; the L_p^m are the generalized Laguerre polynomials and all other quantities $w(z)$, $R(z)$ and z_R are exactly the same as in the Hermite-Gaussian case. Figure 5.3 shows the intensity pattern of some common Laguerre-Gaussian modes with different orders.

5.1.2 High Reflectance Mirrors

For a light amplification purpose, Fabry-Perot cavity allows the laser light to make a maximum number of round trips between two high reflective mirrors so that light

intensity gets amplified without suffering of absorption and scattering. The characteristics of high reflectivity mirrors such as transmittivity (T) and loss (P) determine the maximum amplification gain.

The high reflectivity of the mirrors is achieved by a stack of quarter-wave ($\frac{\lambda}{4}$) dielectric thin layers with alternating high-low index pairs with a high index layer on the outer most sides. The layers are deposited on a super polished mirror substrate which is mostly fused silica (SiO_2) by a technique called Ion Beam Sputtering (IBS). Usually, the constituent materials of layers are tantalum pentoxide (Ta_2O_5) with refractive index $n_H \approx 2.1$ and silicon oxide (SiO_2) with refractive index $n_L \approx 1.47$. The number of $\frac{\lambda}{4}$ layers deposited on the substrate determine wanted transmittivity and therefore the reflectivity.

We consider the case of a single layer of dielectric of index n_1 and thickness l , between a vacuum (index n_0) and mirror substrate (index n_s) (Figure 5.4). Suppose two monochromatic plane waves propagating perpendicularly to this medium. the amplitude of the incident and reflected beam are a_0 and b_0 , respectively. The electric field amplitudes in the dielectric medium are a_1 and b_1 for the forward and backward

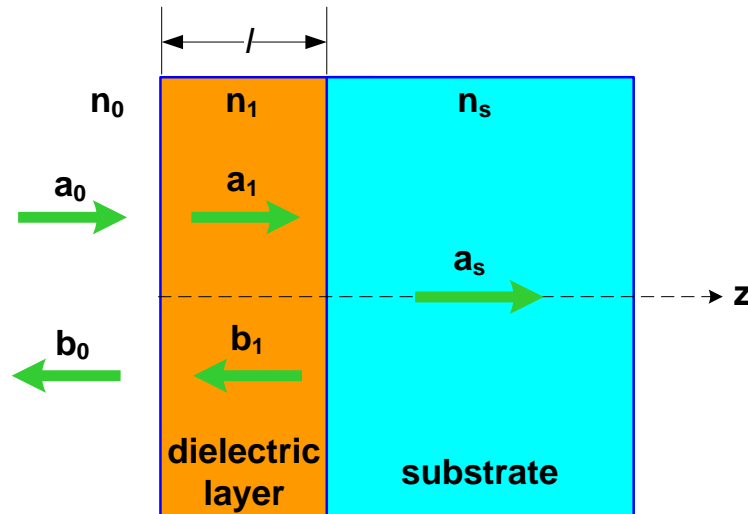


Figure 5.4 (color) Reflection and transmission of optical fields from a dielectric layer on a mirror substrate.

traveling waves. The amplitude of the transmitted field is a_s . We put the origin of propagation axis to the center of dielectric layer as indicated in the figure.

The boundary condition requires that the electric and magnetic fields be continuous at each interface. Therefore [91],

$$a_0 + b_0 = a_1 + b_1, \quad (5.20)$$

$$a_1 e^{ikl} + b_1 e^{-ikl} = a_s, \quad (5.21)$$

$$n_0 a_0 - n_0 b_0 = n_1 a_1 - n_1 b_1, \quad (5.22)$$

$$n_1 a_1 e^{ikl} - n_1 b_1 e^{-ikl} = n_s a_s, \quad (5.23)$$

where $k = 2\pi/\lambda$ and we assumed the length of vacuum and substrate are very large as compared to the thickness of dielectric layer.

If we eliminate a_1 and b_1 from above equations, we have a matrix form,

$$\begin{bmatrix} 1 \\ n_0 \end{bmatrix} + \begin{bmatrix} 1 \\ n_0 \end{bmatrix} \frac{b_0}{a_0} = \begin{bmatrix} \cos kl & -\frac{i}{n_1} \sin kl \\ -in_1 \sin kl & \cos kl \end{bmatrix} \begin{bmatrix} 1 \\ n_s \end{bmatrix} \frac{a_s}{a_0}, \quad (5.24)$$

If we call r and t reflection and transmission coefficients at the interface,

$$r = \frac{b_0}{a_0}, \quad (5.25)$$

$$t = \frac{a_s}{a_0}, \quad (5.26)$$

and the transfer (characteristic) matrix of dielectric layer is,

$$M = \begin{bmatrix} \cos kl & -\frac{i}{n_1} \sin kl \\ -in_1 \sin kl & \cos kl \end{bmatrix}, \quad (5.27)$$

From equation (5.24) we can solve r and t ,

$$r = \frac{n_1(1 - n_s) \cos kl - i(n_s - n_1^2) \sin kl}{n_1(1 + n_s) \cos kl - i(n_s + n_1^2) \sin kl}, \quad (5.28)$$

$$t = \frac{2n_0 n_1}{n_1(n_0 + n_s) \cos kl - i(n_s n_0 + n_1^2) \sin kl}, \quad (5.29)$$

The essential design parameter for use of thin layer is the thickness l which determines the layer's effects on propagating light. If the thickness is half-wave ($\frac{\lambda}{2}$),

then the film is transmissive. In a multilayer film, a stack of alternate layers of high index, n_H , and low index, n_L , each with thickness $\frac{\lambda}{4}$, the product of a characteristic matrices of two adjacent layers is,

$$\begin{bmatrix} 0 & -\frac{i}{n_L} \\ -in_L & 0 \end{bmatrix} \begin{bmatrix} 0 & -\frac{i}{n_H} \\ -in_H & 0 \end{bmatrix} = \begin{bmatrix} -\frac{n_H}{n_L} & 0 \\ 0 & -\frac{n_L}{n_H} \end{bmatrix}, \quad (5.30)$$

If the stack consists of $2N$ layers, then the characteristic matrix of complete multilayer is,

$$M_{2N} = \begin{bmatrix} -\frac{n_H}{n_L} & 0 \\ 0 & -\frac{n_L}{n_H} \end{bmatrix}^N = \begin{bmatrix} \left(-\frac{n_H}{n_L}\right)^N & 0 \\ 0 & \left(-\frac{n_L}{n_H}\right)^N \end{bmatrix} \quad (5.31)$$

The reflectivity of a mirror with a layer structure $(n_H, n_L, n_H, n_L, \dots, n_H, n_L)$ is,

$$R_{2N} = |r_{2N}|^2 = \left(\frac{1 - \frac{n_s}{n_0} \left(\frac{n_H}{n_L}\right)^{2N}}{1 + \frac{n_s}{n_0} \left(\frac{n_H}{n_L}\right)^{2N}} \right)^2, \quad (5.32)$$

High reflectivity can be achieved from an odd number of $\frac{\lambda}{4}$ dielectric thin films with alternating high-low index pairs with a high index film on the outer most sides, and the reflectivity of a mirror with this kind of layer structure $(n_H, n_L, n_H, n_L, \dots, n_H, n_L, n_H)$ is,

$$R_{2N+1} = |r_{2N+1}|^2 = \left(\frac{1 - \frac{n_H}{n_0} \frac{n_H}{n_s} \left(\frac{n_H}{n_L}\right)^{2N}}{1 + \frac{n_H}{n_0} \frac{n_H}{n_s} \left(\frac{n_H}{n_L}\right)^{2N}} \right)^2, \quad (5.33)$$

Under this circumstance, there is a constructive interference at each subsequent high to low index interfaces, and mirror total reflectivity actually builds up gradually through each layers successively.

For a mirror with no losses, we denote $R = |r|^2$ and $T = |t|^2$, and if we apply the principle of energy conservation and taking losses into account, we will have the relation:

$$R + T + P = 1, \quad (5.34)$$

where P represents the losses in the mirror (both in substrate and coating) in terms of scattering (S) and absorption (A), and $P = A + S$. The scattering loss mostly comes from an imperfect reflection at the mirrors. Surface roughness and the defects in the substrate are the main factor to affect it. Super polishing technology enables the manufacturing of substrates with surface RMS roughness of few Å or less [92]. Absorption loss is mostly the result of the impurities in the coatings and contamination on the mirror surface. Due to this, mirror coating materials have to be highly pure and mirrors need to be operated in a clean environment.

5.1.3 Optical Response of Fabry-Perot Cavity

Fabry-Perot cavity or Fabry-Perot interferometer, first invented by C. Fabry and A. Perot in 1899 [83], is a resonator which consists of two high reflective mirrors that form a standing light waves between them. Due to constructive interferences, the laser power circulating in the cavity will be enhanced by a factor G with respect to the laser power coupled to it. Since the availability of high reflectivity mirrors, Fabry-Perot cavities have been used widespread and played a crucial role in many physical fields, such as telecommunications, lasers and spectroscopy, quantum electrodynamics [90], vacuum structure measurements [89], gravitational wave detection [88], and metrology [87]. More recently, Fabry-Perot cavities have been used successfully in storage rings and linear accelerators for various beam diagnostics [85], X-ray generation [84,86] and beam polarimetry techniques [5,8].

Basic Principles

Let us consider an incident laser beam on an optical cavity made of two dielectric mirrors. The electric field of this beam can be written,

$$E = E_{inc} e^{i(\omega t - kz)}, \quad (5.35)$$

where ω is the frequency of the light and $k = \frac{\omega}{c} = \frac{2\pi}{\lambda}$ is the wave-vector. If we note reflectivity and transmittivity of the input mirror (r_1, t_1) and the output mirror

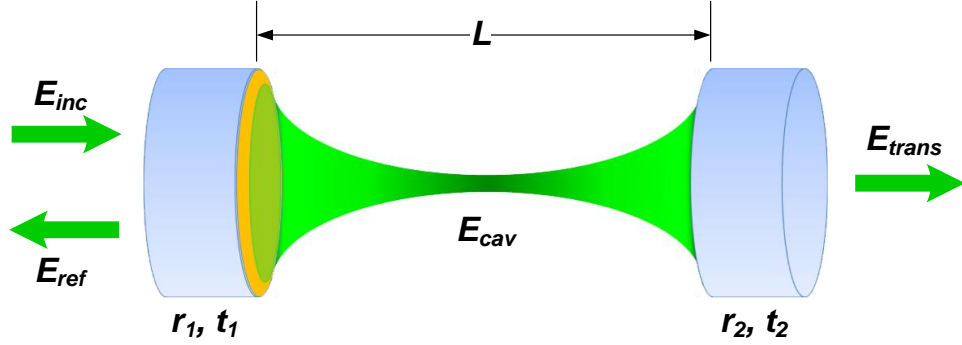


Figure 5.5 (color) Fabry-Perot cavity in optical field.

(r_2, t_2) , the beam incident on one mirror is partially transmitted and partially reflected. The transmitted part enters the cavity and is reflected back and forth many times. On each reflection a fraction escapes the cavity (see Figure 5.5). Since this process is coherent, the amplitudes of the reflections will interfere.

The transmitted field amplitude is the sum of all amplitudes after the second mirror [81],

$$E_{trans} = E_{inc} t_1 t_2 \left[1 + r_1 r_2 e^{i2kL} + (r_1 r_2 e^{i2kL})^2 + \dots \right] = E_{inc} \frac{t_1 t_2}{1 - r_1 r_2 e^{i2kL}}, \quad (5.36)$$

where we assumed the mirrors are in high vacuum ($P < 10^{-8}$ Torr) and neglected the absorption loss from any residual gas in the cavity and L is the length of the cavity. We also can see there is a round-trip phase $2kL$ of the light wave in the cavity. Similarly, the reflected field is,

$$E_{ref} = E_{inc} \left[-r_1 + t_1^2 r_2 e^{i2kL} + t_1^2 r_1 (r_2 e^{i2kL})^2 + \dots \right] = E_{inc} \left[\frac{r_1 t_1^2 e^{i2kL}}{1 - r_2 e^{i2kL}} - r_1 \right], \quad (5.37)$$

The field in the cavity is a standing wave and when properly tuned, the back and forth reflections inside the cavity interfere constructively and give the resonant intra-cavity field,

$$E_{cav} = \frac{-i E_{trans}}{t_2} e^{i2kL} = -i E_{inc} \frac{t_1 e^{i2kL}}{1 - r_1 r_2 e^{i2kL}}, \quad (5.38)$$

In order to simplify the equations, we assume that the two mirrors have the same transmission and reflection coefficients (practically, we select pairs whose character-

istics are the closest). This allows us to write $r_1 = r_2 = r$ and $t_1 = t_2 = t$. The above equations can then be rewritten in this form,

$$E_{trans} = E_{inc} \frac{t^2}{1 - r^2 e^{i2kL}}, \quad (5.39)$$

$$E_{ref} = E_{inc} \left[\frac{rt^2 e^{i2kL}}{1 - r e^{i2kL}} - r \right], \quad (5.40)$$

$$E_{cav} = -i E_{inc} \frac{t e^{i2kL}}{1 - r^2 e^{i2kL}}, \quad (5.41)$$

Intra-cavity Field

The intensity of an electromagnetic wave in vacuum is written in the following form,

$$I = |E|^2, \quad (5.42)$$

From equation (5.41), we can write the intensity of intra-cavity field I_{cav} in this form,

$$I_{cav}(\nu) = I_{inc} \times \frac{T}{(1 - R)^2} \times \frac{1}{1 + \frac{4R}{(1 - R)^2} \sin^2 \left(\frac{2\pi\nu L}{c} \right)}, \quad (5.43)$$

where I_{inc} is the intensity of the incident field. This function reaches its maxima when we have the relation,

$$\nu = n \frac{c}{2L}, \quad n \in \text{integer}, \quad (5.44)$$

which is the resonance condition for a resonator. The parameter $\frac{c}{2L}$ only depends on the cavity length and is called Free Spectral Range (*FSR*).

$$FSR = \frac{c}{2L}, \quad (5.45)$$

Therefore the cavity defines resonance frequencies, which are multiple of the frequency gap *FSR*. This is a condition allows us to get constructive interferences in the cavity between the incident field and the field circulating in the cavity. When it is satisfied, the intra-cavity field and the incident field has the same phase. In other words, we have $kL = n\pi$. In the case of the cavity we built ($L = 0.85 \text{ m}$), the resonance frequency is defined by its $FSR = 176.5 \text{ MHz}$.

From equation (5.43), we can also identify the gain of the cavity,

$$G = \frac{T}{(1-R)^2} \frac{1}{1 + \frac{4R}{(1-R)^2} \sin^2\left(\frac{2\pi\nu L}{c}\right)}, \quad (5.46)$$

and the maximum gain is,

$$G_{max} = \frac{T}{(1-R)^2} \quad (5.47)$$

If we look for the deviation to the resonance frequency $\Delta\nu_c$ for which $G = G_{max}/2$, from equation (5.46), we have,

$$\Delta\nu_c = \frac{FSR}{\pi} \times \arcsin \frac{1-R}{\sqrt{R}}, \quad (5.48)$$

where $\Delta\nu_c$ is called cavity bandwidth. An important quantity called finesse is written by the relation,

$$\mathcal{F} = \frac{FSR}{\Delta\nu_c} = \frac{\pi\sqrt{R}}{1-R}, \quad (5.49)$$

Note that the cavity bandwidth depends on intrinsic characteristics of the mirrors such as reflectivity R and cavity length L while the finesse only depends on mirror reflectivity R . For a given cavity length, an increasing R leads to an increasing G_{max} but results a decreasing $\Delta\nu_c$. For a symmetric 85 cm cavity made of two mirrors with $R = 99.982\%$, $T = 180$ ppm, the cavity bandwidth is $\Delta\nu_c \approx 10kHz$, the finesse is $\mathcal{F} = 17400$ and the maximum gain is $G_{max} \approx 5500$. For cavity mirrors with $R = 99.992\%$, $T = 80$ ppm, the cavity bandwidth is $\Delta\nu_c \approx 4.5kHz$, the finesse is $\mathcal{F} = 39000$ and the maximum gain is $G_{max} \approx 12500$. Here we didn't consider the mirror loss P . When we have high reflectivity and low transmission mirrors, cavity gain is very sensitive to loss P and we have to minimize P in order to keep the actual gain closer to G_{max} .

Transmitted Field

The expression of transmitted intensity can be deduced easily from the intensity in the cavity I_{cav} , as transmitted intensity is equal to the intensity in the cavity multiplied

by the transmittivity of the output mirror,

$$I_{trans}(\nu) = I_{inc} \times \frac{T^2}{(1-R)^2} \times \frac{1}{1 + \frac{4R}{(1-R)^2} \sin^2 \left(\frac{2\pi\nu L}{c} \right)}, \quad (5.50)$$

Reflected Field

The field reflected from the cavity is shown in equation (5.41). Understanding the cavity reflected field is important, since the technique used for establishing the cavity gain uses this signal. If we call $\rho(\nu)$ is the field reflection coefficient of the cavity, using equation (5.41), we have the following relation,

$$\rho(\nu) = \frac{E_{ref}(\nu)}{E_{inc}(\nu)} = r \left[\frac{t^2 e^{i2kL}}{1 - r e^{i2kL}} - 1 \right], \quad (5.51)$$

If we introduce a phase $\Phi_r(\nu)$ to the function $\rho(\nu)$, we have,

$$\rho(\nu) = \mathcal{R}(\nu) \times e^{i\Phi_r(\nu)}, \quad (5.52)$$

where $\mathcal{R}(\nu)$ is the module. By the same way as above, and using a relation: $P =$

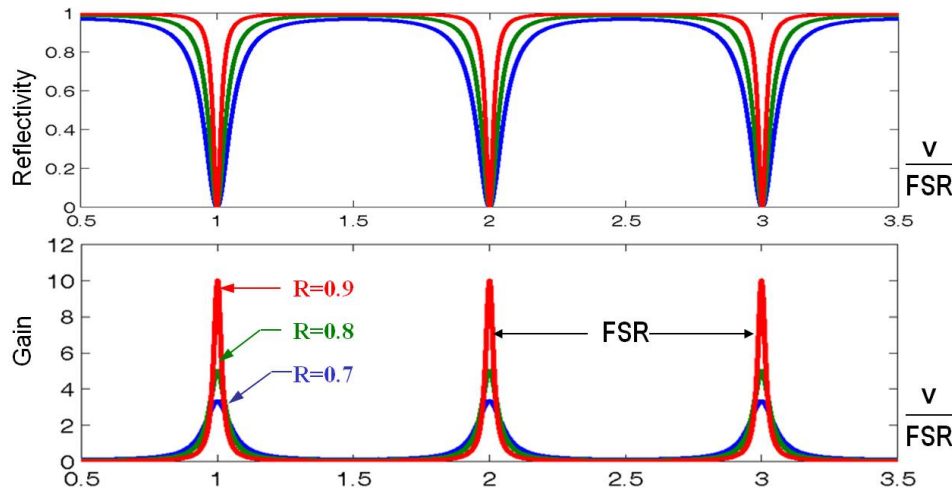


Figure 5.6 (color) Circulating and reflected power in a cavity plotted versus the resonance frequency ν is normalized to the cavity free spectral range (FSR).

$1 - R - T$, we can determine the intensity reflected by the cavity,

$$I_{ref} = I_{inc} \frac{R \left(\frac{P}{1-R} \right)^2 + 4(1-P) \frac{\mathcal{F}}{\pi^2} \sin^2 \left(\frac{\pi\nu}{FSR} \right)}{1 + 4(1-P) \frac{\mathcal{F}}{\pi^2} \sin^2 \left(\frac{\pi\nu}{FSR} \right)}, \quad (5.53)$$

This expression allows us to determine $\mathcal{R}(\nu)$,

$$\mathcal{R}^2(\nu) = \frac{R \left(\frac{P}{1-R} \right)^2 + 4(1-P) \frac{\mathcal{F}}{\pi^2} \sin^2 \left(\frac{\pi\nu}{FSR} \right)}{1 + 4(1-P) \frac{\mathcal{F}}{\pi^2} \sin^2 \left(\frac{\pi\nu}{FSR} \right)}, \quad (5.54)$$

The phase $\Phi_r(\nu)$ of the reflection coefficient $\rho(\nu)$ is deduced from equation (5.51) and can be written in the following form,

$$\tan(\Phi_r(\nu)) = \frac{T \sin \left(\frac{2\pi\nu}{FSR} \right)}{1 + R(R+T) - (2R+T) \cos \left(\frac{2\pi\nu}{FSR} \right)}, \quad (5.55)$$

As we described before, when we have a match between the laser frequency and cavity resonance frequency, we have the relation: $\nu = n \times FSR$, n is an integer. If we get closer to the resonance region, we can rewrite last relations by replacing the frequency of the incident wave ν by the frequency deviation (detuning parameter) $\Delta\nu = \nu - \nu_c$ between the resonance frequency and the laser frequency. Then we have:

$$\rho(\Delta\nu) = \mathcal{R}(\Delta\nu) e^{i\Phi_r(\Delta\nu)}, \quad (5.56)$$

with,

$$\mathcal{R}^2(\Delta\nu) = \frac{R \left(\frac{P}{1-R} \right)^2 + 4(1-P) \frac{\mathcal{F}}{\pi^2} \sin^2 \left(\frac{\pi\Delta\nu}{FSR} \right)}{1 + 4(1-P) \frac{\mathcal{F}}{\pi^2} \sin^2 \left(\frac{\pi\Delta\nu}{FSR} \right)}, \quad (5.57)$$

and,

$$\tan(\Phi_r(\Delta\nu)) = \frac{T \sin \left(\frac{2\pi\Delta\nu}{FSR} \right)}{1 + R(R+T) - (2R+T) \cos \left(\frac{2\pi\Delta\nu}{FSR} \right)} \quad (5.58)$$

The relations (5.56), (5.57) and (5.58) allow us to define a reflection coefficient of the cavity within a resonance region. When the frequency deviation (detuning parameter)

is zero ($\nu = n \times FSR$), the gain is maximum, that means the quantity of energy stored in the cavity is maximum, and when $|\Delta\nu|$ increases, the gain decreases fast (Figure 5.7). If we consider the evolution of the reflected wave's phase as a function of $\Delta\nu$ (Figure 5.7), we notice the phase is positive when $\Delta\nu > 0$ and negative when $\Delta\nu < 0$. So the phase carries an information on the frequency deviation between the cavity resonance frequency and the laser frequency sign. Moreover, if we express $\mathcal{R}(\Delta\nu)$ and $\Phi_r(\Delta\nu)$ when $\frac{\Delta\nu}{FSR}$ goes to zero (and particularly when $|\Delta\nu| < \Delta\nu_c$ where $\Delta\nu_c$ is the cavity bandwidth defined by the equation (5.48), we have,

$$\mathcal{R}(\Delta\nu) = \frac{\mathcal{F} \cdot P}{\pi}, \quad (5.59)$$

$$\Phi_r(\Delta\nu) = \frac{2\pi\Delta\nu}{FSR} \times \frac{T}{P(1-R)}, \quad (5.60)$$

In resonance region, the phase $\Phi_r(\Delta\nu)$ of the wave reflected by the cavity is proportional to the frequency deviation $\Delta\nu$.

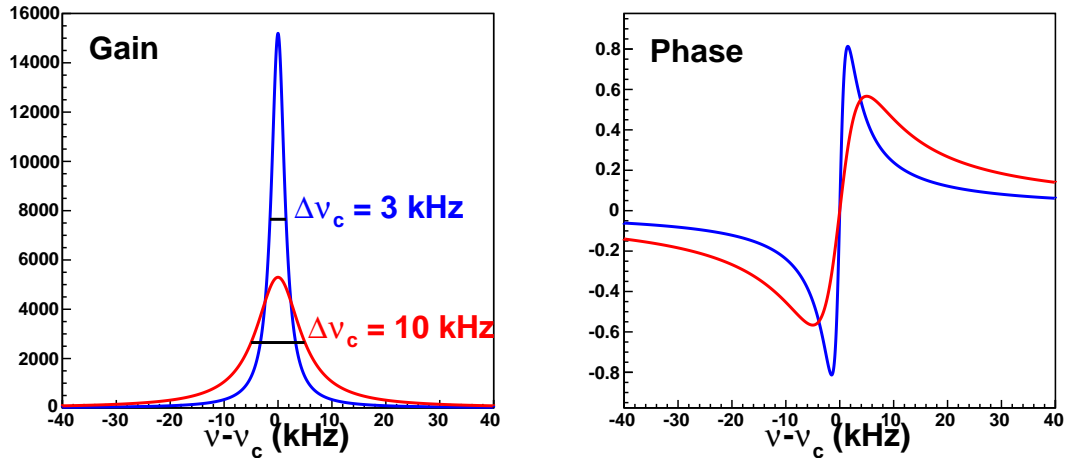


Figure 5.7 (color) Cavity gain $G(\Delta\nu)$ and phase $\Phi_r(\Delta\nu)$ of a 85 cm symmetric cavity, with two different sets of identical mirror with bandwidth of 3kHz and 10 kHz, respectively.

We will show in the next section that the frequency deviation (detuning parameter) $\Delta\nu$ varies rapidly around a resonance region, in order to keep the maximal gain in the cavity, we need a system to keep this deviation to zero. This system will use the information given by the phase of the wave reflected by the cavity.

5.2 Laser Frequency Control

5.2.1 Variations in Laser and Cavity Resonance Frequencies

We just described that the maximum gain is obtained when the frequency deviation (detuning parameter) is zero. However, in free running condition, due to thermal and mechanical noises, drift and jitter in the laser, both the laser frequency and cavity resonance frequency vary with time, so that the detuning parameter would never become zero. Therefore we need a system to allow us to establish a frequency matching between laser and cavity.

For a single-frequency laser, there is a central frequency within its frequency distribution and a quantity called linewidth which is the full width at half-maximum of this optical spectrum that quantifies it. Usually the line width of lasers without frequency stabilization can be on the order of 1 GHz. On the other hand, the laser linewidth from stabilized low-power continuous-wave lasers can be very narrow and reach down to less than 1 kHz. For almost all the lasers, the central frequency is subject to fast deviations called “jitter” and slow deviation called “drift”, depending on time.

The seed laser we use has a linewidth of $5kHz$ and wavelength equals to $\lambda = 1064nm$, that corresponds to a frequency $\nu \approx 2 \times 10^5 GHz$. For our seed laser, jitter and drift given by the manufacturer to be $30kHz/s$ and $50MHz/h$, respectively [93]. These two frequency variations are different in their nature: the first one corresponds to fast variations around the central laser frequency. The second leads to a drift of this central frequency. Compared to the value of the central frequency, these variations seem very tiny. However, we saw in equation (5.48) that a Fabry-Perot cavity defines the width of its resonance peak $\Delta\nu_c$ spaced in frequency by FSR . For average reflectivity mirrors ($R \approx 99.9\%$), $\Delta\nu_c \approx 56kHz$, and for nominal mirrors ($R \approx 99.982\%$) that we used for the Compton polarimeter, $\Delta\nu_c \approx 10kHz$.

So intrinsic drifts in laser frequency can lead to deviations that are large enough to

lose the gain in the cavity. If we take the example of the nominal cavity, a deviation of $5.0kHz$ of the laser frequency with respect to the cavity resonance frequency leads to a 50% loss of the total gain in the cavity. This problem is more and more critical as the finesse of the cavity gets bigger, because the width of the resonance peak $\Delta\nu_c$ is inversely proportional to the finesse.

We just considered the deviations between cavity resonance frequency and laser frequency by only taking into account the intrinsic laser frequency variations. However, the cavity resonance frequency also varies in time.

As we showed in equation (5.44), the cavity resonance peaks are spaced in multiple of the $FSR = \frac{c}{2L}$. Therefore, if we call ν_{res} the resonance frequency, we have,

$$\nu_{res} = n \times \frac{c}{2L}, \quad n \in \text{integer}, \quad (5.61)$$

If we take into account a variation of the cavity length ΔL due to a mechanical or thermal perturbation, we will have a relative resonance frequency variation $\Delta\nu_{res}$,

$$\frac{\Delta\nu_{res}}{\nu_{res}} = \frac{\Delta L}{L}, \quad (5.62)$$

Knowing that the laser frequency we use is around $\nu \simeq 2 \times 10^{14}Hz$, and for a resonance frequency of the same magnitude $\nu_{res} \simeq 2 \times 10^{14}Hz$, If we consider a deviation $\Delta L = 1\mu m$ for a cavity length $L = 0.85m$, we obtain then a shift of the resonance frequency of $\Delta\nu_{res} \approx 235MHz$, which is more than a free spectral range. If we compare this shift to the nominal cavity resonance bandwidth of $\Delta\nu_c = 10kHz$, we notice that a tiny perturbation in cavity length will lead to a mismatch between the resonance frequency and the laser frequency, therefore a total loss in cavity gain. In other words, if we want to have $\Delta\nu_{res} = \Delta\nu_c = 10kHz$, the largest ΔL allowed would be $4.25 \times 10^{-2}nm$. It is impossible to achieve such a tiny stability with any conventional mechanical device. Therefore, a fast feedback system is required in order to achieve this condition.

For a real system where the laser permanently drifts in frequency and we have mechanical, thermal and acoustic perturbations related to the fact that the cavity

is attached to the beam pipe of an electron accelerator, we need a system which maintains all time equality between the cavity resonance frequency and the laser frequency. We will now describe a method called feedback control, which enables us to achieve this equality in these two frequencies.

5.2.2 Feedback Control of Laser Frequency

A feedback control is an engineering technique which controls the input parameter(s) of a dynamic system to achieve a desired output over time. A feedback loop controller usually composed of a discriminator and a controller. The discriminator provides information on the deviation between values of the reference parameter and input parameter we want to control. The controller uses this deviation and modifies the value of input parameter to achieve zero deviation.

For a feedback control between the laser and optical cavity, the feedback loop can act on the cavity length through a piezo-electric transducer attached to the cavity mirror or on the laser frequency also through a piezo-electric actuator bonded to the laser crystal. In the case of the feedback control of the laser frequency, the instantaneous frequency of the laser (ν) is monitored and compared to the reference frequency (ν_c) provided by the optical cavity. The discriminator converts the optical frequency fluctuations into voltage fluctuations with a conversion gain of $D_v(\text{V/Hz})$, thus producing an error signal. This error signal is amplified and compensated in the servo circuit which has a frequency dependent gain coefficient $G(\text{V/V})$. The amplified voltage fluctuations are then fed back negatively to the laser through the actuator which converts them into frequency fluctuations with a conversion gain $A(\text{Hz/V})$. The actuator can be a piezo-electric module or a Peltier module (TEC). In this way the feedback loop monitors and actively suppresses the frequency fluctuations (noise) of the laser. Figure 5.8 illustrates a block diagram for a laser frequency feedback loop.

The free running frequency of a laser, in the absence of any fluctuation, is simply an integral multiple of the laser cavity free spectral range. There are however, sev-

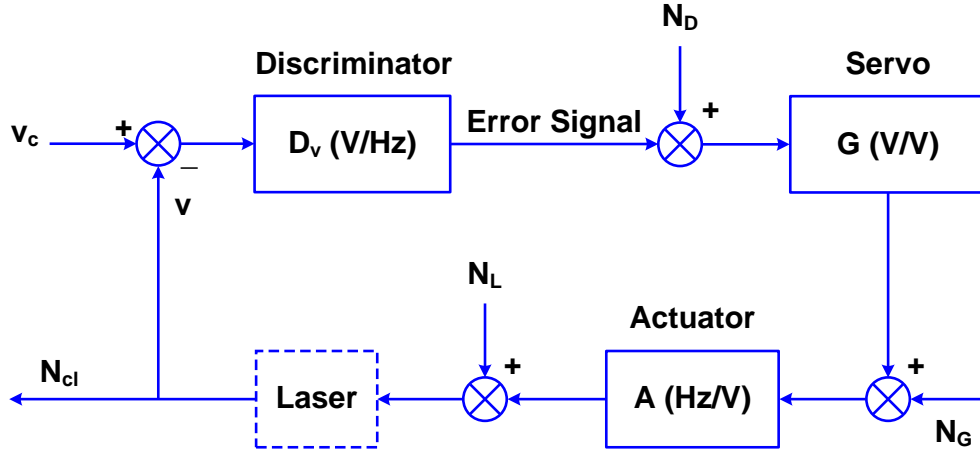


Figure 5.8 A block diagram shows a laser frequency stabilization feedback loop.

eral noise processes which perturb the frequency of the laser. Using active frequency control the spectral density of laser frequency noise can be suppressed over the bandwidth of the feedback loop. The spectral density of the frequency difference between the laser and a resonance of the cavity in closed loop, in terms of the other noise sources, is [95],

$$N_{cl} = \frac{\sqrt{N_L^2 + |A N_G|^2 + |A G N_D|^2}}{|1 + A G D_v|}, \quad (5.63)$$

where N_L is the free running frequency noise of the laser, N_G is the voltage noise in the servo amplifier, and N_D is the voltage noise in the discriminator (photodetector in the system). The photodetector gain D_v is just the slope of the error signal multiplied by the voltage response of the photodetector. For a very large servo gain, $G \gg 1$, the closed loop noise spectrum is,

$$N_{cl} \approx \frac{N_D}{D_v}, \quad (5.64)$$

and it indicates that the closed loop noise of the system is dominated by the noise in the photodetector.

A very effective technique to obtain fast frequency discrimination is through the use of an optical cavity [94]. In this technique, the instantaneous frequency of the laser

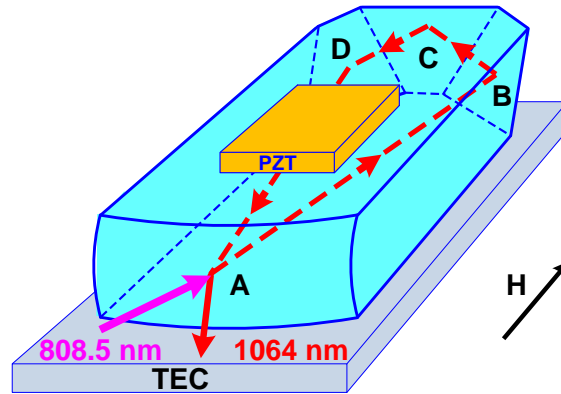


Figure 5.9 (color) A PZT transducer bonded to the top non-optical face of the Nd:YAG crystal of a non-planar ring oscillator (NPRO) laser for fast frequency actuation while the Nd:YAG crystal is placed on a Peltier module (TEC) for slow frequency variation.

is compared to the resonance frequency of the cavity and an error signal proportional to the difference is generated. The most common method by which the error signal is generated is the Pound-Drever-Hall locking techniques [97] which will be described in the next section.

According to our knowledge, the fine tunable lasers available from the industry are non-planar ring oscillator (NPRO) Nd:YAG lasers. The laser (Lightwave, model 126) we use, operates at $\lambda = 1064\text{nm}$, its Nd:YAG crystal is pumped by a GaAlAs laser diode normally emitting 810 nm is cooled by a TEC in order to emit at 808.5 nm, a highly efficient wavelength for Nd:YAG pumping. The principle of non-planar ring oscillator is shown in Figure 5.9.

The light emitted by the diode enters the Nd:YAG crystal at point A. The crystal surfaces are finely polished and coated in such a way that a total internal reflection occur at points B, C, and D on the planar surface, while there is a partial transmission at point A where the surface is curved. The crystal is surrounded by a magnetic field H to match the polarization state of the resonant mode (garnet is a magneto-optic crystal). The main advantage of such a ring laser is the reduction of heat inside the crystal, therefore results in a narrower spectral linewidth as compared to an

Nd:YAG laser with a standard linear laser cavity. The stability is obtained through the monolithic structure of the oscillator and stable output power of the diode itself.

There are two ways to tune the laser frequency:

Slow frequency tuning: The crystal temperature can be varied by applying a DC voltage to a Peltier module (TEC) under the Nd:YAG crystal. The temperature variation leads to a change in index of refraction of the crystal and in oscillator length. The effect of both leads to a change in laser frequency. It has a tuning range of tens of GHz with relatively slow time constant (1 - 10s). Its tuning coefficient A_S is 1.6 GHz/V in a $\pm 10V$ range.

Fast frequency tuning: A piezo-electric transducer (PZT) is bonded to the top, non-optical face of the nonplanar ring oscillator and an applied voltage modulates the oscillator length and therefore the frequency of the laser. The frequency of the laser can vary by tens of MHz at a rate up to 30 kHz. The tuning coefficient A_F is 3.2 MHz/V.

5.2.3 Pound-Drever-Hall Technique

As we described in equation (5.60), around resonance region, the phase $\Phi_r(\Delta\nu)$ of the reflected light is proportional to the frequency deviation $\Delta\nu$ between the laser and cavity resonance frequency. Since there is no detector which is sensitive to the phase of a laser wave, we need to find a system which converts a phase information to an intensity information. Pound-Drever-Hall (PDH) technique uses the cavity resonance frequency as a reference frequency, extracts a voltage signal (error signal) proportional to the frequency deviations of the laser against this reference, and then suppress them using feedback on either the cavity or laser [97]. Since our laser is tunable and cavity mirrors are fixed, we choose to feed this error signal back to the laser actuator and therefore lock the laser to our cavity.

The PDH technique supplies this discriminator by performing a frequency modulation of the incident laser beam into the cavity at the frequency $\frac{\Omega}{2\pi}$. This modulation

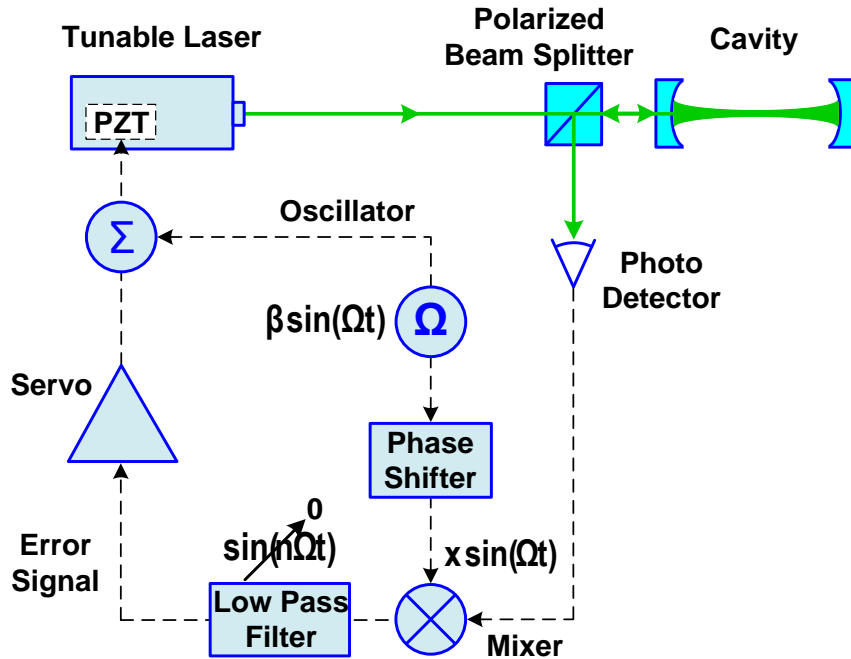


Figure 5.10 (color) Principles of Pound-Drever-Hall method. The beam reflected by the cavity is extracted from the incident beam and detected by a fast photodiode. The signal obtained is then multiplied by a demodulation signal in mixer. The electronic circuit allows to build an error signal which is summed with the modulation signal before being sent to an actuator to control the laser frequency.

creates two sidebands $\nu \pm \frac{\Omega}{2\pi}$ around the carrier frequency ν (Figure 5.11). When we have the condition: $FSR \gg \frac{\Omega}{2\pi} \gg \Delta\nu_c$, the reflected wave contains two sidebands that simply reflected without phase shift (because they are out of resonance), and a phase shifted main peak. The interferences between the main peak and the side bands create an amplitude modulated term that a photodiode can detect. The error signal is obtained by mixing photodiode's output signal with a so-called demodulation signal at the same frequency as modulation signal, but with a different amplitude and phase shifted with respect to it. An electronic filtering allows to detect only the amplitude modulated term that contains information on frequency deviation $\Delta\nu$. The obtained error signal is transferred to an electronic servo, summed with the phase modulation

signal from the modulator, and fed back to the laser frequency control system (Figure 5.10).

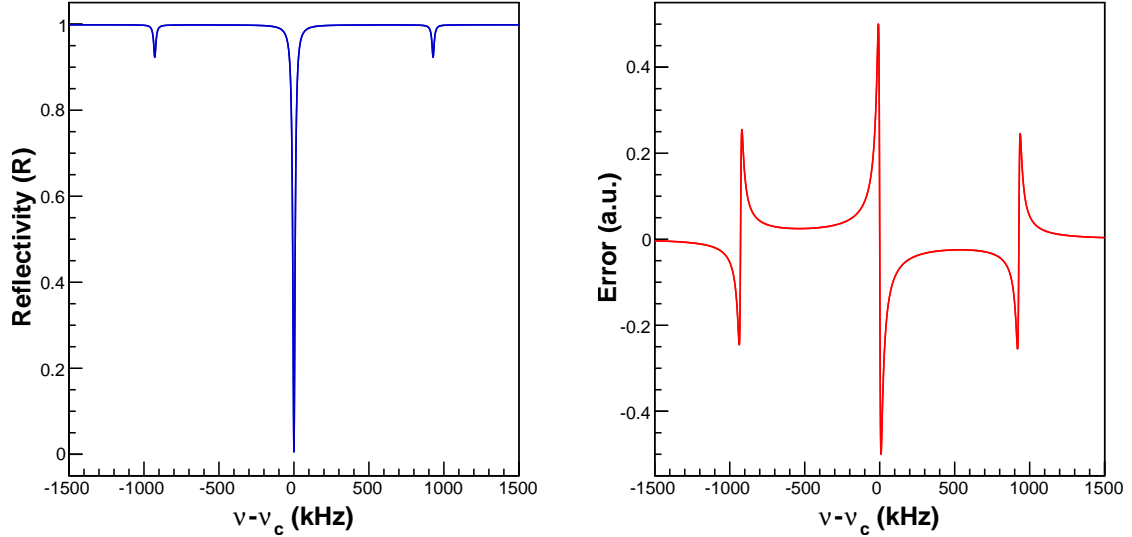


Figure 5.11 (color) The Pound-Drever-Hall error signal along (red curve) with the corresponding reflected signal (blue curve) versus the frequency deviation between the laser frequency (ν) and cavity resonance frequency (ν_c). The modulation frequency $\Omega = 928$ kHz, cavity finesse (\mathcal{F}) is around 10,000, the phase modulation index $\beta = 0.4$ and cavity length is 85 cm.

If we start with a laser beam with an electric field $E = E_0 e^{i\omega t}$. To modulate the phase of this beam, in our case, we apply a sinusoidal voltage signal $V(t) = V_m \cos(\Omega t)$ on PZT bonded onto the Nd:YAG crystal. After a phase modulation, $\phi(t) = \beta \sin(\Omega t)$, the incident electric field to the cavity becomes,

$$E_{inc} = E_0 e^{i(\omega t + \beta \sin(\Omega t))}, \quad (5.65)$$

where $\beta = \frac{2\pi A_F V_m}{\Omega}$ is the phase modulation index and A_F is the tuning coefficient of PZT. After taking care of residual amplitude modulation (RAM) [96] that determines the optimal modulation frequency Ω and modulation amplitude V_m , we have the exponential term of equation (5.65) in first order Bessel function,

$$E_{inc} \approx E_0 e^{i\omega t} \left[J_0(\beta) + 2iJ_1\beta \sin(\Omega t) \right] \quad (5.66)$$

$$= E_0 \left[J_0(\beta) e^{i\omega t} + J_1(\beta) e^{i(\omega+\Omega)t} - J_1(\beta) e^{i(\omega-\Omega)t} \right], \quad (5.67)$$

This expression shows that there are three different beams, a carrier with frequency ω and two sidebands with frequencies $\omega \pm \Omega$, contained in a phase modulated beam incident on the cavity.

In reality, in order to match the carrier frequency $\nu = \omega/2\pi$ with the cavity resonance frequency ν_c , we need to regulate temperature of the laser crystal and by this way to correct the laser frequency by the Peltier module described above. This is accomplished by providing a triangular voltage signal to the “Slow” input of the laser. This only corrects the slow drifts in laser frequency and results an occasional resonance in the cavity. However, due to jitter in laser frequency and noise in the cavity, this frequency need to be fine tuned so that there will be a frequent resonance in the cavity. This is also accomplished by a triangular voltage signal with an amplitude of $\pm 10V$ send through a function generator to the “FAST” input of the laser so that the PZT bonded onto the laser crystal scans the laser frequency. When there is a resonance, we will have voltage signals reflected from and transmitted through the cavity shown as in Figure 5.11 that are detected by a pair of fast photodiodes, respectively. In this procedure, we have three signals (Modulation, Slow Scan and Fast Scan) being sent to the laser and it is called the “open loop” mode, because the feedback loop is not closed and there is no feedback to the laser.

For a small modulation index ($\beta < 1$), most of the intensity is in the carrier I_c and first-order sidebands I_s ,

$$I_0 \approx I_c + 2I_s, \quad (5.68)$$

where $I_0 = |E_0|^2$ is the total intensity of the beam and I_c and I_s are given by,

$$I_c = J_0^2(\beta)I_0, \quad (5.69)$$

$$I_s = J_1^2(\beta)I_0, \quad (5.70)$$

When the cavity is in resonance, only the carrier enters the cavity and the sidebands are simply reflected by a mirror of well known reflectivity R . The reflected field is then the incident field, E_{inc} , multiplied by the complex reflection coefficient, $F(\omega)$, of

the cavity,

$$E_{ref} = E_0 \left[F(\omega) J_0(\beta) e^{i\omega t} + F(\omega + \Omega) J_1(\beta) e^{i(\omega + \Omega)t} - F(\omega - \Omega) J_1(\beta) e^{i(\omega - \Omega)t} \right], \quad (5.71)$$

the complex reflection coefficient $F(\omega)$ of symmetric cavity with no losses is,

$$F(\omega) = \frac{\sqrt{R} \left[\exp \left(i \frac{\omega}{FSR} \right) - 1 \right]}{1 - R \exp \left(i \frac{\omega}{FSR} \right)}, \quad (5.72)$$

where $FSR = \frac{c}{2L}$ is the free spectral range of the cavity of length L . The intensity of the reflected beam $I_{ref} = |E_{ref}|^2$ is,

$$\begin{aligned} I_{ref} = & I_c |F(\omega)|^2 + I_s \left(|F(\omega + \Omega)|^2 + |F(\omega - \Omega)|^2 \right) \\ & + 2\sqrt{I_c I_s} \left(\text{Re} \left[F(\omega) F^*(\omega + \Omega) - F^*(\omega) F(\omega - \Omega) \right] \cos \Omega t \right. \\ & \left. + \text{Im} \left[F(\omega) F^*(\omega + \Omega) - F^*(\omega) F(\omega - \Omega) \right] \sin \Omega t \right) \\ & + (2\Omega \text{ terms}), \end{aligned} \quad (5.73)$$

Around resonance region, in the case that $\frac{\Omega}{2\pi}$ is large compared to the cavity bandwidth $\Delta\nu_c$, we can assume that the side bands are totally reflected, $F(\omega \pm \Omega) \approx -1$, and equation (5.73) becomes,

$$I_{ref} \approx I_c |F(\omega)|^2 + 2I_c - 4\sqrt{I_c I_s} \text{Im}[F(\omega)] \sin \Omega t + (2\Omega \text{ terms}), \quad (5.74)$$

The reflection signal is mixed with the same but phase shifted modulation signal and then go through a low-pass electronic filter centered on modulation frequency $\frac{\Omega}{2\pi}$. This will filter out the constant and higher order terms of Ω in the expression and therefore allows us to extract the error signal,

$$\epsilon = 2\sqrt{I_c I_s} \text{Im} \left[F(\omega) F^*(\omega + \Omega) - F^*(\omega) F(\omega - \Omega) \right], \quad (5.75)$$

A typical error signal is plotted in Figure 5.11. The slope of the error signal (Figure 5.12) around resonance region is found by approximating the reflection coefficient $F(\omega)$ for a high finesse cavity ($\mathcal{F} \approx \pi/(1 - R)$),

$$F(\nu) = 2i \frac{\Delta\nu}{\Delta\nu_c}, \quad (5.76)$$

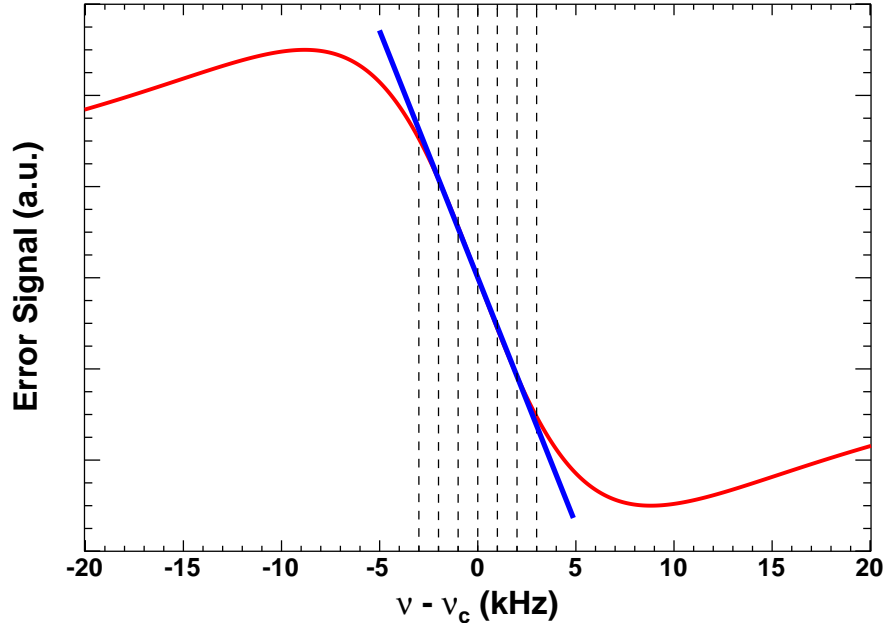


Figure 5.12 (color) The Pound-Drever-Hall error signal ϵ (red curve) versus the frequency deviation between the laser frequency ν and cavity resonance frequency ν_c . The slope (blue curve) shows the proportionality constant D . The modulation frequency $\Omega = 928$ kHz, cavity finesse (\mathcal{F}) is around 10,000 and the phase modulation index $\beta = 0.4$.

where $\Delta\nu = \nu - \nu_c$ is the frequency deviation of the laser frequency ν from the cavity resonance frequency ν_c in Hz . The error signal can now be proportional to $\Delta\nu$ by following relation,

$$\epsilon = -D\Delta\nu, \quad (5.77)$$

$$D = \frac{8\sqrt{I_c I_s}}{\Delta\nu_c}, \quad (5.78)$$

where $\Delta\nu_c$ is the cavity bandwidth. It is important to note that this linearity is only valid between the interval of $\pm\frac{\Delta\nu_c}{2}$. The proportionality constant D defines the ultimate noise limit for a given system. It also indicates that for a narrower bandwidth (higher finesse) cavity the corresponding proportionality constant D is larger so that the required noise level in the feedback loop is lower and therefore harder to lock [97].

As we described above, in the “open loop” mode, the error signal is generated after

the low-pass filter but the feedback loop remains open. When there is a resonance and the intensity of the reflected resonance peak below certain limit (set by us), the servo loop will be activated and the triangular voltage ramp signals applied on the laser PZT and TEC will stop instantaneously. We call this process the “closed loop” mode.

In the next section, we will describe the complete system composed of a cavity and its feedback electronics and control units.

5.3 Description of the Cavity System

We will first describe the mechanical structure of our cavity system and then explain the feedback electronics and control systems.

5.3.1 Mechanical Design of the Cavity

The original cavity in Hall A was built by Saclay. It was a monolithic cavity with fixed cavity mirrors. The two mirrors forming the cavity are aligned by design due to high tolerances applied on the cavity enclosure and the mirror’s substrate. It consists of two mirrors of diameter $D = 10.0mm$ and radius of curvature $R = 0.5m$ placed parallel to each other at a distance of $L = 0.85m$ [8]. In order to keep the interaction luminosity high between the electron and photon beams, the crossing angle α_c chosen to be $23.5mrad$. This makes the cavity mirrors stay very close to the electron beam (the distance between the electron beam and the mirror edge is 5 mm), and the performance of the mirrors degrades over time. Therefore, the cavity, which is placed along the beam line, needs to be removed completely to replace the mirrors. This is to be followed by a tedious task of bench-top alignment. During this process, the mirrors are susceptible to misalignment due to operator error or manufacturing flaws that exist in the mirror itself. After this, the cavity has to be replaced in the beam line and the laser, re-aligned to the cavity. This procedure requires a few days of vacuum

and alignment work. If the alignment is disturbed during this procedure, the entire task needs to be repeated. Hence, a cavity with adjustable mirrors, in-situ mirror replacement and in-situ alignment method has better advantages over a monolithic cavity. To keep the mirrors in position and ensure their alignment, it is possible to use adjustable frames [42].

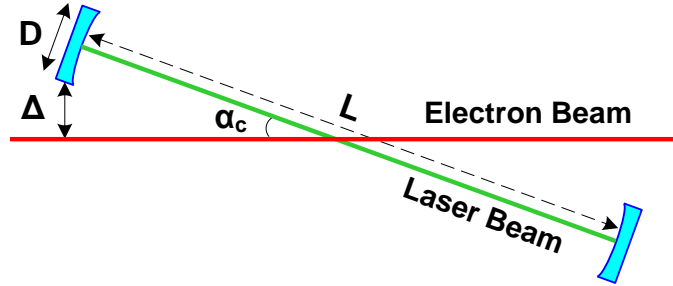


Figure 5.13 (color) Schematic of crossing angle between the laser beam and electron beam.

The geometry of the cavity is determined by the total distance (L) between the two mirrors, the radius of the curvature (R) of the mirrors and the crossing angle (α_c) between the laser beam and electron beam. The constraint defined by small crossing angle α_c is,

$$\alpha_c \approx \frac{(2\Delta + D)}{L}, \quad (5.79)$$

where D is the diameter of the mirror and Δ is the gap between the electron beam axis and the edge of the mirror. The small crossing angle is aiming to increase the electron photon interaction luminosity defined by equation (3.26). Figure 5.13 illustrates the crossing of the laser and electron beams.

We chose to keep the original cavity length $L = 0.85m$ and designed adjustable cavity frames that houses two cavity mirrors. The cavity mirrors are manufactured and coated in a company called Advanced Thin Films (ATF). The substrate is made of fused silica (SiO_2) with a thickness of $4mm$, its diameter is $D = 7.75mm$, and its radius of curvature is $R = 0.5m$. The coating is made of alternating dielectric quarter-wave layers of SiO_2 ($n = 1.47$) and Ta_2O_5 ($n = 2.1$). Figure 5.14 shows a

simplified mirror geometry.

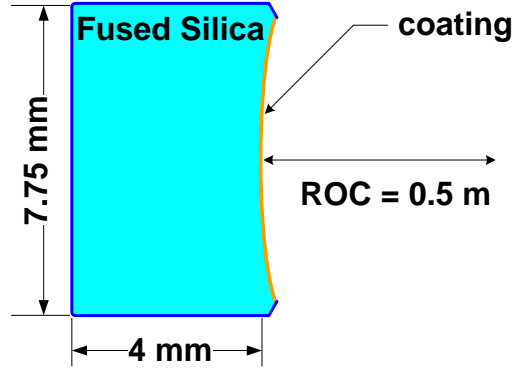


Figure 5.14 (color) Schematic of cavity mirror geometry.

With this design the crossing angle is $\alpha_c = 24.0\text{mrad}$, the σ beam size at the CIP should be $87\ \mu\text{m}$, and the gap between the electron beam and mirror edge $\Delta = 6.125\text{mm}$. The small crossing angle also gives some constraints to the mirror diameter. This means we must choose a mirror diameter as small as possible. However, the minimum diameter of the mirrors can not be too small as compared to the laser beam spot size on them. Due to a mode matching requirement between the laser beam and cavity, the size of the laser beam on the mirrors depends on the choice of cavity length (L), mirror radius of curvature (R) and laser wavelength (λ). Given the values of L , R and λ , we should have a beam size of $\sigma = 224\ \mu\text{m}$ on the mirrors.

The mechanical scheme of the cavity is shown in Figure 5.15. The cavity along with all the other optical elements are mounted on an optics table with a size of $1500\text{mm} \times 1200\text{mm}$ from Newport. This table is placed on a laminar flow damping system consists of four pneumatic posts with auto-leveling valves to isolate the vibrations from the ground [98]. In order to ensure the thermal and mechanical stability, a frame consists of three cylindrical rods and two vertical plates with an octagonal cutout forms the backbone of the cavity structure. The whole structure is made of Invar, FeNi36, a nickel steel alloy known for its uniquely low coefficient of thermal expansion ($\alpha_T = 1.2 \times 10^{-6}\text{K}^{-1}$). The optics table is located inside a small room

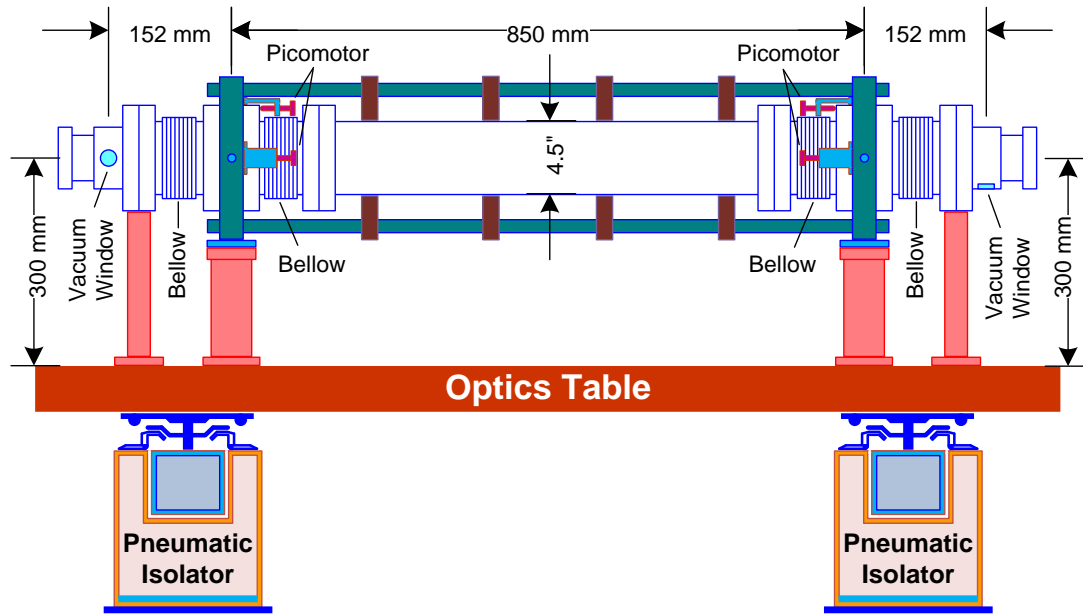


Figure 5.15 (color) A front view of the cavity sitting on an optics table with pneumatic isolators.

equipped with a laminar flow fan filter unit.

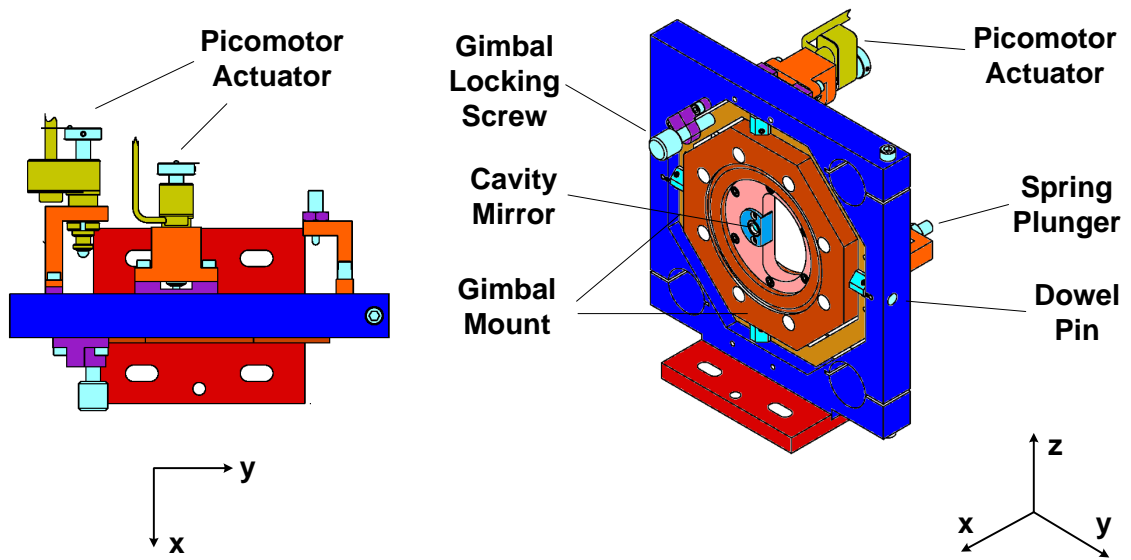


Figure 5.16 (color) The structure of gimbal mounts used for cavity mirror alignment.

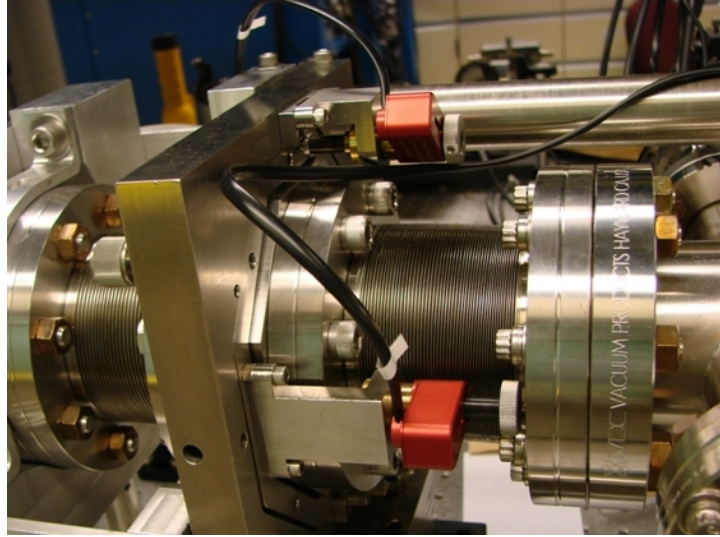


Figure 5.17 (color) Two picomotors are mounted to a pair of gimbal mounts that are used to align a cavity mirror on one side of the cavity.

A cylindrical vessel made of stainless steel with a diameter of 4.5 inches (Figure 5.15) connected to two soft bellows on either side of the gimbals forms the vacuum chamber. The bellows give gimbals a freedom to move freely when they are adjusted by piezo actuators and the whole structure is under vacuum ($\sim 10^{-9}$ Torr). The cavity mirror is mounted on a mirror holder with a fine threaded retaining ring and the mirror holder is attached to a set of two octagonal shaped gimbal mounts that are made of Invar (Figure 5.16). The gimbal mounts are supported by four stainless steel cylindrical bearings from C-Flex that form two axes for each gimbal mounts that allow the gimbals to rotate around them. The mirror holder is machined such that the optical axes of mirror lies on the same axes as the gimbals. The bearings have a diameter of 0.25 inch and length of 0.4 inch, and each can support a load up to 100 lbs. Two remote controlled motorized piezo actuators (picomotors) from Newfocus attached to the gimbal mounts by two “L” shaped brackets used for aligning the mirrors by rotating each gimbal around its axes in a plane transverse (horizontal and vertical) to the laser beam direction. A pair of counteracting spring plungers attached to the gimbals are also hold by two “L” shaped brackets keep the alignment in position. Each spring can support a load up to 13 lbs. According to factory

specification [99] the picomotors have an angular resolution of $< 1.0\mu rad$ and a linear resolution of $< 30nm$ under a resistive force of 5 lbs. We found that, under a vacuum load, this number is small and the alignment reproducibility is poor. The picomotors are not servo motors and their drivers are interfaced to EPICS [100] slow control system that allows us to give a pre-calibrated step size when we want to tilt the mirrors.

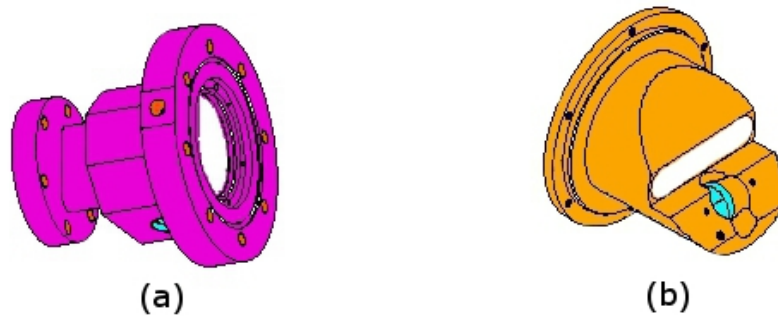


Figure 5.18 (color) (a) Technical drawing of the stainless steel flange with the vacuum window is welded to it. (b) Technical drawing of the aluminum mount that holds a 0.5 inch turning mirror oriented at 45° with respect to the incident laser beam.

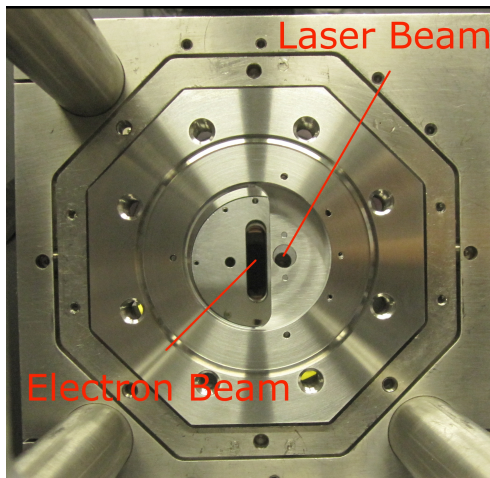


Figure 5.19 (color) A slot with an opening of $1cm$ in the aluminum mount allows the electron beam passes through and crosses with the laser beam at the center of the cavity.

The vacuum windows (W_e and W_s in Figure 5.30) are $3mm$ thick and 0.7 inch

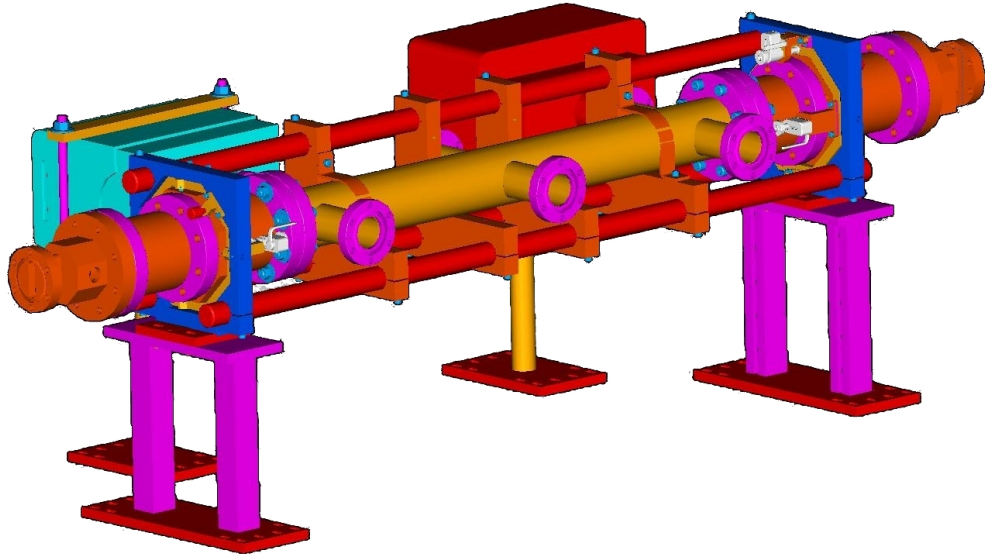


Figure 5.20 (color) Technical drawing of the cavity with two ion pumps attached to it.

diameter fused silica substrates. They allow the laser beam to enter and exit the cavity via a pair of 0.5 inch turning mirrors (M_e and M_s in Figure 5.30) oriented at 45° with respect to the incident laser beam. The vacuum windows are anti-reflection coated for $532nm$ and welded to a stainless steel flanges according to a special procedure called glass-metal soldering. The flanges connect the beam pipe to the outer bellows of the cavity gimbal. Each of the 45° turning mirrors mounted to an aluminum holder that is attached to the stainless steel flange (Figure 5.18). The aluminum holders have a slot of $4cm$ long and $1cm$ wide (Figure 5.19) that allows the electron beam to pass through and steered by a pair of dipoles in Compton chicane at the time of improving the interaction luminosity by “vertical scan”. When the cavity is installed in the beam line, the stainless steel flanges are connected to the beam pipe by another soft bellow that is used to isolate the vibrations from the rest of beam pipe.

Inside the cavity, the vacuum is maintained by two ion pumps (Figure 5.20) and the pressure is measured by a vacuum gauge attached to the cavity. The heavy ion pumps are hold by two posts attached to the optics table and isolated from the cavity by two soft bellows. Figure 5.21 shows the cavity installed in Hall A accelerator

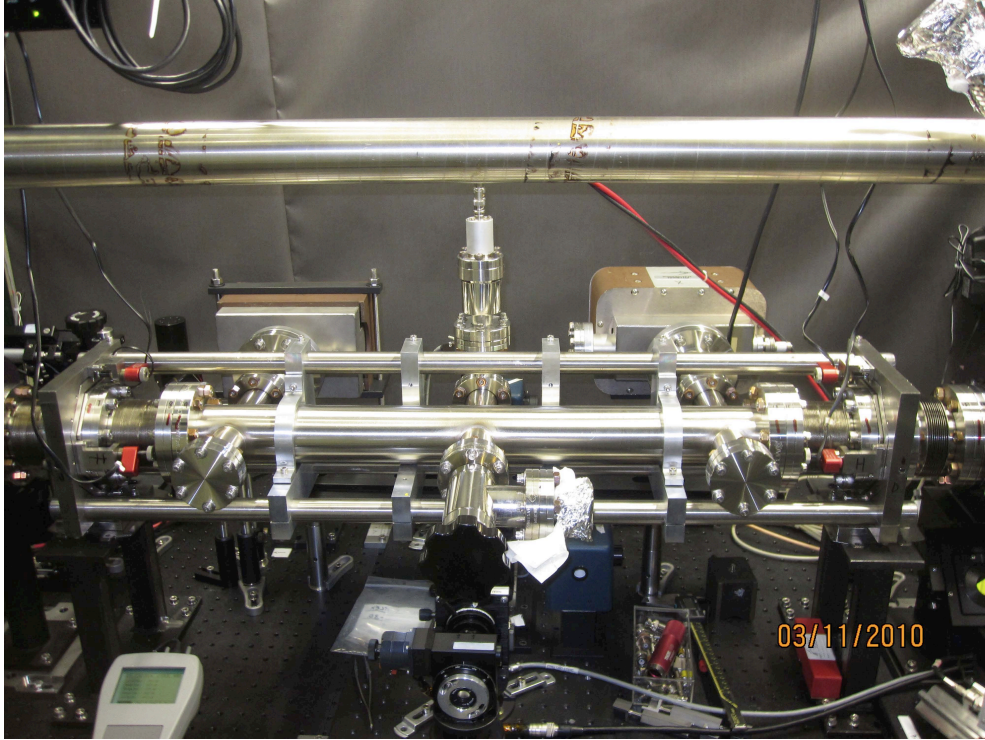


Figure 5.21 (color) A picture shows the cavity installed in Hall A accelerator tunnel at JLab. The electron beam pipe above the cavity is used for a straight beam when the Compton chicane is not used.

tunnel at JLab.

5.3.2 The Control System

Almost all of the optical elements, the lasers and the locking electronics are interfaced to a remote controlled system. The electronic feedback system that uses the Pound-Drever-Hall method has been designed and built by SIG group of Saclay based on the experiences of PVLAS group [101]. It is the same old system that has been used for the locking of the previous IR laser based system [8]. The complete system is composed of the following elements:

Electronics specific to the control loop, the ramp generator, the sinusoidal signal generator (for frequency modulation), the oscilloscope and the workstation are situated in the Hall A Counting House.

The lasers (seed laser, PPLN and fiber amplifier), stepper and servo motors, and their control units, the photodiodes, the preamplifiers and the cavity are situated on the optics table in the tunnel.

The VME crate, used for controlling the electronics, is located in Hall A of Jefferson Lab. The electronics are completely controlled from a workstation in the Counting House, with the help of an interface card. This card permits us to transport numerical signals to the optics table area which is about 100 meters from where the crate is located.

An automatic switching system from “open-loop” mode to “closed-loop” mode around the cavity resonance region permits the system to function automatically. It consists of an electronic circuit and an EPICS program that manages the laser temperature scan.

Figure 5.22 illustrates a functional view of the feedback electronics which consists of the following modular cards:

The “PREAMP” card amplifies signals from the PDR and PDT photodiodes. A 10 V peak-to-peak ramp, together with the 50 mV amplitude and $\Omega = 928kHz$ modulation, is supplied on the laser PZT. The photodiodes are held at a continuous voltage level of 5 V. The current from the photodiodes is transformed into a voltage signal via a transimpedance amplifier that allow us to transmit signals across 100 meters of coaxial cables.

The “ACQSIGN” card builds the error signal from the signal produced by the photodiode preamplifier. A band-pass filter is applied on the reflected signal before it mixed with the modulation signal at frequency Ω and amplified. This filter, centered on Ω , eliminates all harmonics of the modulation frequency Ω except the fundamental one. The value of Ω was determined by minimizing the laser Residual Amplitude Modulation (RAM) [43]. The amplification gain is controllable from the command station. The error signal is then used to build the feedback signals supplied on the fast and slow channels.

The “SERVO” card creates the fast and slow feedback signals applied to the laser

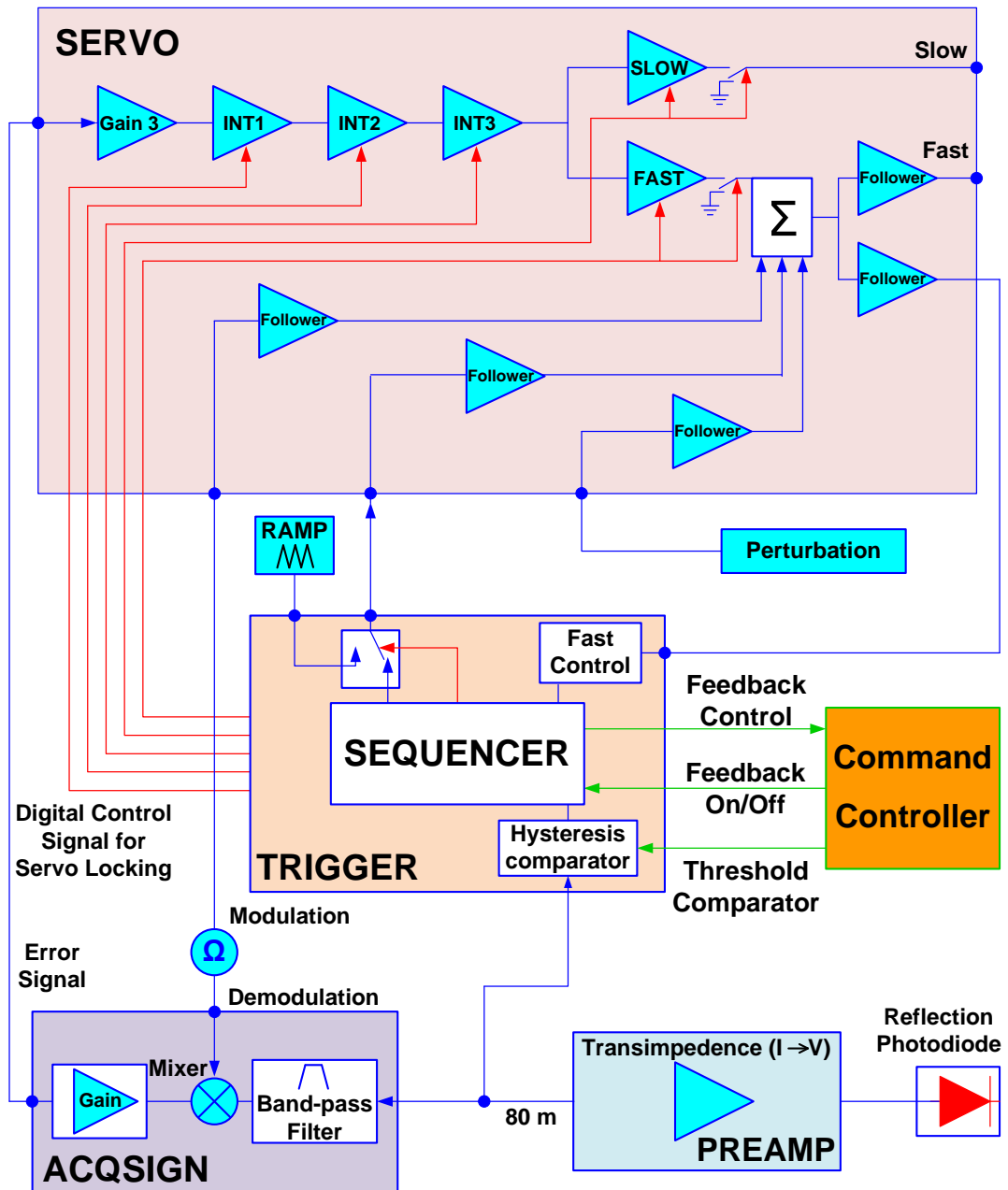


Figure 5.22 (color) Functional view of the feedback electronics built by Saclay (redrawn from [43]).

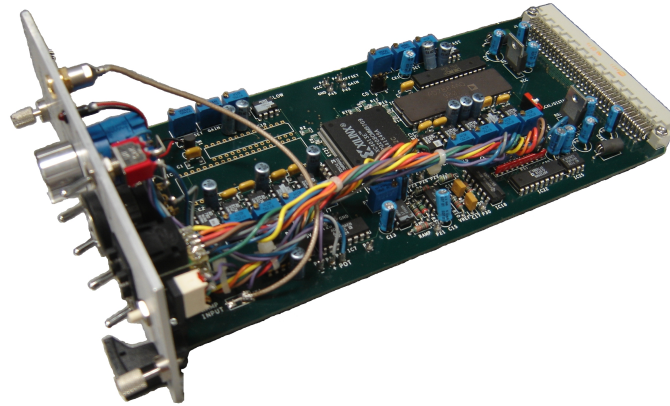


Figure 5.23 (color) A printed circuit board (PCB) layout of the feedback electronics built by Saclay used for cavity locking.

frequency. The error signal is injected into a series of three separate integrators common to the Slow and Fast control loops. The two control modes play complementary roles: the slow mode is for compensating the slow drift in laser frequency while the fast mode allows the efficient reduction of the laser frequency jitter. The output signals of these two modules are applied directly to the two laser control ports.

The “TRIGGER” card switches between the open loop and closed loop modes. The correction signals must be applied only when the laser frequency is close to a cavity resonance frequency. To decide when the corrections must be applied, the reflected signal is also sent to another module called “hysteresis comparator” where, according to its amplitude, the system is switched between the “closed loop” and “open loop” modes. In the “open loop” mode, the corrections to the laser frequency are not sent to the laser PZT whereas in the “closed loop” mode, these slow and fast correction signals are sent to the laser and the ramp is switched off. Figure 5.24 illustrates the automatic locking procedure by this card.

A trigger threshold $V_{threshold}$ is regulated from the control station based on the intensity of the reflection signal monitored by an oscilloscope. The release signal V_{DC} is placed 100 mV above $V_{threshold}$. When the laser frequency crosses a resonance, the reflection signal from the PDR photodiode displayed as a drop in voltage and we call it the “reflection dip”. When the “reflection dip” below $V_{threshold}$, the “TRIGGER” card

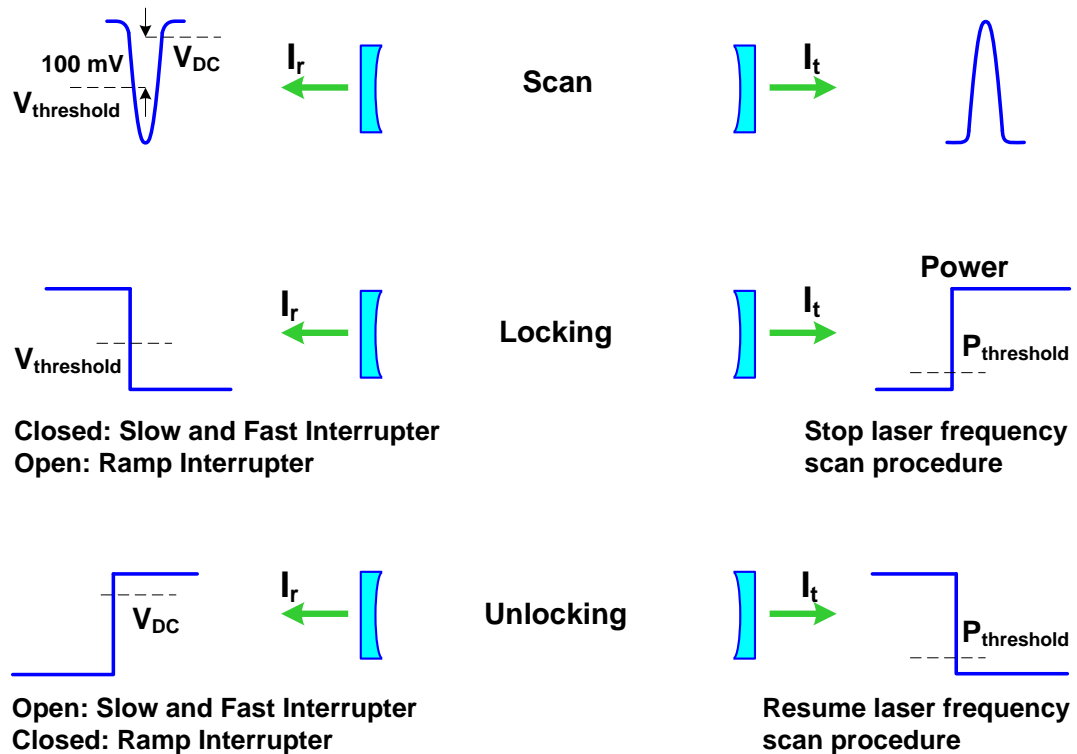


Figure 5.24 (color) A schematic illustration of automatic locking procedure of cavity. (redrawn from [43]).

sends the signal to close the loop that results an interruption of the Slow ramp at the output of the Fast and Slow integrators (Figure 5.22). The sequencer automatically achieves frequency agreement when the laser frequency finds itself near a resonance frequency. To cross the resonance, a voltage ramp must be applied to the laser PZT via the Fast input in the “open loop”. When the loop is closed, if the photodiode signal (PDR) climbs above V_{DC} , then the inverse operations are performed. If the laser frequency is far from the frequency range of the Fast ramp (10 V correspond to $FSR/2 \approx 45\text{ MHz}$), an EPICS program in the system applies a slowly varying triangular voltage ramp to a Peltier module attached to the laser crystal via laser’s Slow input until the frequency crosses the resonance. When the loop is closed, power builds up in the cavity. The laser frequency scans are stopped when the power detectors (S_1 and S_2 in Figure 5.25) at the cavity exit measures a nonzero power.

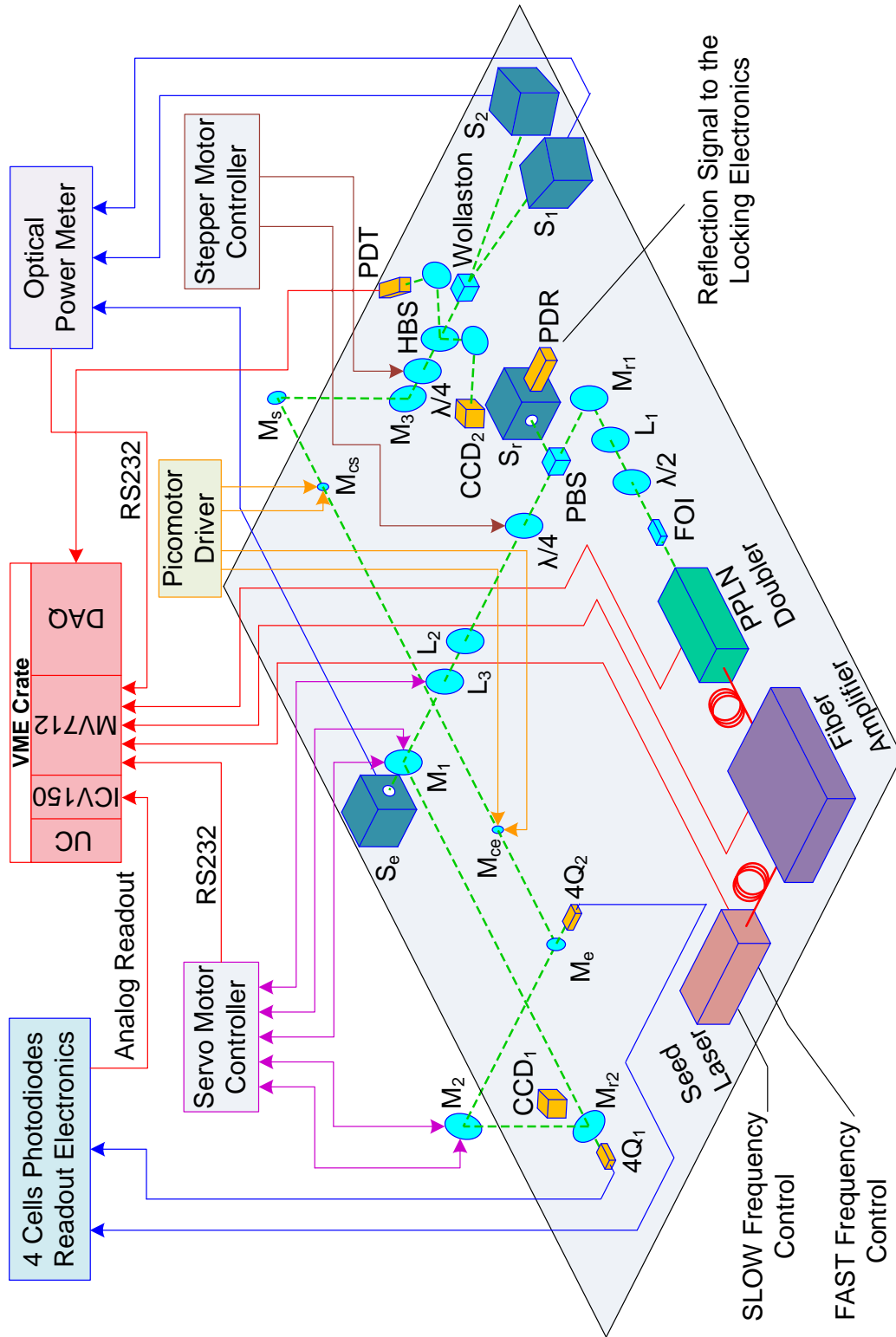


Figure 5.25 (color) A functional view of the cavity system (adapted from [8]).

The “Command Controller” module is part of the slow control program. It is used for regulating and activating the entire system from the work station in Counting House. This includes the optical elements, as well as the electronic controls. It allows the real-time control of analog and digital inputs and outputs to the various crates and modules via the EPICS interface. A VME crate in Hall A takes the following cards: an ICV150 card (digital-analog converter ADAS) that measures the voltages of the control signals (PDR, PDT, fast ramp, slow ramp); an ICV196 card that provides the digital interface between the electronic-card sequencer and the control screens by sending and receiving TTL signals; an MV712 card that allows RS232 commands to control devices such as the laser, PPLN temperature controller and fiber amplifier. With the help of “Command Controller” module we can control the entire locking assembly from a control station with the following functionality: threshold voltage level $V_{threshold}$; the servo loop gain; the state of the feedback loop and integrators (ON/OFF); and the laser frequency scan program. Figure 5.25 shows a functional view of the cavity system with control units that are connected to optical elements and lasers.

5.4 Experimental Procedures

In chapter 3, we presented very briefly the optical setup of the Compton polarimeter. Previously, we explained the technique to achieve power amplification inside the cavity. In order to achieve the highest possible cavity gain, the laser beam needs to be shaped appropriately required by the cavity geometry so that it couples to the cavity with most of its power before gets amplified in a fundamental mode. Except for that, there are also some additional conditions, such as the incoming beam needs to be very well aligned with respect to the cavity optical axis, and two cavity mirrors have to be highly parallel with respect to each other.

Characterizing and understanding the cavity mirrors are as important as getting the maximum cavity gain. Because intra cavity parameters are inaccessible for a

measurement, therefore there is an indirect method to estimate them.

In this section, we will describe techniques related to these procedures.

5.4.1 Cavity Mode Matching

Cavity Optics

Light trapped in a cavity will reflect multiple times from the mirrors, and due to the effects of interference, only certain modes which are reproduced on every round-trip of the light through the cavity are the most stable and will be sustained, the others being suppressed by destructive interference. The most common types of optical cavities consist of two facing plane (flat) or spherical mirrors. The geometry and length of the cavity require the incoming Gaussian beam to be matched in order to have resonances. In other words, the wavefront radius of curvature of the Gaussian beam must be equal to the radius of the curvature of the one of the mirrors in order to minimize losses by diffraction.

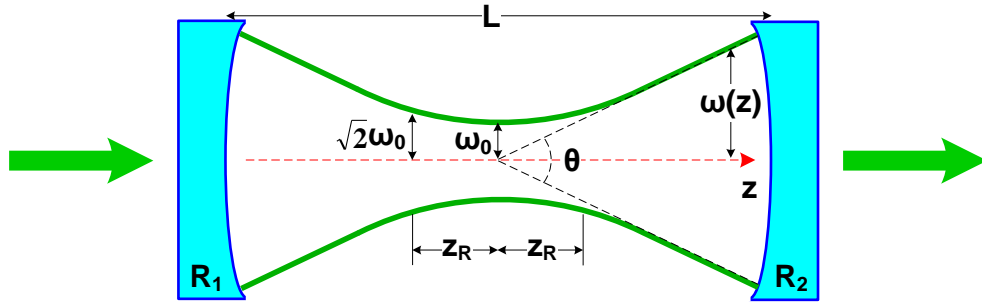


Figure 5.26 (color) A Gaussian beam in a cavity.

For a Gaussian beam confined in a cavity with two curved mirrors of radii of curvature R_1 and R_2 , and a length L (see Figure 5.26), the wavefront radius of curvatures $R(z_1)$ and $R(z_2)$ can be calculated by equation (5.11),

$$R(z_1) = z_1 \left[1 + \left(\frac{z_R}{z_1} \right)^2 \right] = -R_1, \quad (5.80)$$

$$R(z_2) = z_2 \left[1 + \left(\frac{z_R}{z_2} \right)^2 \right] = +R_2, \quad (5.81)$$

where $z_2 - z_1 = L$ and z_R is the Rayleigh range. For a symmetric cavity with $R_1 = R_2 = R$, we have $z_2 = -z_1$ and the beam waist w_0 will locate at the center of the cavity, and if we substitute z_R with L and R in equation (5.9), we have,

$$w_0 = \left(\frac{\lambda L}{2\pi}\right)^{\frac{1}{2}} \left(\frac{1+g}{1-g}\right)^{\frac{1}{4}}, \quad (5.82)$$

where $g = 1 - \frac{L}{R}$ is the cavity stability parameter. It is obvious that when parameter g is in range $-1 \leq g \leq 1$, the Gaussian beam spot sizes can exist. In other words, for a cavity with two mirrors with radius of curvature R and spacing L , when g is within that range, it forms a stable periodic focusing system for optical rays. From equation (5.82), we can also determine the beam size on cavity mirror face,

$$w_1 = w_0 \sqrt{\frac{2}{1+g}}, \quad (5.83)$$

In our cavity, $R = 0.5\text{m}$, $L = 0.85\text{m}$ therefore the stability factor $g = -0.7$. The beam sizes (4σ or $1/e^2$) required at the center of the cavity and on the mirrors are $w_0 = 348\mu\text{m}$ and $w_1 = 896\mu\text{m}$, respectively. Due to the special requirement for the cavity waist size, our cavity was chosen between a concentric and confocal cavity.

Power Loss Due to Mode Mismatch

Misalignment of laser beam with respect to aligned cavity mirrors breaks axial symmetry inside the cavity and leads to the excitation of higher order modes. Therefore the fundamental Gaussian mode is attenuated and the power inside the cavity is reduced.

As shown in Figure 5.27, there are two independent geometrical misalignments: a shift Δ between the cavity optical axis and the laser beam axis, an angular tilt α between the laser beam axis and the cavity axis. For a small misalignment, TEM_{10} will be excited (Figure 5.2), and the power losses $\Delta P/P$ ($\Delta P = P_0 - P_{in}$, P_0 is the power coupled to the cavity without any mismatch) due to axial Δ and angular α

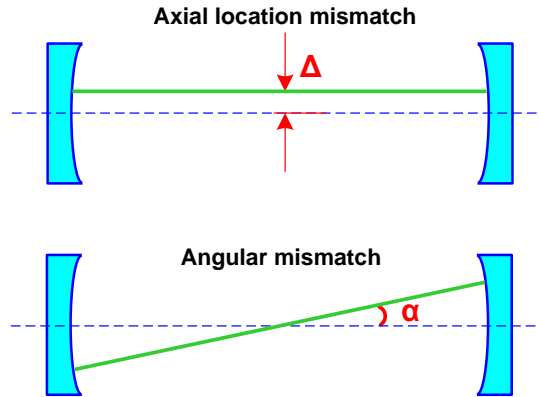


Figure 5.27 (color) A schematic illustration of axial and angular mismatch of the laser to the cavity.

mismatch can be calculated as [102, 103],

$$\frac{\Delta P}{P} = \left[\frac{\alpha \pi w_0}{\lambda} \right]^2, \quad (5.84)$$

$$\frac{\Delta P}{P} = \left[\frac{\Delta}{w_0} \right]^2, \quad (5.85)$$

For the case of the cavity we have installed, the cavity waist size required is $w_0 = 348 \mu\text{m}$, and for a power loss $\Delta P/P$ of 1%, the required tolerances for Δ and α are $35 \mu\text{m}$ and $50 \mu\text{rad}$, respectively.

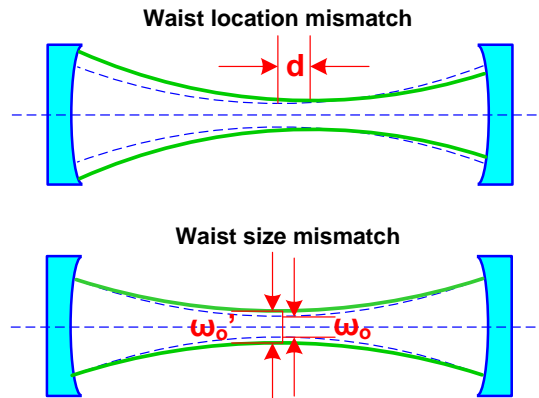


Figure 5.28 (color) A schematic illustration of waist size and location mismatch.

There is also a mode mismatch due to mismatches in laser and cavity waist sizes

and locations which can cause power losses in the laser beam coupling to the cavity (Figure 5.28). When these mismatches are present, LG₁₀ mode will be excited (Figure 5.3). In first order one gets [102, 103],

$$\frac{\Delta P}{P} = \left[\frac{\Delta w}{w_0} \right]^2, \quad (5.86)$$

$$\frac{\Delta P}{P} = \left[\frac{\lambda d}{2\pi w_0^2} \right]^2, \quad (5.87)$$

where $\Delta w = w'_0 - w_0$ is the mismatch in waist sizes between the laser and cavity, d is the shift of the laser waist location with respect to the cavity waist location and λ is the laser wavelength.

Theoretically one can model the power loss due to mismatches in waist sizes and locations. Figure 5.29 shows the coupling coefficient of fundamental mode (TEM₀₀) to the cavity versus mismatch in waist sizes and locations of the laser and cavity.

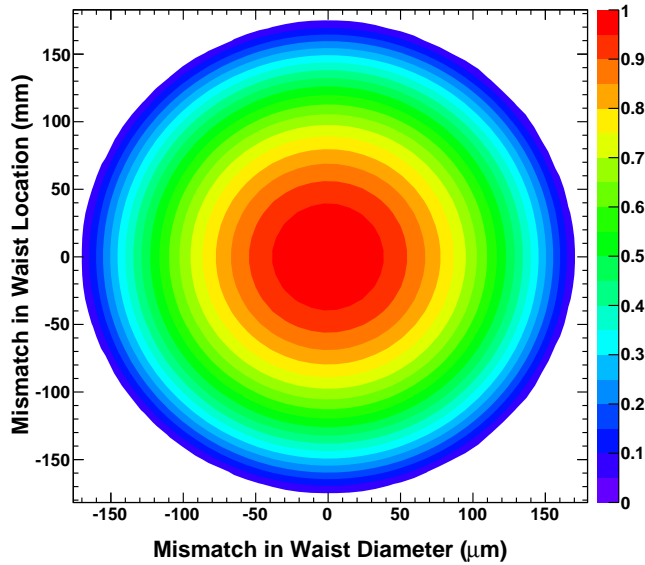


Figure 5.29 (color) A counter plot shows the coupling coefficient of fundamental mode (TEM₀₀) to the cavity versus mismatch in waist sizes and waist locations of the laser and cavity.

Mismatches from alignment, waist size and locations are always coupled together. The effect is loss of coupling in the fundamental mode so that there is less power

available for amplification in the cavity and results to a smaller amplification gain.

Astigmatism and ellipticity of laser beam are also the causes of mode mismatch. Since the optical cavity is symmetric in both direction (x : horizontal and y : vertical) and optimized for one waist size and location, these effects also can excite higher order modes such as TEM₂₀ (Figure 5.2). These effects have been evaluated in [104]. If we define the ellipticity of a laser beam with $\beta = \frac{w_y}{w_x}$, the relative power loss due to this ellipticity is,

$$\delta P = \frac{\beta}{1 + \beta^2} \left(\frac{\beta^2 - 1}{\beta^2 + 1} \right), \quad (5.88)$$

This power loss can be reduced further by using a pair of cylindrical lenses that make the beam spot more circular and also reduce the astigmatism as well.

Mode Matching of Laser Beam to the Cavity

As we described above, the laser and cavity mirrors not only have to be highly aligned to each other but also have to be matched in waist sizes and locations in the cavity. This will ensure that the laser beam is focused at the center of the cavity with the correct size (4σ or $1/e^2$) of $348 \mu\text{m}$ so that we can minimize the higher order modes and increase the coupling in the fundamental TEM₀₀ mode. In order to achieve this, a careful study of laser beam transport to the cavity is necessary.

In our optical system, the frequency doubled green beam after the two dichroic mirrors DC₁ and DC₂ (Figure 5.30) is focused by lens L₀ with a focal length of $f_0 = 75\text{mm}$. The dimensions of this beam were measured by Spiricon [105] CCD camera which has a precision of $5\mu\text{m}$ and it shows that the beam was focused at 6.0cm after the enclosure box with sizes of $w_x = 370\mu\text{m}$ and $w_y = 450\mu\text{m}$, in the horizontal and vertical plane, respectively. A diverging lens L₁ with a focal length of $f_1 = -1.0\text{m}$ at 405mm from the PPLN Doubler expands the beam very slowly. Here we want to keep the beam collimated so that it doesn't get clipped when it passes through the Faraday optical isolator (FOI) which has a small aperture diameter of 3.5mm . Another reason is that, it is the region where we want to keep all the

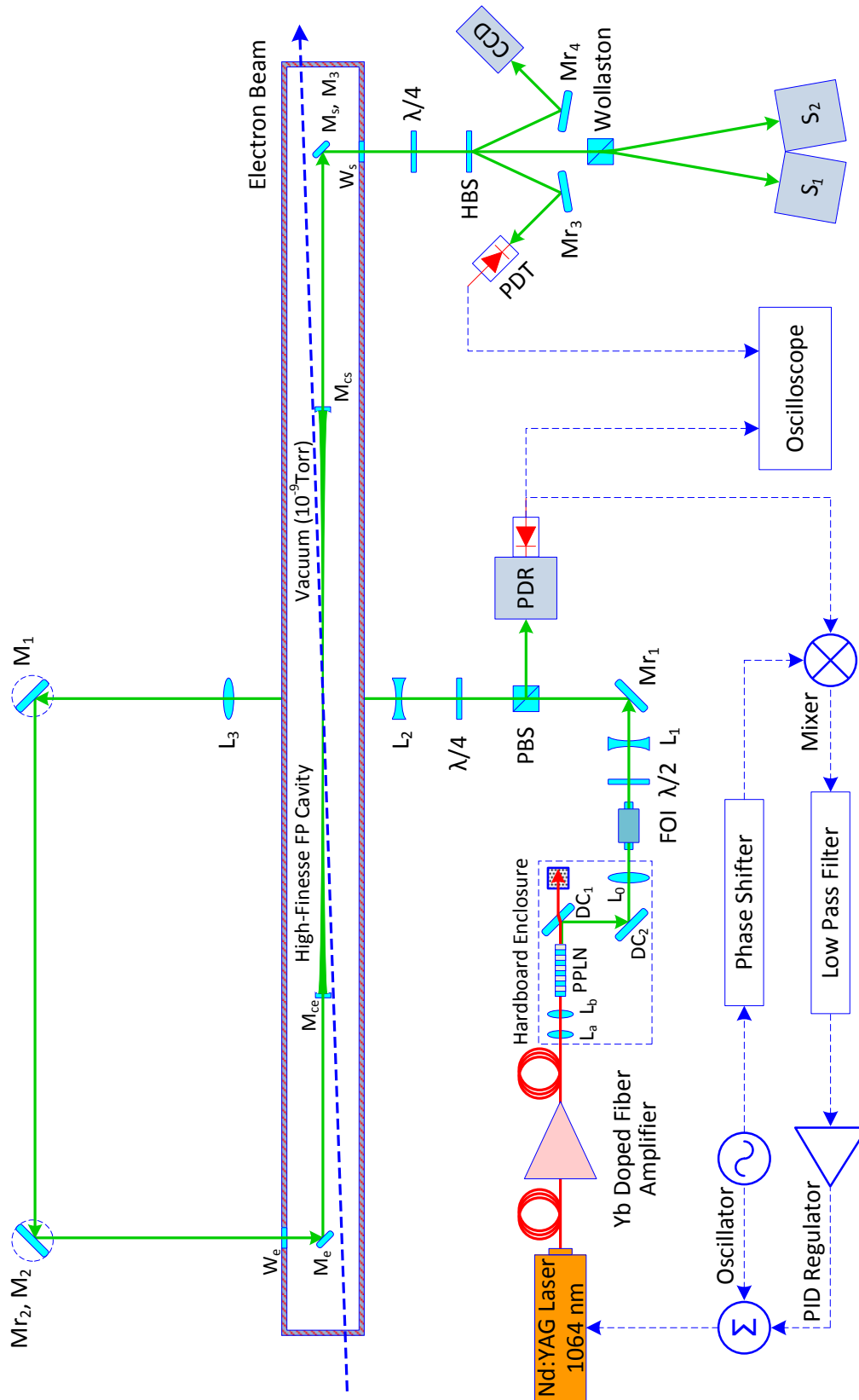


Figure 5.30 (color) A schematic of optics and electronic feedback system.

polarization shaping elements, such as $\frac{\lambda}{2}$ plate, polarized beam splitter (PBS) and $\frac{\lambda}{4}$ plate. These elements have a stringent angular acceptance requirements for preserving the purity of polarization states, therefore a well collimated beam is desired. Here we also have taken into account the power damage threshold of these elements. For the power level we have (1.74 W after the doubling setup), it was not an issue. In order get a correct waist size at the cavity center, we installed another two lenses L_2 and L_3 with focal lengths of $f_2 = -50\text{mm}$ and $f_3 = 200\text{mm}$ at 820mm and 1.0m from the PPLN doubler, respectively. Figure 5.31 shows the distances of each optical elements with respect to each other. Here in our setup, L_1 and L_2 are on fixed mounts and L_3 is mounted on a remote controlled translation stage. This will allow a fine tuning by remote control after the cavity is installed.

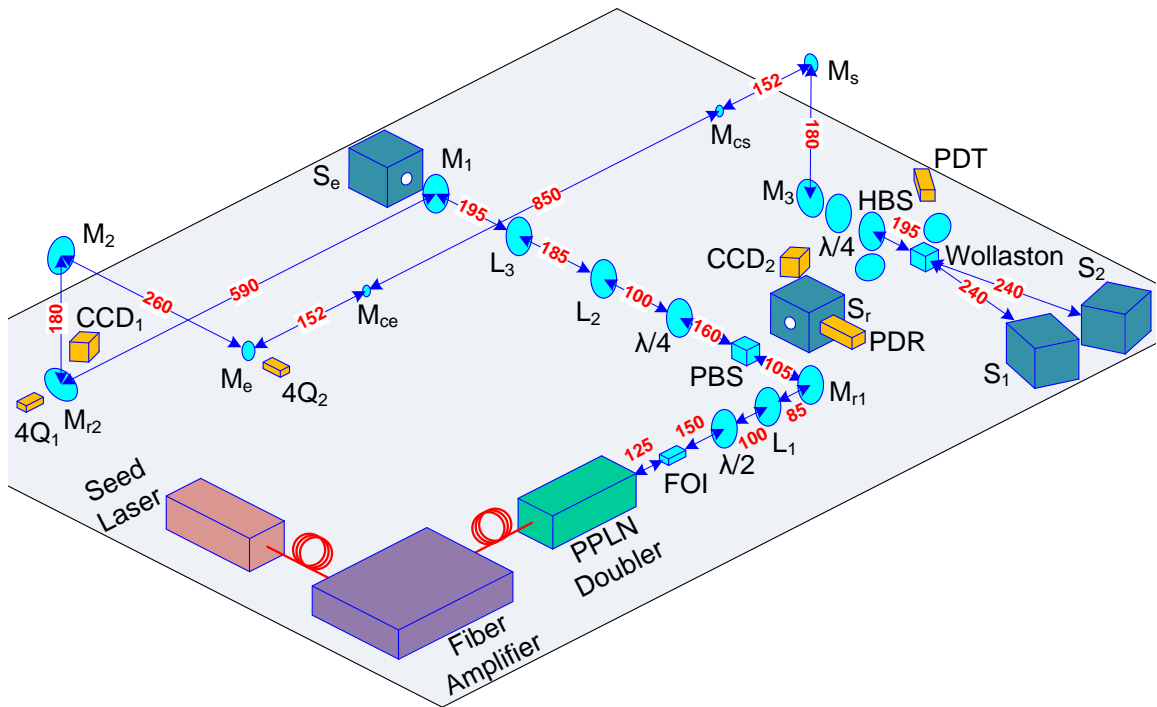


Figure 5.31 (color) Schematic view of the optical scheme with the locations of optical elements (units are in mm).

The beam transport calculation was done by a software called OptoCad [106] that traces Gaussian beams through optical systems. It is a Fortran95 based open source

package, written and maintained by Roland Schilling. It is mainly used in gravitational physics community for modeling and designing their optical setups. OptoCad automatically traces the laser beam through all given components and computes the parameters of the optical system (beam sizes, eigen-modes, mode-matching factors, etc.); optionally, it plots the beams and optical components to a PostScript file. A to-scale schematic drawing of the laser and cavity system is shown in Figure 5.32. Since OptoCad only plots components in 2D, in order to properly model the system, we had to compensate the optical paths for some optical elements which is not lying on the optics table plane (in the propagation direction of laser beam, optical elements from M_2 to M_e in Figure 5.31).

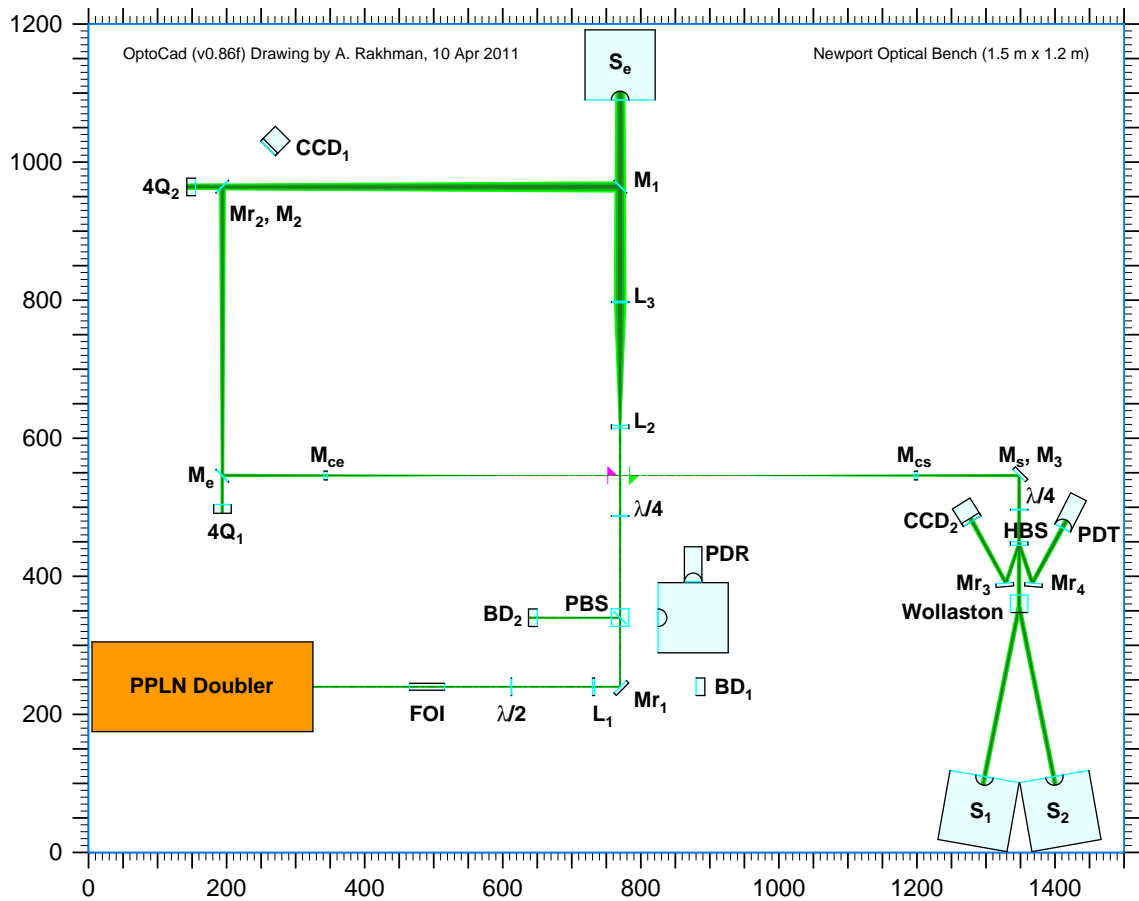


Figure 5.32 (color) A to-scale schematic drawing of laser and optical components by OptoCad.

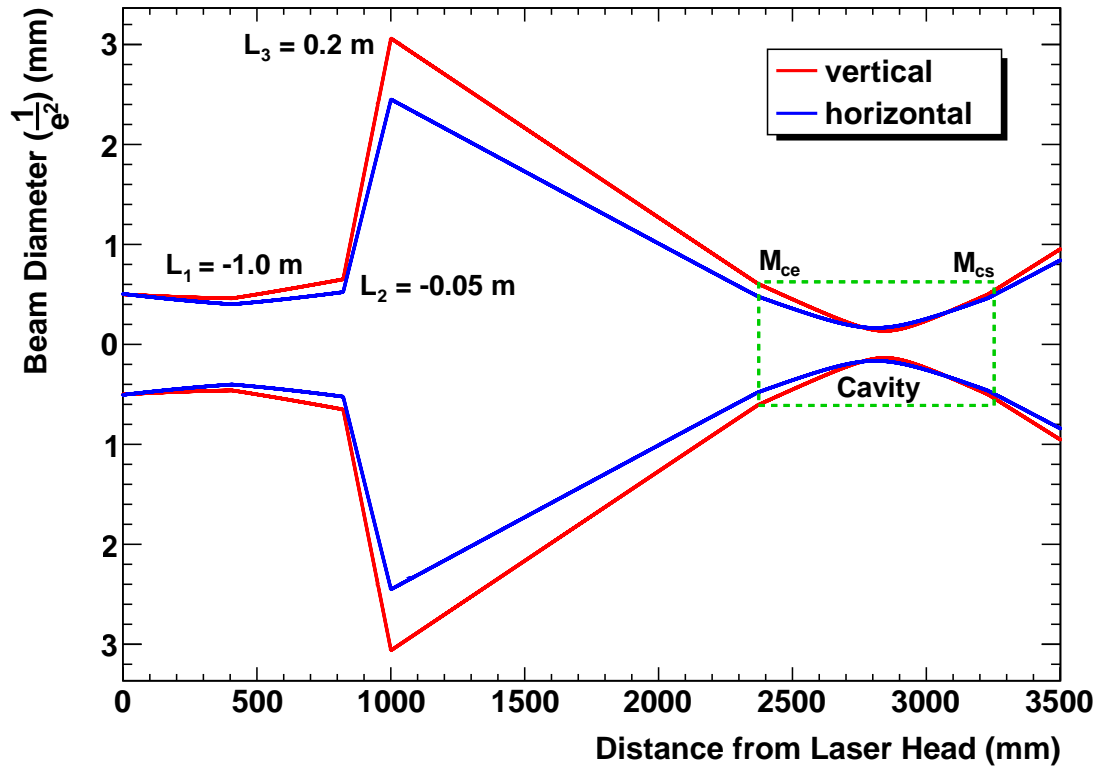


Figure 5.33 (color) The calculated beam size versus the distance along the beam path from the face of PPLN doubler.

Figure 5.33 shows the calculated beam sizes from OptoCad versus the distance along the beam path from the face of the PPLN doubler. We also took into account the focusing effect comes from the curvature of cavity mirrors. The experimental checking of laser waist size at the center of cavity is not possible with the Spiricon CCD camera. Therefore, we created an optical path (2.375m) from the doubling unit to a spare cavity mirror substrate which has the same path length from the doubling unit to the cavity with all the lenses and optical elements are in place. This substrate is uncoated and made of the same material (fused silica) and has the same radius of curvature as cavity mirrors. Since we have a space to mount the Spiricon CCD camera, we can experimentally check the beam sizes and the waist location after this mirror substrate, and therefore compare it to our calculation. A small correction with

L_3 (few mm) was necessary in order to get an average beam size of $350\mu m$ at a distance of $425mm$ from this mirror substrate. Due to the ellipticity and small astigmatism in our beam, the maximum possible theoretical mode matching coefficient defined by equations (5.86) and (5.87) was 96.7%. Using cylindrical lenses could correct it, but it would also make the optics more complex, therefore we decided to ignore it. A final alignment and fine tuning with L_3 were still needed once the cavity is closed up and evacuated with vacuum pumping, and it is done by monitoring the cavity power while it stays locked. We will describe the cavity and beam alignment procedure in the next section.

5.4.2 Cavity and Beam Alignment

Beam Alignment

As we described in the previous section, misalignments of laser beam with respect to aligned cavity mirrors often come from the axial and angular misalignments in x (horizontal) and y (vertical) directions. Therefore, they can be described by four parameters: Δx , Δy , $\Delta\alpha_x$, $\Delta\alpha_y$.

In order to control these parameters, we need to have an alignment scheme with four degrees of freedom. In our setup, a periscope system consists of two remote controlled steering mirrors M_1 , M_2 (Figure 5.25) is used to align the incoming laser beam with respect to the cavity optical axis with an angular resolution of $10\ \mu rad$ [8]. The mirrors are mounted on motorized servo frames from Physik Instrumente (PI) [107] (Figure 5.34). The controller box C-844 can take up to four motors. The motors are connected to the controller box through RS-232 mode and interfaced to the VME crate that holds the command-control cards.

Beam position variations are monitored with two 4-cell quadrant photodiodes noted as $4Q_1$ and $4Q_2$ that detect a small amount of transmitted light ($< 0.1\%$) behind $M_{r,2}$ and M_e (Figure 5.25). These photodiodes are made of Si and have an active area of $6.5mm \times 6.5mm$ and a resolution of $250\mu m$. There is a pinhole diaphragm with

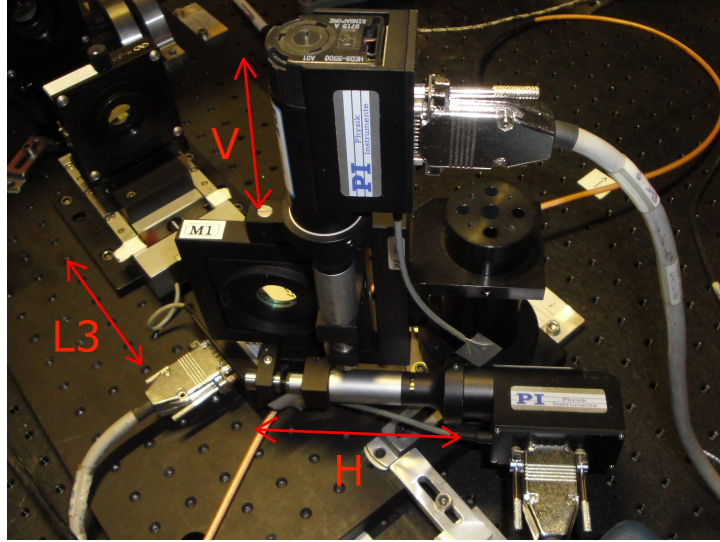


Figure 5.34 (color) A picture shows the steering mirror M_1 mounted on a motorized mirror frame with two servo actuators and the lens L_3 is placed on a motorized linear stage equipped with another servo actuator.

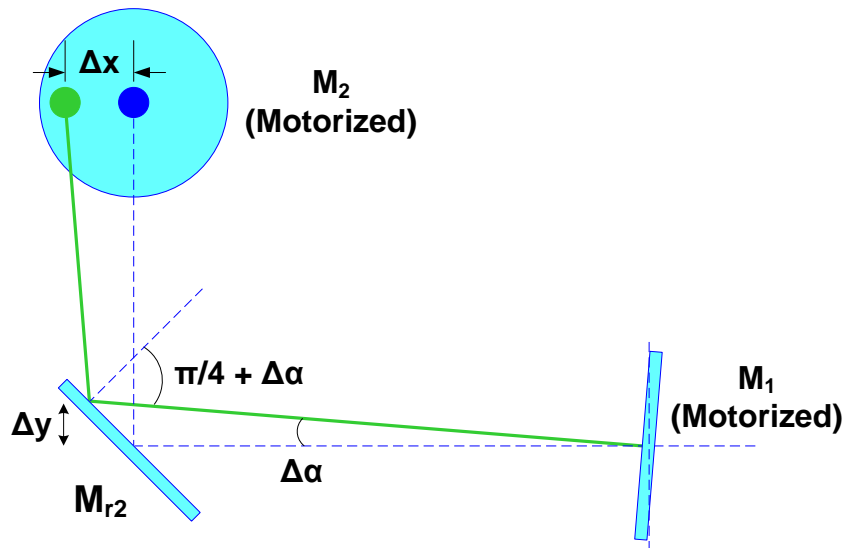


Figure 5.35 (color) A schematic shows a periscope system composed of two motorized mirrors achieve displacement and tilt of laser spot on cavity mirror (redrawn from [43]).

a diameter of 2.5mm in front of each photodiodes. The analog signals read by their electronics are fed to ICV150 card connected to VME crate and being monitored by

control system.

A displacement parallel to the cavity optical axis is obtained by performing a rotation of the same angle in directions correspond to mirror M_1 and M_2 . But the directions x and y are reversed between M_1 and M_2 (Figure 5.35). To get a displacement in the horizontal plane, we need to use motor “M2V” and “M1H” with twice more steps on M_2 than M_1 and do the opposite for the vertical plane. For a tilt around the cavity optical axis, we only need to tilt M_2 in its horizontal or vertical axis. Since these motors are servo motors, after each alignment that gives maximum cavity power, we can take note of their corresponding positions for future reference.

Before we install the cavity mirrors, we need to align the incident beam to the cavity optical axis. This can be accomplished by using a pair of pinhole diaphragms that have the same geometry as the cavity mirrors. They can be mounted on the mirror mount in the adaptor ring mounted to the cavity gimbals (Figure 5.16). The hole has a diameter of 1mm (Figure 5.36), the alignment is achieved by maximizing the intensity transmitted by the diaphragm.

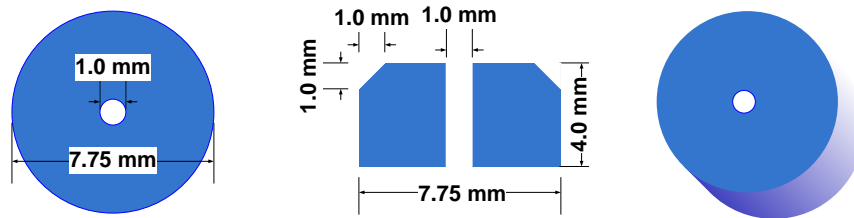


Figure 5.36 (color) A schematic of a pinhole used for aligning the laser beam to cavity optical axis.

Cavity Alignment

After determining the moving sequences of motors for each steering mirrors, we can optimize the coupling. But since our cavity is an adjustable cavity, the cavity mirrors also need to be highly aligned. There are two kinds of misalignments need to be considered: an angular tilt θ and an axis shift ρ of one mirror with respect to the

other. Ref. [104] estimated the mechanical tolerance for the alignment of cavity mirrors by,

$$D \leq \frac{R^2}{2R - L} \left(\frac{\rho}{R} + \theta \right), \quad (5.89)$$

where R and L are the radii of curvature of the mirrors and length of the cavity, respectively. D is the distance between the optical center and geometrical center of a mirror. For our cavity, $R = 0.5\text{m}$, $L = 0.85\text{m}$, we get,

$$D[\text{mm}] = \frac{5}{3} \left(2\rho[\text{mm}] + \theta[\text{mrad}] \right), \quad (5.90)$$

the order of magnitude of the mechanical tolerances for our cavity are $O(0.3\text{mm})$ for the axis shifts and $O(0.6\text{mrad})$ the angle tilts both in horizontal and vertical directions.

Once the step of aligning the incident beam to the cavity optical axis is complete, we can align the cavity entry mirror to the incident beam. This is accomplished by coinciding the spot of reflected beam from the cavity entry mirror, M_{ce} , to the incident beam spot on mirror M_{r2} . It can be monitored by a CCD camera (CCD_1) in front of M_{r2} (Figure 5.25). After this step, we can align the exit cavity mirror, M_{cs} , to the incident. While the laser frequency being scanned and cavity is “open loop”, the criteria to check the cavity mirror alignment is to observe the resonance modes that are monitored by CCD_2 at the exit of cavity and the reflection signal being monitored by an oscilloscope connected to the fast photodiode PDR. We might see some higher order modes (Figure 5.37) and occasionally the fundamental mode at the beginning. But when tuned right, there should always be a fundamental mode (TEM_{00}) and some TEM_{10} modes present.

Getting a bigger reflection peak (reflection dip) that correspond to a fundamental mode can be tedious and may take a long time to achieve depending on the specific cavity tune. But there is simpler and easier method.

This method consists of performing the incident beam tuning in closed loop. Suppose that the initial coupling in the fundamental mode is good enough to allow the feedback loop to be used. When the locking parameters are setup correctly, cavity can

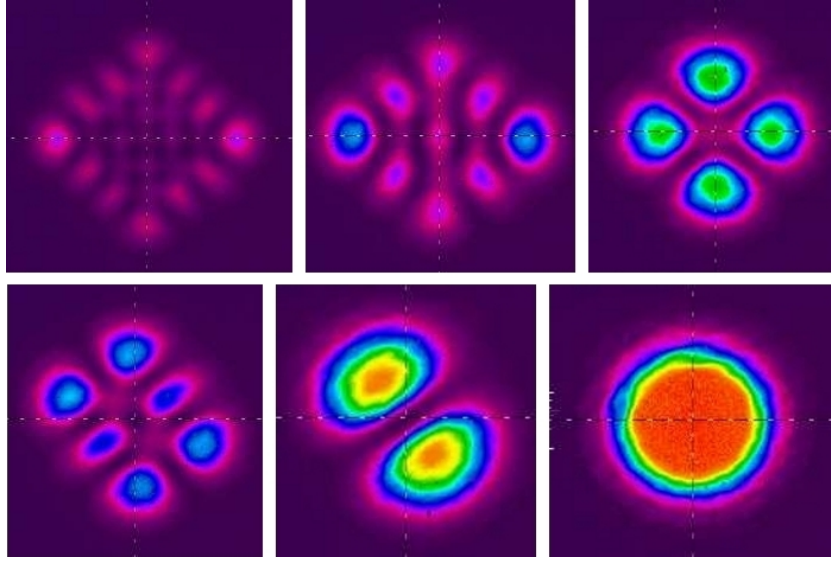


Figure 5.37 (color) The fundamental mode and higher order modes observed by a CCD camera at the end of the cavity.

be locked to a fundamental mode even with a smaller reflection peak (for example, 100 mV peak out of a 800 mV base signal). Since our motors are extremely quiet, a small motion in any of them does not perturb the lock. Now we can play with mirrors M_1 and M_2 combined with lens L_3 to improve the tune by monitoring the intra-cavity power measured by two photodiodes S_1 and S_2 . During any of these steps, if we lose the lock, we can wait for sometime for the lock to come back or go to the opposite direction or use the previous settings of steering mirror positions to recover.

5.4.3 Determination of Cavity Parameters

Once laser beam and cavity is aligned with respect to each other, cavity can be locked. But we need to know the real parameters correspond to a “running cavity”. It is obvious that, it is impossible to directly measure parameters like the cavity gain (G), bandwidth ($\Delta\nu_c$) and the corresponding power (P_{cav}) inside the cavity. Therefore, all of the various methods developed so far for measuring cavity parameters rely on “external” information. A simplest method is the measurement of the cavity decay time.

When the laser frequency is locked to the cavity resonance frequency, the energy built up in the interior of the cavity is at a maximum. We thus observe a reflection signal at a low level, corresponding to the fact that nearly all of the incident wave is transmitted by entrance mirror into the cavity. Inversely, we simultaneously observe that the the transmission of the cavity is at a high level proportional to the stored energy. If we suddenly cut off the trajectory of the laser beam before it enters the cavity, we then see, in the transmission and reflection of the cavity since the laser is extinguished, a decrease in the power level from the established power level to the dark current of the diodes. Cutting off the trajectory of the laser beam can be done in three ways: use an acousto-optic modulator (AOM) which deflects the beam when a high voltage signal applied to the acousto-optic crystal; or one can block the laser beam with a fast mechanical system called “chopper” (it is much too slow); or switch off the laser pumping diode so that the incident laser power is off. For both cases, we need to correct the measured decay time for the response time of the AOM or laser diode. We chose not to introduce an AOM in the system, due to a reason that it changes the mode matching of the system. In the later method, while the cavity is locked and the laser is on its “standby” mode, we switch off the laser diode and immediately record the transmitted power via a digital oscilloscope triggered to it.

The intensity of the trapped light will decrease by a constant factor during each round trip within the cavity due to both absorption and scattering losses in the cavity mirrors. The intensity of light ($I(t)$) within the cavity is then determined as an exponential function of time.

$$I(t) = I_{max}e^{-\frac{t}{T_d}}, \quad (5.91)$$

where I_{max} correspond to the maximum laser intensity inside the cavity and T_d is called as cavity decay time. For high finesse, T_d is directly related to the cavity parameters by [101, 108],

$$T_d \approx \frac{\mathcal{F}L}{\pi c} = \frac{1}{2\pi\Delta\nu_c}, \quad (5.92)$$

where \mathcal{F} is the finesse, L is cavity length, c is speed of light and $\Delta\nu_c$ is cavity

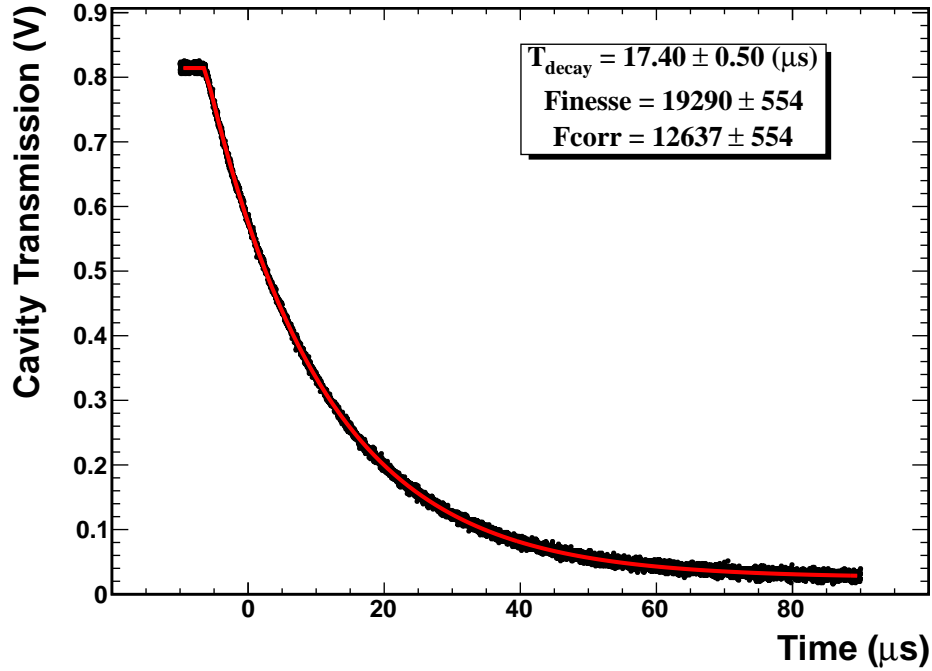


Figure 5.38 (color) Decay time of the cavity. The theoretical curve (red line) is fitted to the experimental data (black dots) to extract the cavity decay time. The finesse is corrected for the laser decay time of $6\mu s$.

bandwidth. The measurement of T_d allows us to access the value of the finesse and the value of the cavity bandwidth. Here, it is necessary to take into account of the decay time of the laser itself in order to determine the decay time of the cavity correctly. The decay of the laser diode can be described by,

$$P(t) = P_{max}e^{-\frac{t}{T_L}}, \quad (5.93)$$

where T_L is the laser decay time. If we convolute equation (5.92) with equation (5.93), we will get [43],

$$I(t) = I_{max} \frac{T_L}{T_d - T_L} \left(T_d e^{-\frac{t}{T_d}} - T_L e^{-\frac{t}{T_L}} \right), \quad (5.94)$$

which describes the decay of the laser light inside the cavity with the correction of laser decay time.

Figure 5.38 shows a cavity decay curve measured for our installed cavity and a theoretical fit uses equation (5.94) to extract the decay time. Here, after correcting the

fitted value of decay time to the measured laser decay time and taking the sampling error of oscilloscope as $0.5\mu s$, we have $T_d = 11.40 \pm 0.5 \mu s$.

Now, the maximum cavity gain G_{max} , optical coupling c_{00} of TEM₀₀ mode and mirror characteristics such as loss (P) and transmittivity (T) need to be calculated before we determine the intra-cavity power. Several papers have discussed theoretical models to calculate these parameters [8, 109, 110]. The models in Refs. [8, 109] are similar and one needs to measure the power going into the cavity P_{inc} and the power transmitted out of the cavity P_{trans} externally. Other parameters still need to be determined by more auxiliary measurements from the reflection signal. If we ignore the power contained in modulation sidebands, the loss ratio $\beta = \frac{P}{T}$ of the mirrors can be written as,

$$\beta = \frac{1}{2} \left[\frac{P_{inc}}{P_{trans}} \left(1 - \frac{V_r^{locked}}{V_r^{unlocked}} \right) - 1 \right], \quad (5.95)$$

where V_r^{locked} is the reflected voltage measured when the cavity is in locked state, and $V_r^{unlocked}$ is the reflected voltage measured when the cavity is in unlocked state. Now the optical coupling c_{00} is related to β by,

$$c_{00} = \frac{P_{trans}}{4P_{inc}} \left[1 + \frac{P_{inc}}{P_{trans}} \left(1 - \frac{V_r^{locked}}{V_r^{unlocked}} \right) \right]^2 = \frac{P_{trans}}{P_{inc}} (1 + \beta)^2, \quad (5.96)$$

According to Figure 5.39, and measured values of P_{inc} and P_{trans} , we can calculate β and c_{00} , which eventually allow us to calculate T , P , G_{max} and P_{cav} . Table 5.1 summarizes the cavity parameters measured during PREx. Note that the incident and transmitted powers are measured by Thorlabs PM140 powermeter which has an overall accuracy of 1%.

There is also a graphical method which uses the cavity reflection signal to measure the cavity bandwidth. In this method we determine the full width at half-maximum (FWHM) of the reflection peak in a unit of time. Then, one converts from time units to frequency units, by getting the gap between the two sidebands equal to twice the modulation frequency. This measurement is difficult to make, because perturbations (cavity length variation due to vibrations etc.) may deform the peak

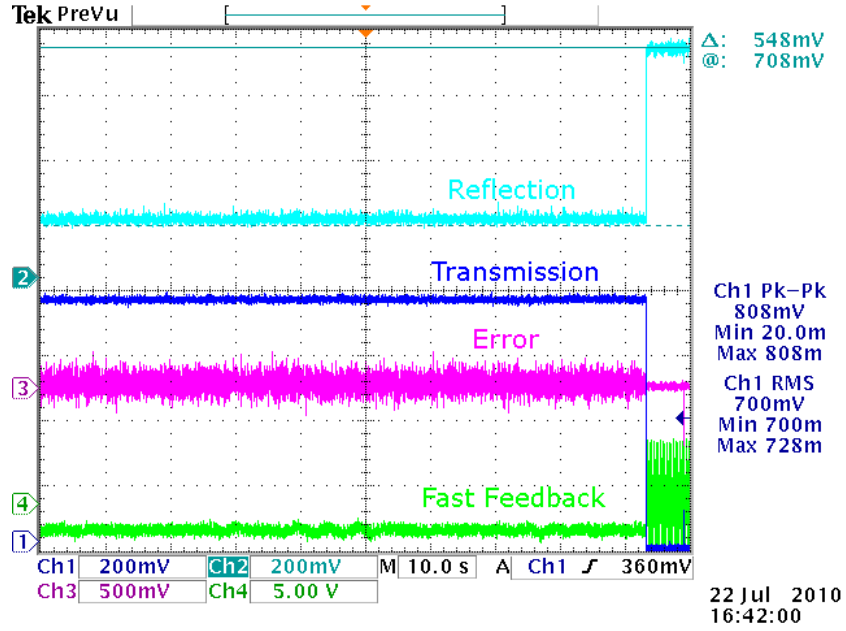


Figure 5.39 (color) A snapshot of a digital oscilloscope shows cavity locking signals correspond to locked and unlocked state of the cavity.

Parameters	Value
Incident Laser Power: P_{inc} (W)	1.24 ± 0.012
Transmitted Power: P_{trans} (W)	0.75 ± 0.007
Finesse: \mathcal{F}	12600 ± 550
Cavity Bandwidth: $\Delta\nu_c$ (kHz)	14.00 ± 0.32
Optical Coupling: Coefficient c_{00}	0.79 ± 0.08
Loss Ratio: β	0.14 ± 0.013
Mirror Transmittivity: $T = \frac{\pi}{\mathcal{F}(1 + \beta)}$ (ppm)	200 ± 9
Mirror Losses: $P = \frac{\pi\beta}{\mathcal{F}(1 + \beta)}$ (ppm)	30 ± 3
Maximum Gain: $G_{max} = \frac{T}{(P + T)^2}$	3800 ± 170
Intra-cavity Power: $P_{cav} = c_{00}G_{max}P_{inc}$ (W)	3750 ± 120

Table 5.1 Characterization of the cavity parameters during PREx.

when the laser frequency sweeps the resonance region defined by the cavity. Therefore, the measurement is not very accurate. Figure 5.40 shows a theoretical fit to the reflection and transmission signals used to extract the cavity bandwidth and therefore the cavity finesse.

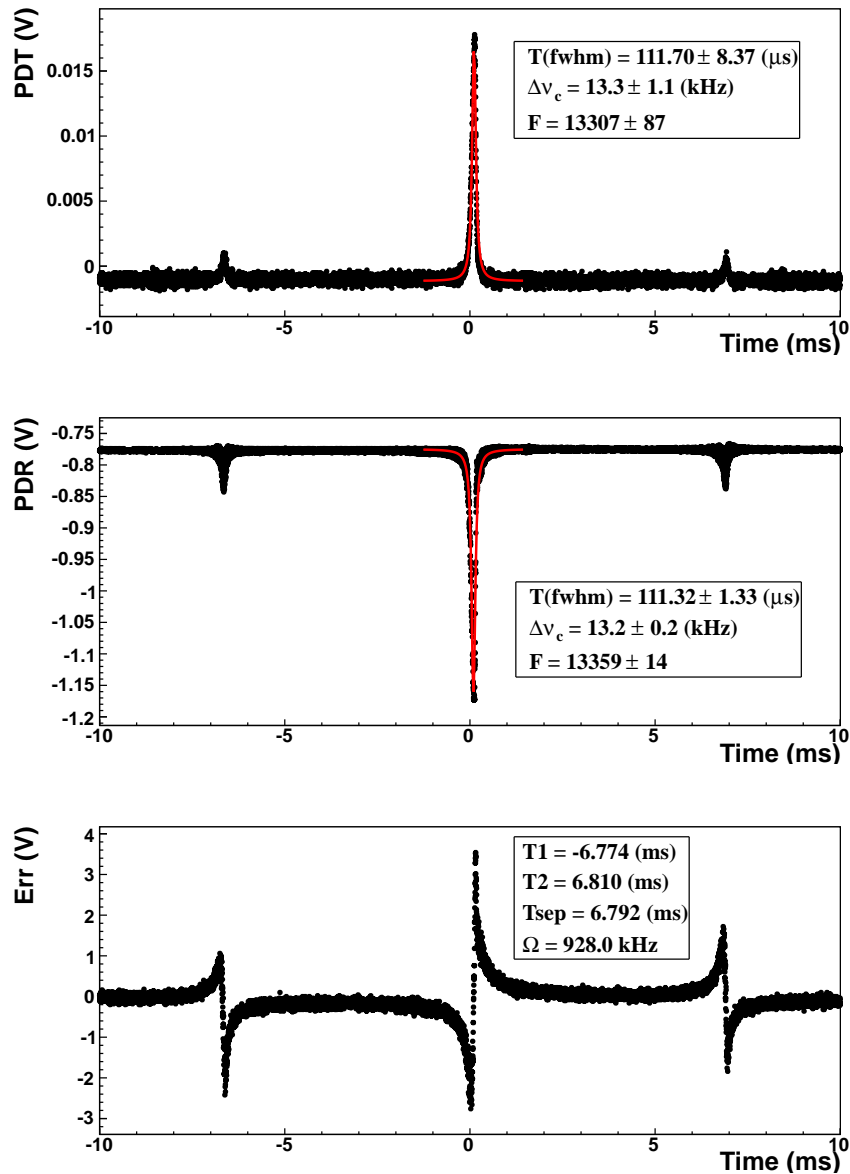


Figure 5.40 (color) A theoretical fit to the reflection and transmission signals used to extract the cavity bandwidth when the cavity is in “open loop” mode.

The analysis of the shape of the reflected and transmitted signals, when the cavity is in “open loop”, may also give some information on cavity bandwidth. Several papers [111,112] discuss the dynamic behavior of Fabry-Perot cavities with very high finesse or very large length. They exhibit an oscillatory reflection and transmission signals around the resonance peak when the input laser frequency or cavity length is being scanned by a triangular ramp. They show that oscillations in the signals are the result of interferences between the amplitude and the phase of the cavity and laser fields. Based on the analysis of “ringing” on the transmitted and reflected power, they created a theoretical model to predict the cavity finesse by fitting the measured signals to the theoretical curve.

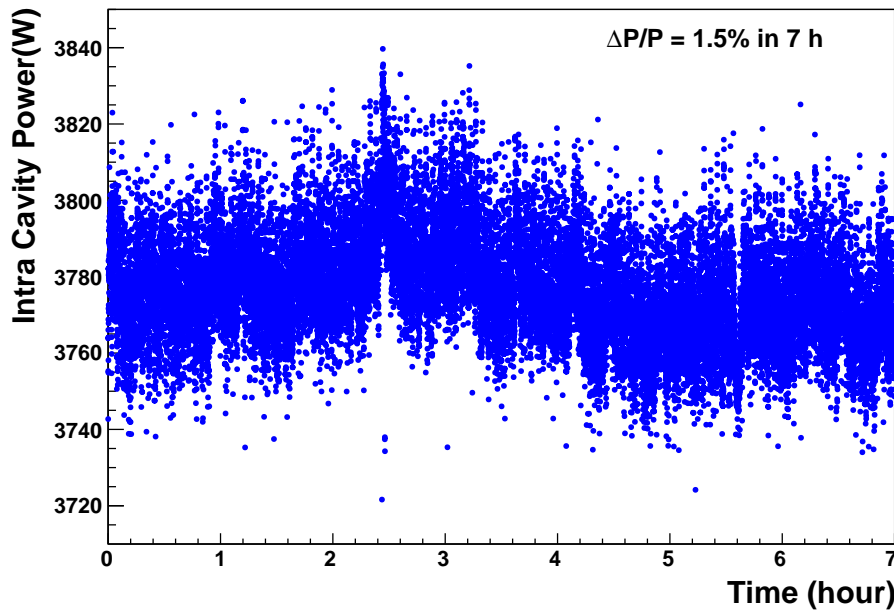


Figure 5.41 (color) The intra-cavity power stability is monitored for 7 hours.

The stability of cavity gain therefore the intra-cavity power is monitored for more than 7 hours with a statistical stability of 1.5%. Figure 5.41 shows the time evolution of the power for a lock achieved during PREx with electron beam passing through the Compton chicane.

We have described the optical and electronic principles of our laser and cavity system and described the results. Robust cavity locking with stable high power is essential, but in order to pursue a Compton polarimetry, we have to create a highly circularly polarized photon beam at the Compton interaction point (CIP) in order to observe Compton scattering asymmetry and therefore to be able to measure the electron beam polarization. We will describe the polarization aspects of our system in the next chapter.

Chapter 6

Beam Polarization

The goal of building a high finesse green Fabry-Perot cavity for a Compton polarimeter is not only to provide a high energy photon flux but also to create highly circular photons for the longitudinally polarized electrons, so that there will be an efficient Compton scattering. Creating a highly circular photon beam and knowing its degree of circular polarization (DOCP) with good precision are vital to achieve high precision Compton polarimetry.

In this chapter, we will first describe the basic concepts of polarized light and techniques of measuring it. The combination of Fabry-Perot cavity with a polarized laser light, once more makes the creation and measurement of the polarization inside the cavity more complex. Therefore, we have to measure a transfer function that allows us to determine the DOCP indirectly. Knowing the birefringence of our system is important for systematic error estimation in intra-cavity polarization determination. Finally, we will briefly present the results of electron beam polarization measurement based on the integration of the Compton photons scattered off the longitudinally polarized electrons.

6.1 Polarization of Light

6.1.1 Introduction

For a monochromatic plane wave with angular frequency ω and wave vector \mathbf{k} ($|\mathbf{k}| = k = \frac{2\pi}{\lambda}$) traveling along the axis Oz , its electric field $\mathbf{E}(\mathbf{x}, \mathbf{y}, \mathbf{z}, \mathbf{t})$ in an isotropic media can be written by,

$$\mathbf{E}(\mathbf{x}, \mathbf{y}, \mathbf{z}, \mathbf{t}) = (E_x \hat{\mathbf{x}} + E_y \hat{\mathbf{y}}) e^{-i(\omega t - \mathbf{k}z)}, \quad (6.1)$$

where E_x and E_y are the transverse components in x and y directions and can be defined by,

$$E_x = A_x, \quad (6.2)$$

$$E_y = A_y e^{i\delta}, \quad (6.3)$$

where A_x and A_y are real amplitudes, and δ is the angular phase difference between them. On plane Oxy , the electric field vector $\mathbf{E}(\mathbf{x}, \mathbf{y}, \mathbf{t})$ can be written with its real components in the following matrix form [113],

$$\mathbf{E}(\mathbf{x}, \mathbf{y}, \mathbf{t}) = \begin{pmatrix} X(t) \\ Y(t) \end{pmatrix} = \begin{pmatrix} A_x \cos(\omega t) \\ A_y \cos(\omega t - \delta) \end{pmatrix}, \quad (6.4)$$

The evolution of equation (6.4) defines an ellipse with the following form,

$$\frac{X^2(t)}{A_x^2} + \frac{Y^2(t)}{A_y^2} - 2 \frac{X(t)Y(t)}{A_x A_y} \cos \delta = \sin^2 \delta, \quad (6.5)$$

and the sign of δ defines the helicity of this ellipse. The most general polarization state of an electro-magnetic wave is an elliptical one.

Elliptic polarization may be referred to as right-handed or left-handed, and clockwise or counter-clockwise, depending on the direction in which the electric field vector rotates. Unfortunately, two opposing historical conventions exist. In this chapter, we follow a convention of defining the polarization from the point of view of the receiver.

Using this convention, left or right handedness is determined by pointing one's left or right thumb toward the source, against the direction of propagation ($-\mathbf{z}$), and

then matching the curling of one's fingers to the temporal rotation of the field. If we choose the propagation direction of the field is along Oz , the helicity state h_γ is related to δ by using the following relationship,

$$h_\gamma = \begin{cases} +1, & \text{Left-handed (counter-clockwise),} & \text{if } \delta \in [0, \pi] \\ -1, & \text{Right-handed (clockwise),} & \text{if } \delta \in [-\pi, 0] \end{cases}$$

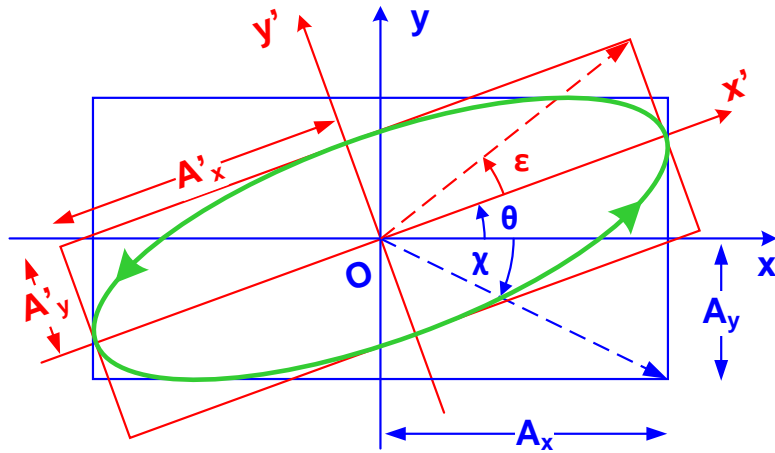


Figure 6.1 (color) The rotated polarization ellipse.

In Figure 6.1, we may determine the axes of the polarization ellipse by changing from the coordinate frame Oxy to a frame $Ox'y'$ by the rotation angle θ ,

$$\tan(2\theta) = \frac{2A_x A_y}{A_x^2 - A_y^2} \cos \delta, \quad (6.6)$$

where θ is the orientation of the ellipse which takes a value from 0 to $\frac{\pi}{2}$. We can also define the ellipticity in two coordinate frames as,

$$\tan(\epsilon) = \frac{A'_y}{A'_x}, \quad (6.7)$$

$$\tan(\chi) = \frac{A_y}{A_x}, \quad (6.8)$$

There are particular configurations for which the ellipse reduces to a line or a circle. Therefore, we can define the linear and circular polarization as,

- If $\delta = 0$ (π), then the polarization is linear.
- If $\delta = \pm \frac{\pi}{2}$ and $A_x = A_y$, the polarization is circular (Left/Right).

6.1.2 Jones Representation

We also use vector notation to represent the polarization states of light that was proposed by R. C. Jones [114, 115] in 1941. In Jones representation, polarized light is represented by a Jones vector, and linear optical elements are represented by Jones matrices. When light passes through an optical element, the resulting polarization of the transmitted light is found by taking the product of the Jones matrix of the optical element and the Jones vector of the incident light. The polarization state of the previous case can be represented by Jones vector \mathbf{J} with two components (amplitudes),

$$\mathbf{J} = \begin{pmatrix} A_x \\ A_y e^{i\delta} \end{pmatrix}, \quad (6.9)$$

where the propagator $e^{-i\omega t}$ was deliberately omitted because it does not contribute to the description of the polarization state. It is convenient to work with Jones vector of various polarization states. Waves linearly polarized along \mathbf{x} -(\mathbf{y} -) direction and those linearly polarized at an angle θ from the \mathbf{x} -axis are written as,

$$\hat{\mathbf{H}} = \begin{pmatrix} 1 \\ 0 \end{pmatrix}, \quad \hat{\mathbf{V}} = \begin{pmatrix} 0 \\ 1 \end{pmatrix}, \quad \hat{\mathbf{\Theta}} = \begin{pmatrix} \cos \theta \\ \sin \theta \end{pmatrix}, \quad (6.10)$$

elliptically polarized and, particularly left or right circularly polarized states can be written as,

$$\hat{\mathbf{E}} = \begin{pmatrix} \cos \chi \\ \sin \chi e^{i\delta} \end{pmatrix}, \quad \hat{\mathbf{L}} = \frac{1}{\sqrt{2}} \begin{pmatrix} 1 \\ +i \end{pmatrix}, \quad \hat{\mathbf{R}} = \frac{1}{\sqrt{2}} \begin{pmatrix} 1 \\ -i \end{pmatrix}, \quad (6.11)$$

Here it can be seen that, two linearly independent vectors form a basis in the representation of a polarization state. The general state of elliptical polarization can

be expressed as the superposition of both left and right circular states,

$$\hat{\mathbf{E}} = \frac{1}{\sqrt{2}} \left[(\cos \chi - i \sin \chi e^{i\delta}) \hat{\mathbf{L}} + (\cos \chi + i \sin \chi e^{i\delta}) \hat{\mathbf{R}} \right], \quad (6.12)$$

The power carried by the left and right circular components of the field is written,

$$I_L = \frac{1}{2} (1 + \sin 2\chi \sin \delta), \quad (6.13)$$

$$I_R = \frac{1}{2} (1 - \cos 2\chi \sin \delta), \quad (6.14)$$

For an elliptically polarized light, it carries certain number of left and right circularly polarized photons with spin equal to $+\hbar$ and $-\hbar$ along the direction of propagation of the light with powers I_L and I_R carried by each components respectively. The number of left (N_γ^L) and right (N_γ^R) circularly polarized photons define the degree of circular polarization (DOCP) as,

$$DOCP = \frac{N_\gamma^L - N_\gamma^R}{N_\gamma^L + N_\gamma^R} = \frac{2A_x A_y}{A_x^2 + A_y^2} \sin \delta, \quad (6.15)$$

For a fully polarized light with pure circular polarization, $DOCP = \pm 1$, and with pure linear polarization the $DOCP = 0$. The Compton asymmetry measured at the point of interaction is directly proportional to the $DOCP$. Therefore, a photon beam with $DOCP \sim 100\%$ is desired. A difference in amplitude ($A_x \neq A_y$) and a phase shift between the two components ($\delta \neq \frac{\pi}{2}$) give rise to an elliptical polarization. As soon as the polarization becomes elliptical, it introduces some quantity of photons with spins opposed to the desired direction with the power proportional to them.

Jones representation uses the amplitude and phase information (which are not observables) of the wave for calculating the $DOCP$. It is suitable to light that is already fully polarized. Light which is randomly polarized, partially polarized, or incoherent must be treated using the Stokes vector and Mueller matrix formalism.

6.1.3 Stokes Parameters

The Stokes parameters are based on Mueller matrix with a set of values that describe the polarization state of light. They were defined by G. G. Stokes in 1852, as a

mathematically convenient way to describe the polarization state of light with its observable quantities, such as, intensity and the orientation of the polarization ellipse. The Stokes vector is defined by [113],

$$P = \begin{pmatrix} P_0 = A_x^2 + A_y^2 \\ P_1 = A_x^2 - A_y^2 \\ P_2 = 2A_x A_y \cos \delta \\ P_3 = 2A_x A_y \sin \delta \end{pmatrix} = \begin{pmatrix} I \\ I_x - I_y \\ I_{+\frac{\pi}{4}} - I_{-\frac{\pi}{4}} \\ I_L - I_R \end{pmatrix}, \quad (6.16)$$

where I is the beam intensity; I_x , I_y , $I_{+\frac{\pi}{4}}$ and $I_{-\frac{\pi}{4}}$ are the intensities after a linear polarizer oriented along \hat{x} , \hat{y} , $\hat{x} + \hat{y}$ and $\hat{x} - \hat{y}$ respectively. I_L and I_R are the intensities after circular left and right polarizers respectively. For a fully polarized wave, we have,

$$P_0 = \sqrt{P_1^2 + P_2^2 + P_3^2}, \quad (6.17)$$

In this formalism, the left and right circular states are defined by,

$$\hat{\mathbf{L}} = \begin{pmatrix} 1 \\ 0 \\ 0 \\ 1 \end{pmatrix}, \quad \hat{\mathbf{R}} = \begin{pmatrix} 1 \\ 0 \\ 0 \\ -1 \end{pmatrix}, \quad (6.18)$$

The ellipticity (ϵ) and the orientation (θ) of polarization ellipse with respect to the reference axis Ox is represented by,

$$\tan(\epsilon) = \frac{A'_y}{A'_x} = \frac{P_3}{P_0 + \sqrt{P_1^2 + P_2^2}}, \quad (6.19)$$

$$\tan(2\theta) = \frac{P_2}{P_1}, \quad (6.20)$$

The degree of linear polarization (*DOLP*) and the degree of circular polarization (*DOCP*) also can be defined as [113],

$$DOLP = \frac{\sqrt{P_1^2 + P_3^2}}{P_0}, \quad (6.21)$$

$$DOCP = \frac{P_3}{P_0}, \quad (6.22)$$

and the total degree of polarization (*DOP*) is,

$$DOP = \sqrt{DOLP^2 + DOCP^2} = \frac{\sqrt{P_2^2 + P_2^2 + P_3^2}}{P_1}, \quad (6.23)$$

6.1.4 Creating Circularly Polarized Light

In terms of polarization aspect, our optical setup needs to fulfill several functions:

- Creation of a highly circularly polarized photon beam at the interaction point inside the cavity and switching of left and right polarization at regular intervals.
- Extraction of the reflection signal from the cavity for the feedback system.
- Monitoring of laser beam polarization in situ.

In our setup, the IR beam from the fiber amplifier comes out as vertically polarized with the extinction ratio of $20dB$ ($\frac{1}{100}$). The frequency doubled green beam after the PPLN doubler is linear and the *DOLP* is measured as 99.88%. The beam then passes through a Faraday isolator (FOI) composed of two Glan-Laser polarizers (made of calcite) at the entry and at the exit, and a Faraday rotator (see Figure 5.25). The FOI used to protect the laser from the light reflected by the rest of the optical elements. The entry polarizer creates a vertical polarized light with respect to its optical axis. The polarization is rotated by 45° by the Faraday rotator made of terbium gallium garnet ($Tb_3Ga_5O_{12}$) crystal located inside a permanent magnet. After the exit polarizer, the incident beam will be polarized at 45° . When the reflected beam from the rest of the optics passes the exit polarizer, it will have a polarization at 45° and will be rotated at the Faraday rotator by another 45° so that it become horizontally polarized at the entry polarizer. The entry polarizer will deflect the horizontally polarized beam so that there will be no reflection send back to the PPLN therefore to the laser itself. The FOI will lead to an isolation up to $40 dB$.

The next element is half-wave plate ($\frac{\lambda}{2}$) that rotates the output polarization from FOI to make it horizontally polarized all the way up to the polarizing beamsplitter

(PBS). Table 6.1 summarizes the transport of linearly polarized light from the PPLN doubler to quarter-wave plate ($\frac{\lambda}{4}$).

Optical Element	DOLP (%)	Angle (degree)
PPLN Doubler	99.88 ± 0.1	89.9 ± 0.5
Faraday Isolator (FOI)	99.98 ± 0.1	-45.0 ± 0.5
Half Wave Plate ($\frac{\lambda}{2}$)	99.99 ± 0.1	0.11 ± 0.5
Fixed Turning Mirror (M_{r1})	99.20 ± 0.1	0.00 ± 0.5
Polarizing Beam Splitter (PBS)	99.99 ± 0.1	0.00 ± 0.5

Table 6.1 Measurement of the degree of linear polarization (DOLP) after various optical elements.

Here the measurement is made with the help of a rotatable Glan laser polarizer (from Thorlabs) with an extinction ratio of $50dB$. The principle of polarization measurement with rotatable linear polarizer will be described in the next section. The angle is measured with respect to a plane defined by the optics table.

A left or right circularly polarized beam can be achieved by sending a linearly polarized beam through a quarter-wave plate ($\frac{\lambda}{4}$) with its optical axis oriented at $\pm 45^\circ$ with respect to it. Our quarter-wave plate (from Thorlabs) is a zero-order crystalline quartz with a total thickness of 2 mm . It is placed on a motorized mount (from Suruga) which allows us to reverse the helicity of circular polarization in a time interval of 40 seconds.

One of our highest priorities is to provide the highest degree of circular polarization at the Compton interaction point (CIP). In our setup, the polarization state is controlled by polarizing beamsplitter and the quarter-wave plate. This will ensure that we have a circularly polarized beam generated after the quarter-wave plate and the signal reflected by the cavity can be separated from the incident beam after the polarizing beamsplitter. However, we must take into account the unavoidable

degradation of the polarization between the output of the quarter-wave plate and the CIP. A mirror can induce a parasitic phase shift $\delta = \delta_s - \delta_p$ between the vertical (s -polarized) and horizontal (p -polarized) components of electric field vector A_x and A_y by reflecting different quantities of light between the two components. This effect is called birefringence. Birefringence induces ellipticity in the polarization and therefore degrades the DOCP. This effect can be reduced by using dielectric mirrors. In our setup, the main source of birefringence is the dielectric steering mirrors after the first quarter-wave plate since they have different reflection coefficient for TE (s -polarized) and TM (p -polarized) waves with 45° angle of incidence. The dielectric mirrors we use (from CVI, part number: Y2-1025-45-UNP) thus have a difference of $\approx 0.5\%$ between reflection coefficients R_p and R_s at 45° .

In order to minimize this effect, we adopted a well established compensated mirror scheme for polarization transport used in previous Saclay setup [8] which was originally proposed by SLAC [3]. In this scheme, two pairs of identical 45° dielectric mirrors ($M_1 - M_{r2}$ and $M_2 - M_e$) are oriented at the same angle of incidence, but with perpendicular incident planes. In this way, the s -wave at the first mirror becomes the p -wave at the second mirror. If the mirrors are identical, then the difference in reflectivity and in phase between the components may be canceled after the last mirror (M_e). With this scheme, without the cavity mirrors in place, we obtained a maximum left circular polarization of 99.6% for a quarter-wave plate angle of -50° (counter clock wise) and a maximum right circular polarization of -98.1% for an angle of 50° (clock wise). The difficulty of making the incident angle exactly 45° for all the mirrors drive us to adjust the optical axis of quarter-wave plate. Table 6.2 summarizes the DOCP and corresponding ellipse orientation measurement after the quarter-wave plate and at the CIP without cavity mirrors in place. Here, we think the asymmetry of 1.5% between the two polarization states may be due to the fact that the mirrors may not be manufactured in the same coating process. We also checked a possible birefringence effect comes from the cavity vacuum window (W_e) (see Figure 5.30) without vacuum. We measured an unnoticeable difference in circular polarization before and

after the vacuum window. However, when the cavity is under vacuum (10^{-9} Torr), there would be birefringence coming from the pressure difference between air and vacuum. We will discuss the vacuum birefringence more in the following section.

Optical Element	DOCP (%)	Angle (degree)
quarter-wave plate	99.96 ± 0.1 (Left)	45.0 ± 0.5 (Left)
(after QWP1)	-99.98 ± 0.1 (Right)	-45.0 ± 0.5 (Right)
at the CIP	99.57 ± 0.1 (Left)	50.0 ± 0.5 (Left)
(without cavity)	-98.07 ± 0.1 (Right)	-50.0 ± 0.5 (Right)

Table 6.2 Measurement of the degree of circular polarization (DOCP) after quarter-wave plate and at the CIP without cavity mirrors.

One of the advantages of combining the quarter-wave plate with the polarizing beamsplitter (PBS) is being able to extract the cavity-reflected beam from the incident beam. Figure 6.2 illustrates the principle of this scheme. The PBS (from Edmund Optics, extinction ratio: 27 dB) is made of two optically glued right angle BK-7 prisms. It transmits the beam with horizontal polarization to the plane of incidence (p -polarized), and reflects the beam with vertical polarization to the plane of incidence (s -polarized). In our system, we oriented the half-wave plate so that the direction of incoming polarization to the PBS is horizontal by maximizing the transmitted power after the PBS. Then the quarter-wave plate after the PBS creates a left or right circular polarized beam at the cavity entry mirror. When it reflects back, it experiences a phase shift of π and becomes right or left circular. This reflected beam now will become vertically polarized after it passes through the quarter-wave plate. The PBS reflects this beam at 90° before it gets collected by a fast photo diode called PDR.

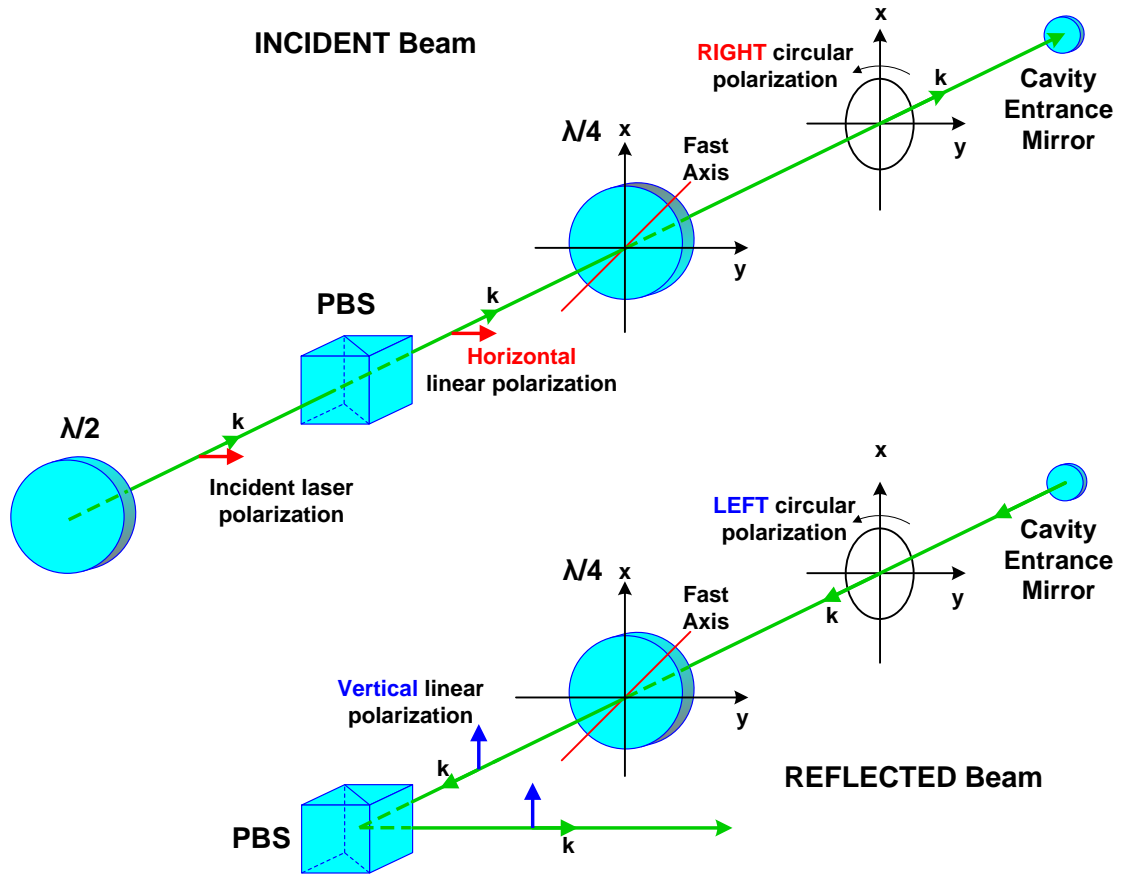


Figure 6.2 (color) A schematic illustration of extracting the cavity-reflected beam from the incident beam (redrawn from [43]).

6.2 Intra-Cavity Polarization

As we stated in previous chapter, when it is locked, the cavity is closed under high vacuum. Therefore, there is no direct way to measure the intra-cavity parameters including the cavity polarization. Just like measuring the transmitted power out of the cavity and determining the intra-cavity power from it, we can only measure the laser polarization at the cavity exit and determine the intra-cavity polarization according to cavity polarization transfer function. We first start with methods polarization measurement and then describe the model on which the transfer function based.

6.2.1 Laser Polarization Measurement

According to our knowledge, there are two most frequently used methods for light polarization measurement. Both involves the rotating polarization retarders such as linear polarizer and quarter wave plate. There are also many commercial equipments which have the capability of measuring the degree of polarization with relatively good accuracy and speed. Based on the experience of Jefferson Lab Compton group, we decided to pursue laser polarization measurement with half-commercial solution which uses rotatable linear polarizers, quarter-wave plates and Wollaston prism.

Measurements with Linear Polarizer

One type of polarization measurement is made with the help of a rotatable linear polarizer and a detector. The detector consists of a 2 inch integrating sphere (from Thorlabs) and a Si photodiode (from Newport). The Si photodiode has a minimum measurable power of 1pW (with 1% measurement accuracy) and an acceptable power density of $2\text{W}/\text{cm}^2$ ($2\text{mW}/\text{cm}^2$) with an attenuator (without attenuator). The polarizer is a Glan laser polarizer (from Thorlabs) with an extinction ratio of 50 dB and a power damage threshold of $1.0\text{ MW}/\text{cm}^2$ and surface quality of $\lambda/10$.

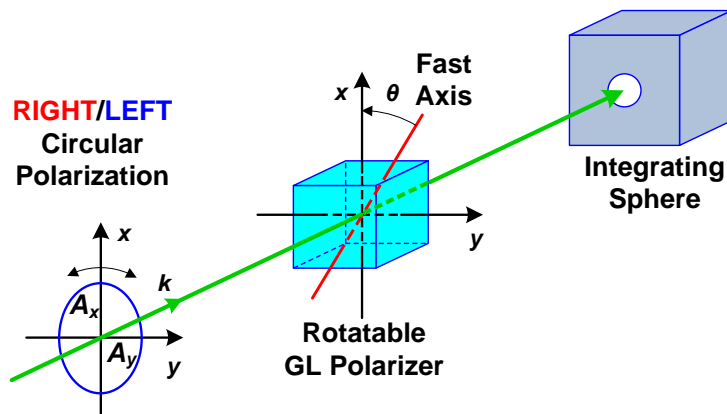


Figure 6.3 (color) A schematic illustration of a polarization measurement station with linear polarizer and a detector.

Figure 6.3 illustrates our polarization measurement station. In the reference frame of the axes of the polarization ellipse, the normalized Jones vector is written,

$$\hat{E}_{L/R} = \frac{1}{\sqrt{A_x^2 + A_y^2}} \begin{pmatrix} A_x \\ \pm i A_y \end{pmatrix}, \quad (6.24)$$

where the sign “ \pm ” correspond to a left or right polarization state, respectively. The Jones matrix of a polarizer whose optical axis rotates an angle θ with respect to the reference axis Ox is,

$$P_\theta = \begin{pmatrix} \cos^2 \theta & \sin \theta \cos \theta \\ \sin \theta \cos \theta & \sin^2 \theta \end{pmatrix}, \quad (6.25)$$

and the polarization after the polarizer is,

$$\hat{E}'_{L/R} = P_\theta \hat{E}_{L/R}, \quad (6.26)$$

and the intensity at the exit of the polarizer can be expressed as,

$$I_{L/R} = |\hat{E}'_{L/R}|^2 = \frac{A_x^2 \cos^2 \theta + A_y^2 \sin^2 \theta}{A_x^2 + A_y^2}, \quad (6.27)$$

Turning the polarizer, we find the extrema:

$$I_{max} = \frac{A_x^2}{A_x^2 + A_y^2}, \quad (6.28)$$

$$I_{min} = \frac{A_y^2}{A_x^2 + A_y^2}, \quad (6.29)$$

and a functional relationship between the rotating angle θ and the intensity $I(\theta)$,

$$I(\theta) = I_{max} \cos^2 \theta + I_{min} \sin^2 \theta, \quad (6.30)$$

Using the definition of *DOCP* in equation (6.15), for a fully polarized beam, we find,

$$DOLP = \frac{I_{max} - I_{min}}{I_{max} + I_{min}}, \quad (6.31)$$

$$DOCP = \frac{2}{\sqrt{\frac{I_{max}}{I_{min}}} + \sqrt{\frac{I_{min}}{I_{max}}}}, \quad (6.32)$$

Here the relative error in the *DOCP* measurement can be estimated by,

$$\frac{\Delta DOCP}{DOCP} = \frac{1}{2} \frac{I_{max} - I_{min}}{I_{max} + I_{min}} \sqrt{\left(\frac{\Delta I_{min}}{I_{min}}\right)^2 + \left(\frac{\Delta I_{max}}{I_{max}}\right)^2} \quad (6.33)$$

Figure 6.4 shows a typical polarization measurement scheme with a rotating linear polarizer and a detector we described above. The dots are the data and the blue and red curves are the theoretical fit to extract the polarization. The fit function uses the beam intensity defined by equation (6.30). Here the polarizer is mounted on a remote controlled stepper motor (from Suruga) and we chose 5° for the step size of a scan angle and made a full ellipse rotation. The measured power from the Si photodiode is also being recorded along with the corresponding angle position with the help of an automated script. In order to cancel out the systematic error, the transmitted power after the polarizer is also normalized to the laser power fluctuation upstream which was measured together in-situ. The whole process takes about 10 minutes to complete.

Measurements at the Cavity Exit Line

Polarization measurement at the cavity exit is made with an ellipsometer; a system composed of a quarter-wave plate, holographic beam sampler (HBS), a Wollaston prism and two Si photodiodes (S_1 and S_2) (see Figure 6.5). This system is also used for an online monitoring of cavity exit polarization. This scheme has been developed by Saclay and used in the previous IR setup [8]. It has also been adopted by other groups [5].

At the exit of the cavity, the beam reflects from a pair of compensating mirrors M_2 and M_3 . It then passes through a quarter-wave plate followed by the HBS (from Gentec-EO). The HBS allow us to sample two beams at an angle of 10° on either side of the incident beam, each carrying 1% of its total power. One of the sampled beams will be used for monitoring the cavity resonance mode by a CCD camera known as CCD₂ and the other will be collected by a fast Si photodiode known as PDT. The signal in PDT will be send to the Compton polarimeter data acquisition system

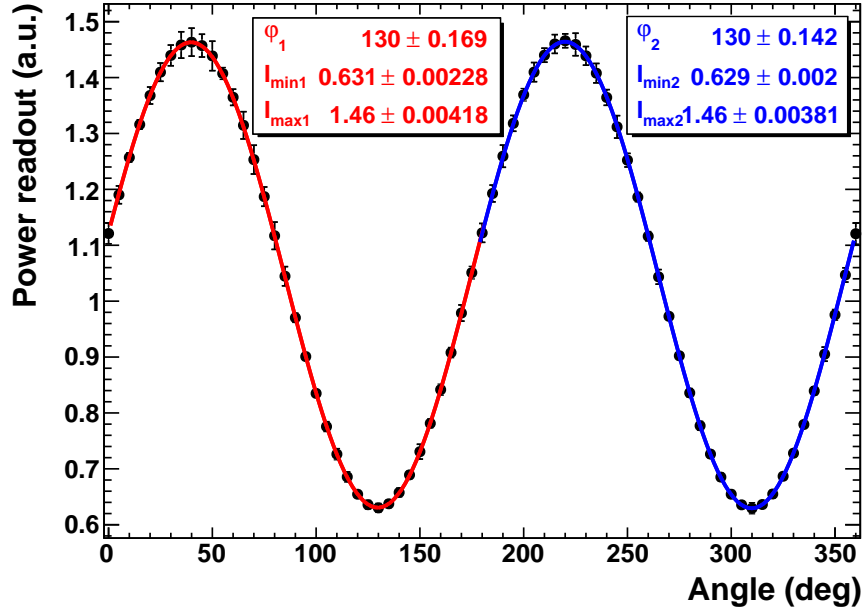


Figure 6.4 (color) A plot of linear polarizer scan angle versus the transmitted power that was used for measuring the polarization. The dots are the data and the blue and red curves are the theoretical fit to extract the polarization.

(DAQ) for cavity status determination (Locked/Unlocked). The Wollaston prism is made of two calcite prisms that are optically glued together. The optical axes of prisms oriented orthogonal to each other and it leads to an angular separation of the s - and p -waves once a elliptic polarized light passes through them. The Wollaston prism we use (from CVI) has an extinction ratio of 50 dB , a power damage threshold of $5W/cm^2$ and a separation angle of 20° .

We describe our ellipsometer using the Stokes formalism. The polarization state (\hat{S}) of incident beam is characterized by a Mueller matrix composed of four Stokes parameters by $\hat{S} = (P_0, P_1, P_2, P_3)$. During polarization measurement, when the quarter-wave plate rotated to an angle θ from its optical axis, the powers at the exit of Wollaston will be read by detectors S_1 and S_2 . The scan makes a full rotation and two powers correspond to a rotation angle position will be recorded and analyzed later.

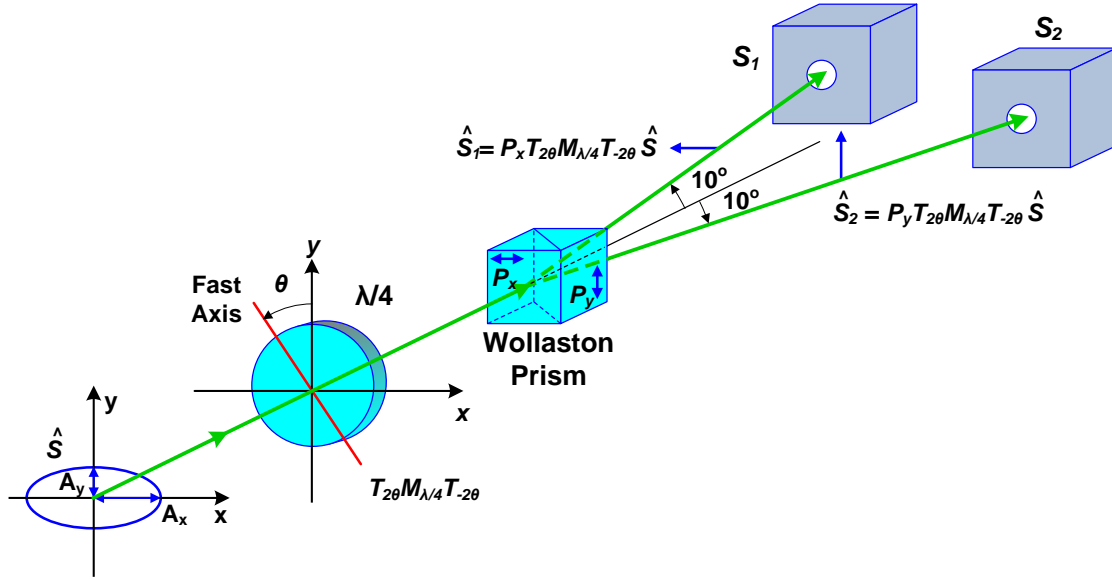


Figure 6.5 (color) A schematic of polarization measurement station at the cavity exit line (redrawn from [43]).

If we denote the powers read by S_1 and S_2 as \hat{S}_1 and \hat{S}_2 , just like the Jones matrix, we can construct its transfer matrix with Mueller matrices representing each optical elements in the system. If we let $P_{x/y}$ be the matrix of a polarizer (prism in the Wollaston) aligned along the axis Ox/Oy , $T_{2\theta}$ the rotation matrix for an angle θ in quarter-wave plate and $M_{\frac{\lambda}{4}}$ the matrix for the quarter-wave plate whose optical axis is on Oy , we can write,

$$\hat{S}_1 = P_x T_{-2\theta} M_{\frac{\lambda}{4}} T_{2\theta} \hat{S}, \quad (6.34)$$

$$\hat{S}_2 = P_y T_{-2\theta} M_{\frac{\lambda}{4}} T_{2\theta} \hat{S}, \quad (6.35)$$

where

$$P_{x/y} = \begin{pmatrix} 1 & \pm 1 & 0 & 0 \\ \pm 1 & 1 & 0 & 0 \\ 0 & 0 & 0 & 0 \\ 0 & 0 & 0 & 0 \end{pmatrix}, \quad M_{\frac{\lambda}{4}} = \begin{pmatrix} 1 & 0 & 0 & 0 \\ 0 & 1 & 0 & 0 \\ 0 & 0 & 0 & 1 \\ 0 & 0 & -1 & 0 \end{pmatrix}, \quad (6.36)$$

and

$$T_{2\theta} = \begin{pmatrix} 1 & 0 & 0 & 0 \\ 0 & \cos 2\theta & -\sin 2\theta & 0 \\ 0 & \sin 2\theta & \cos 2\theta & 0 \\ 0 & 0 & 0 & 1 \end{pmatrix}, \quad (6.37)$$

we obtain expressions for the vectors \hat{S}_1 and \hat{S}_2 ,

$$\hat{S}_1 = \frac{1}{2}(P_0 - P_1 \cos^2 2\theta + P_2 \cos 2\theta \sin 2\theta - P_3 \sin 2\theta) \begin{pmatrix} 1 \\ 1 \\ 0 \\ 0 \end{pmatrix}, \quad (6.38)$$

$$\hat{S}_2 = \frac{1}{2}(P_0 + P_1 \cos^2 2\theta - P_2 \cos 2\theta \sin 2\theta + P_3 \sin 2\theta) \begin{pmatrix} 1 \\ -1 \\ 0 \\ 0 \end{pmatrix}, \quad (6.39)$$

The intensities I_1 and I_2 received by the spheres S_1 and S_2 are given, respectively, by the first component of \hat{S}_1 and \hat{S}_2 .

For an angle $\theta = \frac{\pi}{4}$, the DOCP is expressed by the intensities I_1 and I_2 as,

$$DOCP = \frac{I_1 - I_2}{I_1 + I_2} = \frac{P_3}{P_0}, \quad (6.40)$$

This scheme requires a very precise alignment of the slow axis of the quarter-wave plate to the horizontal axis of the Wollaston prism. It was experimentally determined with a Glan polarizer. We oriented the Wollaston in such a way as to make its axes correspond to the horizontal (Ox) and vertical (Oy) directions on the optics table. Without the quarter-wave plate, we oriented the fast axis of the polarizer parallel to the axis (Ox) by maximizing the power on S_1 . Then inserted the quarter-wave plate between them and rotated it until we see a maximum on S_1 again. This will calibrate the fast axis of quarter-wave plate and we found it to be 1.5° from its mechanical zero on the frame it is mounted to.

Here, equation (6.40) tells us that when $\theta = \frac{\pi}{4}$, our system can provide an online monitoring of polarization after the cavity. But it does not provide the information about the orientation of polarization ellipse. It can be done by complete characterization of all four Stokes parameters by a full rotation (scan) of quarter-wave plate. We can express them in terms of rotation angle θ as [44],

$$\begin{aligned}
 P_0 &= I_1(\theta) + I_2(\theta), \\
 P_1 &= \frac{I_2(\theta) - I_1(2\pi - \theta)}{\cos^2 2\theta}, \\
 P_2 &= \frac{I_1(\theta - \frac{\pi}{2}) - I_1(2\pi - \theta)}{\cos 2\theta \sin 2\theta}, \\
 P_3 &= \frac{I_1(\theta - \frac{\pi}{2}) - I_1(\theta)}{\sin 2\theta},
 \end{aligned} \tag{6.41}$$

Figure 6.6 shows a plot of typical quarter-wave plate scan at the cavity exit used

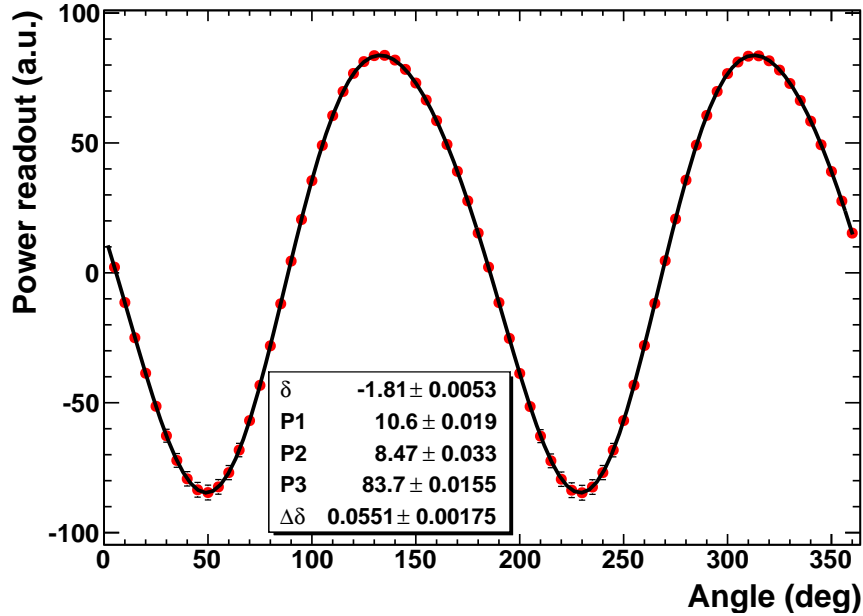


Figure 6.6 (color) Extraction of Stokes parameters from a quarter-wave plate scan at the cavity exit. The plot shows a total power measured by two photodiodes S_1 and S_2 versus the scan angle.

for the extraction of Stokes parameters. The plot shows a total power measured by two photodiodes S_1 and S_2 versus the quarter-wave plate scan angle. The red dots are data and black curve is the theoretical formula based on equation (6.41). Equations (6.19) and (6.20) allow us to determine the orientation and ellipticity of polarization ellipse.

We have discussed two independent way of measuring the degree of polarization. When we make the polarization transfer function measurement, we use linear polarizer method for measuring the CIP polarization and the exit line polarization measurement can be accomplished by both methods.

6.2.2 Polarization Transfer Function

The principle of our approach is to be able to characterize the state of polarization at the center of cavity for a measured state of polarization at the cavity exit. The transfer function gives a full information of the elements of Jones matrix for a given optical system based on a well known initial and final state of polarization. Therefore, using transfer matrix, one can propagate a polarized beam through this system and predict (calculate) its final state or using the inverse of transfer matrix, a final state of polarization can be back propagated to its initial state.

In our case, the transfer function allows us to determine the polarization and its orientation at the cavity center (or CIP) based on the degree and orientation of polarization measured at the cavity exit. Since this can only be done without the cavity, the system we have to model is composed of two mirrors M_s and M_3 (see Figure 6.7). The Jones vector representing the state of polarization at the CIP can be written as,

$$\hat{J}_{CIP} = \frac{1}{\sqrt{a^2 + b^2}} \begin{pmatrix} a \\ \pm ib \end{pmatrix}, \quad (6.42)$$

it will have the following relationship with the Exit polarization vector J_{Exit} ,

$$\hat{J}_{Exit} = [TF] \bullet \hat{J}_{CIP}, \quad (6.43)$$

where $[TF]$ represents the transfer function between them. $[TF]$ is a matrix which includes information about a phase shift δ upon reflection on the mirror, a polarization orientation rotation θ introduced by the mirror with respect to the axis Ox and another rotation angle α caused by any change of orientation of the coordinate frame. The associated matrices will have the following form,

$$R(\delta) = \begin{pmatrix} e^{i\frac{\delta}{2}} & 0 \\ 0 & e^{-i\frac{\delta}{2}} \end{pmatrix}, \quad T(\alpha) = \begin{pmatrix} \cos \alpha & -\sin \alpha \\ \sin \alpha & \cos \alpha \end{pmatrix}, \quad (6.44)$$

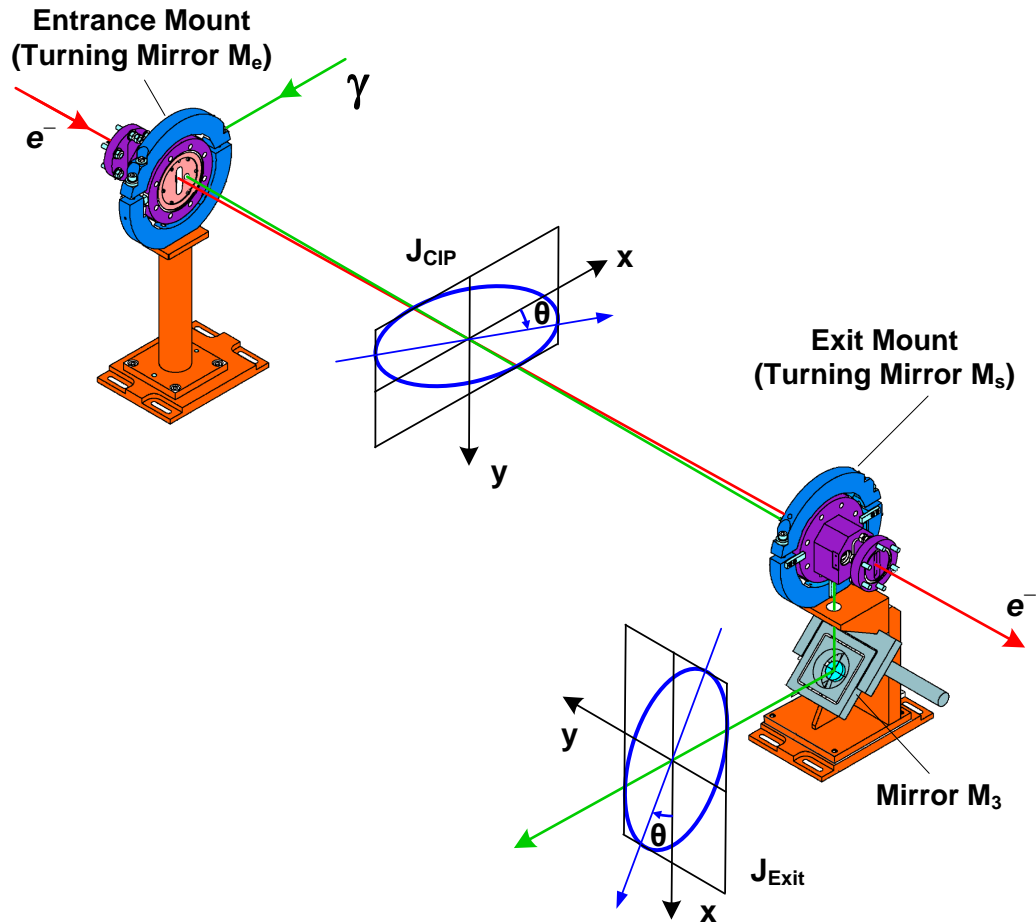


Figure 6.7 (color) A propagation of polarization ellipse from the CIP to the entrance of cavity exit line. The schematic illustrates a case when the cavity between the two stands is removed.

$$P(\theta) = \begin{pmatrix} \cos \theta & \sin \theta \\ -\sin \theta & \cos \theta \end{pmatrix} \quad (6.45)$$

The characteristic transfer matrix of a dielectric mirror is represented by the product of above matrices,

$$\begin{aligned} M(\delta, \theta, \alpha) &= P(-\theta)R(\delta)P(\theta)T(\alpha) \\ &= \begin{pmatrix} \cos \frac{\delta}{2} + i \sin \frac{\delta}{2} \cos 2\theta & i \sin \frac{\delta}{2} \sin 2\theta \\ i \sin \frac{\delta}{2} \sin 2\theta & \cos \frac{\delta}{2} - i \sin \frac{\delta}{2} \cos 2\theta \end{pmatrix} \begin{pmatrix} \cos \alpha & -\sin \alpha \\ \sin \alpha & \cos \alpha \end{pmatrix}, \end{aligned} \quad (6.46)$$

and the total transfer matrix of a system composed of two mirrors M_s and M_3 is,

$$[TF] = [M_s(\delta_s, \theta_s, \alpha_s) \bullet M_3(\delta_3, \theta_3, \alpha_3)], \quad (6.47)$$

and \hat{J}_{CIP} is calculated by,

$$\hat{J}_{CIP} = [TF]^{-1} \bullet \hat{J}_{Exit}, \quad (6.48)$$

As we can see from equation (6.47), for a system with two dielectric mirrors, in order to get its full transfer matrix, we have six parameters to characterize. This can be accomplished first by preparing a set of polarization states with well known DOCP and ellipse angle at the CIP and then measure the corresponding polarization state at the cavity exit. Once we have the initial and final state vectors based on these states with orientations covering from 0 to π , theoretically we have enough number of equations to solve and determine the parameters. Figure 6.8 illustrates a station used for generating a set of eigenstates for transfer function measurement. It composed of a Glan-Laser polarizer and a quarter-wave plate. When we have a desired polarization state is generated with an ellipse orientation, we rotate both elements by the same angle which leads to a rotation of ellipse angle for a fixed degree of polarization. The measurement of DOCP after this station (which we call CIP here) was done by a system explained in Figure 6.3. The exit polarization measurement was accomplished by the ellipsometer shown in Figure 6.5.

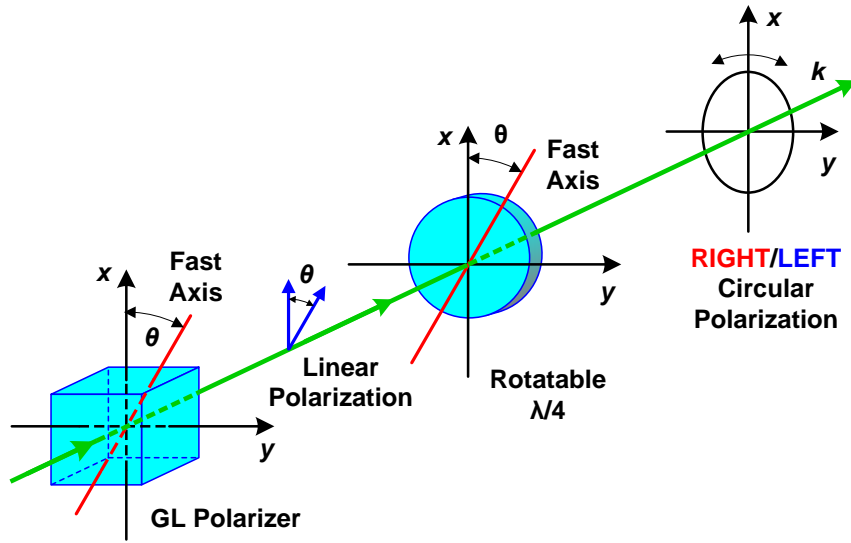


Figure 6.8 (color) A schematic illustration of an eigenstate generator at the CIP.

CIP		Exit	
DOCP (%)	Angle ($^{\circ}$)	DOCP (%)	Angle ($^{\circ}$)
91.7	50.1	78.5	137.1
91.6	30.3	78.2	124.5
91.6	9.9	82.8	111.6
91.6	169.8	90.0	97.6
91.4	149.7	96.2	79.1
92.2	129.4	99.1	40.0
92.7	109.0	96.8	179.3
92.2	89.4	90.4	163.2
92.1	69.5	83.4	149.9

Table 6.3 A DOCP and ellipse orientation measurement at the cavity exit line with respect to a series of left circular polarization states of 92.0% set at the CIP.

In summer 2010, we spent more than one month to experimentally determine the polarization transfer function of newly installed green cavity system in the Hall A of Jefferson Lab. It involves breaking up the cavity vacuum, removing the cavity mirrors and conduct a set of polarization measurements both at the CIP and at cavity exit line. Table 6.3 summarizes a measurement DOCP and orientation of the ellipse at the CIP and Exit for the incident left circular polarization of 92.0%. We also have another set of data for the right circular polarization state of -92.0% to be used in transfer function determination.

The data in Table 6.3 are used in a root [116] program to extract the transfer matrix parameters for mirrors M_s and M_3 . We also have an auxiliary set of measurement for the circular polarization states of $\pm 97\%$ to validate the transfer function. Our calculation shows that using $\pm 97\%$ data gave an average uncertainty of $(\Delta DOCP)_{CIP}/(DOCP)_{CIP} = 0.12\%$ in determination of DOCP at the CIP. We also validated this transfer function for our nominal polarization state created by the first quarter-wave plate (QWP1).

State of Polarization	Left	Right
Measurement		
DOCP (%)	99.57	-98.07
Angle ($^\circ$)	58.60	19.35
Calculation		
DOCP (%)	99.26	-97.59
Angle ($^\circ$)	83.52	17.5

Table 6.4 The measured and calculated values of DOCP and ellipse angle at the CIP.

Table 6.4 shows a comparison between the measured and calculated values of DOCP and corresponding angle at the CIP. It can be seen from the table that, the DOCP calculation from the transfer function agrees with the measurement at the

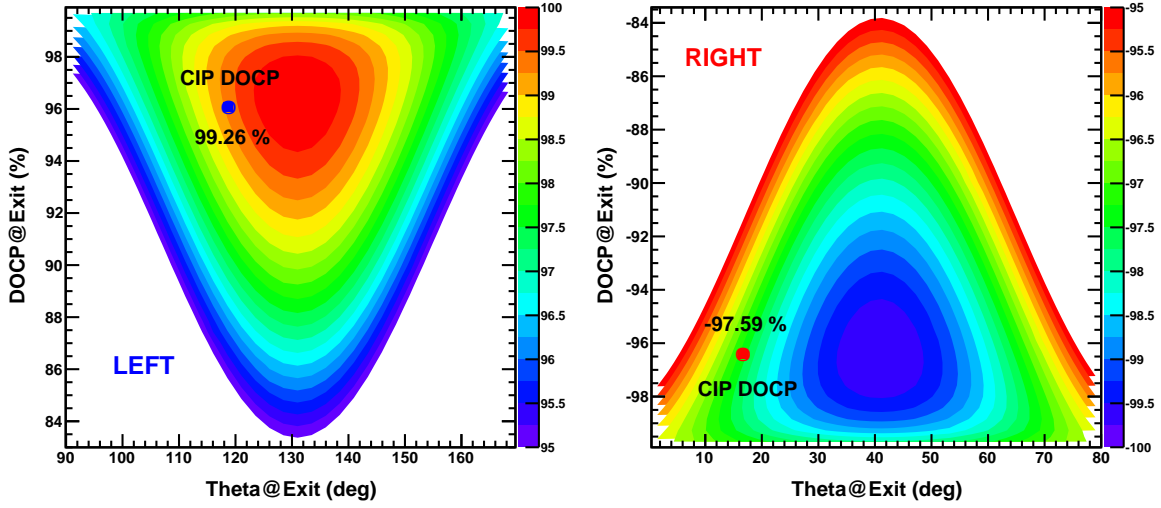


Figure 6.9 (color) A counter view of the transfer function for the left and right circularly polarized states of the CIP with respect to the exit DOCP and ellipse angle.

level of $(\Delta DOCP)_{CIP}/(DOCP)_{CIP} = 0.49\%$, while the largest uncertainty in the determination of polarization angle orientation was $\delta\theta = 25^\circ$.

Once we have the parameters extracted and validated with good precision ($< 0.5\%$), the transfer function is fully established and can be used for determining the CIP polarization from any exit polarization state. Figure 6.9 shows a counter view of transfer function for the left and right circularly polarized states obtained with the above measurement.

In the next subsection, we will discuss how we used this transfer function to determine the CIP polarization during PREx experiment.

6.2.3 Determination of the DOCP at the CIP

The determination of DOCP at the CIP needs two parameters from the exit line measurement: the DOCP and angle θ . We can write the functional relationship between them as following,

$$(DOCP)_{CIP} = TF[DOCP_{Exit}, \theta_{Exit}] \quad (6.49)$$

As we mentioned before, the ellipsometer at the cavity exit line is capable of monitoring the exit polarization online. But, in order to get a full information about the CIP polarization, we have need to have ellipse angle information available, therefore a full quarter-wave plate scan is necessary. Since running the quarter-wave plate (QWP2) disrupts the signal going into the Compton DAQ, we can only do a quarter-wave plate scan when the DAQ is not running and the cavity stay locked. For a typical running condition of the Compton polarimeter, we do as many quarter-wave plate scans as possible at the cavity exit and analyze them in order to determine the CIP polarization. Table 6.5 shows a list of exit line polarization and corresponding CIP polarization calculated by the transfer function during PREx running conditions. As we can see from the table, the stabilities of $DOCP_{Exit}$ and θ_{Exit} over the 2 month period were at the level of 0.1% and 0.6° , respectively.

Left Circular			Right Circular		
$DOCP_{Exit}$	θ_{Exit}	$DOCP_{CIP}$	$DOCP_{Exit}$	θ_{Exit}	$DOCP_{CIP}$
95.7 %	-60.6°	99.3 %	-96.6 %	15.5°	-97.4 %
96.0 %	-60.3°	99.4 %	-96.6 %	15.5°	-97.5 %
96.0 %	-61.8°	99.3 %	-96.4 %	17.0°	-97.7 %
95.7 %	-61.4°	99.3 %	-96.3 %	17.3°	-97.7 %
95.8 %	-62.0°	99.2 %	-96.5 %	16.0°	-97.5 %
95.9 %	-62.1°	99.2 %	-96.5 %	16.0°	-97.5 %
95.9 %	-61.9°	99.2 %	-96.5 %	15.5°	-97.4 %
95.8 %	-62.6°	99.1 %	-96.5 %	16.7°	-97.6 %

Table 6.5 Calculation of the DOCP at the CIP from the DOCP and θ measured at the cavity exit line using the transfer function.

The stability of intra-cavity polarization is also very important. During the locked state of the cavity, we monitored the long term stability of the exit line polarization

online. Figure 6.10 shows a record for right-circular polarization state monitored for 7 hours. The data shows the measured variations are on the order of 0.03%.

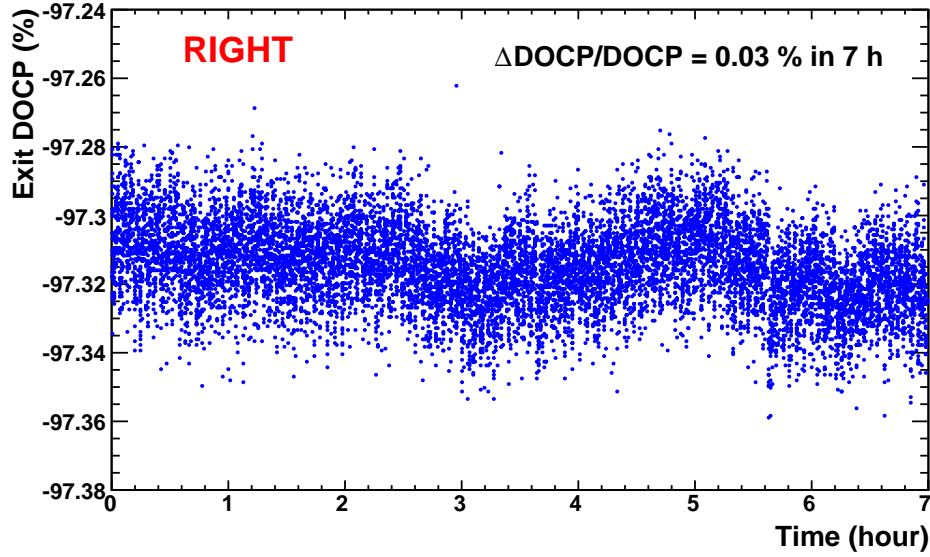


Figure 6.10 (color) The evolution of polarization at the cavity exit versus time with electron beam in Compton chicane.

After averaging the above measurements and calculations, we can summarize the average DOCP and corresponding ellipse angle orientation correspond to the running conditions during PREx as shown in Table 6.6.

CIP		Exit	
DOCP (%)	Angle (°)	DOCP (%)	Angle (°)
99.26	83.52	95.90	-61.05
-97.59	17.50	-96.53	16.21

Table 6.6 The average DOCP and ellipse angle calculated at the CIP and measured at the cavity exit line during PREx.

The source of systematic errors and their values are summarized in Table 6.7. Since the measurement of transfer function was accomplished without cavity mirrors

in place, we end up getting other sources of errors depend on their installation. Our estimation shows that the total systematic error bounded to 0.7% by cavity versus without cavity in place, assumed to be from other sources (birefringence of mirrors, etc.).

Source of Error	Error (%)
DOCP at exit line	0.02
θ at exit line	0.13
Variation in time	0.04
Validation of transfer function	0.49
Transmitting through M_e	0.10
Transmitting through M_s	0.10
Coupling	0.10

Table 6.7 Summary of errors on the measurement of the polarization in the center of the cavity.

Without a detailed study on various birefringence, we summarize the average left and right laser polarizations ($\mathcal{P}_\gamma = DOCP_{CIP}$) during PREx period as following,

$$\mathcal{P}_\gamma^L = 99.26\% \pm 0.70\% (\text{sys}) \pm 0.10\% (\text{stat}),$$

$$\mathcal{P}_\gamma^R = -97.59\% \pm 0.70\% (\text{sys}) \pm 0.13\% (\text{stat}),$$

So far we haven't discussed about possible birefringence effect from cavity system. Just like the birefringence of the steering mirrors we pointed out before, the cavity mirrors or their dielectric layers could be birefringent and therefore raises the problem of polarization at the CIP. In the next subsection, we will give a brief overview about birefringence induced by various factors in our cavity system.

6.2.4 The Birefringence of the Cavity System

Birefringence refers to the phase delay introduced between two perpendicular polarization components of a wave while traveling in an anisotropic medium. If the birefringence is homogenous over the laser beam spot size, it can be compensated; if it is not, it can not be compensated. For a system like we have, possible birefringence effects could be induced by optical elements.

The cavity mirrors may introduce a birefringence because of thermoelastic deformation due to high power circulating inside the cavity [118, 119].

The mirror mounting system could be a source of birefringence. Ref. [104] estimated the order of magnitude of the birefringence according to the pressure supplied on the mirror and the mirror thickness.

The glass-metal welding [117] and the pressure difference between vacuum and air acting on the vacuum window of the cavity [104] also can induce a birefringence.

A birefringence can also be induced by multi-layer coatings or a birefringent substrate of the cavity mirrors [120–122, 124]. A substrate with birefringent qualities acts simply like a retarder plate and, at the entrance and exit of the cavity, causes a modification of polarization. This effect can be studied by measuring the difference in polarization of the signal transmitted through the substrate.

In Ref. [43], according to a measured finesse, a method to estimate the birefringence induced by the multilayer coatings is described based on the following relation,

$$\Phi_r < \frac{\pi}{2\mathcal{F}}, \quad (6.50)$$

where Φ_r is the birefringence of the mirrors and \mathcal{F} is the finesse of the cavity. This implies that, according to the measured finesse of our cavity, the maximum birefringence $\Phi_r \approx 1.0 \times 10^{-4}$ rad. The cavity gain related to this birefringence is [43],

$$G = \frac{T^2}{(1-R)^2} \frac{1}{1 + \left(\frac{\mathcal{F}\Phi_r}{\pi}\right)^2}, \quad (6.51)$$

However, Ref. [43] also showed that the DOCP inside the cavity depends on the frequency difference between the laser and cavity resonance defined by the cavity bandwidth. This effect is $\pm 0.1\%$ change in DOCP inside the cavity over the bandwidth of our cavity.

In conclusion, estimating all these birefringence is not trivial. Furthermore, we didn't have enough knowledge about studying these birefringence effects before we install the cavity in the accelerator tunnel. But the method based on the above estimate, at least gives us an order of magnitude of the birefringence we have in our system.

6.3 Electron Beam Polarization

All our effort so far is about how to make a reliable photon target for the electron beam so that there is an efficient Compton scattering. In this section, without going into the details, we will briefly present the results of electron beam polarization measurement conducted for the first time with our newly installed setup during PREx.

6.3.1 Compton Spectrum

The electron beam polarization measurement can be achieved by one of the three ways at the down stream of cavity: detecting the backscattered Compton photons, detecting the scattered Compton electrons, detecting both the photons and electrons simultaneously. The Compton polarimeter we have measures electron beam polarization based on the detection of scattered Compton photons during electron helicity reversal at a rate of 120 Hz. In Chapter 3, we gave a small description about the photon detector and the data acquisition system it uses.

Figure 6.11 shows the scattered photon rates measured with the photon detector for an electron beam energy and current of 1.0 GeV and 50 μA , respectively. During the data taking laser polarization flips from left to right state at a regular interval and

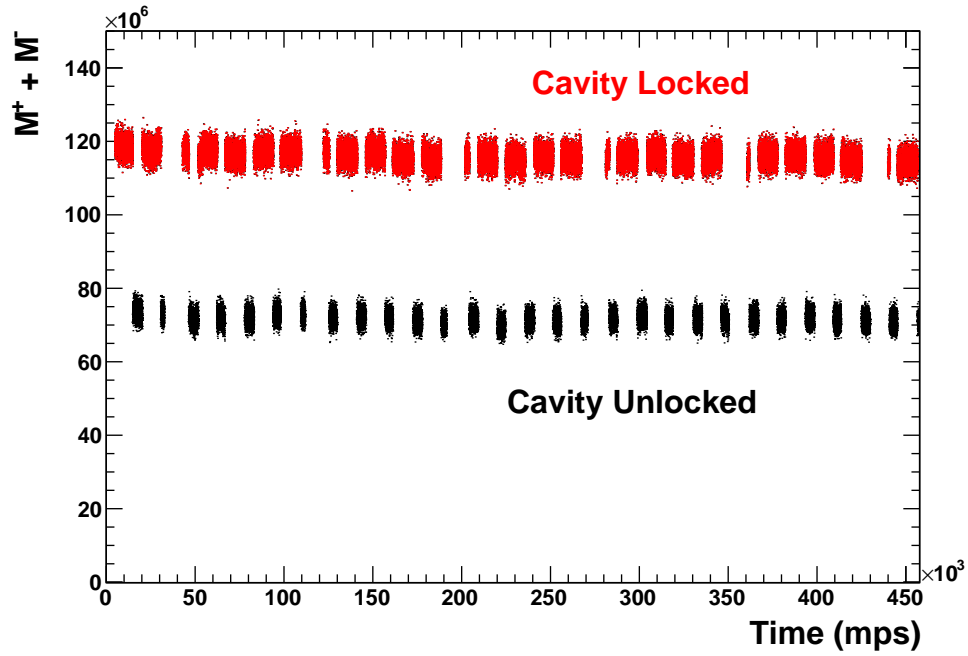


Figure 6.11 (color) Scattered Compton photon rates (red) along with the background rates (black) during a run.

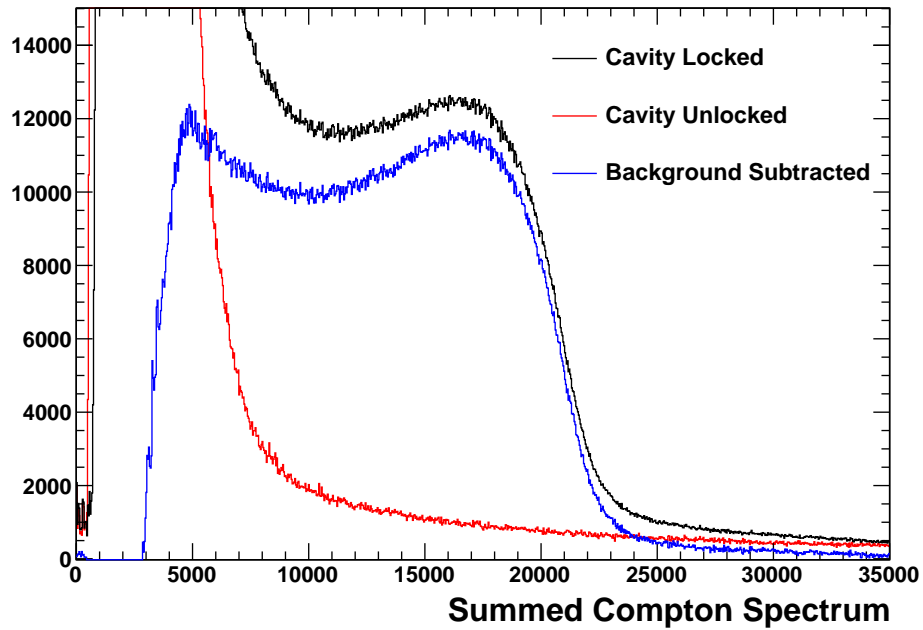


Figure 6.12 (color) A measured Compton photon energy spectrum.

cavity is unlocked, in order to cancel the systematic effects caused by electron beam properties. In this period, background and other noises are also being measured and used for subtracting it from the rates measured when the cavity is locked.

The measured Compton photon energy spectrum is shown in Figure 6.12. The horizontal axis is energy deposited in the GSO crystal in summed raw-ADC units.

6.3.2 Experimental Asymmetry

The integrating photon detector DAQ uses an FADC and stores the signal for each electron helicity window, according to this relation [45],

$$S_n = N_n \langle P \rangle - Acc_n, \quad (6.52)$$

where the S_n is the physics signal extracted from one of the six FADC accumulator, N_n is the number of samples that have been summed into accumulator n , $\langle P \rangle$ is the average pedestal value for each sample, and Acc_n is the integrated ADC value for the helicity window.

The accumulator values are used to calculate the asymmetry \mathcal{A}_{exp} according to [45],

$$\mathcal{A}_{exp} = \frac{S_+ - S_-}{S_+ + S_-}, \quad (6.53)$$

for each laser helicity period, separate sums of accumulator values for all electron helicity windows are made. A sum is also made of accumulator values for the adjacent cavity-unlocked periods, to determine background, B , for the cavity-locked period.

The measured asymmetry needs to take into account the background, such that equation (6.53) becomes,

$$\mathcal{A}_{exp} = \frac{(\langle P \rangle - \langle B \rangle) - (\langle M^- \rangle - \langle B \rangle)}{(\langle M^+ \rangle - \langle B \rangle) + (\langle M^- \rangle - \langle B \rangle)}, \quad (6.54)$$

where $\langle \rangle$ denotes the mean accumulator value per helicity window over each cavity (-locked or -unlocked) period. Here, M^\pm is the measured integrated signal plus background for positive (negative) helicity electrons (where $S = M - B$). \mathcal{A}_{exp} is calculated separately for each laser polarization.

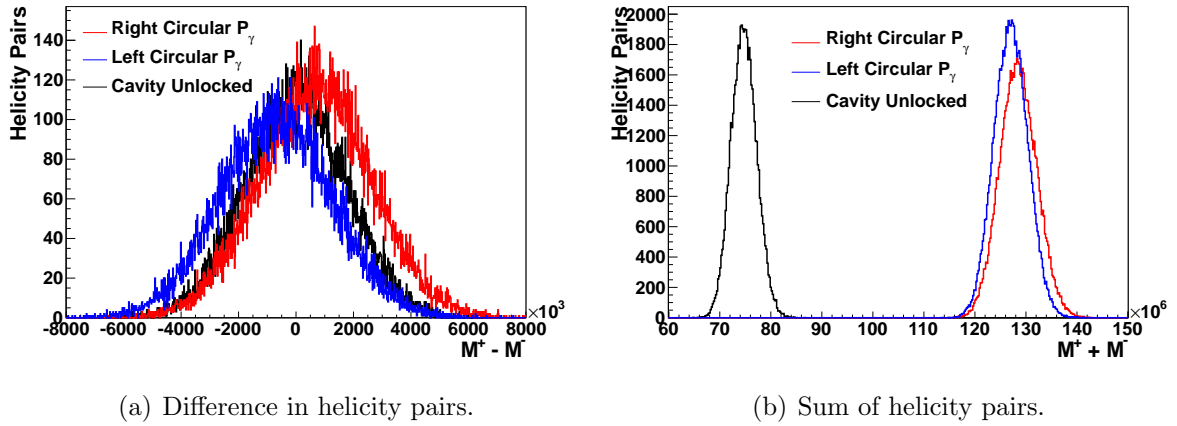


Figure 6.13 (color) Histograms of the Compton asymmetry for an entire run.

Figure 6.13(a) shows a histogram of difference in electron helicity pairs and Figure 6.13(b) shows the sum of helicity pairs. Figure 6.14 shows a histogram of a background subtracted Compton asymmetry taken for every pair in a single two hour run.

Here it worth to mention that, before the measurement of experimental asymmetry, the photon detector has to be calibrated to a well known photon energy combined with a simulation result. Calibration procedures include the photon detector response to the scattered Compton photons and data acquisition system (DAQ) and data analysis is well described in Ref. [45]. It is not the goal of this thesis to explain them, therefore they will not be described in here.

6.3.3 Electron Beam Polarization

Finally electron beam polarization \mathcal{P}_e is extracted from the measured experimental asymmetry \mathcal{A}_{exp} , according to,

$$\mathcal{A}_{exp} = \mathcal{P}_e \mathcal{P}_\gamma \mathcal{A}_{th}, \quad (6.55)$$

where \mathcal{A}_{th} is the theoretical asymmetry. Figure 6.15 shows the electron polarization measurement based on an average of two experimental asymmetry numbers obtained for left and right laser cycles during a run.

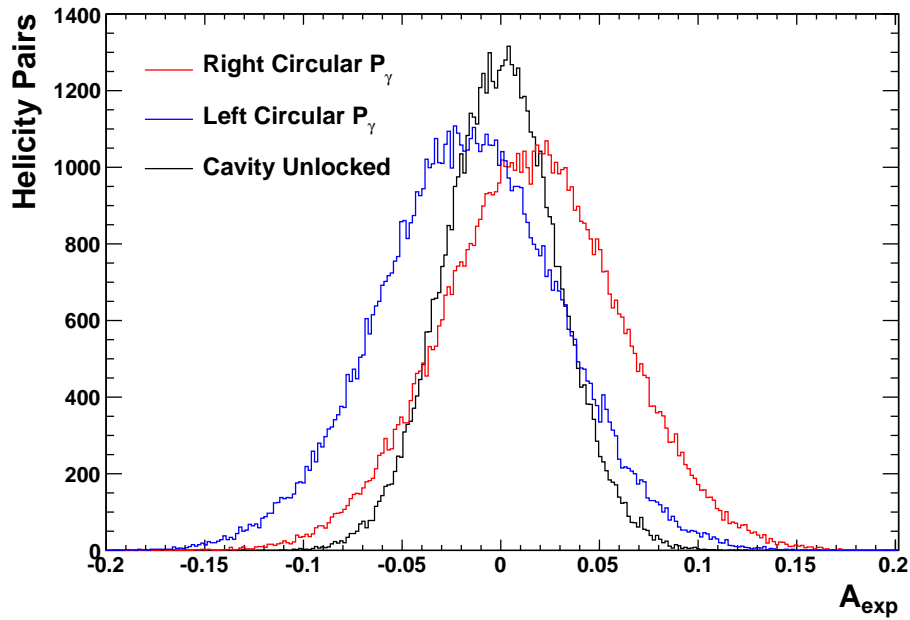


Figure 6.14 (color) Histogram of a background subtracted Compton asymmetry taken for every pair in a single one hour run.

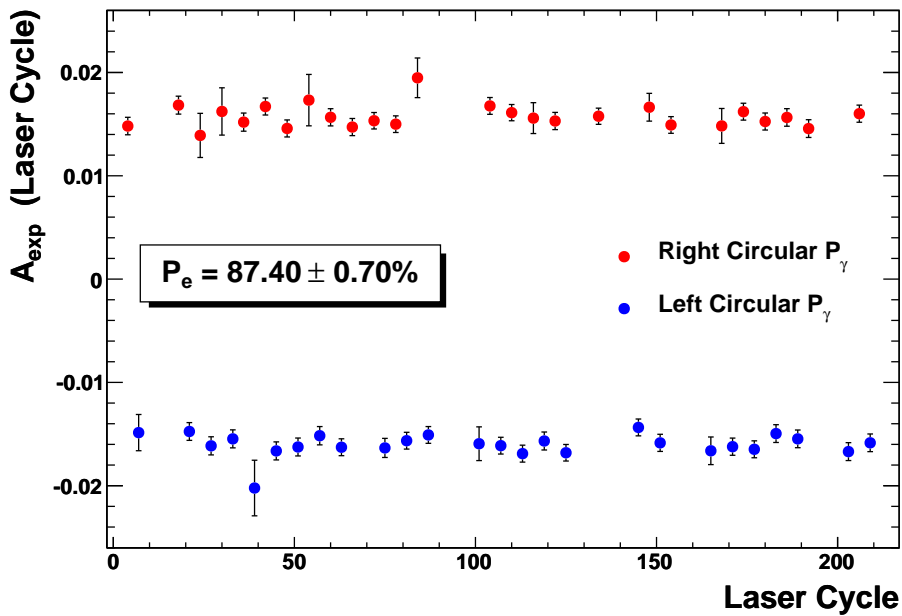


Figure 6.15 (color) An average asymmetry is used for calculating the electron beam polarization for a typical run.

The system that we installed in the hall A tunnel allows us to obtain a reliable intra-cavity power and stable photon-beam polarization for the measurement of electron beam polarization. The signal to noise ratio of the scattered Compton events were adequate to reach a high precision electron beam polarimetry.

Chapter 7

Conclusions

This thesis work has shown that the green laser and cavity project was successful. The laser power available for Compton scattering inside the cavity was enough to reach a high luminosity electron photon interaction, even at low electron beam energy. The frequency doubled green beam power was stable against the concern that PPLN may not withstand at a high power for an extended period of time. The cavity mechanical and locking stability was excellent during the three month period of PREx running, despite the concern of very high radiation and acoustically noisy environment in Hall A tunnel at JLab.

By making the green laser and cavity project successful, we provided Hall A with a unique laser source to carry out precision Compton polarimetry. The green cavity extends the operating dynamic range of Compton polarimeter from previous range of 3.0 GeV \sim 10.0 GeV to a new range of 1.0 GeV \sim 10.0 GeV. It cut short polarization measurement time as compared to the previous IR system, due to the high luminosity it generates. Through this project, we tested the low energy (1.0 GeV) electron beam polarimetry for the first time in JLab history. During the running period of PREx, the new Compton polarimeter based on green laser system achieved its 1.0% precision goal.

We have demonstrated that the frequency locking of a frequency doubled green laser generated by seeding an Nd:YAG NPRO laser to the fiber amplifier makes the

intra-cavity power scalable. This allows a possibility of boosting the intra-cavity power by increasing the injection power to the cavity. According to our estimate, with the present performance of the PPLN and its doubling efficiency, it is feasible to get ~ 10 kW intra-cavity power in 532 nm. If this is demonstrated, in addition to its Free Electron Laser (FEL) program, perhaps, it will bring a new photon source for JLab with the possibility of opening up a new research area.

Regarding the photon beam polarization inside the cavity, its always tricky to get a solid number. But with a careful and dedicated study, it should be possible to accomplish this in the near future. Recent study [125] at HERA shows that it is possible get 0.3% level precision for the intra-cavity polarization. Future high precision parity experiments at JLab would rely heavily on the green Compton polarimeter we built. This requires to improve the current precision by at least a factor of two. Since the systematic error in laser polarization is one of the dominant errors in our polarimeter, it requires a careful and systematic study.

Finally, new concepts [123] regarding the future development of Compton polarimeter at JLab with a pulsed mode locked lasers seem very attractive. If this concept is pursued and successful, it will make the system even more robust and efficient, especially in more noisy and undesirable electron beam environment after the 12 GeV upgrade of JLab.

I hope this document will provide some technical information for future design, construction and operation of an optical cavity in an accelerator environment.

Appendices

Appendix A

Technical Drawings of Cavity System

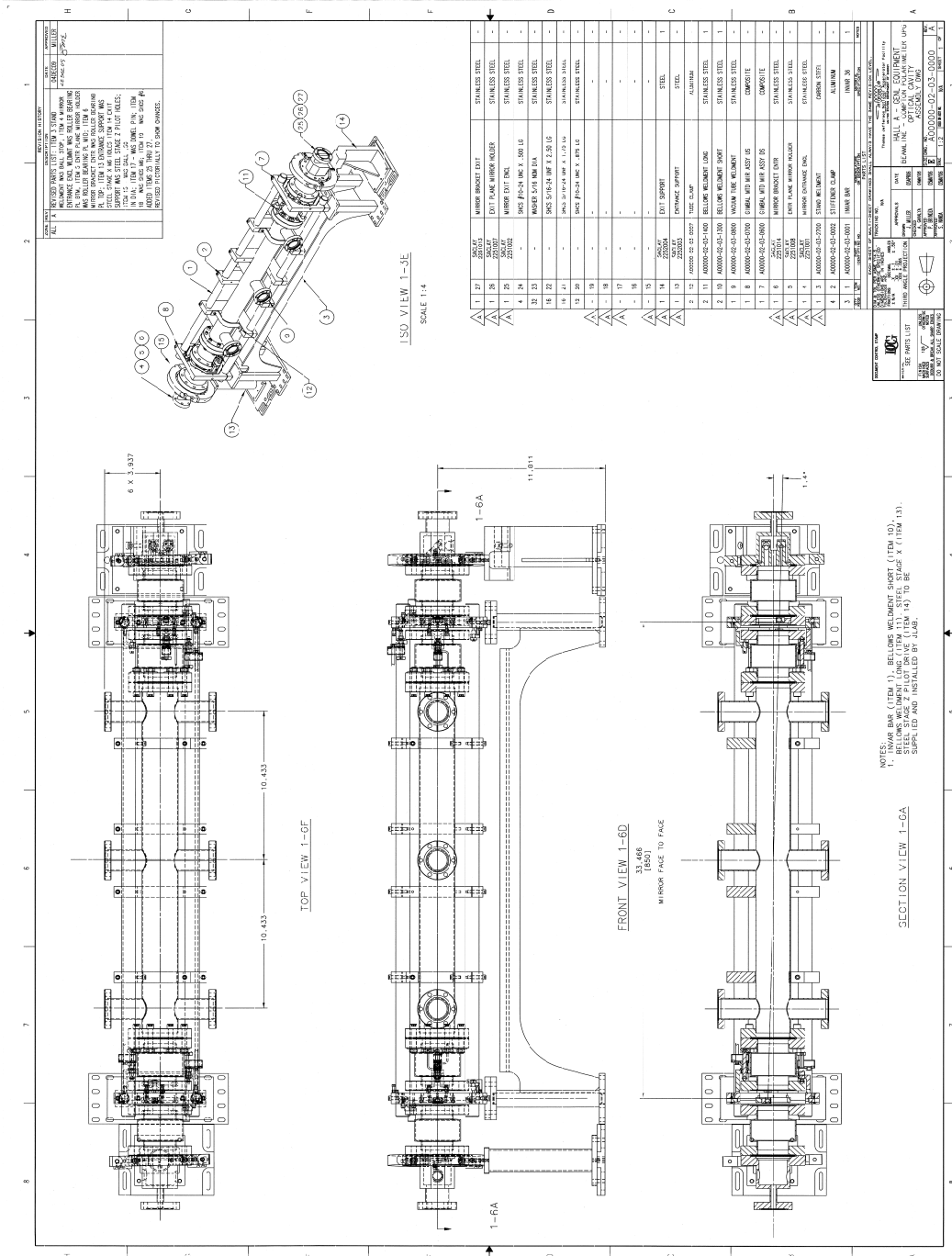


Figure A.1 Cavity assembly.

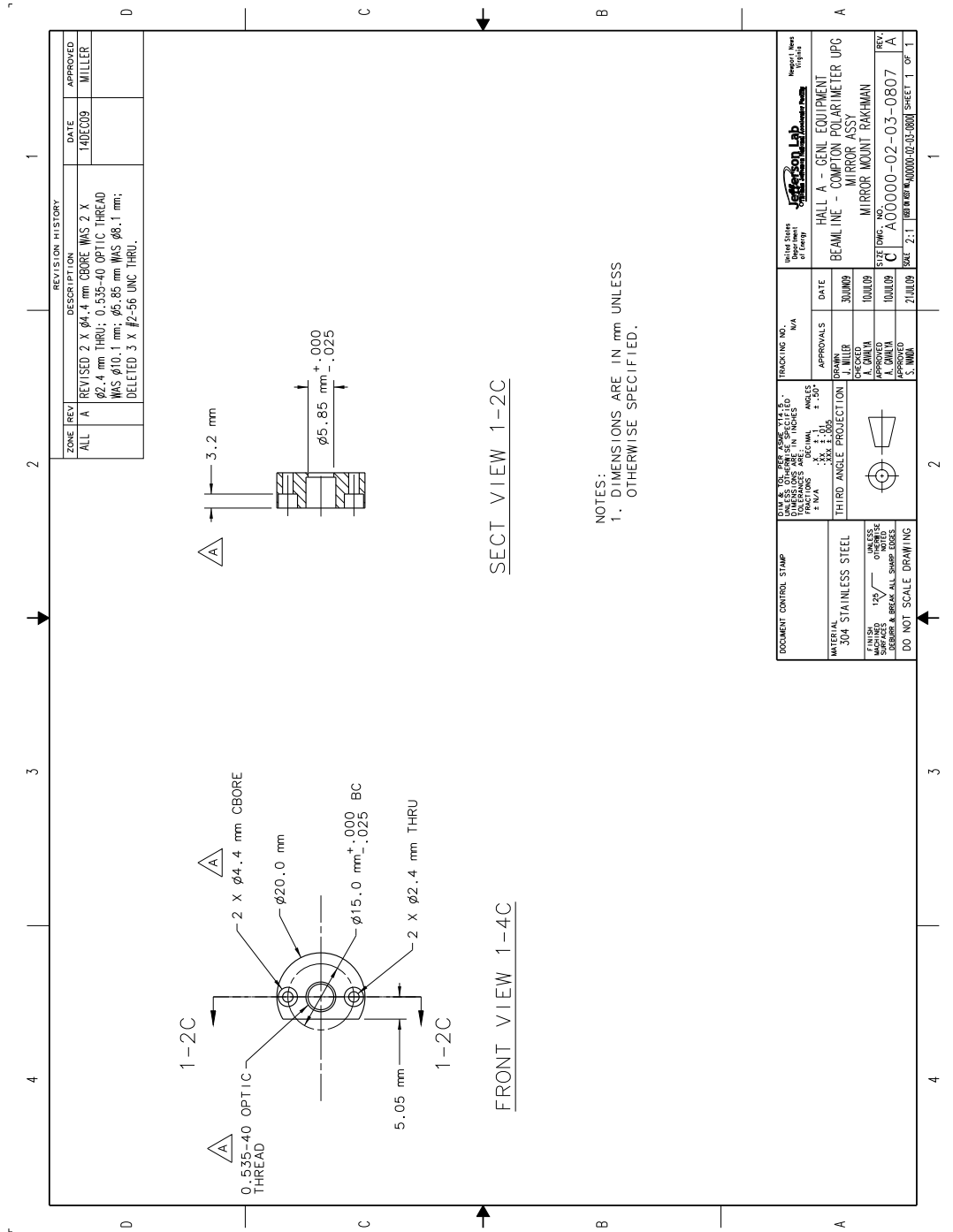


Figure A.4 Cavity Mirror Holder.

Bibliography

- [1] C. S. Wu *et al.*, “Experimental Test of Parity Conservation in Beta Decay”, *Phys. Rev.*, **105**, 1413–1415 (1957).
- [2] C. Y. Prescott *et al.*, “Parity Non-Conservation In Inelastic Electron Scattering”, *Phys. Lett.*, **B77**, 347–352 (1978).
- [3] C. Woods, “The Scanning Compton Polarimeter for the SLD Experiment”, SLAC-PUB-7319, (1996).
- [4] I. Passchier *et al.*, “A Compton Backscattering Polarimeter for Measuring Longitudinal Electron Polarization”, *Nucl. Instr. and Meth*, **A414**, 446–458, (1998)
- [5] M. Beckmann *et al.*, “The Longitudinal Polarimeter at HERA”, *Nucl. Instr. and Meth*, **A479**, 334–348, (2002)
- [6] D. Hasell *et al.*, “The BLAST Experiment”, *Nucl. Instr. and Meth*, **A603**, 247–262, (2009).
- [7] Y. Imai *et al.*, “The Compton Backscattering Polarimeter of the A4 Experiment”, *Prog. in Part. and Nucl. Phys.*, **55**, 332–335, (2005).
- [8] N. Falletto *et al.*, “Compton Scattering off Polarized Electrons with a High-Finesse Fabry-Perot Cavity at JLab”, *Nucl. Instr. and Meth*, **A459**, 412–425, (2001)

-
- [9] S. Escoffier *et al.*, “Accurate Measurement of the Electron Beam Polarization in Jlab Hall A Using Compton Polarimetry”, *Nucl. Instr. and Meth*, **A551**, 563–574, (2005)
- [10] K. Kumar, P. Souder, R. Michaels, G. Urciuoli (spokespersons) *et al.*, “A Clean Measurement of the Neutron Skin of ^{208}Pb Through Parity Violating Electron Scattering”, *Jefferson Lab Proposal E06-002*, (2005).
- [11] R. D. Carlini, S. Kowalski, S. A. Page (spokespersons) *et al.*, “A Precision Test of the Standard Model and Determination of the Weak Charges of the Quarks through Parity-Violating Electron Scattering”, *Jefferson Lab Proposal E08-016*, (2007).
- [12] H. de Vries *et al.*, “Nuclear Charge-Density-Distribution Parameters From Elastic Electron Scattering”, *Atomic and Nuclear Data Tables*, **36**, 495–536, (1987).
- [13] J. Alcorn *et al.*, “Basic instrumentation for Hall A at Jefferson Lab”, *Nucl. Instr. and Meth*, **A522**, 294–346, (2004)
- [14] P. S. Cooper *et al.*, “Polarized Electron-Electron Scattering at GeV Energies”, *Phys. Rev. Lett.* **34**, 1589–1592 (1975).
- [15] L. Kaufman, *PhD Thesis*, University of Massachusetts Amherst, (2007).
- [16] M. Poelker, “High Power Gain-Switched Diode Laser Master Oscillator and Amplifier”, *Appl. Phys. Lett.* **67**, 2762–2764, (1995).
- [17] H. Goldstein, *Classical Mechanics*, 3rd ed. (Pearson Education, Singapore 2002), p. 184.
- [18] D. J. Griffiths, *Introduction to Quantum Mechanics*, 1st ed. (Prentice Hall, New Jersey 1995), p. 154.
- [19] J. Kessler, *Polarized Electrons*, 2nd ed. (Springer, New York 1985), p. 9.

-
- [20] G. Bardin *et al.*, “Conceptual Design Report of a Compton Polarimeter for CE-BAF Hall A”, (1996).
- [21] M. Steigerwald, “MeV Mott Polarimetry at Jefferson Lab”, Proceedings of the 14th International Spin Physics Symposium, Osaka, Japan, 935-942 (2000).
- [22] J. Grames, *PhD Thesis*, University of Illinois Urbana-Champaign, (2000).
- [23] E. A. Chudakov (Editor), “JLab Hall A General Operations Manual”, (*The Hall A Collaboration*), June 23, (2010).
- [24] A. H. Compton, “A Quantum Theory of the Scattering of X-rays by Light Elements”, *Phys. Rev.* **21**, 483–502 (1923).
- [25] A. Denner, S. Dittmaier, “Complete $O(\alpha)$ QED Corrections to Polarized Compton Scattering”, *Nucl. Phys.*, **B540**, 58–86, (1999).
- [26] C. Y. Prescott, “Spin Dependent Compton Scattering for use in Analyzing Electron Beam Polarizations”, SLAC-TN-73-1, (1973).
- [27] V.N. Baier and V.A. Khoze, *Sov. J. Nucl. Phys.*, **9**, 238, (1969).
- [28] H.C. Dehne *et al.*, “Measurement of Beam-Polarization in the Storage Ring PETRA”, *AIP Conf. Proc.*, **51**, (1978).
- [29] A.S. Artamonov *et al.*, “A High Precision Measurement of the Υ -Meson Mass”, *Phys. Lett.*, **B118**, 225–229, (1982).
- [30] D.B. Barber *et al.*, “A Precision Measurement of the Υ' -Meson Mass”, *Phys. Lett.*, **B135**, 498–504, (1984).
- [31] W.W. Mackay *et al.*, “Measurement of the Υ Mass”, *Phys. Rev.*, **D29**, 2485–2490, (1984).
- [32] D. Gustavson *et al.*, “A Backscattered Laser Polarimeter for e^+e^- Storage Rings”, *Nucl. Instr. and Meth*, **165**, 177–186, (1979).

-
- [33] M. Placidi and R. Rossmanith, “ e^+e^- Polarimetry at LEP”, Nucl. Instr. and Meth, **A274**, 79–94, (1989).
- [34] M. Baylac *et al.*, “First Electron Beam Polarization Measurements with a Compton Polarimeter at Jefferson Laboratory”, Phys. Lett., **B539**, 8–12, (2002).
- [35] V. Gharibyan *et al.*, “The TESLA Compton Polarimeter”, LC-DET-2001-047, February (2001).
- [36] W. Hillert, “Compton Polarimetry at Bonn Electron-Stretcher Accelerator”, PESP 2008, October (2008).
- [37] B. Sobloher, “Polarization and Polarimetry at HERA”, PST 2009, September (2009).
- [38] A. Acha *et al.*, “Precision Measurements of the Nucleon Strange Form Factors at $Q^2 \sim 0.1\text{GeV}^2$ ”, Phys. Rev. Lett., **98**, 032301, (2007).
- [39] S. Nanda, D. Lhuillier, “Conceptual Design Report of a Hall A Compton Polarimeter Upgrade”, Jefferson Lab, (2004).
- [40] Struck GmbH, <http://www.struck.de/>
- [41] I. Freitag, InnoLight GmbH, <http://www.innolight.de/>
- [42] S. Solimeno *et al.*, “Fabry-Perot Resonator with Oscillating Mirrors”, Phys. Rev., **A43**, 6227–6240, (1991).
- [43] M. N. Falletto, *PhD Thesis*, Université Joseph Fourier-Grenoble 1, (1999).
- [44] S. Escoffier, *PhD Thesis*, Université Paris VII, (2001).
- [45] M. Friend *et al.*, “Upgraded photon calorimeter with integrating readout for Hall A Compton Polarimeter at Jefferson Lab”, [arXiv:1108.3116v2](https://arxiv.org/abs/1108.3116v2), (24 Aug 2011).
- [46] D. Parno, *PhD Thesis*, Carnegie Mellon University, (2011).

- [47] R. W. Boyd, *Nonlinear Optics*, 3rd ed. (Academic Press, London 2008), p. 2.
- [48] P. A. Franken, *et al.*, “Generation of Optical Harmonics”, *Phys. Rev. Lett.*, **7**, 118–119, (1961).
- [49] J. A. Armstrong, *et al.*, “Interactions between Light Waves in a Nonlinear Dielectric”, *Phys. Rev.*, **127**, 1918–1939, (1962).
- [50] G. D. Boyd, D. A. Kleinman, “Parametric Interaction of Focused Gaussian Light Beams”, *J. Appl. Phys.*, **39(8)**, 3597–3639 (1968).
- [51] J. A. Giordmaine, “Mixing of Light Beams in Crystals”, *Phys. Rev. Lett.*, **8(1)**, 19–20, (1962).
- [52] P. Maker, *et al.*, “Effects of Dispersion and Focusing on the Production of Optical Harmonics”, *Phys. Rev. Lett.*, **8(1)**, 21–22, (1962).
- [53] M. M. Fejer, *et al.*, “Quasi-phasematched second harmonic generation: Tuning and tolerances”, *IEEE J. Quantum. Electron.*, **QE-28**, 2631–2654, (1992).
- [54] D. S. Hum, M. M. Fejer, “Quasi-phasematching”, *C. R. Physique*, **8**, 180–198, (2007).
- [55] D. S. Hum, “Frequency conversion in near-stoichiometric lithium tantalate fabricated by vapor transport equilibration”, *PhD Thesis*, Stanford University, (2007).
- [56] D. R. White, *et al.*, “Theory of second-harmonic generation with high-conversion efficiency”, *IEEE J. Quant. Electron.*, **QE/6(12)**, 793–796, (1970).
- [57] I. Shoji, *et al.*, “Absolute scale of second-order nonlinear-optical coefficients”, *J. Opt. Soc. Am. B*, **14(9)**, 2268–2294, (1997).
- [58] D. A. Roberts, “Simplified characterization of uniaxial and biaxial nonlinear optical crystals: a plea for standardization of nomenclature and conventions”, *IEEE J. Quant. Electron.*, **28(10)**, 2057–2074, (1992).

- [59] A. Smith, AS-Photonics, “SNLO Software”, <http://www.as-photonics.com/> (Accessed August 15, 2011).
- [60] G. D. Miller, “Periodically poled lithium niobate: modeling, fabrication, and nonlinear-optical performance”, *PhD Thesis*, Stanford University, (1998).
- [61] M. Houe and P. D. Townsend, “Thermal polarization reversal of lithium niobate”, *Appl. Phys. Lett.*, **66**, 2667–2669, (1995).
- [62] R. V. Roussev, “Optical-Frequency Mixers in Periodically Poled Lithium Niobate: Materials, Modeling and Characterization”, *PhD Thesis*, Stanford University, (2006).
- [63] J. Schwesyg, “Interaction of light with impurities in lithium niobate crystals”, *PhD Thesis*, Universität Bonn, (2011).
- [64] F. S. Chen, “Optically induced change of refractive indices in LiNbO_3 and LiTaO_3 ”, *J. Appl. Phys.*, **40(8)**, 3389–3396, (1969).
- [65] Y. Furukawa, *et al.*, “Photorefraction in LiNbO_3 as a function of $[\text{Li}]/[\text{Nb}]$ and MgO concentrations”, *Appl. Phys. Lett.*, **77(16)**, 2494–2496, (2000).
- [66] Y. Furukawa, *et al.*, “Optical damage resistance and crystal quality of LiNbO_3 single crystals with various $(\text{Li})/(\text{Nb})$ ratios”, *J. Appl. Phys.*, **72(8)**, 3250–3254, (1992).
- [67] L. E. Myers and W. R. Bosenberg, “Periodically poled lithium niobate and quasi-phased-matched optical parametric oscillators”, *IEEE J. Quant. Electron.*, **33**, 1663–1667, (1997).
- [68] Y. Furukawa, *et al.*, “Green-induced infrared absorption in MgO doped LiNbO_3 ”, *Appl. Phys. Lett.*, **78(14)**, 1970–1972, (2001).
- [69] W. Sellmeier, “Zur Erklärung der abnormen Farbenfolge im Spectrum einiger Substanzen”, *Ann. Phys. Chem.*, **219**, 272–282 (1871).

- [70] Wikipedia, “Lithium Niobate”, http://en.wikipedia.org/wiki/Lithium_niobate (Accessed September 5, 2011).
- [71] M. Yamada, *et al.*, “Fabrication of periodically reversed domain structure for SHG in LiNbO₃ by direct electron beam lithography at room temperature”, *Electron. Lett.*, **27**, 828–829, (1991).
- [72] G. D. Miller, *et al.*, “42%-efficient single-pass cw second harmonic generation in periodically poled lithium niobate”, *Opt. Lett.*, **22**, 1834–1836, (1997).
- [73] D. A. Bryan, *et al.*, “Increased optical damage resistance in lithium niobate”, *Appl. Phys. Lett.*, **44**, 847–849, (1984).
- [74] K. Muuchi, *et al.*, “Harmonic blue light generation in bulk periodically poled MgO:LiNbO₃”, *Electron. Lett.*, **32**, 2091–2092, (1996).
- [75] K. Muuchi, *et al.*, “Efficient 340-nm light generation by a ridge-type waveguide in a first-order periodically poled MgO:LiNbO₃”, *Opt. Lett.*, **28**, 1344–1346 (2003).
- [76] H. Furuya, *et al.*, “High-beam-quality continuous wave 3W green-light generation in bulk periodically poled MgO:LiNbO₃”, *Jpn. J. Appl. Phys.*, **45**, 6704–6706, (2006).
- [77] N. Pavel, *et al.*, “Room-temperature, continuous-wave 1-W green power by single-pass frequency doubling in a bulk periodically poled MgO:LiNbO₃ crystal”, *Opt. Lett.*, **29(8)**, 830–832, (2004).
- [78] R. Paschotta, *et al.*, “82% efficient continuous-wave frequency doubling of 1.06 μm with a monolithic MgO:LiNbO₃ resonator”, *Opt. Lett.*, **19(17)**, 1325–1328, (1994).
- [79] M. G. Pullen, *et al.*, “Efficient generation of >2W of green light by single-pass frequency doubling in PPMgLN”, *Appl. Opt.*, **47(10)**, 1397–1400, (2008).

-
- [80] D. H. Jundt, “Temperature-dependent Sellmeier equation for the index of refraction, n_e , in congruent lithium niobate”, *Opt. Lett.*, **22(20)**, 1553–1555, (1997).
- [81] A. E. Siegman, “Lasers”, University Science Books, Mill Valley, California, (1986).
- [82] A. E. Siegman, “How to (Maybe) Measure Laser Beam Quality”, Tutorial presentation at the Opt. Soc. Am. Annual Meeting Long Beach, California, Oct. (1997).
- [83] G. Hernandez, “Fabry-Perot Interferometers”, Cambridge University Press, Cambridge, UK, (1986).
- [84] A. Variola, A. Loulergue, F. Zomer, “ThomX Conceptual Design Report”, Laboratoire de l’Accélérateur Linéaire (LAL) Technical Note, (2009).
- [85] S. Miyoshi *et al.*, “Photon generation by laser-Compton scattering at the KEK-ATF”, *Nucl. Instr. and Meth*, **A623**, 576–578, (2010).
- [86] K. Sakaue *et al.*, “Development of a laser pulse storage technique in an optical super-cavity for a compact X-ray source based on laser-Compton scattering”, *Nucl. Instr. and Meth*, **A637**, S107–S111, (2011).
- [87] J. R. Lawall, “Fabry-Perot metrology for displacements up to 50 mm”, *J. Opt. Soc. Am. A*, **22**, 2786–2798 (2005).
- [88] A. Abramovici *et al.*, “LIGO, the Laser Interferometer Gravitational-Wave Observatory”, *Science*, **256**, 325–333, (1992).
- [89] E. Zavattini *et al.*, “Experimental Observation of Optical Rotation Generated in Vacuum by a Magnetic Field”, **96**, 110406, (2006).
- [90] Y. Yamamoto and R. E. Slusher, “Optical Processes in Microcavities”, *Physics Today*, **46**, 66–73, (June 1993).

-
- [91] G. R. Fowles, “Introduction to modern optics”, 2nd ed., Dover Publications Inc., New York, (1989).
- [92] Advanced Thin Films, Boulder, CO, <http://www.atfilms.com/>, private communication.
- [93] JDS Uniphase Corporation, Milpitas, CA, <http://www.jdsu.com/en-us/Pages/Home.aspx> (Accessed Oct. 15, 2011).
- [94] R. W. P. Drever *et al.*, “Laser phase and frequency stabilization using an optical resonator”, *Appl. Phys. B*, **B31** (2), 97 –105, (June 1983).
- [95] T. Day, “Frequency Stabilized Solid State Lasers for Coherent Optical Communications”, *PhD Thesis*, Stanford University, (1990).
- [96] G. Cantatore, *et al.*, “Frequency locking of a Nd:YAG laser using the laser itself as the optical phase modulator”, *Rev. Sci. Instrum.*, **66** (4), 2785 – 2787, (April 1995).
- [97] E. D. Black, “An introduction to Pound-Drever-Hall laser frequency stabilization”, *Am. J. Phys.*, **69** (1), 79 – 87, (January 2001).
- [98] Newport Corporation, Irvine CA, <http://www.newport.com/servicesupport/Tutorials/default.aspx?id=136> (Accessed Oct. 15, 2011).
- [99] Newport Corporation, Irvine CA, <http://www.newport.com/store/product.aspx?id=853235&lang=1033> (Accessed Oct. 15, 2011).
- [100] Argonne National Laboratory, Argonne, IL <http://www.aps.anl.gov/epics/>
- [101] A. M. De Riva, *et al.*, “Very high Q frequency-locked Fabry-Perot cavity”, *Rev. Sci. Instrum.* **67** (8), 2680 – 2684, (August 1996).
- [102] D. Z. Anderson, “Alignment of resonant optical cavities”, *Appl. Opt.*, **23** (17), 2944 – 2949, (September 1984).

- [103] E. Morrison, *et al.*, “Automatic alignment of optical interferometers”, *Appl. Opt.*, **33**, 5041–5045, (1994).
- [104] F. Zomer, “A high power Fabry-Perot resonator for precision Compton polarimetry with the longitudinally polarized lepton beams at HERA”, *PhD Thesis*, Laboratoire de l’Accélérateur Linéaire (LAL), (2003).
- [105] Ophir-Spiricon, LLC, North Logan, UT www.ophiropt.com
- [106] OptoCad, Rechenzentrum der Max-Planck-Gesellschaft am Max-Planck-Institut für Plasmaphysik, Germany, <http://home.rzg.mpg.de/~ros/optocad.html>
- [107] PI (Physik Instrumente) L.P., Auburn, MA <http://www.physikinstrumente.com/>
- [108] G. Rempe, *et al.*, “Measurement of ultralow losses in an optical interferometer”, *Opt. Lett.*, **17** (5), 363 – 365, (1992).
- [109] C. Hood *et al.*, “Characterization of high-finesse mirrors: Loss, phase shifts, and mode structure in an optical cavity”, *Phys. Rev. A*, **64**, (2001).
- [110] D. A. Smith and D. I. Shernoff, “Simple measurement of gain and loss in ultra-slow loss optical resonator”, *Appl. Opt.*, **22** (12), 1722 – 1723, (June 1985).
- [111] M. J. Lawrence, *et al.*, “Dynamic response of a Fabry-Perot interferometer”, *J. Opt. Soc. Am. B*, **16** (4), (April 1999).
- [112] J. Poirson, *et al.*, “Analytical and experimental study of ringing effects in a Fabry-Perot cavity. Application to the measurement of finesse”, *J. Opt. Soc. Am. B*, **14** (11), 2811 - 2817, (November 1997).
- [113] D. Goldstein, “Polarized Light”, 3rd ed. , Marcel Dekker Inc., New York, NY, (2003).

-
- [114] R. C. Jones, “A new calculus for the treatment of optical systems, I. Description and Discussion of the Calculus”, *J. Opt. Soc. Am. A*, **31** (7), 488 – 493, (1941).
- [115] H. Hurwitz and R. C. Jones, “A new calculus for the treatment of optical systems, II. Proof of three general equivalence theorems”, *J. Opt. Soc. Am. A*, **31** (7), 493 – 499, (1941).
- [116] ROOT program and library, CERN, Switzerland <http://root.cern.ch/drupal/>
- [117] J. E. Logan, *et al.*, *Opt. Com.*, **107** 342–346, (1994).
- [118] P. Hello, “Optical aspects of interferometric gravitational wave detector”, *Pro. Opt.* **38**, 85, (1998).
- [119] W. Winkler, *et al.*, “Birefringence-induced losses in interferometers”, *Opt. Comm.*, **112**, 245, (1994).
- [120] S. Carusotto, *et al.*, “The ellipticity introduced by interferential mirrors on a linearly polarized light beam orthogonally reflected”, *Appl. Phys.*, **B48**, 231, (1989).
- [121] P. Micossi, *et al.*, “Measurement of the birefringence properties of the reflecting surface of an interferential mirror”, *Appl. Phys.*, **B57**, 95, (1993).
- [122] D. Jacobet *et al.*, “Supermirror phase anisotropy measurement”, *Opt. Lett.*, **20**, 671, (1995)
- [123] D. Gaskell, *Private Communication*.
- [124] S. Moriwaki *et al.*, “Measurement of the residual birefringence of inferential mirror using a Fabry-Perot cavity”, *Appl. Phys.*, **b65**, 347, (1997).
- [125] V. Brissonet *et al.*, “Per mill level control of the circular polarisation of the laser beam for a Fabry-Perot cavity polarimeter at HERA”, *J. Inst.*, June (2010).

Curriculum Vitae

Personal

Name: Abdurahim Rakhman
Gender: Male
Birth place: Kucha, [Xinjiang Uyghur Autonomous Region](#), China
Marital status: Married (two sons)

Education

Ph.D., Physics **Syracuse University**, Syracuse, NY December, 2011
Thesis: The Design and Construction of a Green Laser and Fabry-Perot Cavity System for Jefferson Lab's Hall A Compton Polarimeter
Advisor: Paul Allen Souder [[URL](#)]

M.S., Physics **Syracuse University**, Syracuse, NY December 2005

Diploma **The Abdus Salam ICTP**, Trieste, Italy August 2003
Thesis: The Diffusion Mechanism of *Si* and *O* in Liquid *SiO*₂ by Molecular Dynamics Simulations.
Advisor: Sandro Scandolo [[URL](#)]

M.S./B.S., Physics **Xinjiang University**, Ürümchi, China July 2000
Thesis: The Fabrication of Ion Implanted Porous Silicon Thin Films and Studies on Photoluminescence and Humidity Sensitivity Properties.

Publications

1. "Measurement of the Neutron Radius of ²⁰⁸Pb Through Parity-Violation in Electron Scattering", S. Abrahamyan *et al.*, submitted to *Phys. Rev. Lett.*
2. "Upgraded photon calorimeter with integrating readout for Hall A Compton Polarimeter at Jefferson Lab", M.Friend *et al.*, submitted to *Nucl. Instrum. Meth. A* [[PDF](#)]

3. “Beam-Target Double Spin Asymmetry A_{LT} in Charged Pion Production from Deep Inelastic Scattering on a Transversely Polarized ^3He Target at $1.4 < Q^2 < 2.7 \text{ GeV}^2$ ”, J.Huang *et al.*, accepted by *Phys. Rev. Lett.* [[PDF](#)]
4. “New Precision Limit on the Strange Vector Form-Factors of the Proton”, HAPPEX Collaboration, submitted to *Phys. Rev. Lett.* [[PDF](#)]
5. “Single Spin Asymmetries in Charged Pion Production from Semi-Inclusive Deep Inelastic Scattering on a Transversely Polarized ^3He Target”, X.Qian *et al.*, *Phys. Rev. Lett.* **107**, 072003 (2011) [[PDF](#)]
6. “High Precision Measurement of the Proton Elastic Form Factor Ratio $\mu_p G_E/G_M$ at Low Q^2 ”, X.Zhan *et al.*, *Phys. Lett. B* **705**, 59–64 (2011) [[PDF](#)]
7. “A Green Fabry-Perot Cavity for Jefferson Lab Hall A Compton Polarimetry”, **A.Rakhman**, S.Nanda, P.Souder, *AIP Conf. Proc.*, **1149**, 1165–1169 (2009)[[PDF](#)]
8. “Phase contrast micro-CT with an ultrafast laser-based X-ray source”, R.Toth, J.C.Kieffer, A.Krol, S.Fourmaux, T.Ozaki, H.Ye, R.E.Kincaid, **A.Rakhman**, *Proc. of SPIE*, **5918**, 280–287 (2005)[[PDF](#)]
9. “Novel type humidity sensor based on the porous $\text{Si}_3\text{N}_4/\text{Si}$ composite fabricated by using N^+ -implantation and anodization”, C.Z.Tu, Z.H.Jia, **A.Rakhman**, *Phys. Stat. Sol. A*, **201**(14), 3217–3220 (2004)[[PDF](#)]
10. “The nature of humidity sensitivity of porous silicon treated by high temperature”, C.Z.Tu, **A.Rakhman**, Z.H.Jia, M.D.Tao, *Proc. of the 4th East Asian Conference on Chemical Sensors*, Hsinchu, Taiwan, pp. 497–501 (1999)

Honors & Awards

- ICTP Diploma Programme Scholarship (Italy, United Nations), ICTP, Italy, 2002.
- Gwanghwa Fellowship (Taiwan), Xinjiang University, China, 1998.
- People’s Scholarship (Ministry of Education, China), Xinjiang University, China, 1997 – 2000.
- Kojima Yasutaka Scholarship (Japan), Xinjiang University, China, 1996.

Membership

- American Physical Society (APS) student member - since 2009.
- Jefferson Lab Hall A Collaboration member - since 2008.